Turun yliopisto
University of Turku

MICHELSON INTERFEROMETER WITH PORCH SWING BEARING FOR PORTABLE FTIR SPECTROMETER

Tuomas Välikylä

TURUN YLIOPISTON JULKAISUJA – ANNALES UNIVERSITATIS TURKUENSIS
Sarja - ser. AI osa - tom. 487 | Astronomica - Chemica - Physica - Mathematica | Turku 2014

University of Turku

Faculty of Mathematics and Natural Sciences

Department of Physics and Astronomy

Physics

Doctoral Programme in Physical and Chemical Sciences

Supervised by

Jyrki Kauppinen
Professor emeritus
Department of Physics and Astronomy
University of Turku
Finland

Tom Kuusela
Docent
Department of Physics and Astronomy
University of Turku
Finland

Reviewed by

Kai-Erik Peiponen
Professor
Department of Physics and Mathematics
University of Eastern Finland
Finland

Dannis Brouwer
Associate professor (UHD)
Faculty of Engineering Technology (CTW)
University of Twente
Netherlands

Opponent

Bortolino Saggin
Professor
Department of Mechanical Engineering
Politecnico di Milano
Italy

Front cover drawing by Jaakko Alajoki

The originality of this thesis has been checked in accordance with the University of Turku quality assurance system using the Turnitin OriginalityCheck service.

ISBN 978-951-29-5724-8 (PRINT)

ISBN 978-951-29-5725-5 (PDF)

ISSN 0082-7002

Painosalama Oy - Turku, Finland 2014

Abstract

The interferometer for low resolution portable Fourier Transform middle infrared spectrometer was developed and studied experimentally. The final aim was a concept for a commercial prototype. Because of the portability, the interferometer should be compact sized and insensitive to the external temperature variations and mechanical vibrations. To minimise the size and manufacturing costs, Michelson interferometer based on plane mirrors and porch swing bearing was selected and no dynamic alignment system was applied. The driving motor was a linear voice coil actuator to avoid mechanical contact of the moving parts. The driving capability for low mirror driving velocities required by the photoacoustic detectors was studied. In total, four versions of such an interferometer were built and experimentally studied.

The thermal stability during the external temperature variations and the alignment stability over the mirror travel were measured using the modulation depth of the wide diameter laser beam. Method for estimating the mirror tilt angle from the modulation depth was developed to take account the effect from the non-uniform intensity distribution of the laser beam. The spectrometer stability was finally studied also using the infrared radiation.

The latest interferometer was assembled for the middle infrared spectrometer with spectral range from 750 cm^{-1} to 4500 cm^{-1}. The interferometer size was $(197 \times 95 \times 79)$ mm^3 with the beam diameter of 25 mm. The alignment stability as the change of the tilt angle over the mirror travel of 3 mm was 5 μrad, which decreases the modulation depth only about 0.7 percent in infrared at 3000 cm^{-1}. During the temperature raise, the modulation depth at 3000 cm^{-1} changed about $1 \ldots 2$ percentage units per Celsius over short term and even less than 0.2 percentage units per Celsius over the total temperature raise of 30 °C. The unapodised spectral resolution was 4 cm^{-1} limited by the aperture size. The best achieved signal to noise ratio was about 38 000:1 with commercially available DLaTGS detector. Although the vibration sensitivity requires still improving, the interferometer performed, as a whole, very well and could be further developed to conform all the requirements of the portable and stable spectrometer.

Tiivistelmä

Työssä kehitettiin ja testattiin interferometri kannettavaan matalan resoluution keski-infrapuna–alueen Fourier-muunnosspektrometriin. Tavoitteena oli kaupallisen prototyypin esiversio. Kannettavavn laitteen tulee olla pienikokoinen sekä sietää ympäristön lämpötilan vaihteluita ja tärinöitä. Koon ja valmistuskustannuksien minimoimiseksi, valittiin tasopeileillä toteutettu Michelsonin interferometri, jossa on kiikkutyyppinen peilin liikutusmekanismi. Lisäksi aktiivista optiikan asennon säätöä ei käytetty. Ajomoottorina oli puhekelaan perustuva lineaariliikuttaja, koska se ei vaadi mekaanista kontaktia liikkuvaan kappaleeseen. Mahdollisuutta ajaa peiliä hitaalla nopeudella tutkittiin, jotta laite sopisi myös fotoakustiselle ilmaisimelle. Yhteensä neljä interferometria rakennettiin ja tutkittiin kokeellisesti.

Lämpöstabiilisuutta ympäristön lämpötilan vaihtelujen aikana sekä optiikan keskinäisen asennon vakautta peilin ajomatkalla mitattiin käyttäen leveän laser-säteen modulaation syvyyttä. Työssä kehitettiin menetelmä peilin kallistuskulman arvioimiseksi modulaation syvyydestä, joka on mitattu käyttäen laser-sädettä, jonka intensiteetti on jakautunut epätasaisesti. Spektrometrin vakautta tutkittiin lopulta myös käyttäen infrapunasäteilyä.

Viimeisin interferometri koottiin toimimaan spektrin keski-infrapuna–alueella välillä 750 cm^{-1}–4500 cm^{-1}. Interferometrin mitat olivat ($197 \times 95 \times 79$) mm^3 ja säteen halkaisija 25 mm. Optiikan asennon vakaus ilmaistuna peilin kallistuskulman muutoksena kolmen millimetrin ajomatkalla oli 5 μrad. Se vastaa 0.7 prosenttiyksikön modulaation syvyyden laskua aaltoluvulla 3000 cm^{-1}. Ympäristön lämpötilan nousun aikana modulaatio aaltoluvulla 3000 cm^{-1} muuttui lyhyellä aikavälillä noin $1 \ldots 2$ prosenttiyksikköä Celsius-astetta kohti ja kokonaisuudessaan noin 0.2 prosenttiyksikköä Celsiusta kohti koko 30 °C lämpötilan nousun aikana. Apodisoimattoman spektrin erotuskyky oli noin 4 cm^{-1}, johon apertuurin koko sen rajoitti. Paras saavutettu signaali-kohina–suhde oli noin 38 000:1, kun käytettiin kaupallisesti saatavilla olevaa DLaTGS-ilmaisinta. Vaikka interferometrin tärinänsieto vaatiikin vielä parantelua, sen suorituskyky oli erittäin hyvä ja siitä voidaan helposti kehittää versio, joka täyttää kaikki kannettavan ja vakaan spektrometrin vaatimukset.

Acknowledgements

At first, I wish to thank my supervisors professor Jyrki Kauppinen, whose extreme expertise on FTIR, inspiring attitude and great ideas have been invaluable, and docent Tom Kuusela, who has carefully read the manuscripts and given countless amount of advices how to make the thesis better. I am also very grateful to Juha Peura, Jorma Tallberg, Jorma Heinonen, Jaakko Lehtinen and the other personnel of the Laboratory of Optics and Spectroscopy for forwarding my research.

I thank also Juha Fonsen for pairing me off with Jyrki Kauppinen and Gasera Ltd in 2008, which was the starting point for this work. I wish to thank Ismo Kauppinen and Juho Uotila from Gasera from all the support they had given. Additionally, I am very grateful for the mechanical design by Jari Kauhaniemi, the electrical engineering by Jukka Nakari and the software development by Kari Roth and also the spirit of Gasera people.

This work has been financially supported by the Graduate school of the modern optics and photonics, Turku University Foundation and Gasera Ltd. I thank these supporters for believing in my ideas and work.

I would like to thank my little brother Matti Välikylä and mechanical engineer Christel Isaksson from Gasera Ltd for introducing me to the simple beam bending theory. Big thanks also to my little brother Ville Välikylä for helping with some source material. Jaakko Alajoki, my little brother, made the cheerful drawing in the front cover and I'm grateful for that.

I warmly thank my colleague and very good friend Janne Ahokas for supporting and helping in many tight situations and in numerous problems I have encountered during this work.

Finally, I wish to thank my loving partner Päivi Järvensivu and my two wonderful sons, Aapo and Otto, for countless unforgettably happy moments with you.

Contents

Chapter 1

Introduction

Fourier transform infrared (FTIR) spectrometer is one common instrument to study the properties of material or the composition of the sample. It is based on the interaction between the infrared radiation and the matter. The energy absorbed or emitted by the sample material is measured as the function of the wavelength of the radiation. The result is the spectrum of the sample material and reveals the structure of the molecules in the sample. In addition to the studies of the material itself, one important application of this method is the gas analysis, where the components of the gas mixture and their concentrations are determined, which is the main application of this work.

FTIR spectrometers and gas analysers have been commercially available for a long time. The first FTIR spectrum was calculated in 1949 by Peter Fellgett [1]. The most of the spectrometer models are intended for laboratory environment where the conditions are gentle to the delicate instruments. For example, the temperature in laboratories is quite constant and vibrations are low. The applications can be extended if the instrument tolerates harsher conditions and keeps sufficient stability. For example, the portable or even hand-held gas analyser is very useful in the industry, rescue services, customs and other security businesses. The compact size, small mass and rugged structure are obvious requirements of the portable device. Additionally, the instrument should keep its performance after the changes of the external temperature and under external vibrations.

The stability of FTIR spectrometer is limited mostly by the very sensitive optical instrument, the interferometer, which is an essential component of any FTIR spectrometer, because the infrared radiation has to be modulated by the interference. The interferometer is based on the beam splitter and usually few flat mirrors, which must stay aligned to each other in accuracy of tens of nanometers, which is very high demand. The stability of the alignment is critical because the output signal strength decreases rapidly when the misalignment increases. This makes the interferometer very sensitive to the thermal expansions and strong, especially shock, vibrations.

The stability requirements of the other measurement techniques are often looser but they have essential limitations compared to FTIR spectrometers. For instance, the instruments based on the tunable diode lasers or other similar techniques have narrow bands or are able to detect only one or

a few specified sample gases. Instead, FTIR spectrometer produces a broad band spectrum, which can be used to detect simultaneously even tens of gas components from one sample. The grating spectrometers could make that also but they have been replaced by FTIR spectrometers because of the better detection limits and more accurate wavelength results obtained with FTIR.

The portable spectrometers available in the market, or built for some other purpose, have some of the properties required by the portability. However, the temperature stability is very often an issue. Usually, the low cost or small instruments are not sufficiently stable and the stable ones are too bulky and expensive. For example, the instruments for space-borne usage are typically very stable but their expenses are too much for a commercial product. The other example is a small commercially available interferometer, whose small size is wasted because of the need for extra thermal stabilisation. The worst laboratory instruments loose their signal completely even after a few Celsius temperature change.

The main objective is to design an interferometer for portable or even hand-held FTIR spectrometer. The final aim is a commercial product but, in this work, an early prototype is sufficient. Thus, the manufacturing costs were tried to keep low. The latest interferometer built in this work was the small Michelson interferometer based on porch swing bearing. The interferometer size was minimised so that it was finally limited by the beam splitter size set by the diameter of the infrared beam. The beam diameter was fixed to ensure sufficiently high throughput and signal to noise ratio. The very high thermal stability was achieved without the need for the thermal stabilisation or the dynamic alignment of the mirrors. The interferometer was finally assembled in the spectrometer and few sample spectra were successfully recorded.

This thesis is arranged in to three main parts. Chapter 2 summarises the principles of FTIR spectrometry and interferometers. The objectives of the work are specified in detail and the principal technical solutions are reasoned. In Chapter 3, the linear motion produced by the mirror suspension mechanism is analysed, the manufacturing tolerances are estimated and the bending of the compliance elements required is shortly discussed. In Chapter 4, all four interferometers are thoroughly discussed. Additionally, many measurement methods used during the work are described there. Some parts of this work are already published in two peer reviewed articles. These are summarised in Chapter 5 and reprinted in the appendices.

Chapter 2

FTIR interferometers

2.1 FTIR spectroscopy

Infrared spectroscopy studies the interaction between the matter and the infrared radiation. Atoms and molecules can emit and absorb the photons according their quantum states. The energy of such a photon is $E = \varsigma c\nu$, where $\varsigma = 6.626 \cdot 10^{-34}$ Js is Planck's constant, c is speed of light and ν is the wavenumber. In this thesis, the wavenumber ν is defined as reciprocal of the wavelength, or $\nu = 1/\lambda$, as commonly done in the spectroscopy. The wavenumber is often defined as $\nu' = 2\pi\nu$. Additionally, the quantity ν is sometimes called frequency. The spectroscopists use this definition mainly for historical reasons but also for easy relation between wavelengths and wavenumbers.

In spectroscopy, the absorbed or emitted light is measured as a function of the wavenumber. The measurement result is called a spectrum. Because quantum states depend on the molecular structure, the spectrum reveals that structure. Alternatively, if the structure of studied molecules are known the spectrum of a unknown sample can be used to identify what molecules are in the sample and also what are their concentrations.

Hence, the wavelength of the light is to be measured, methods in spectroscopy are usually based on either the dispersion or the interference. However, the prism spectrometers are no longer used because the other methods have better performance. The first devices utilising the interference were grating spectrometers based on the diffraction in the grating. Especially in infrared spectroscopy, the grating spectrometers are mainly replaced by Fourier transform spectrometers where the interference is produced in the interferometer. Fourier spectrometers have several advantages over grating spectrometers. The first is Jacquinot, or throughput, advantage: Fourier transform spectrometer can collect more energy per spectral element than a grating spectrometer. The Fellgett, or multiplex, advantage is that in Fourier spectrometer all spectral elements are measured simultaneously but the grating spectrometer measures the elements separately, one by one. Because the signal to noise ratio depends on the measurement time, the Fourier spectrometer results higher signal to ratio in the equal time than the grating spectrometer. Alternatively, to obtain equal signal to ratio, one has to use longer measurement time with grating spectrometer than with

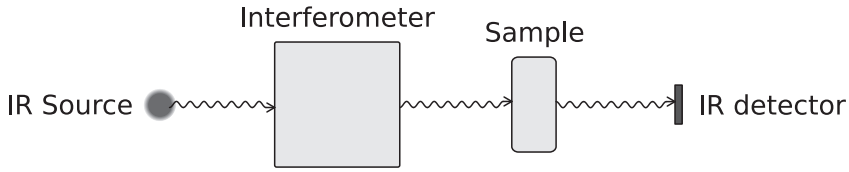

Figure 2.1 Principle of Fourier transform infrared transmission spectrometer. The infrared radiation is modulated in the interferometer, transmitted through the sample and finally detected.

Fourier spectrometer. The third important advantage is the linearity of the wavenumber scale in Fourier transform spectrometer. Because all the spectral elements are measured simultaneously, the measurement errors affect similarly to all elements. Therefore, it is not possible that any single spectral line is distorted differently than the other lines. Ghost lines, typical to the grating spectrometer, can not be produced. Additionally, the actual wavenumbers recorded by Fourier spectrometer are highly linearly proportional to the measured wavenumbers while the grating spectrometer has non-linear wavenumber scale. Furthermore, Fourier spectrometer usually distorts the spectral lines less that the grating spectrometer because of the different instrument functions. The lines of the grating spectrometer are typically wider and lower than of Fourier transform spectrometer. The response of the infrared detectors depends on the frequency. Fourier transform spectrometer can be easily set to drive the interferogram so that the most interesting part of the spectrum is recorded in the frequency band where the detector has the lowest noise.

The principal measurement setup of the Fourier transform transmission spectrometer is depicted in Fig. 2.1. The infrared light is transmitted through the interferometer, which modulates the light using the interference. The modulated light beam runs through the sample and finally to the detector. The homogenous sample absorbs the radiation according to Beer's law

$$I = I_0 \, \mathrm{e}^{-\beta c x}, \tag{2.1}$$

where β is the absorption coefficient per unit concentration, c in concentration and x in the absorption length or the travel length of the light in the sample. The intensity without the sample $I_0(\nu)$, or the background, and with the sample $I(\nu)$, or the signal, are recorded. The ratio I/I_0 is the transmission spectrum and the logarithm $-\ln(I/I_0)$ is the absorbance spectrum. Often, the absorbance is calculated using 10-base logarithm, which scales the absorption coefficient values β with $1/(\ln 10)$. The spectra are automatically calibrated automatically because the instrument function (or the instrument response) is equal on both and cancels out.

The infrared spectrum is usually divided in to the near, mid and far infrared bands as defined in Table 2.A. The interferometer of this thesis is

Table 2.A Three bands of the infrared spectroscopy.

Band	Abbreviation	Range in wavenumbers $[\mathrm{cm}^{-1}]$	Range in wavelengths $[\mu\mathrm{m}]$
Near infrared	NIR	12500 ... 3300	0.8 ... 3
Middle infrared	MIR	3300 ... 500	3 ... 20
Far infrared	FIR	500 ... 10	20 ... 1000

intended for the mid infrared (MIR) region, or the wavenumbers approximately from 500 cm^{-1} to 5000 cm^{-1}. Spectra of the most usual gases, as water, carbon dioxide and carbon hydrides, are in this band. Additionally, the oxygen O_2 and nitrogen N_2, have no lines in MIR. Thus, the MIR region is very suitable for analysing the samples taken from air.

The resolution $\delta\nu$ of the spectrum is the width of the absorption or emission line. In this work, it is defined as the full width at half height, FWHH, of the single spectral line, which is a quite common definition. Conversely, the resolution gives the smallest distance between the adjacent lines when the lines are still distinctive. The resolution is said to be low if it is over approximately 1 cm^{-1}. The low resolution spectra are sufficient for the gas analysis, so this thesis concentrates on them. The better resolution is mainly required in the research in the laboratories and it needs very much different instrumentation.

2.2 Two beam interferometers

2.2.1 Interference of monochromatic light

The electric field of the completely monochromatic electromagnetic plane wave has the form $E(\mathbf{r},t) = E_0 \exp\left[i\left(\mathbf{k}_\mathrm{w}\cdot\mathbf{r} - \omega t\right)\right]$, where $\mathbf{k}_\mathrm{w}$ is the wave vector, $\mathbf{r}$ is the position vector, ω is angular frequency and t is time. The absolute value of the wave vector is $|\mathbf{k}_\mathrm{w}| = \nu' = 2\pi\nu$. If two monochromatic plane waves, E_1 and E_2, with equal frequency are interfering in vacuum, the resultant electromagnetic field is

$$E^2 = E_1^2 + E_2^2 + 2E_1E_2\cos\phi,$$

where ϕ is the phase difference of the waves. Because the frequency of the light is very high, the light intensity is observed instead of the electric field. The intensity is proportional to the square of the electric field or $I \propto E^2$. Therefore, the total intensity observed is

$$I = I_1 + I_2 + 2\sqrt{I_1 I_2}\cos\phi. \tag{2.2}$$

The ideal wave has only single wavelength or wavenumber ν_0 so its spectral distribution is an infinitely narrow and infinitely high peak. However,

the ideal plane waves do not appear in nature because they would have no weakening and thus be infinitely long. The actual plane waves have wider and finitely high spectral distribution $E(\nu)$. The kind of plane plane wave propagating in the z direction and having the amplitude of the infinitesimal spectral element $E(\nu)\,\mathrm{d}\nu$ is described by

$$\mathrm{d}\mathcal{E}(z,t) = E(\nu)\,\mathrm{d}\nu\ \mathrm{e}^{i2\pi\nu(z-vt)},$$

where v is the phase velocity of the wave or $v = \omega/(2\pi\nu)$. The total wave is described then by

$$\mathcal{E}(z,t) = \int_{-\infty}^{\infty} E(\nu)\,\mathrm{e}^{i2\pi\nu(z-vt)}\ \mathrm{d}\nu,$$

which is called a wave packet. If the term in the exponent is marked as $\Delta = z - vt$, this equation can be written in the form of Fourier transforms:

$$\left\{\begin{array}{rcl} \mathcal{E}(\Delta) &=& \displaystyle\int_{-\infty}^{\infty} E(\nu)\,\mathrm{e}^{i2\pi\nu\Delta}\ \mathrm{d}\nu \quad = \quad \mathcal{F}\left\{E(\nu)\right\} \\ E(\nu) &=& \displaystyle\int_{-\infty}^{\infty} \mathcal{E}(\Delta)\,\mathrm{e}^{-i2\pi\nu\Delta}\ \mathrm{d}\Delta \quad = \quad \mathcal{F}^{-1}\left\{\mathcal{E}(\Delta)\right\}. \end{array}\right. \tag{2.3}$$

Therefore, the wave packet $\mathcal{E}(\Delta)$ and the spectral distribution $E(\nu)$ are Fourier transform pair. If the spectral distribution is a box function or

$$E(\nu) = \left\{\begin{array}{ll} 1 & \nu_1 \le \nu \le \nu_2 \\ 0 & \text{elsewhere} \end{array}\right.$$

and $E(-\nu) = E(\nu)$, the wave packet is

$$\mathcal{E}(\Delta) = 2\,(\nu_2 - \nu_1)\,\mathrm{sinc}\left[\pi\Delta\,(\nu_2 - \nu_1)\right]\cos\left[\pi\Delta\,(\nu_2 + \nu_1)\right],$$

where the sinc function is defined as $\mathrm{sinc}\,x = (\sin x)/x$. The wave packet and its spectral distribution are illustrated in Fig. 2.2. The wave packet dies out firstly at $1/(\nu_2 - \nu_1)$. The corresponding length is defined as the coherence length of the wave packet, which is, in this case,

$$\delta z = \frac{1}{\nu_2 - \nu_1}. \tag{2.4}$$

Thus the coherence length increases when the spectral distribution is narrowing. The coherence length is an important property of the reference laser for the interferometer. This is discussed in detail in Chapter 2.3.5 from page 31.

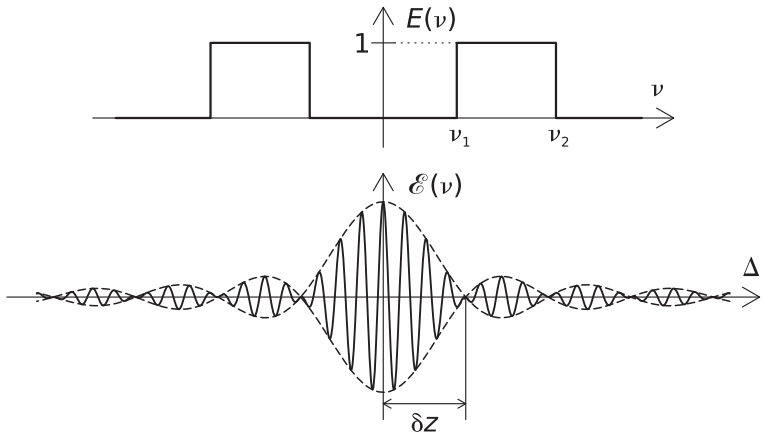

Figure 2.2 Example of the wave packet $\mathcal{E}(\Delta)$, which is a Fourier transform pair with its spectral distribution $E(\nu)$. The coherence length δz is the half of the length where the wave packet firstly dies out.

2.2.2 Interferogram and spectral distribution

In an ideal two beam interferometer, the light beam having intensity I_0 is divided to two parts with equal intensity. In this case, the intensities in Eq. (2.2) are $I_1 = I_2 = I_0/2$. The intensity of the exit beam is then

$$I_{\text{out}}(\phi) = I_0 \left(1 + \cos\phi\right), \tag{2.5}$$

where ϕ is the phase difference between the two interfering beams. The phase difference is $\phi = 2\pi\nu x$, where the refractive index is assumed to unity and x is the optical path difference, which is the difference of the travel lengths of the beams in the interferometer. If the light source has spectral distribution $E(\nu)/2$, the infinitesimal spectral element from ν to $\nu + \mathrm{d}\nu$ produces an interference record

$$\mathrm{d}I_{\text{out}}(x,\nu) = \frac{1}{2}E(\nu)\left[1 + \cos\left(2\pi\nu x\right)\right]\,\mathrm{d}\nu.$$

The total interference record is then

$$I_{\text{out}}(x,\nu) = \frac{1}{2}\int_0^\infty E(\nu)\left[1 + \cos\left(2\pi\nu x\right)\right]\,\mathrm{d}\nu.$$

Actually, the recorded signal is the interferogram, which is the total interference record without the constant component $\frac{1}{2}\int_0^\infty E(\nu)\,\mathrm{d}\nu$. If the spectrum is defined also in the negative wavenumbers, or $E(\nu) = E(-\nu)$, the interferogram is

$$I(x) = \int_{-\infty}^{\infty} E(\nu)\,\mathrm{e}^{2\pi\nu x}\,\mathrm{d}\nu = \mathcal{F}\left\{E(\nu)\right\}.$$

Therefore, the interferogram $I(x)$ and the spectral distribution are a Fourier transform pair as

$$\begin{cases} I(x) &= \displaystyle\int_{-\infty}^{\infty} E(\nu)\,\mathrm{e}^{i2\pi\nu x}\,\mathrm{d}\nu &= \mathcal{F}\{E(\nu)\} \\ E(\nu) &= \displaystyle\int_{-\infty}^{\infty} I(x)\,\mathrm{e}^{-i2\pi\nu x}\,\mathrm{d}x &= \mathcal{F}^{-1}\{I(x)\}\,. \end{cases} \tag{2.6}$$

The Fourier transform spectroscopy is based on this fact. The optical path difference x is varied by the interferometer using usually the moving mirrors. At the same time, the interferogram is recorded as a function of optical path difference. Fourier transform of the interferogram is the spectrum of the recorded light beam.

2.2.3 Modulation depth

The interference record from the practical two-beam interferometer as a function of the optical path difference x is

$$I_{\mathrm{out}}(x) = A_0\big[1 + m\cos(2\pi\nu x)\big] \tag{2.7}$$

where A_0 is a product of the input intensity I_0 and the reflectance values of all optical components and the transmittance of the beam splitter, thus it differs slightly from the ideal interferometer in Eq. (2.5). Usually, reflectance values of mirrors are close to unity, so the coefficient is $A_0 \approx I_0 R_{\mathrm{BS}} T_{\mathrm{BS}}$, where only the reflectance R_{BS} and transmittance T_{BS} of the beam splitter, and possible compensating plate, are considered. The interferogram $I(x)$ is the changing component of the signal or $I(x) = I_{\mathrm{out}}(x) - A_0$. Therefore, the interferogram is proportional to the modulation depth m. It describes the signal strength in relation to the maximum possible signal of the interferogram. Any imperfections of the interferometer decrease the modulation depth and thus the signal. Therefore, it is a measure of the quality of the interferometer and thus is one of the most essential quantities in the interferometer design.

The modulation depth of an ideal interferometer is $m = 1$. Generally, anything that causes extra optical path difference across the interfering output beams or the errors to the wave front of the plane wave, decrease the modulation depth. Thus, the unflatnesses of the surfaces of the optical components decline in the modulation but it can be avoided by using sufficiently flat optical surfaces as discussed later in Chapter 2.3.1. Therefore, the tilting and shearing are the most common phenomena that decrease the modulation depth. In tilting, output beams of the interferometer have an small angle Θ between them, or are not exactly parallel. Rays in opposite edges of beams have an extra optical path difference in relation to each

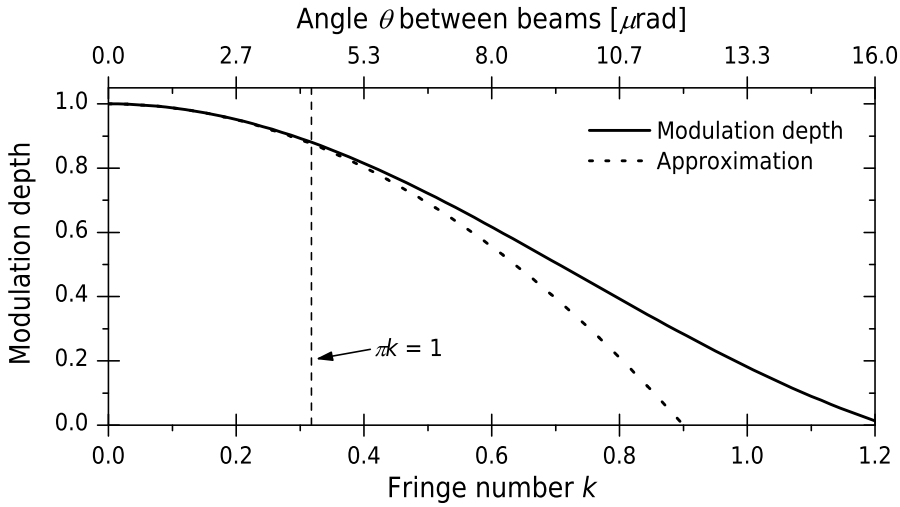

Figure 2.3 The modulation depth and its approximation. The angle θ values correspond the beam diameter 25 mm and the wavenumber 3000 cm^{-1}. The validity limit of the approximation in Eq. (2.8) is marked with a dashed line.

other [2], which decreases the modulation depth. If output beams are plane waves and circular with diameter D, then the modulation depth is [3–5]

$$m = \frac{2J_1\left(\pi D\theta\nu\right)}{\pi D\theta\nu} \approx 1 - \frac{\left(\pi D\theta\nu\right)^2}{8}, \tag{2.8}$$

where J_1 is Bessel function of the first kind. The last approximation is valid if $(\pi D\theta\nu) < 1$. The Eq. (2.8) can be expressed also as

$$m = \frac{2J_1\left(\pi k\right)}{\pi k}, \tag{2.9}$$

where k is the number of fringes across the beam:

$$k = D\theta\nu. \tag{2.10}$$

The Eq. (2.9) can be used if the light is monochromatic because then fringes can be observed. If the aperture is square, Bessel function is replaced by the sinc function ($\operatorname{sinc} x = (\sin x)/x$). The plot of the function in Eq. (2.9) is in Fig. 2.3. Derivations of these equations are presented in Appendix A.1.

The shearing is a lateral shift of the beams, or the shift ϵ in the direction perpendicular to their direction of propagation [2]. Again, the rays on the opposite sides of the beam have an extra optical path difference and the modulation depth is decreased. If the beam is circular with diameter D, the modulation depth is [6]

$$m = \frac{2J_1\left(2\pi\nu\epsilon D\right)}{2\pi\nu\epsilon D}. \tag{2.11}$$

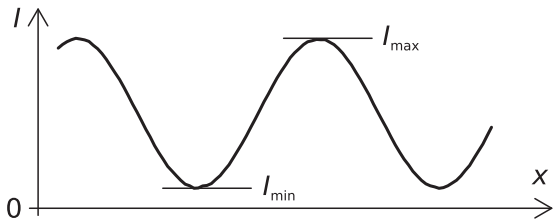

Figure 2.4 Determining the visibility m_{vis} from the sinusoid intensity signal.

This function has the same form as Eq. (2.8), so it acts correspondingly, as in Fig. 2.3.

The absolute value of the modulation depth is not always possible to determine in practice. Using the broadband infrared radiation, the interferogram is not sinusoid and the modulation depth is not easy to determine. Additionally, the detectors are usually AC connected and so the average level of the signal is lost. If the broadband radiation is used, only the changes in the modulation depth are studied. It is usually done by using 100 % transmittance line, which is the transmittance spectrum of the current background compared to the initial background selected as a reference. If the interferometer has been stable between these two background measurements, the transmittance curve is a constant line at height 1 or 100 %, hence the name. The absolute modulation depth can be recorded using the monochromatic light as the laser light, because then the interference signal is nearly sinusoid. If measured with DC level, the visibility of the output signal intensity is equal to the modulation depth. The visibility is

$$m_{\mathrm{vis}} = \frac{I_{\max} - I_{\min}}{I_{\max} + I_{\min}}, \tag{2.12}$$

where $I_{\max}$ and $I_{\min}$ are the maximum and the minimum values of the intensity of the interferometer output radiation, when the optical path difference has been varied. Determining the visibility is illustrated in Fig. 2.4. The measuring the modulation depth is described in more detail in Chapter 4.2. The visibility has been also called obliquity.

2.2.4 Michelson interferometer

In 1890's, A. A. Michelson presented his first interferometer, which still carries his name [2]. Michelson interferometer was firstly applied in spectroscopy in 1950's after Fourier transform spectroscopy was introduced [7]. The original and the simplest model of the interferometer consists of two plane mirrors and the beam splitter. However, there are a wide variety of the modifications of the original version, which try to improve the disadvantages of the original design. However, the original one is the simplest interferometer for FTIR.

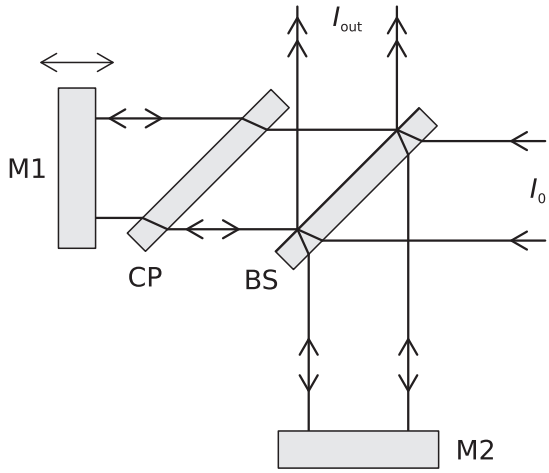

Figure 2.5 Michelson interferometer with a collimated light beam. The beam splitter BS divides the input beam I_0 to the end mirrors M1 and M2 and the compensating plate CP cancels the phase errors from the substrate material. The optical path difference is varied by moving M1 along a linear path.

Typical construction of the Michelson interferometer for low resolution infrared spectroscopy is presented in Fig. 2.5. The beam splitter divides the input beam to two parts, which have ideally equal intensity. The other part is reflected back from the mirror M1 in the first arm and the other part from the mirror M2. The beams are then combined by the beam splitter and pointed out from the interferometer. Because these two beams go through the different path, their travel lengths are different. The difference is called optical path difference and it determines the phase difference between the wave fronts of the beam. The optical path difference is varied by moving either of the plane mirrors, here the mirror M1. In mid-infrared region, the beam splitter is typically a substrate having a special coating on one side. The substrate adds extra optical path difference to the beam transmitting it, which is compensated by the similar substrate plate without beam splitting coating. This plate is called the compensating plate and can be added in to the first arm, or more commonly, right over the beam splitter separated only by a small air gap. Then, the both beams are transmitted through the substrate equally by four times.

The interferometer optics forms the images of the mirror M2 and the source S_0 as presented in Fig. 2.6. If the distance between the image M2' and the mirror M1 is d, then the distance between the source images S_1 and S_2 is $2d$. According to Fig. 2.6, the optical path difference between the rays from the source images is $x = 2nd\cos\phi$, where n is the refractive index of the medium. If the first interference maximum is considered, or if $\phi = 0$, and the medium is air, or $n \approx 1$, the optical path difference is $x = 2d$. This is also intuitively clear, because the light travels twice the path from each mirror. This assumption is also valid if the source S_0 is collimated,

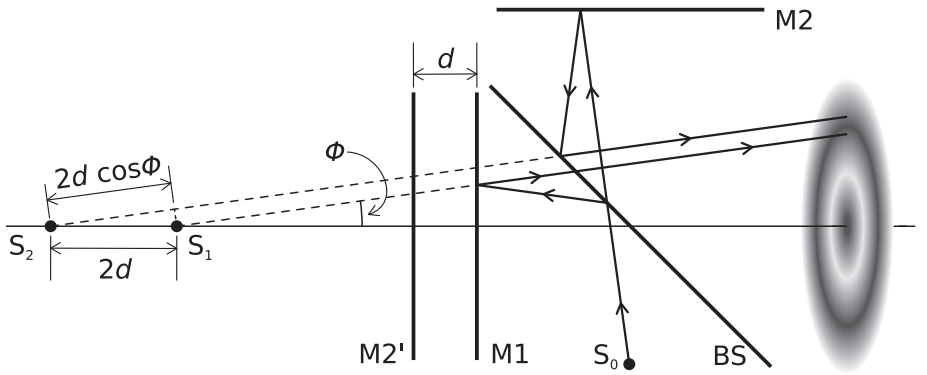

Figure 2.6 Interference in the Michelson interferometer. The beam splitter BS forms the image M2' of the movable mirror M2. Sources S_1 and S_2 are images of the S_0, and thus fully coherent.

or is infinitely far from the beam splitter. Then the wavefront is planar and the fringe pattern has uniform intensity, which depends sinusoidally on the optical path difference. If $\phi = 0$, the output intensity of Michelson interferometer is

$$I_{\text{out}}(x) = I_0\big[1 + \cos(2\pi\nu x)\big],$$

as in Eq. (2.5). The interference maximums occur when $\nu x = l$, or correspondingly $x = l\lambda$, where $l = 0, \pm 1, \pm 2, \ldots$.

If the mirror M2 is tilted in relation to M1 and the distance $d = 0$, then images $\S_1$ and $\S_2$ are on the same vertical axis in Fig. 2.6. From the screen, they seems to be side by side, as in Fig. 2.7(a). Two coherent rays intersect on the screen at the point P. Because they have traveled the different paths, they have the optical path difference η. These two rays are the part of the spherical wave fronts, which coincide at two points on the screen, as illustrated in Fig. 2.7(b). The cross sections of the wave fronts are circular on the screen. According to Fig. 2.7(b), the coordinates of the intersecting point P can be calculated using the equations for the intersection of two circles (see Appendix B.1). The coordinates of the point P are

$$\begin{cases} x &= \dfrac{r_2^2 - r_1^2}{4x_0} \\ y &= \sqrt{r_2^2 - (x + x_0)^2}, \end{cases} \tag{2.13}$$

where the radii are $r_1 = \sqrt{R_1^2 - h^2}$ and $r_2 = \sqrt{R_2^2 - h^2}$, where R_1 and R_2 are the optical path lengths of the rays and h is the distance of the screen from the sources and $R_2 = R_1 + \eta$. Equation (2.13) can be rearranged to

$$\frac{y^2}{B^2} - \frac{x^2}{(B/A)^2} = 1, \tag{2.14}$$

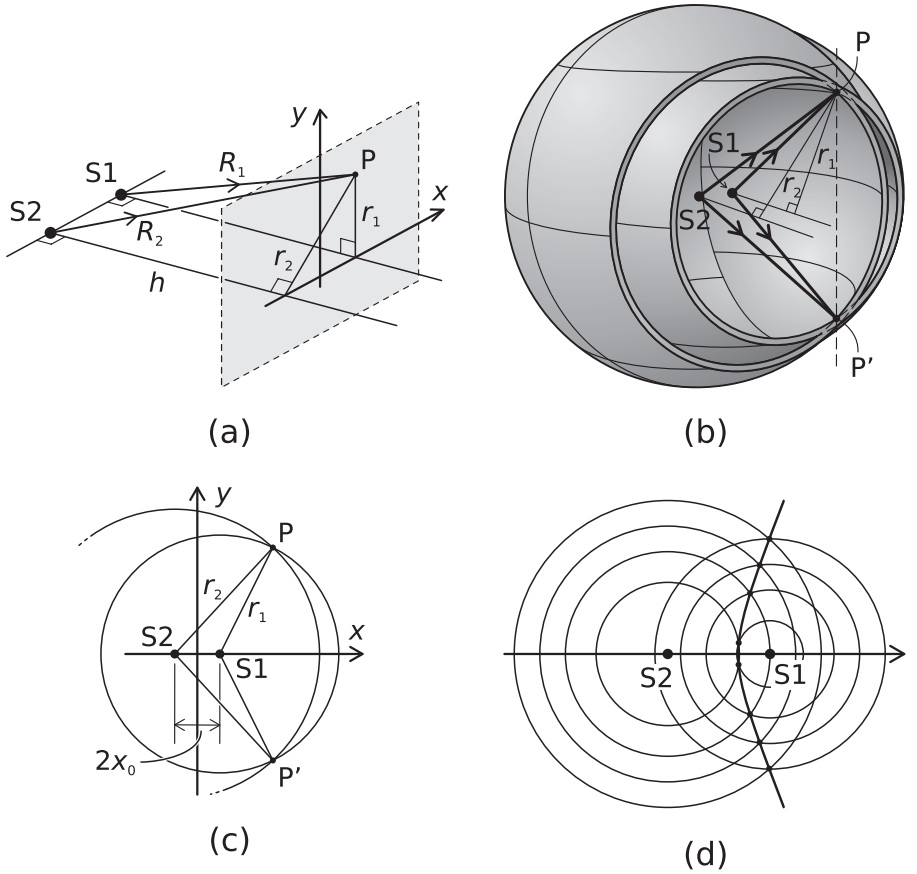

Figure 2.7 Interference in the Michelson interferometer with a tilted mirror. Two coherent sources, S_1 and S_2, are next to each other seen from the screen, as in (a). A spherical wave front intersects on the screen at P and P', as in (b) and (c). If all wave fronts are considered, or the radius R_1 is varied while keeping the optical path difference η constant, points P and P' draw a hyperbola on the screen.

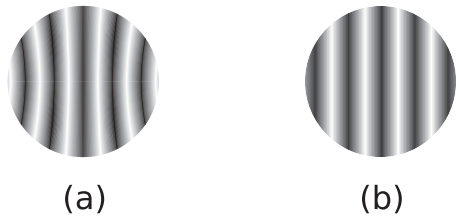

Figure 2.8 Examples of fringe patterns from a tilted Michelson interferometer with spherical waves (a) and plane waves (b).

where $A^2 = (2x_0/\eta)^2 - 1$ and $B^2 = \frac{1}{4}\eta^2 - h^2 - d^2$. The equation describes a hyperbola, which is illustrated in Fig. 2.7(d). The phase difference between the interfering rays is constant along this hyperbola, so the fringes on the screen are hyperbolic. Figure 2.8(a) shows the schematic fringe pattern of the tilted interferometer. If sources move away from the screen, the wave front becomes close to planar and fringes approach straight lines, as in Fig. 2.8(b).

The optical path difference is varied by moving the mirror M1 linearly. In practice, the mirror motion has non-linearities, which cause the tilting of the mirror and also the shifting perpendicular to the motion axis. Because of the plane mirrors, the shifting will not produce shearing of the beams, which would have occurred with retroreflectors such as cube corner mirrors. Therefore, the mirror tilting is the major issue with Michelson interferometer built using the plane mirrors.

One common way to reduce mirror tilting is the dynamic alignment, where the alignment of the moving mirror is monitored and corrected if needed. The traditional dynamic alignment system is to minimize the phase differences between three small laser beams placed in the triangle [8] on the mirror. The mirror can be aligned constantly during the mirror movement or just between the complete scans. The dynamic alignment systems are used especially on the high resolution spectrometers, where the mirror is traveled even several meters.

The other way to minimize the tilting is using an optical compensation. This is done by replacing the plane mirrors by retroreflectors. Typical retroreflectors are cube corner or cat's eye mirrors illustrated Fig. 2.9 [2,9]. The cube corners are made of three orthogonally placed plane mirrors and the cat's eyes of the parabolic mirror and the spherical mirror [10]. With retroreflectors, the incoming and the reflected beams are ideally parallel but shifted laterally as in one of the first optical compensations depicted in Fig. 2.10(a) [11,12]. The tilting is practically compensated but the modulation can be affected by the shearing. The other end mirror assemblies are

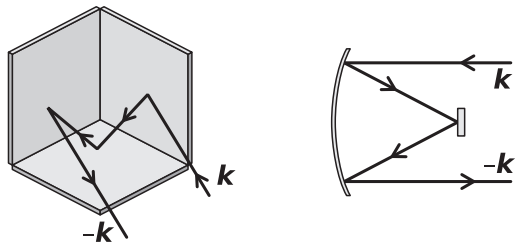

Figure 2.9 Two typical retroreflectors used in FTIR: the corner cube mirror (a), made of three orthogonal plane mirrors, and cat's eye (b), made from the parabolic and the spherical mirrors. In both, the incoming $\mathbf{k}$ and the reflected beams $-\mathbf{k}$ are parallel but laterally shifted.

represented in Fig. 2.10(b) [5, 9]. However, the shearing can also be compensated by suitable optical construction, usually having the plane mirrors with the cube corners. Two examples of both tilt and shear compensated mirror assemblies are in Fig. 2.10(c) and Fig. 2.10(d). In the first example, one arm has a cube corner and the other a plane mirror [2]. In the second example, two cube corners are mounted back-to-back [5]. Additional to these examples, there is wide variety of the mirror assemblies with more and more complicated optical systems.

The cat's eyes require large space so they are not suitable for portable devices. The biggest disadvantage of the cube corners is that the angles between the plane mirrors of the cube corner have to be 90°with interferometric accuracy to avoid tilting [5, 7]. This makes the corner cubes with acceptable accuracy quite expensive. The imperfections of the cube corners can be compensated, for instance, by adding an angle adjustment mechanism [8] to them or by using the end mirror assembly presented in the bottom left example in Fig. 2.10(b) where the light travels only one path instead of the six possible paths in the top left assembly. However, the cube corners are larger than the single plane mirrors and all of these compensation methods makes the corner cube assembly even larger, which makes using them in portable device further more difficult.

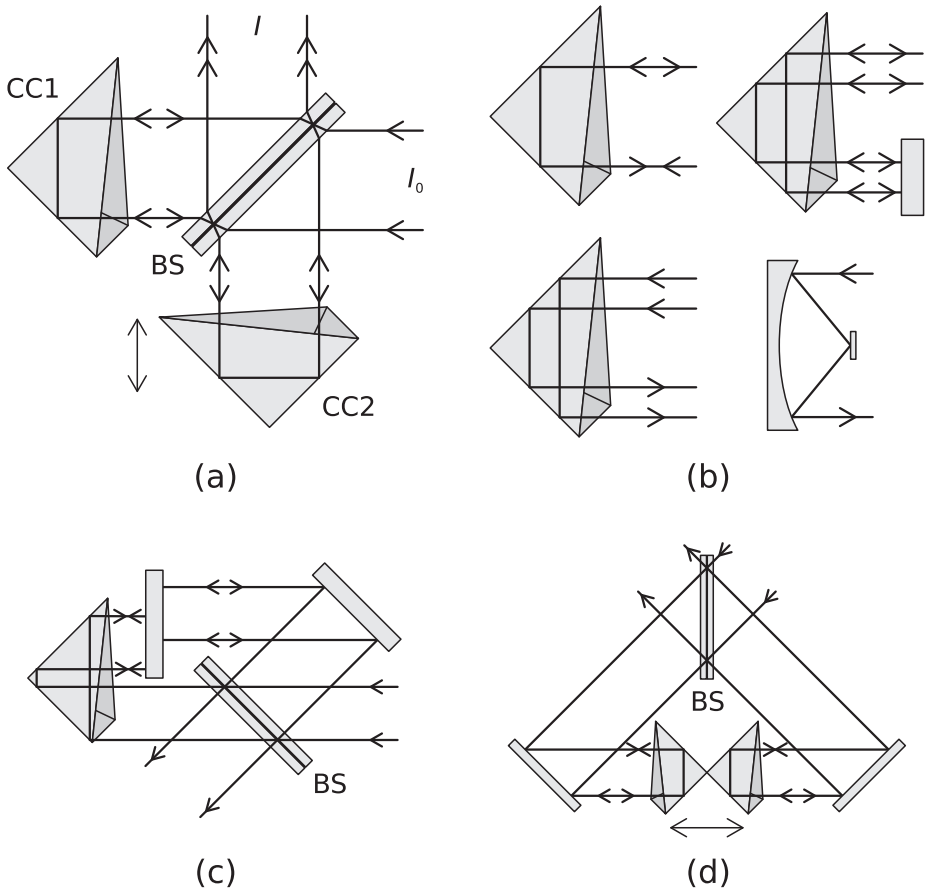

Figure 2.10 Examples of interferometers with tilt or shear compensation and driven by the linear motion. The first one, (a), is Michelson where the plane mirrors are replaced by the cube corners CC1 and CC2 [5, 8, 11, 12]. In (b), four examples of end mirror assemblies are presented [5, 9]. Interferometer (c) is designed by On-Line Technologies [2]. The cube corners can be also assembled back-to-back, as in (d), which minimizes the shearing problem [5]. This interferometer can be also driven by rotating the cube corner pair.

2.2.5 Interferometers with rotating mirror systems

The one major disadvantage of the Michelson interferometer is the mirror driving by the linear motion [5, 7]. The tilting during the motion may be challenging but it can be solved by suitable mechanics or optical compensation. More difficult issue is the environmental vibration, because the most of the vibrational energy is stored as the translational motion rather than the rotational motion, so the rotational vibrations are generally much weaker than the translational vibrations. This has been utilized by driving the interferometer mirror with rotational motion. The rotationally driven interferometer may be even orders of magnitude less sensitive to the environmental vibrations than linearly driven [7]. The drawback is that the more complicated optical construction is required. Additionally, the rotating mirror systems require more space than linearly driven.

Figure 2.11 represents six examples about interferometer constructions based on the rotational motion of the plane mirror assemblies. In examples (a) and (b), the optical path difference is varied by rotating a mirror pair and a common end mirror [5, 7]. The model (c) is Carousel interferometer, which is used later in this thesis as an reference example of good interferometer for portable use. It has very good temperature stability and it is not very sensitive to external vibrations [7]. The following one, (d), is Perkin-Elmer Dynascan, which have rotatable table with four plane mirrors. The last two, (e) and (f), are examples requiring several mirrors: the first has 8 plane mirrors and the second even 10 plane mirrors [13]. It would be very difficult to obtain a compact and stable interferometer using that much mirrors.

Many of the above interferometers used the roof-top mirrors, especially Carousel interferometer. It has two plane mirrors mounted together on one side as depicted in Fig. 2.12. The roof-top acts as a perfect retroreflector on the plane, whose normal $\mathbf{N}$ is parallel to the intersection of the mirror planes. This phenomenon is independent of the angle between the incident beam and the plane with normal $\mathbf{N}$. However, the roof-top mirror can be further generalized so that the angle between the mirrors is $90^\circ + \alpha$. Then the angle between the incoming and the reflected beams is 2α on the plane with normal $\mathbf{N}$. Pendium and Double Pendium interferometers are based on the roof-tops [5]. The tilting and shearing are both compensated. They have loose manufacturing tolerances, because no interferometric accuracy is required in any roof-top. Unfortunately, they are clearly larger than Michelson interferometer and the driving system becomes easily very massive.

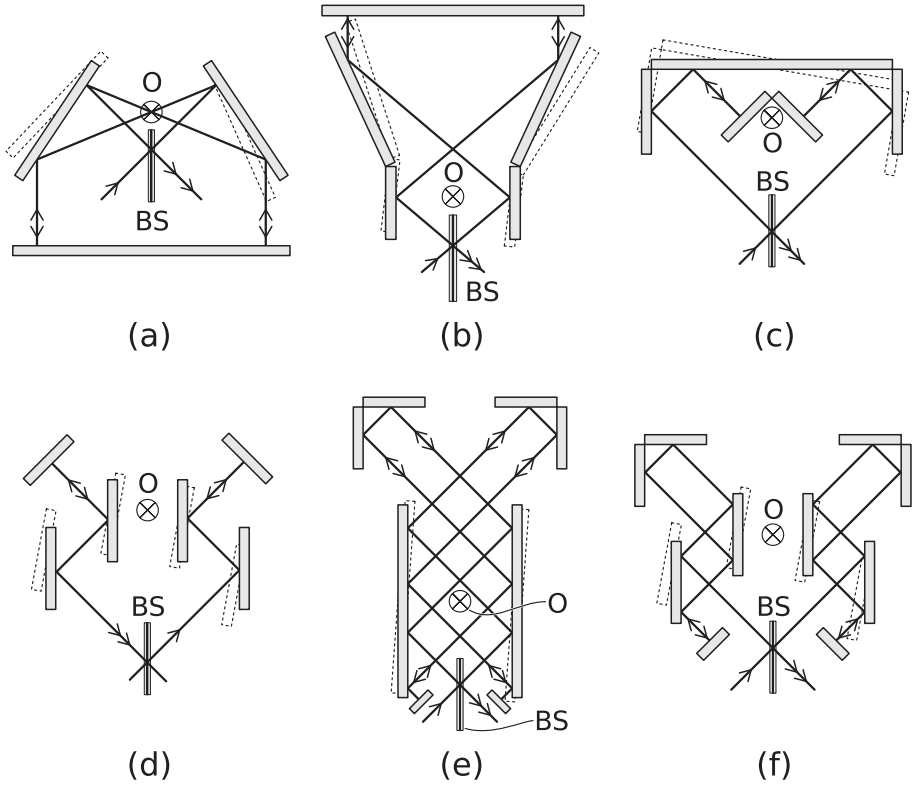

Figure 2.11 Examples of interferometers based on the rotational motion and assembled using only plane mirrors. The O is axis of the rotation, perpendicular to the sheet, and BS is the beam splitter. The motion of movable mirrors is illustrated with dashed lines. The first two, (a) and (b), are examples from [5, 7]. The next one, (c), is Carousel interferometer [7]. Drawing (d) is the interferometer in Perkin-Elmer Dynascan [2, 7]. Interferometers (e) and (f) have 8 or 10 plane mirrors respectively [13].

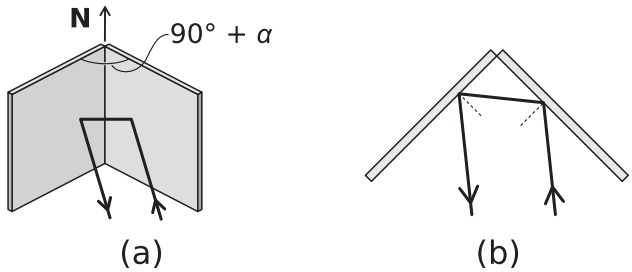

Figure 2.12 Roof-top mirror is made of two plane mirrors, as in figure (a). It is a perfect retroreflector on the plane, whose normal **N** is parallel to the intersecting line of two plane mirrors. That is illustrated in (b). The retroreflection is perfect regardless of the angle between the incident beam and the plane with normal **N**.

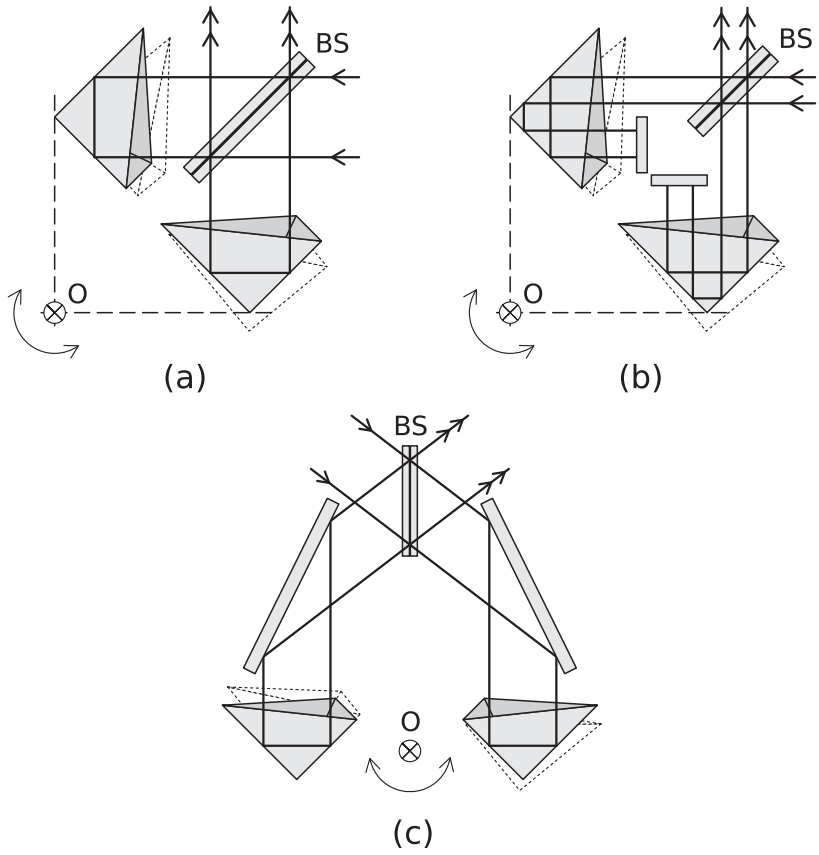

Figure 2.13 Few examples of interferometers based on the rotational motion and the cube corners.The O is axis of the rotation, perpendicular to the sheet, and the BS is the beam splitter. The motion of the movable mirrors is illustrated with dashed lines. The double pendulum (a) was used by Bomem Inc [2]. The enhanced version of the double pendulum is construction (b), which doubles the maximum optical path difference compared to the model (a) [5,14]. Bruker's Rocksolid™ is in (c) [2,15].

The retroreflectors can be used also when the mirror driving is based on the rotational motion. Few examples of these are presented in Fig. 2.13. The first one, (a), has Michelson construction but the plane mirrors are replaced by corner cubes, which are on the rotatable mount. It has been used by Bomem Inc [2]. The enhanced version of it, in Fig. 2.13(b), has two extra plane mirrors [5, 14]. The resolution is doubled hence the the equal movement of the mirrors causes two times more optical path difference. The model (c) is Bruker's patented RockSolid™ [2,15]. The interferometer with two cube corners back-to-back, already mentioned in Fig. 2.10(d) on page 16 can be also driven by rotating the cube corner pair around their common corner. Interferometer based on rotational motion and retroreflectors have usually very massive driving system and, additionally, the dynamic alignment cannot be used although it is not usually required [5].

Target of this thesis is to design small and stable interferometer. Although, the retroreflectors and the rotational driving would help with the temperature stability and sensitivity to external vibrations, they would make the system much larger than desired. Especially, the rotational driving systems are bulky. Additionally, the most compact retroreflectors, the cube corner mirrors, are expensive because of the very tight angle tolerances. The classic Michelson construction is optically the most simplest interferometer for FTIR. Thus it can be made also smaller than the other designs. The major drawback is that it is more sensitive to the external vibrations than many other designs. However, Michelson construction has been used in space-borne interferometers [16–18, for e.g.], thus it should be possible to control the vibrations.

2.2.6 Other interferometer types

There exist a wide variety of interferometer types, which are intended for special purposes. For instance, some sample materials, such as samples in a condensed-phase require very short scanning times or very fast mirror velocity. Using linear back-and-forth or rotational swinging motion it is difficult to achieve sufficiently fast velocities. This has been solved in rapid scanning interferometers by continuously rotating eccentric mounted cube corner or wedged plane mirror [2, 19]. The scanning speed may be up to 100 . . . 360 scans per second or even 1000 scans/s [19–22]. The rapid scanning is not suitable for slow detectors for example the photoacoustic detectors, which require quite slow mirror velocities.

Another special requirement is the field-widening. The resolution of the interferometer depends on the source size observed by the interferometer, see Chapter 2.3.2. If source is very large, as the twilight or airglow, the resolution would be extremely low. Field-widened interferometers are designed so that the resolution is still acceptable. One solution is refractively scanned interferometers where the optical path difference is varied by moving the prism over beam on the other arm of the interferometer [2, 23].

The refractive scanning may be produced also by rotating a flat window transmitting infrared radiation about its centre. A concept of a small interferometer based on refractive scanning and a photoacoustic detector is presented [24] but, as the author knows, it is not reported in public if this kind of device has never been built.

The last type discussed here is the step-scan interferometer. These devices move the mirror in very small steps. After each step the mirror is hold in position and the signal is sampled. Step scanning is used in imaging spectrometry, photoacoustics or high-speed time-resolved spectroscopy [2]. The photoacoustic detecting requires modulation of the infrared radiation, which can be done using a separate chopper, which cuts the signal periodically, or by moving the mirror sinusoidally over one or a few wavelengths.

2.3 Spectrometer components, SNR and signal recording

2.3.1 Optics in FTIR

Beamsplitter

A beamsplitter is an optical component, which divides the input infrared beam into two beams having, ideally, equal intensity. The most essential quantities of the beamsplitter are the transmittance T_{BS} and the reflectance R_{BS}. Both of these depend on the wavenumber of the radiation. If the beamsplitter absorbs no radiation, then $R_{\mathrm{BS}} + T_{\mathrm{BS}} = 1$. The relative efficiency of the beamsplitter is defined as [2, 9]

$$E = \frac{2R_{\mathrm{BS}}T_{\mathrm{BS}}}{(2R_{\mathrm{BS}}T_{\mathrm{BS}})_{\mathrm{ideal}}} = 4R_{\mathrm{BS}}T_{\mathrm{BS}}.$$

With no absorption, the efficiency is $E = 4R_{\mathrm{BS}}\,(1 - R_{\mathrm{BS}})$, which has maximum at $R_{\mathrm{BS}} = \frac{1}{2}$. Thus, the maximum relative efficiency is achieved when $R_{\mathrm{BS}} = T_{\mathrm{BS}} = 0.50$.

The first reflected and transmitted beams of the incoming monochromatic light, whose intensity at the wavenumber ν is I_0, are illustrated in Fig. 2.14. Then the mean intensity of each of two output beams is $I_0(\nu)R_{\mathrm{BS}}T_{\mathrm{BS}}$. The intensity $I_0(\nu)\left(R_{\mathrm{BS}}^2 + T_{\mathrm{BS}}^2\right)$ is reflected back to the source. The varying, or the modulated, component of the output has the amplitude $2I_0(\nu)R_{\mathrm{BS}}T_{\mathrm{BS}}$. [2] Therefore, even with an ideal beamsplitter, the detector receives only the half of the energy of the input radiation. Furthermore, the light is typically polarised in the beamsplitter [2].

The most common materials for beamsplitter are germanium (Ge), silicon (Si) and poly(ethylene terephtalate), known also as Mylar, [2]. Germanium and silicon are typically used in mid- and near infrared bands. Mylar is mainly used in the far infrared. The mid-infrared beamsplitter are vapour-deposited on a substrate. The broadband of these beamsplitters could be widened by using multiple layers deposited on each other.

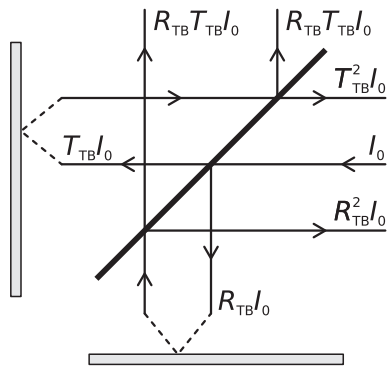

Figure 2.14 Intensities of the first reflections and transmissions in the beamsplitter. The beam paths are separated for clarity.

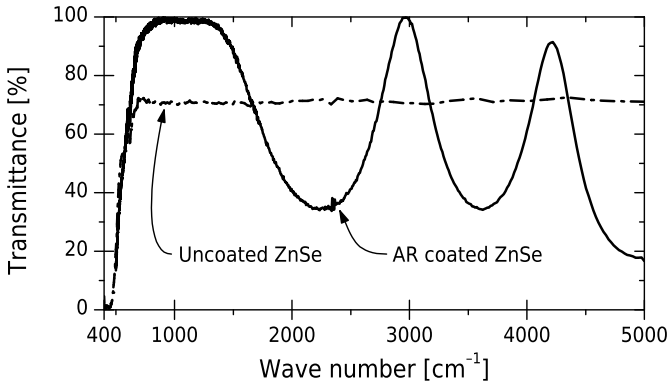

Figure 2.15 The transmittance of uncoated and anti-reflection (AR) coated 5 mm thick ZnSe windows [29]. Transmittance values may have had different reference data.

There are at least tens of substrates, which transmit the infrared radiation. The most used materials in mid-infrared are potassium bromide KBr and zinc selenide ZnSe [2,25]. Also fused silica, or quartz, and calcium fluoride CaF_2 and barium fluoride BaF_2 are often used [26]. Usually, the material for infrared have terrible mechanical properties. Many of them are hard and brittle, as BaF_2, or very soft, as KBr [26,27]. The zinc selenide substrate was selected for this work because it has much better mechanical properties than KBr although KBr would have provided wider transmission region [27,28]. Additionally, ZnSe is not hygroscopic as KBr is, so it will tolerate the normal air moisture. ZnSe is yellow-red cubic crystalline, whose index of refraction is from 2.3 to 2.5 in the mid-infrared region [26,28]. The transmission range is approximately from 500 cm^{-1} to 5000 cm^{-1} or even up to 17000 cm^{-1} depending of the material quality and coatings [26,27]. Typical transmission curve of ZnSe is plotted in Fig. 2.15. Therefore, it is then very good material for mid-infrared region except the situation when strong acids may be in contact with it [26,28].

The beam is reflected successively inside the beam splitter from its surfaces. Additional reflections occurs between the beamsplitter and the compensating plate. These are reduced by slightly wedging the substrate plates and placing them in a small angle. Then the undesired extra interference patterns has several fringes so they modulation depth is negligible. Usually, the substrate plates are also anti-reflection coated to decrease the reflections.

The beam splitter and the compensating plate shift the transmitting beam laterally as illustrated in Fig. 2.5. This is called the parallel shift. It is the distance between axes of the incident and the transmitted beams. The shift can be calculated using the law of refraction (Snell's law). Because it can be a few millimeters, the end mirrors M1 and M2 should be placed off from the beam splitter center to avoid beam cutting by the mirror edges. For the same reason, slightly over-sized beamsplitter should be used.

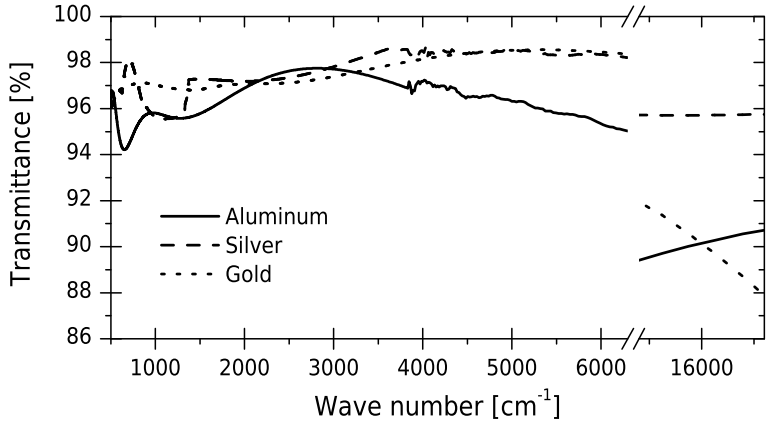

Figure 2.16 Typical reflectances of three metal coatings with scratch protection layer and using unpolarised light and 12° angle of incidence [29].

Mirrors

In FTIR spectrometry, the mirror optics is preferred and the lenses are avoided because the lens materials have poor transmission characteristics. The beamsplitter and the compensating plates are obvious exception because of the limited availability of the beamsplitter materials. Additionally, some sealing windows are usually required, for instance, in sample cells. [1] The plane mirrors are usually the best choice because they do not have aberration. The most important property of the plane mirrors, and also the beam splitter and the compensating plate, is the surface flatness because the unflatnesses cause phase errors to the wavefront, which declines the modulation depth. The flatness should be better than one tenth of the lowest wavelength of interest, or $\lambda_{\min}/10$ [2].

The mirror reflectances are typically very high and depend weakly on the wavelength according to Fig. 2.16. Because the Michelson interferometer has only two plane mirrors, the energy loss caused by the mirrors is low and the beam splitter practically determines the efficiency of the interferometer. In this work, aluminum coated mirrors were mainly used because their price-quality ratio was evaluated better than the silver or gold coatings.

Other than plane mirrors are required for collimating the radiation from omnidirectional source and focusing the beam to the detector. Because they are not part of the interferometer itself, they do not have as high quality requirements as the interferometer optics. In this work, off-axis parabolic mirrors are used in collimating and focusing. The shape of the off-axis parabolic mirror is defined by its clear aperture CA and the focal length f or the effective focal length f_{EFF} as illustrated in Fig. 2.17. The effective focal length is more useful in practice. [2] The elliptical mirrors are also widely used in spectrometers but because they require extra space they are not usually used in compact sized and low resolution spectrometers.

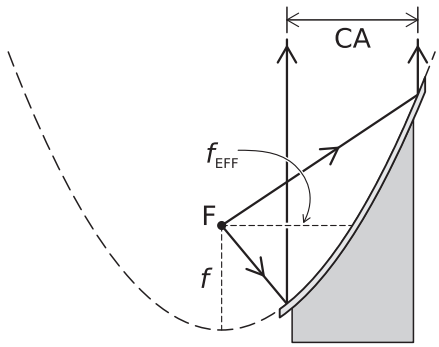

Figure 2.17 Definition of the quantities defining the shape and the dimensions of the off-axis parabolic mirror: the clear aperture CA and the focal length f. Alternatively to the focal length, one can use the effective focal length f_{EFF}.

2.3.2 Infrared sources and collimating

The ideal source for mid-infrared radiation is the heated black body radiator. The radiance emitted by the black body per unit area per wavenumber per steradian is

$$u(\nu, T) = \frac{2\varsigma c^2 \nu^3}{\exp\left[\varsigma c\nu / (k_{\mathrm{B}} T)\right] - 1}, \tag{2.15}$$

where T is temperature of the source in Kelvin, ς is Planck's constant, k_{B} is Boltzmann constant and c speed of light in vacuum [2, 30]. Emissivity of the source is assumed to 1. Few examples of the energy density are plotted in Fig. 2.18.

One of the most common infrared sources is a silicon carbide rod, commercially known as Globar [2, 30]. It is heated by the electric current. Additionally, the other types of resistively heated ceramic elements are used. For example, heat sources originally designed for igniting flammable gases are common. The other formerly common source materials, tungsten and zirconium–thorium–cerium oxide, or Nernst glower, are mainly replaced by Globar or ceramic sources because they have better emissivity in mid-infrared region [30]. Globar sources are typically used at temperatures between 1000 K and 1800 K [1]. Selecting the temperature is always a trade-off between the life-time and the intensity. Often used compromise is 1300 K, which enables the life-time of many years [2, 25, 30].

Point sources produce the spherical wave front, which had to be collimated to planar before accessing the beam to an interferometer. The most general optical assemblies for collimating are presented in Fig. 2.19. Twymann-Green assembly [31], (a), is based on lenses so it is seldom used in infrared. The assemblies (c) and (d), use parabolic reflectors, which have often lower costs than the off-axis parabolic mirror system in (b). The assembly (d) is also known as Pfund system [32]. The collimating system in (e) can be used to adjust the apparent source size, which affects the

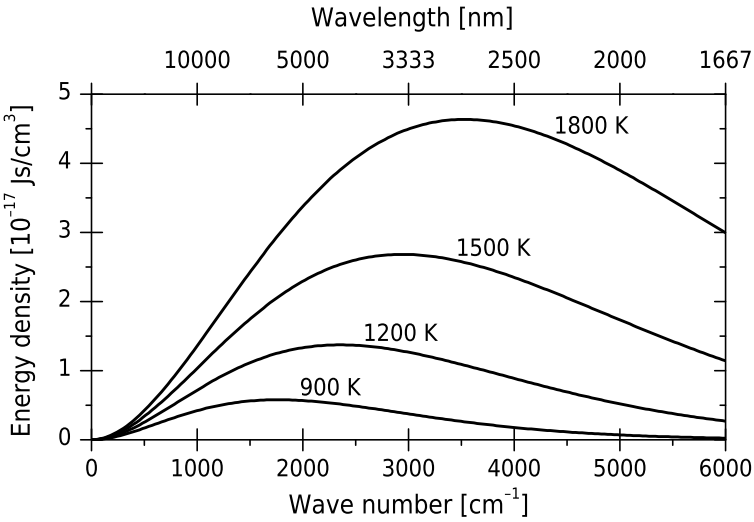

Figure 2.18 Energy density $u(\nu, T)$ of the black body radiation at four temperatures.

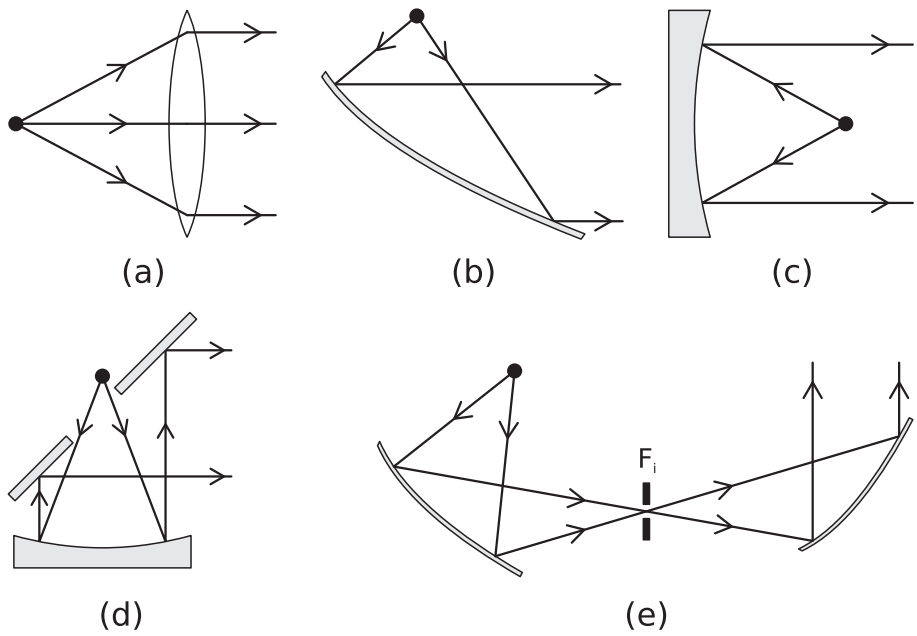

Figure 2.19 The most general collimating assemblies. The assembly (a) is Twymann-Green system with lenses [31]. The second, (b), uses off-axis parabolic mirror [23]. The next two, (c) and (d), are based on parabolic mirrors. The lowest model, (e), has elliptical and off-axis paraboloid mirrors. The apparent source size can be adjusted by an iris placed on the intermediate focal point F_i [2].

spectral resolution. The size can be changed by the iris placed on the focus of the elliptical mirror [2]. Interferometer in this work uses off-axis parabolic mirrors in collimating and focusing because they had the smallest space requirements and will not cut the beam. The chosen mirrors have very short effective focal lengths to cover as large solid angle around the source as possible and to maximise the radiation energy transferred to the interferometer.

The radiation energy transmitted to the interferometer from the source is proportional to the throughput Θ, known also as étendue. If the area of the collimating lens is A and the solid angle of the source seen from the interferometer is Ω, the throughput is [2, 23]

$$\Theta = \Omega A = a\Omega_0 = \frac{aA}{f^2}, \tag{2.16}$$

where a is the area of the source, Ω_0 is the solid angle of the lens seen from the source and f is the focal length of the lens. The quantities are illustrated in Fig. 2.20. Because the finite size of the source, the light rays with a certain wavenumber entering the interferometer are not exactly parallel. This affects the spectrum by two ways. The spectral lines are shifted and broadened. The actual line positions ν_{actual} are obtained from the measured ones by [23]

$$\nu_{\text{actual}} = \frac{\nu_{\text{measured}}}{1 - \Omega/(4\pi)}. \tag{2.17}$$

The line broadening can be modeled by convolving the spectrum with a box function. For example, if the spectrum has a line at ν_0, the spectrum is convolved with the box function [23]

$$\sqcap_\Omega(\nu, \nu_0) = \begin{cases} \dfrac{2\pi}{\nu_0}, & |\nu| \leq \dfrac{\nu_0 \Omega}{4\pi} \\ 0, & \text{elsewhere.} \end{cases} \tag{2.18}$$

The value of the resolution is increased, because the infinitely narrow line is widened and will have FWHH, the full width at half height, of $\nu_0\Omega/(2\pi)$.

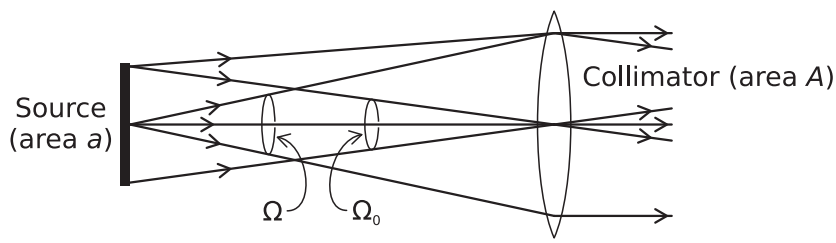

Figure 2.20 Quantities required to estimate the throughput Eq. (2.16) when collimating the radiation from the finite sized source.

When using the off-axis parabolic mirrors for collimating, the throughput can be estimated by using the effective focal length and, as the area A, the appropriate circular area of the mirror because the mirror usually resembles a round disc seen from the source.

2.3.3 Infrared detectors

Infrared detectors consist usually the sensing element, the supporting electronics and possibly the cooling system. The performance of the detector are usually described by the specific detectivity D^*, which is equivalent to the signal to noise ratio of the detector of unit area, in unit bandwidth and with 1 W incident radiation. The specific detectivity depends on the wavelength, the modulation frequency and the field of view, thus the conditions, where it was determined, must be taken account when comparing the detectors. If the detector noise is less than the signal from the photon emission of the surroundings of the field of view, the detector is said to be background limited. The best performance of FTIR spectrometer is achieved, when the signal to noise ratio, SNR, is determined by the detector SNR. Then the noise from other noise sources is less than the detector noise. Infrared detectors are usually more or less frequency dependent. Thus, the mirror velocity should be as constant as possible to avoid producing extra noise from altering frequency. [2, 33]

In general, the infrared detectors can be divided in to three groups based on the interaction between the sensing element and the infrared radiation. Thermal detectors have an element, which has some property that is very sensitive to the temperature. The most used thermal detectors are the pyroelectric detectors made of deuterated l-alanine-doped triglysine sulfate and called DLaTGS detectors [2, 25, 33]. They sense only the change of the infrared radiation, so the signal must be modulated. Noise level of DLaTGS detectors is very low. However, the detector material is hygroscopic, so it must be sealed, and also piezoelectric so it acts as an accelerometer or a microphone.

The second group are quantum detectors, which are semi-conductors, where photons can easily excite electrons from the valence band to the conduction band [2, 33]. The most common material is mercury cadmium telluride, or MCT [2, 25, 33] but many other materials are also used, such as PbS, PbSe and InSb. MCT detectors have typically much better specific responsivity D^* and is less dependency on frequency. However, the MCTs have to be cooled 77 K, which is usually done using liquid nitrogen, so they are not suitable for portable instruments.

The third method is a photoacoustic detecting where the modulated infrared radiation is absorbed to the sample material inside the small cell. The material expands and a pressure pulse is generated and detected by the microphone. The state-of-the-art microphone is the silicon cantilever mi-

crophone, which position is measured with an interferometer [34–36]. The photoacoustic detector has very interesting properties. Firstly, its shape and size can be varied much more freely than other detectors types. It is possible to optimise the detector form and dimensions for the specific interferometer output. Secondly, its response is much more linear than the other detector types. Furthermore, it measures directly the absorbed energy so recording background spectra is not required. The major difference between the photoacoustic detectors and more common DLaTGS and MCT detectors is the significantly lower frequency response. While the DLaTGS and MCT detectors bandwidths are typically from 1 kHz to 100 kHz or even up to 1 MHz, the photoacoustic detectors are best operated at 1 kHz. Therefore, mirror velocities of the most spectrometers are too high for photoacoustic detectors, so low mirror velocities were studied in this work.

2.3.4 Signal to noise ratio

Signal to noise ratio, SNR, of the spectrometer is approximately

$$\mathrm{SNR} \propto \frac{\xi u(\nu,T)\Theta\,\Delta\nu\,D^*\sqrt{t}}{\sqrt{A}}, \tag{2.19}$$

where, ξ is the interferometer optical efficiency per unit wavenumber interval, $u(\nu,T)$ is the black body energy density given by Eq. (2.15), Θ is the interferometer throughput, $\Delta\nu$ is the spectral resolution, t is the measurement time and A is the area of the detector active element. The area factor is applicable when the detector is DLaTGS or MCT. Therefore, it is feasible to select a detector material with high D^* and as small active area as possible. Additionally, increasing the source temperature enhance SNR but generally shortens its life-time. Lengthening the measurement time and lowering the resolution also increase SNR. Thus, the low resolution is used in gas analysers to obtain better SNR and thus better detection limits. The throughput of the interferometer may be limited by the source or the detector size or their collimating optics. The optimal situation is when the image of the source formed on the detector just fits the detector size, or the throughput of the detector side Θ_D is equal to the throughput of the source side Θ_S, which is called throughput matching [2]. The best performance of the interferometer is achieved, when the signal to noise ratio, SNR, is determined by the detector operating as background limited. Then the noise is determined by the photons from the surroundings in the field of view of the detector.

2.3.5 Recording and processing the signals

Processing the interferogram

The interferogram is digitized to the computer, which does the Fourier transform and the other signal processing. The digitizing means that the interferogram is truncated and discretely sampled, which both affect to the spectrum. In the truncation the interferogram is multiplied by the box function, which corresponds convolving the spectrum with the sinc function. The discrete sampling aliases the spectrum. Thus, the resulted spectrum has multiple copies of the actual spectrum spread periodically over each other. These effects are illustrated in Fig. 2.21 using the spectrum of monochromatic light. The FWHH of the lines, or the resolution of the resulted spectrum, is approximately

$$\Delta\nu = \frac{1.21}{2L}, \tag{2.20}$$

where L is the total optical path difference of the interferogram. Because the resolution is limited also by the finite source, the optimal truncation is obtained when

$$\frac{\nu_0\Omega}{2\pi} = \frac{1.21}{2L} \tag{2.21}$$

To avoid aliasing the spectral components on each other, the sampling must be done at the frequency at least twice the maximum frequency of the signal to be recorded. Additionally, the signal should be analogically low pass filtered to minimise aliasing of the high frequency noise.

The truncation of the interferogram produces side lobes to the spectral lines. They are usually undesired and decreased by the apodisation function, which is applied to the interferogram before Fourier transform [2, 23]. Apodisation, also known as windowing, has some side effects of which the broadening is the most important. Every apodisation function broadens the spectral peaks and lowers their heights. There are vast number of different apodisation functions, which are used in signal processing [37]. The few common functions, their Fourier transforms and FWHH values are summarised in Table 2.B and plotted to Fig. 2.22. In this thesis, Hanning and Blackmann-Harris 3-Term functions are mostly used. Furthermore, the spectra are often interpolated using the zero-padding method.

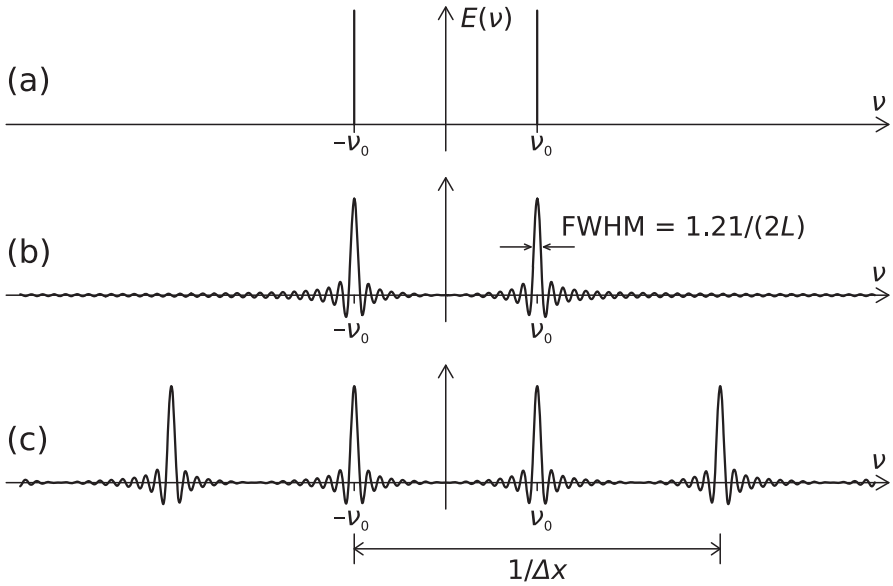

Figure 2.21 Effect of truncation and sampling of the interferogram of the light with monochromatic spectrum. The original spectrum (a) is firstly convolved by sinc function because of the truncation. Then the sampling aliases the spectrum periodically resulting to (c).

Table 2.B Summary of four common apodisation functions $W(x)$, their Fourier transforms and FWHH values of the resulting spectral lines. The box function corresponds the truncation of the interferogram. Each function is $W(x) = 0$, if $|x| > L$.

Name	$W(x), \lvert x\rvert \le L$	$\mathcal{F}^{-1}\{W(x)\}$	FWHH
Box	1	$2L\,\mathrm{sinc}\,(2\pi\nu L)$	$\dfrac{1.21}{2L}$
Triangle	$1-\dfrac{\lvert x\rvert}{L}$	$L\,\mathrm{sinc}^2\,(\pi\nu L)$	$\dfrac{1.77}{2L}$
Hanning	$\cos^2\left(\dfrac{x}{2L}\pi\right)$	$\left[L+\dfrac{(2\nu L)^2}{1-(2\nu L)^2}\right]\mathrm{sinc}\,(2\pi\nu L)$	$\dfrac{2.00}{2L}$
Black-mann-Harris 3-Term	$\displaystyle\sum_{j=0}^{2} a_j \cos\left(\frac{j\pi}{L}x\right)$, where: $a_0 = 0.42323$, $a_1 = 0.49755$, $a_2 = 0.07922$	$\displaystyle L\sum_{j=0}^{2} a_j\Big(\mathrm{sinc}\left[\pi\left(2L\nu+j\right)\right] + \mathrm{sinc}\left[\pi\left(2L\nu-j\right)\right]\Big)$	$\dfrac{2.27}{2L}$

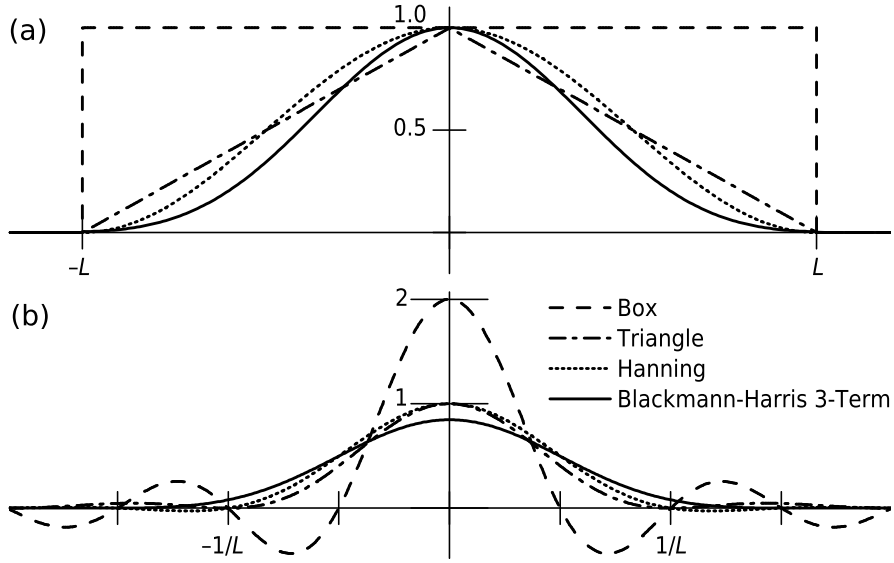

Figure 2.22 Four common apodisation functions in time space, in the plot (a). The Fourier transforms and FWHH values (the full width at half height) of these functions are in the plot (b).

Recording the optical path difference and triggering the sampling

In addition to the recording the interferogram, the corresponding optical path difference has to be determined. Because the optical path differences are very short, they are normally measured using the interference of the monochromatic light, which is usually from a laser. The reference laser beam goes along the equal light path as the infrared beam and thus the interference is observed at the output. Intensity of this light is detected. The signal is very close to sinusoid, whose period corresponds to optical path difference of one wavelength of the reference laser. If the time between two successive zero crossings is Δt, the mirror velocity is

$$v_{\text{mirror}} = \frac{\lambda_{\text{L}}}{4\Delta t}, \tag{2.22}$$

where λ_{L} is the laser wavelength, because the change in the optical path difference is in Michelson interferometer twice the travel of the moving mirror. The mirror velocity is often given as the laser frequency f_{L}, or the frequency of the laser signal, which is

$$f_{\text{L}} = \frac{1}{2\Delta t} = \frac{2}{\lambda_{\text{L}}} v_{\text{mirror}}. \tag{2.23}$$

In practice, the laser and infrared beams are not exactly parallel but have an small angle between them. This causes a constant error to the wavenumber values. The error can be corrected by calibrating the wavenumbers using

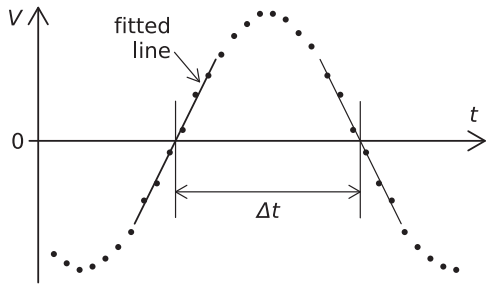

Figure 2.23 Determining the half period Δt of the laser signal by interpolation method.

accurately known spectral lines. One often used line is a water line at 1918 cm^{-1}.

The period Δt is usually determined by removing the DC level from the laser signal and then determining the zero crossings either analogically or digitally. [38] When analogical zero crossing detector is used, the sampling of the interferogram is triggered according to the zero crossings. If digital method is preferred, the laser and infrared signals are over-sampled with high sampling rate. The each zero crossing is interpolated from the laser signal data by, for instance, fitting a line or low order polynomial to data nearby the zero crossing as illustrated in Fig. 2.23. The interferogram is then interpolated using the estimated zero crossing positions. The result is the interferogram and corresponding optical path difference values.

Distortions and the noise in the laser signal decreases the accuracy of zero crossing values. Firstly, the noise should be low. However, often the major error sources are low frequency swaying of the DC level of the laser signal and alterations of the laser wavelength. The swaying causes sawtooth like errors to zero crossings, which can be reduced by processing the laser signal with a high pass filter with low cutting frequency. The wave length issues can be minimised by using stabilised laser. Other typical error sources are the unflat frequency response of the laser detector and scattered light from the surroundings.

Formerly, the gas lasers were almost exclusively used as the source of the reference light because of their stability and long coherence length. The most common laser is the red Helium-Neon laser which vacuum wavelength is 632.8 nm. However, in the last years, the solid state lasers have become common especially in portable instruments hence they are much smaller than gas lasers, their coherence length is sufficient and the wave length stability has been improved [21, 39, 40].

The center of the interferogram of the zero optical path difference is important to determine. If the sampling does not coincide with the zero optical path difference, phase errors are produced to the spectrum. The sampling can be triggered with using the white light as a third beam in the interferometer. Its interferogram has very narrow centreburst, which can be

used to determine the zero optical path difference. White light centreburst can be also positioned off the infrared centreburst to trigger the sampling. However, if the two-sided interferogram is measured, the phase errors can be taken account by calculating the amplitude spectrum or the power spectrum

$$\left|E(\nu)\right| = \sqrt{\left[\mathcal{F}_{\sin}\left\{I(x)\right\}\right]^2 + \left[\mathcal{F}_{\cos}\left\{I(x)\right\}\right]^2} \tag{2.24}$$

where $\mathcal{F}_{\sin}$ and $\mathcal{F}_{\cos}$ are Fourier sine and cosine transforms.

2.4 Thermal stability and velocity errors

2.4.1 Thermal stability

Stability measured with modulation depth

The thermal stability is one important property of portable spectrometers. The external temperature may change even tens of degrees in Celsius during the operation. Most interferometers are too unstable for portable use. The most sensitive devices, especially those intended for laboratory usage, may completely lose the modulation even after a few degrees change [41–43]. There are also available some compact spectrometers, which, however, have to be equipped with a thermal stabilisation even though the interferometer would have a dynamic alignment. However, several thermally stable interferometers are available and they are shortly discussed later.

Interferometer thermal stability is usually measured with the change in the modulation depth over a temperature change. The modulation stability is generally reported as the percentage units per one Celsius temperature change. Unfortunately, this is not explicit measure of the modulation change. Firstly, the change of the modulation depth depends non-linearly on the tilt angle or the amount of the shearing. Additionally, the tilting and shearing are often non-linearly, and even non-monotonically, related to the thermal expansion. Furthermore, the modulation depth is approximately proportional to the square of the wavenumber according to Eq. (2.8) and Eq. (2.11). So, the decrease of 10 percent units at 2000 cm^{-1} corresponds about 40 percentage units at 4000 cm^{-1}. As a summary, the rate of the modulation change per temperature depends on many factors. Therefore, when reporting the modulation depth changes, it should be also reported the applicable wavenumber and temperature ranges and other things involved. In that sense, information given in many commercial brochures of the spectrometers is often too incomplete to make proper comparisons.

In additional to the tilting and shearing, the thermal stability of the source and the detector affect also the spectrometer response [7, 44]. Thus, the sources are usually equipped with a feedback system to control their temperature and the detectors have temperature stabilisation and cooling system. In this thesis, the stability of the sources and detector is not discussed in detail because this work concentrates on the interferometer itself.

Concepts of thermal design

The aim of the thermal design is to reduce the effect of the thermal expansion. The different expansion between the interferometer parts causes the misalignment of the optics. The differences in the thermal expansion are resulted from the temperature gradients in the interferometer or the different coefficients of the thermal expansion between the interferometer components. For example, the optics has usually very much lower coefficient of thermal expansion than the other parts usually made of aluminum or some other alloy.

In general, the interferometer can be designed so that either the thermal changes of the structure are completely avoided, or the structure tolerates the changes and responses them rapidly [45]. The first view is not suitable for portable devices because the design requires huge thermal mass, insulation and possibly active stabilisation system [46]. The second way is better for compact sized instrument, because it is based on materials with good thermal conductivity, such as aluminum, and small masses and a careful thermal design. Possibly, the special conducting paths for thermal energy are needed to minimize the temperature gradients, which often produce misalignments. Therefore, the second way was used in thermal design of this work.

Ideally, the whole interferometer would be made from one material. The solid interferometers, manufactured from almost uniform material, typically from a glass, are introduced [47,48]. However, mirrors and the beam splitter are bonded to the body structure. Glass materials have quite poor mechanical properties so they are not best choice for the body of the portable instrument. The more general method is to use some easily machinable material, as aluminum, in the body and mountings. The best way is to use a single block of uniform material, which have openings for beams and the optics. Then the whole block is scaled uniformly during the temperature change.

Optical components are best mounted on their reflective side at three fixed positions, for example, using three studs machined directly to the mounting block [49]. Hence, the alignment of optics is determined by the optically active surface. Bonding and gluing of optics should be generally avoided because deformation of the glue layer may cause tilting. Additionally, too rigidly mounted optics may break by forces from the thermal expansion. The better way is to clamp the optics mechanically and use a spring force in pressing. The spring forces are typically very linear over the small deflections produced by thermal expansion. However, the gluing is sometimes desired, for example, to reduce sensitivity to strong shock vibrations [50]. The stable mounting between -70 °C $\ldots -11$ °C has been achieved with the spectrometer for Mars Infrared Mapper for ESA ExoMars Pasteur mission [50]. The mounting was based on special spacers between

the optical component and the mounting block. Later in the same project, compliant elements were added to the mounting and the alignment was reported to be stable in cooling from the room temperature to −70 °C [51].

Interferometers with reported thermal stability

Thermal stability of few spectrometers are reported in the literature. Some modulation depth figures per Celsius are given. Unfortunately, many instruments are just claimed as "stable" or "working" in a certain temperature interval, which prevents the comparison. Thermal stability has been completely ignored in published material. The stability represented by the modulation change during the temperature change are summarised in Table 2.C. The modulation values from literature were converted to the percentage units per Celsius at 3000 cm^{-1} always when possible.

One of the nearest commercially available instruments is Agilent 4100 Exoscan, which is a hand-held spectrometer intended for external or internal reflectance measurements [40]. It is based on Michelson interferometer built with plane mirrors and dynamic alignment system. In this work, dynamic alignment will not be used for simplicity. For some reason, any modulation depth figures are not reported, as the author knows, although seems to be an advanced product.

Stabilities of ABB MB3000 and Gasmet™ DX-4000 are quite well specified. The temperature stability of ABB MB3000 is specified as less than 1 % per Celsius at 4000 cm^{-1}. Its interferometer is double pendulum type with cube corner end mirrors as in Fig. 2.13(a). Mirrors are moved by the double pivot mechanism [53]. DX-4000 is based on GICCOR™ interferometer and has the thermal stability less than two percents of measuring range per 10 °C temperature change [52]. Despite the stability and robustness, both spectrometers are briefcase sized and too heavy for truly portable use.

FTRX Monolithic 20™ [54] (FTRX llc) is OEM FTIR spectrometer having Steel version of Michelson interferometer. The fixed mirror is planar and the other arm is assembled from the moving corner cube and another fixed plane mirror as in the upper right corner of Fig. 2.10(b) [47]. The stability is specified only by stating that the deviation of the 100 % line is less than 2 % during 16 hours. The last examples of stable commercially available spectrometers, are portable FTIR spectrometers Turbo FT™ and Model 102 (D&P Instruments Ltd.) [20, 21]. Turbo FT is refractively scanned rapid scan spectrometer. Model 102 is based on Michelson interferometer. However, the both have MCT detectors requiring liquid nitrogen cooling, which limits the portability substantially.

Possibly, the best thermal stability has been achieved with Carousel interferometer. The modulation depth at 10000 cm^{-1} decreased less than one percent during the temperature change from 20 °C to 50 °C or averagely about 0.03 percentage units per Celsius [5, 7]. At 3000 cm^{-1}, it corre-

sponds to approximately one ninth of this, or 0.003, because of the squared dependence of the modulation on the wavenumber, as in Eq. (2.8). The instability was probably originated from fluctuations of the source emission rather than the misalignment. Carousel is based on the rotational motion of the block of five plane mirrors, as in Fig. 2.11(c) on page 18, so it is principally larger than the Michelson interferometer. As the author knows, it is not commercially available anymore.

Good stability is achieved also with space-borne spectrometers and interferometers. For example, Mars infrared mapper for ESA ExoMars Pasteur mission was reported to "work" in range -70 °C $\ldots -11$ °C [50]. It had a double pendulum interferometer with the beam splitter glued to the aluminum frame via thermally designed spacers. In addition, other examples exists [51, 56], but usually the space borne equipment is manufactured individually and technical solutions are often expensive although they could be sometimes applied to instruments on the ground.

Some authors have reported the thermal stability using the emission spectra [57] or the height of the interferogram centreburst [55]. However, these are not very well comparable with the modulation depth or 100 % line values, which is unfortunate because the interferometer presented by Herrala et al [55] is very interesting. It is compact sized and based on Michelson type, where the movable mirror is supported by parallel springs, or possibly porch swing bearing. The interferometer was aligned at 25 °C and the centreburst height was approximately halved from that at the extremes of interval from 5 °C to 40 °C. If the initial alignment was very close to perfect, the modulation depth was approximately halved, which indicates about 3 percentage units loss per Celsius, which is quite much. No further reports were found on this interferometer so maybe its developing was discontinued.

2.4.2 Velocity errors

In principle, the driving velocity of the mirror, or the rate of change of the optical path difference, does not affect to the interferogram measured as a function of optical path difference. However, the measurement equipment works in time space and has practically always unflat frequency response, so the mirror velocity should be very stable to avoid distortions of the interferogram. Especially, infrared detectors are strongly frequency dependent. Additionally, the laser signal may be distorted by the varying frequency, which reduce the accuracy of the optical path difference recording. Furthermore, the periodic velocity error, for example from a harmonic vibration, adds an extra modulation to the interferogram, which produces ghost lines around the every peak of the spectrum because of the shift and modulation theorems of Fourier transforms [23, 58]. Harmonic vibrations may also cause the periodic misalignment, which would immediately affect the measured spectrum by fluctuations of the modulation depth.

Table 2.C Specifications and the modulation stability of reference instruments. The first six are commercially available and the rest are otherwise reported. Values of the modulation depth change are estimated from figures given in the literature and are given in percentage units per Celsius at 3000 cm^{-1}. The interferometer is abbreviated as ifm and Δt is the temperature range.

Spectrometer or interferometer (manufacturer)	Size [mm]	Mass [kg]	Δt [°C]	Modulation stability [% units per °C]	Comment and sources
Agilent 4100 Exoscan (Agilent Technologies Ltd)	21×17×10	3	−30 . . . +50		External or internal reflectance [40]
Gasmet DX-4000 (Gasmet Technologies Ltd)	45×39×16	14	+5 . . . + 30	< 0.2	GICCOR ifm [52]
ABB MB3000 (ABB Inc.)	44×37×28	24	+10 . . . +35	0.6	Layout in Fig. 2.13(a) [39, 53]
FTRX Monolithic 20 (FTRX llc)	27 × 21 × 8	5	+20 . . . +40		End mirror: Fig. 2.10(b) [47, 54]
Turbo FT (D&P Instruments Ltd.)	20×20×15	< 4	+20 . . . +30	"stable"	Refractively scanned; MCT [20, 22]
Model 102 (D&P Instruments Ltd.)	36×23×20	< 7	+20 . . . +30	"stable"	MCT [21, 22]
Carousel ifm			+20 . . . +50	0.003	Layout: Fig. 2.11(c) [5, 7]
Mars infrared mapper (ESA ExoMars Pasteur mission)			−70 . . . −11	"worked"	Space-borne; double pendulum ifm [50]
Michelson ifm (VTT, Herrala et al)	21 × 15 × 7		+5 . . . + 40	3[a]	Porch swing; [a]centreburst height [55]

2.5 Bearings for Michelson interferometer

2.5.1 Requirements for motion linearity

In this thesis, by the linear mirror motion it is meant two things. Firstly, the optical path difference depends linearly on the mirror displacement. That is, the mirror path is a straight line or very close to it. Secondly, the mirror is not rotated during the motion or its plane remains perpendicular to the travel path. The tilt angle is the angle of the rotation from the ideally aligned mirror. The tilted mirror produces extra optical path difference between the beams reflected from the opposite edges of the mirror, which decreases the modulation depth. The output signal strength is proportional to the modulation depth as in Eq. (2.7). The maximum allowed decrease of the modulation depth sets the limits for the tilt angle, which has to be achieved during a single scan and from scan to scan. To keep the modulation depth above 0.95, the tilt angle should be less than about 14 μrad with the beam diameter of 25 mm and the wavenumber of 3000 cm^{-1}, according to Eq. (2.8). This wavenumber is one common reference convention when reporting the modulation values and thus it is used also in this thesis. The previous tilt angle corresponds to about 350 nm difference between the opposite mirror edges, or the optical path difference of about 700 nm. Griffiths and de Haseth have presented tighter limits in their book [2] but 0.95 was regarded as sufficient for this work.

A linear motion is realised with a bearing system, which also supports the moving mirror and its mounting components. Suitability of the certain bearing system depends largely on its purpose: the high resolution spectrometer, where the mirror is driven over several meters, has very different requirements than the low resolution model, where the mirror travels only few millimeters. The numerous different bearing systems have been presented and they are summarised in the following. The porch swing bearing is emphasized hence it is used in this work.

2.5.2 Fluid bearings

The fluid bearings are based on a thin layer of fluid, gas or liquid, between the sliding surfaces. The one of the first types was air bearing where the compressed air was pumped on the small gap between the moving parts [9]. This thin airbed supported the moving mass containing the mirror to be moved. Instead of air, the hydraulic oil has been used between the sliding surfaces [59]. These provide very smooth motion and low velocity errors but supports for the compressed air or the hydraulic systems are very massive.

One interesting construction is the magnetic suspension, where the movable part levitates on the magnetic field [60]. The bearing has no mechanical contact, which provides the smooth motion and minimal wearing. The magnetic bearing has been used at least in the interferometer of Adeos I

satellite [61]. The bearing has not become common possibly because the design and assembly seems to very complicated.

2.5.3 Bearings with mechanical contact

Linear motion can be rather easily realised by the bearing based on the mechanical contact. One possibility is the piston moving in the cylinder, or any other syringe like construction. The materials of the sliding surfaces should be selected with care to control the friction. Especially, the difference between the static and dynamic friction is important when avoiding the stick and slip motions. Another mechanical bearings are ball bearings and different rail guides. One example is balls rolling on V-shaped guide. Although the mechanical bearings have typically low expenses, the mechanical contact produces often vibrations and non-smooth motion because of the friction. To minimise the vibrations, one may require extreme cleanliness in the manufacturing and adding an extra lubrication, which needs maintenance. The wearing in mechanical contact limits the life time of the bearing.

2.5.4 Porch swing bearings

The porch swing bearing is basically a four bar link mechanism for a linear motion, as illustrated in Fig. 2.24. These mechanisms have been known for very long time. They are very commonly used in numerous places from desktop lights and bicycle derailleurs to heavy machines [62, 63]. In interferometers, pivots of the linkage are generally made of compliance elements such as flat springs. The four most often used pivot structures are presented in Fig. 2.25. The simplest is the flat spring, as in the drawing (a). Its stability can be improved by adding stiffening clamps to springs so that the compliant section shortens to a hinge as in (b). In both configurations, more than two flat springs can be used and springs can have openings. The third type is based on flexure pivots, as in the drawing (c). All of these three linkages produce some vertical shift of the movable arm. This shift

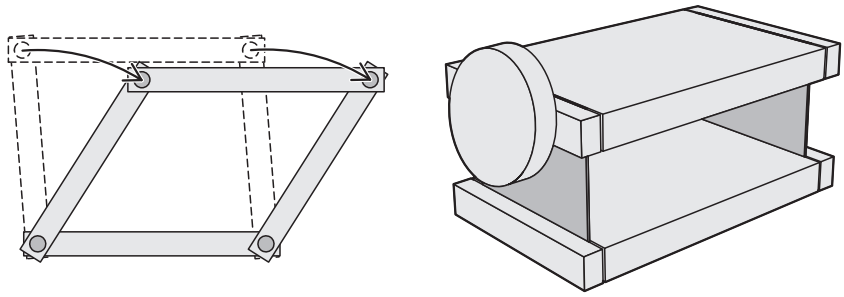

Figure 2.24 The left one is a parallel four bar link mechanism and the right is a basic porch bearing assembled using two parallel flat springs and a round mirror.

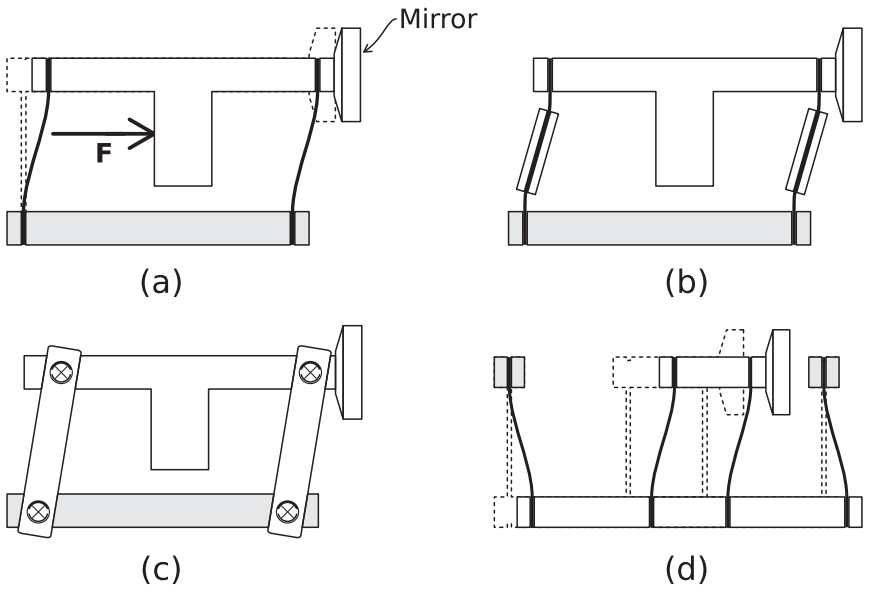

Figure 2.25 Four porch swing bearing structures. In type (a), flexures are parallel flat springs, which can be stiffened using clamps, as in (b). The third typical way, (c), is to use flexure pivots. Porch swings can be cascaded in series, as in (d), which completely removes the vertical motion. The grayed parts are fixed. Figure is partly reproduced from [68].

can be avoided by cascading two porch swings in series, as in the drawing (d) [62, 64, 65]. However, the vertical motion, or the motion along the reflective plane, has minor effect when using plane mirrors. Very complicated porch swing structures can be made [62, 66, 67] but these are not needed in this work.

Porch swing bearings have none of the disadvantages of fluid bearings or bearings with sliding surfaces mentioned in two previous chapters. The porch swing has quite a simple structure, which can be made extremely small. Proper compliance elements are virtually frictionless, which provides very smooth motion. They have practically no wear if they are not loaded over the material elastic limits, which is easily assured. Any lubrication is not required so the bearing is maintenance free. Hence, porch swing bearings based on compliance elements are very suitable for the FTIR interferometers and, in fact, have been already applied. The major limitation is the rather short travel length, which enables only low or moderate spectral resolution. The mirror motion produced by the porch swing bearing is discussed in Chapter 3.2.

The first known report about the porch swing in interferometers is by Walker and Rex [2,18]. They used flexure pivots as in 2.25(c). This kind of interferometer has been operated successfully in harsh environments such as helicopters [69], in an air balloon [70] or during a rocket flight [71]. In the interferometer in the Nimbus III space flight, some kind of parallel

spring suspended moving shaft was used [17]. The porch swing driving has been used for visible band imaging spectrometer in a telescope [72] and in a commercial open path emission spectrometer [57]. The basic system, as in (a), has been used also in many devices [9, 55, 73]. Many patents, as [74–78], are also related to the porch swing design. The porch swing driving is also used in a few commercial products, but they typically use a dynamic alignment system, which is avoided in this work. One interesting variation is the interferometer in ABB MB3000 spectrometer [39, 53]. Its double pivot system corresponds to the mechanism in Fig. 2.25(b), but movable mirrors are corner cubes mounted to stiffening plates. Reflector faces are opposite each other and the beam splitter is in the middle of them. This driving is said to very robust and stable.

2.6 Interferometer design basis in this work

The aim of this work is to design an interferometer for a portable, or even hand-held, FTIR spectrometer. Hence, the instrument should be compact sized, Michelson interferometer assembled with plane mirrors was selected as a basis. It is the simplest interferometer type for FTIR. Therefore, it makes possible to minimise the size with a given beam diameter. The plane mirrors cost less than more commonly used cube corner mirrors. Additionally, the plane mirrors require less space than the corner cubes. Michelson interferometer is also simple to align, which is an advantage especially in mass production.

Because of the plane mirrors, the linear mirror driving is required. The required mirror travel length is few millimeters, because the instrument is intended for low resolution spectroscopy. The porch swing bearing made using the flat spring strips with the stiffening clamps was chosen. This four bar link suspension enables very linear motion over the desired mirror travel. The compliance elements in pivots provide virtually frictionless driving, very smooth motion and have no wear. Therefore, they are nearly ideal for the long term use.

The interferometer alignment was decided to make passive, or without any dynamic alignment system, although many existing interferometers are equipped with a dynamic alignment system to stabilise the instrument. The permanently aligned system is preferred in this work because it provides the simpler structure, low expenses and a smaller size. The permanent alignment requires a careful thermal design especially in the mounting of the optical components.

Chapter 3

Mirror driving with porch swing bearing

3.1 Circular trajectory

In this chapter, the trajectory of the mirror mounted to the porch swing is discussed. The non-idealities of the porch swing bearing produce non-linear motion of the mirror, which declines the modulation depth of the interferogram. Firstly, these motion errors are studied based on the paper by Välikylä and Kauppinen [68] (see also Chapter 5). Next, the bending of the flexure elements used to realize the pivots for the porch swing is considered in Chapter 3.4. A more detailed analysis is presented, for instance, in [63, 79–81].

If the porch swing bearing is ideal, lengths of opposite sides of the mechanism are equal and parallel. The side view of the structure resembles a parallelogram. When one arm is pushed, opposite arms stay parallel with each other. Any point in the movable arm follows actually a circular trajectory, so the motion is principally non-linear, as depicted in Fig. 3.1. However, if the travel length of the arm is short compared to other dimensions of the structure, the motion is nearly linear in the direction of the desired motion.

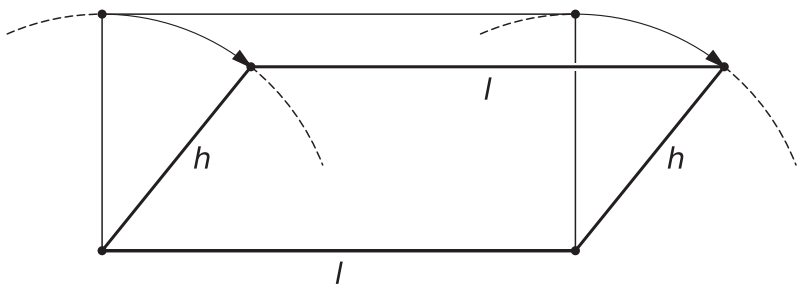

Figure 3.1 Schematic drawing of trajectory of the perfect porch swing.

3.2 Parasitic motions

3.2.1 Definition of the parasitic motions

The purpose of the interferometer bearing is to realize the linear motion of the movable mirror. Any undesired motions of the mirror are called parasitic motions. Thus, even a perfect porch swing produces parasitic motion because the trajectory of the arm, and the mirror mounted on it, is circular. In practice, the porch swing is never perfect but has many different errors originated from manufacturing and assembly. The imperfections of the structure cause the unwanted rotations and shifts of the movable arm and the mirror of the interferometer.

All possible parasitic motions of the arm are rotations around any of the coordinate axes determined in Fig. 3.2 or displacements on the xy-plane. When the interferometer is assembled by using only plane mirrors, the modulation depth is affected almost only by tilting about the x and the y axes or pitch and yaw rotation, respectively. The rotation about the z axis, or rolling, has no effect on the modulation. Displacements in the x and the y directions are usually so small that they have only minor effect in comparison with the tilting, especially if mirrors are larger than the light beam. The upper arm shifts always in the y direction because of the circular trajectory, but a with small travel in the z direction, this shift is very small.

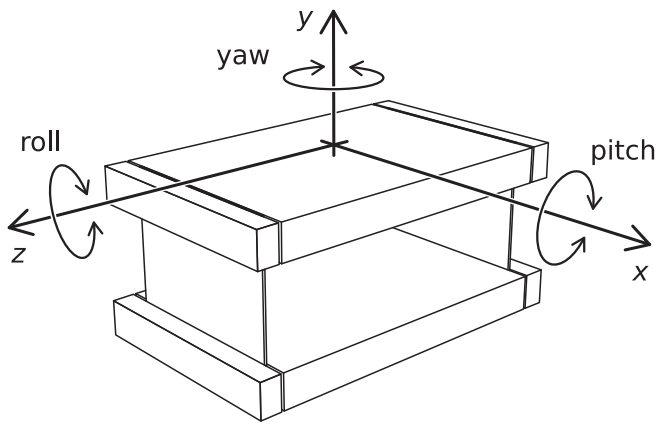

Figure 3.2 The directions of the coordinate axes and the names of the rotations. Figure is reproduced from [68].

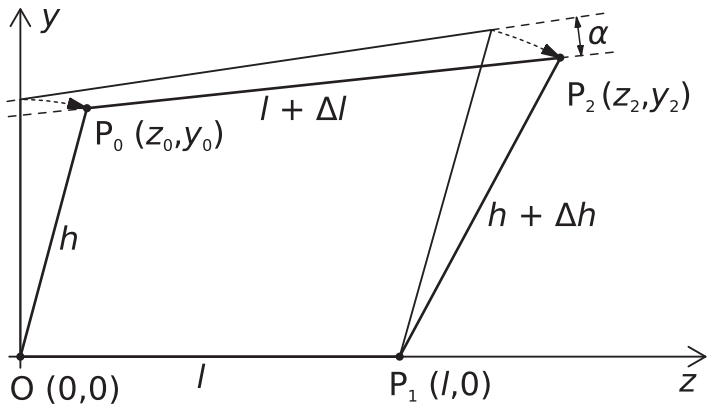

Figure 3.3 Side view of the porch swing structure with manufacturing errors Δl in the arm and Δh the flexure lengths, which produce the pitch angle α when the upper arm is pushed to P_0. The errors are exaggerated. Figure is reproduced from [68].

3.2.2 Unequal lengths of the arms or the flexure elements

General model in two dimensions

Unequal lengths of arms or unequal lengths of flexure elements cause the pitch tilting of the moving arm. In pseudo-rigid model, flexures are approximated as rigid links that have pivots in their ends. The structure looks as a quadrilateral, as in Fig. 3.3. Actually, the flat springs bend to an S-form, which affects the accuracy of the model, because the flexure length h does not keep constant. When displacements and angles are large, the accuracy can be improved by using the effective flexure length h, which is approximately 15 percent smaller than the actual flexure length h_{actual}, or more precisely $h = 0.8517 h_{\text{actual}}$ [81, p. 350]. In the literature, also the ratio $h = \frac{5}{6} h_{\text{actual}} \approx 0.83 h_{\text{actual}}$ is presented [82, 83]. However, this difference is ignored here, because flexures will be used with rigid clamps, or reinforced sections, in their centre thus flexible regions will be so short that they are actually pivots.

The equations for the pitch tilt angle of the structure in Fig. 3.3 can be derived by the intersection of two circles. The derivation is presented in Appendix B.1. The first circle is centred at P_0 and has the radius of $l + \Delta l$ and the second at P_1 with the radius of $h + \Delta h$. These circles intersect at P_2, whose coordinates are

$$z_2 = z_0 + \frac{a}{d}(l - z_0) + \frac{p}{d} y_0 \tag{3.1}$$

$$y_2 = \left(1 - \frac{a}{d}\right) y_0 + \frac{p}{d}(l - z_0), \tag{3.2}$$

where

$$\begin{aligned} y_0 &= \sqrt{h^2 - z_0^2} \\ d &= \sqrt{(l - z_0)^2 + y_0^2} \\ a &= \frac{(l + \Delta l)^2 - (h + \Delta h)^2 + d^2}{2d} \\ p &= \sqrt{(l + \Delta l)^2 - a^2}. \end{aligned}$$

The pitch tilt angle α is the angle of the rotation of the arm from the initial alignment to the current position. The initial pitch θ_0 is the angle between the upper arm and the z axis when the porch swing is not pushed, or $z_0 = 0$:

$$\theta_\mathrm{i} = \sin^{-1}\left(\frac{y_2 - h}{l + \Delta l}\right) \approx \frac{y_2 - h}{l + \Delta l} = \frac{p_\mathrm{i} l - a_\mathrm{i} h}{d_\mathrm{i}(l + \Delta l)}, \tag{3.3}$$

where the subscript i refers to the initial condition. The approximation is valid, if the errors Δl and Δh are small. If the arm is pushed over a small travel z_0, the corresponding angle is

$$\theta = \sin^{-1}\left(\frac{y_2 - y_0}{l + \Delta l}\right) \approx \frac{p\,(l - z_0) - a\left(h^2 - z_0^2\right)^{1/2}}{d(l + \Delta l)}. \tag{3.4}$$

The change of the tilt angle is the difference between these two angles or $\alpha = \theta - \theta_0$. If we assume that the interferometer is perfectly aligned at its initial position, the modulation depth of the interferometer at z_0 can now be estimated by substituting the tilt angle α to Eq. (2.8) on page 9.

The effect of length errors, Δl and Δh, on the tilt angle were illustrated by calculating the tilt as a function of the arm displacement z_0 in four example cases with typical porch swing dimensions. Table 3.A summarises dimensions of these examples. The dimension error was 0.2 mm, which is quite large and thus can be regarded as an upper limit. Results of the pitch angles are depicted in Fig. 3.4 on page 46. Because pseudo-rigid model was used, tilt values are best applicable when flexures have reinforced sections in their centre.

Firstly, the tilt angle depends on the arm length difference Δl nearly linearly but approximately quadratic on the flexure length Δh error. The pitch caused by the arm length difference is about from 30 to 35 times greater than the pitch produced by the flexure length difference. So, the pitch may be much more sensitive to the error in the arm lengths, which is not immediately clear from Eq. (3.3) and Eq. (3.4). The pitch produced by the arm length error depends almost linearly on the arm displacement z_0,

Table 3.A Example cases used in calculations of the tilting and manufacturing tolerances. These cases cover roughly the range of most designs mentioned in the literature. Labels are later used in figure legends. Flexure length values correspond to the pseudo-rigid model.

Example number	Label	Arm length l [mm]	Flexure length h [mm]
1	50/50	50	50
2	100/50	100	50
3	150/50	150	50
4	50/100	50	100

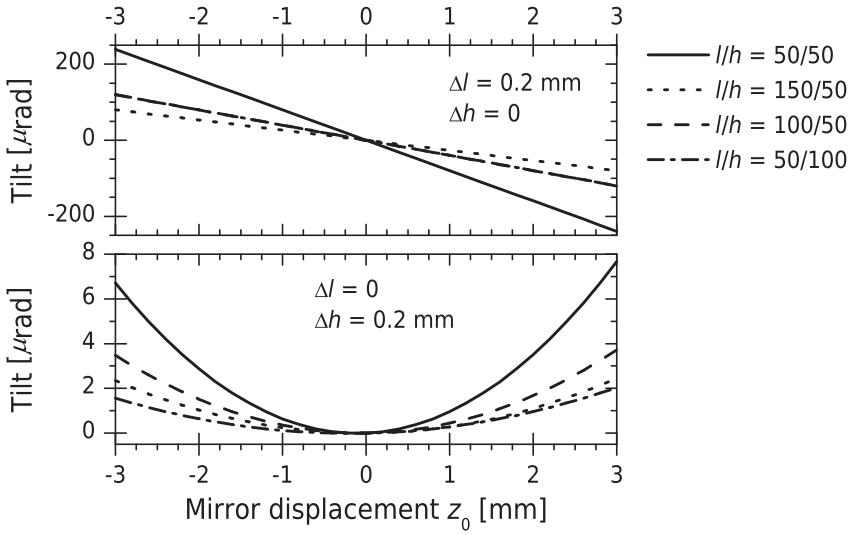

Figure 3.4 The calculated pitch angles of the upper arm of the porch swing or the mirror tilt angles. The difference of the arm lengths is Δl and the difference in the flexure lengths is Δh. The error, 0.2 mm, can be regarded as an upper limit. Figure is reproduced from [68].

but the flexure length error causes approximately quadratic and slightly asymmetric dependence.

The smallest example porch swing, $l/h = 50/50$, was clearly the worst of four examples. The error value 0.2 mm was relatively the largest in this example. The best porch swing was the one, which had the longest arm, or the case $l/h = 150/50$. The long arm decreases the effect of the arm length error while the tilting from the flexure length error is still low.

Small angles model

If the flexure elements are approximated as rigid links and the travel length of the arm and the deflection angles are small, the pitch rotation can be estimated simpler than Eq. (3.3) and Eq. (3.4). If the error in the flexure lengths is Δh, the pitch angle after travel z_0 is [64, 82, 84]

$$\alpha \approx -\frac{z_0^2 \Delta h}{2h^2 l}. \tag{3.5}$$

If the flexures have equal lengths but instead the arms have the length difference Δl, the pitch angle at z_0 is [64]

$$\alpha \approx \frac{z_0 \Delta l}{hl}. \tag{3.6}$$

The derivations of these equations are presented in Appendix B.2.

The approximations show also that the sensitivity of the porch swing to two different errors, Δl and Δh, is very different. If the tilt angles calculated from Eq. (3.5) and Eq. (3.6) are equal, we obtain, after rearranging, the ratio of the length differences as

$$\frac{\Delta h}{\Delta l} = \frac{2h}{z_0}. \tag{3.7}$$

Using dimensions of a typical design, $h = 50$ mm and $z_0 = 3$ mm, the ratio is approximately 33. Thus, to produce a certain tilt angle, about 33 times greater error is required in the flexure lengths than in the arm lengths. In the other words, the bearing is much more sensitive to arm length errors than flexure length errors.

Comparison of models

The validity of small angle approximations, or Eq. (3.5) and Eq. (3.6), were studied by comparing them to the general model, or Eq. (3.3) and Eq. (3.4). Tilt angle values from each model were calculated using example porch swings defined in Table 3.A on page 46 and the length error value 0.2 mm.

Firstly, both models are very close to each other when the error is in the arm length. This is mainly because this error dominates the parasitic pitch rotation. The models differ clearly from each other when the tilt is caused only by the flexure length error Δh. However, the tilting is much smaller with only the flexure length error than with the arm length difference, as illustrated in Fig. 3.4. Therefore, the difference of the models may be insignificant in some cases.

The tilt angle differences calculated from the models were also determined. The differences were divided by the results of the general model, which should be more accurate of these two models. The resulted relative differences are plotted to Fig. 3.5 on page 48. If only the arm length l had

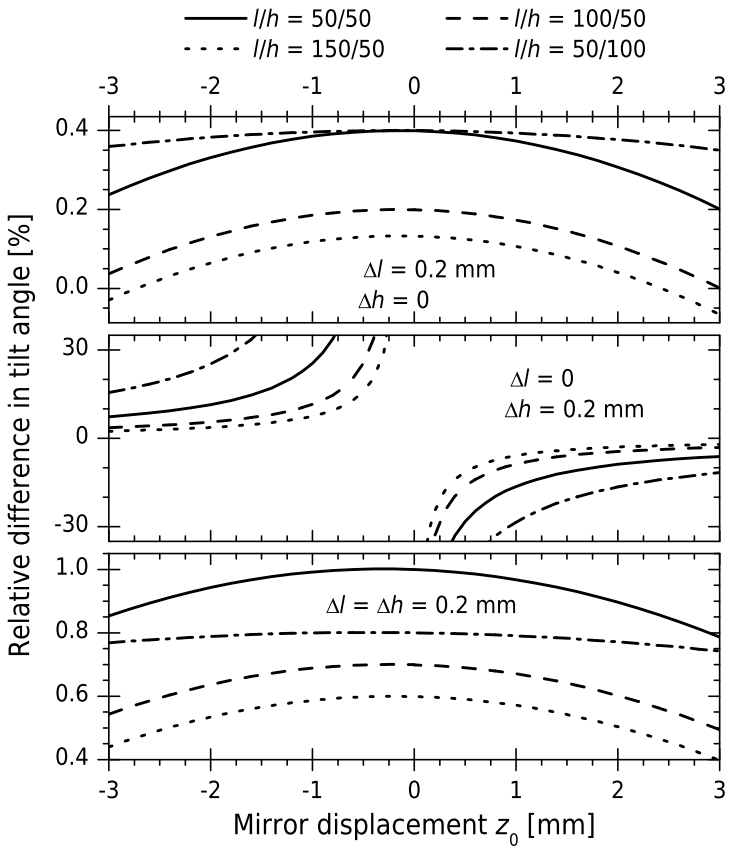

Figure 3.5 Comparison of the pitch tilt angles from the general model (Eq. (3.3) and Eq. (3.4) on page 45) and the small angles model (Eq. (3.5) and Eq. (3.6) on page 47). The tilt angles are divided by the results from the general model. The error value 0.2 mm can be regarded as an upper limit.

the error 0.2 mm, the small angle model Eq. (3.6) differed from the general model less than about 0.4 %. If both the arm and flexure length had an equal error of 0.2 mm, the corresponding difference was below 1 %. When there was only the flexure length error, $\Delta h = 0.2$ mm, the tilt angles differed very much, especially if the the arm displacement z_0 was near zero. However, the tilt angles were also very small in this situation as illustrated in Fig. 3.4, where the actual tilt angles are plotted. The relative error becomes very large mainly because of the small numerical values in the denominator of the ratio of the angle differences. According to the lower part of Fig. 3.4, the tilt angle is less than about 1 μrad when $|z_0| \leq 1$ mm. This results in a modulation depth of about 0.9997 at 3000 cm^{-1} with of 25 mm diameter and uniform intensity profile. This magnitude of the decrease in the modulation depth is very challenging to observe.

Jones [64] reported few measured pitch angles. His porch swing had dimensions of $l = h = 76$ mm. Flexure elements were flat springs, whose

thickness was $t = (0.2 \ldots 0.5)$ mm and the width 25.4 mm. When the length difference of arms was $\Delta l = 0.25$ mm, he measured about ± 440 μrad as the pitch at the arm position $z_0 = 10$ mm. His Eq. (3.6) gives 433 μrad and the general model 438 μrad. With an equal error in spring lengths, the pitch was ± 34 μrad. Corresponding calculated values are 28 μrad from Eq. (3.6) and 29.5 μrad from the general model. So, calculated values are quite close to measured values although the effective length was not considered.

Muranaka et al [82] measured the tilting with length errors in arms or flexures. Their results fitted to small angles model very well, also with the error Δh in spring lengths. However, they did not realise the actual Δh but simulated it by asymmetrically mounted stiffener clamps.

Some support for the general model was obtained in the measurements of this work. These measurements are presented in detail later in Chapter 4.5.2 from page 106.

3.2.3 Non-parallel flexure elements

Two extra imperfections of the porch swing structure are non-parallel neutral axes of flexures and non-parallel principal axes of inertia of the flexures [84]. Neutral axes of flexures become non-parallel if flexures are rotated by a small angle θ around the z axis as presented in Fig. 3.6(a). This may result, for example, by inaccurate mounting. It is assumed that flexures still tend to rotate arms around their tilted neutral axes although it may not be exactly correct. The resulting yaw rotation angle is then roughly [84]:

$$\beta = \frac{\theta z_0^2}{2lh}. \tag{3.8}$$

The effective length of the flexure has to be added to this equation if required. The non-parallelism of inertia axes of flexures results when ends of porch swing arms are slightly askew or flexures are slightly rotated around the y axis as illustrated in Fig. 3.6(b). If the angle between principal axes of

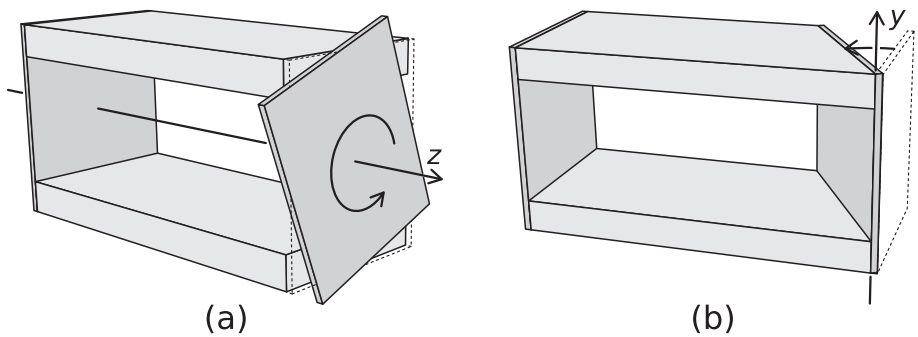

Figure 3.6 Schematic drawing about two imperfections, non-parallel neutral axes of flexures (a) and non-parallel principal axes of inertia of flexures (b), causing parasitic yaw rotations. The errors are strongly exaggerated.

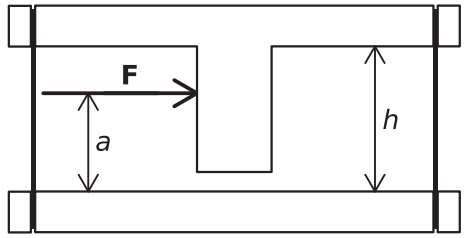

Figure 3.7 Vertical alignment of the driving force **F**. The ideal position of force is at $a = \frac{1}{2}h$.

inertia of flexures is ϕ, the resulted yaw rotation angle is approximately [84]:

$$\beta = \frac{\phi z_0}{l}, \tag{3.9}$$

These relations are rough approximations and actually other parasitic motions probably occur at the same time. Derivations of relations are derived in Appendix B.3.

3.2.4 Misalignment of the driving force

The upper arm is moved by the driving force **F** as depicted in Fig. 3.7. Ideally, this force lies along a line, which is parallel to the z axis and runs through the center of the cross-section on the xy plane of the porch swing. Any deviation from these conditions causes extra forces or moments to the structure and leads to the tilting of the moving arm. Flat springs are probably more sensitive to these errors than flexure pivots or springs with reinforced middle sections. Unfortunately, these misalignments are hard to estimate analytically and usually some numerical methods, such as finite element analysis, are needed [84]. However, few approximations of the effect of the vertical position a of the force **F** have been presented. Muranaka et al [82] have derived the pitch rotation using the theory of beam bending and obtained a result

$$\alpha = z_0 \frac{2\,(h-2a)\,t^2}{l^2 h^2}\left[1 + \frac{3}{175}\left(\frac{z_0}{t}\right)^2\right], \tag{3.10}$$

where a is the distance of the driving force from the lower arm (see Fig. 3.7) and t is thickness of the spring. Muranaka et al verified their equation experimentally. Jones [64] presents the pitch rotation as

$$\alpha = \left(\frac{z_0}{h}\right)\frac{6\,(h-2a)\,t^2}{3l^2 h + 2t^2\,(3a-h)}. \tag{3.11}$$

Both models produce a zero pitch if $a = h/2$, which is the ideal position of the driving force.

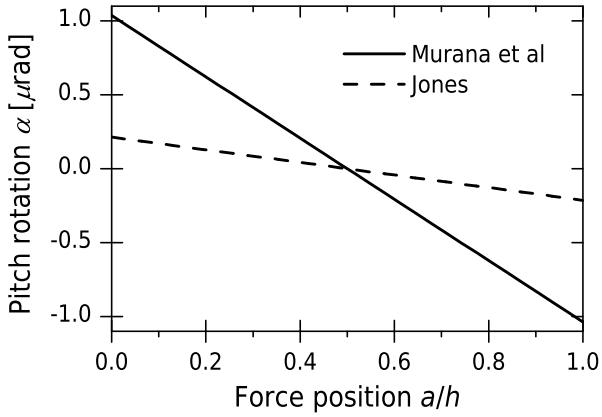

Figure 3.8 The pitch rotation produced by vertically misaligned driving force **F**. The models Eq. (3.11) [64] and Eq. (3.10) [82], are compared. Dimensions of porch swing were $l = 150$ mm and $h = 50$ mm. The spring was $t = 0.20$ mm thick. The travel of the arm was $z_0 = 3.0$ mm.

If the spring thickness t is assumed very small in comparison with the other dimensions and the term $\frac{3}{175}\left(z_0/t\right)^2$ is assumed much smaller than 1, both Eq. (3.10) and Eq. (3.11) reduce to [64, 82]

$$\alpha \approx z_0 \frac{2\left(h-2a\right)t^2}{l^2h^2}.$$

However, the typical thickness of the flat spring is 0.20 mm and the usual arm travel 3 mm. Then, we have $\frac{3}{175}\left(z_0/t\right)^2 \approx 3.9$ so it cannot be neglected. If we have a porch swing, which arms are $l = 150$ mm long and the flexure elements are flat springs with $h = 50$ mm length and the driving force at $a = h$, the sum in the denominator in Eq. (3.11) is approximately $\left(3 \cdot 10^6 + 8\right)$ mm^3. Then, neglecting the last term is reasonable.

Using the above porch swing dimensions, the angle of the pitch rotation is plotted as a function of the vertical position of the driving force to Fig. 3.8. The model of Muranaka et al estimates the pitch substantially larger than Jones' model. However, the tilt reaches only about 1 μrad at 3 mm travel, which is well acceptable in most cases.

3.2.5 Other error sources

If the driving force is coupled mechanically to the arm, the friction in the contact point can cause tilting of the arm [62]. This effect can be reduced, for instance, by using "a wobble-pin" [62] or a slide bearing in the contact area. In this work, a thin glass plate between the pushing pin and the arm is used. However, the problems caused by the friction are usually avoided by using a non-contact coupling with a voice coil as the driving motor.

The combined weight of the arm and flexure elements was ignored in previous sections although the asymmetric mass distribution or the gravity

orientation may cause different loads on flexure elements, which may result in parasitic rotations [64]. These can be minimised by designing the movable arm as light as possible, maximizing the stiffness of flexures, and using as wide flexure elements as possible without widening the arm. However, if the structure is very lightweight, arms itself or clamps holding the flexures may experience bending if they are not rigid enough and, furthermore, screws may have to be evenly tightened [64, 84].

If flexure elements are flat springs, the asymmetric bending of flexures can result from the non-homogeneous spring material, variations of the thickness, or uneven width of the springs [64]. All these may result in parasitic motions. However, the tilting caused by these errors, is usually much smaller than the tilting produced by other errors, such as, the length difference of the arms or the non-parallelism of the arm ends.

Walker and Rex [18] used the flexure pivots as the flexure elements. They used an eccentric mounting in one pivot to enable adjustment of the pivot center because rotation axes of the pivots had variations produced by the tolerances in manufacturing and mounting. The adjustment was used to minimize the parasitic rotations originating from the length differences caused by the misaligned pivot centers.

3.2.6 Stiffener clamps enhance motion linearity

Flat springs will bend asymmetrically because of errors in the assembly and differences in the spring material. Springs can be made more similar with each other by mounting stiffener clamps on the middle of them. Additionally, stiffener clamps increase the stiffness of flexure elements in the x direction, which reduces sensitivity to yaw tilting. The flat spring with clamps acts more as two pivots or hinges but without problems caused by the eccentricity of flexure pivots. Symmetrically assembled clamps were already illustrated in Fig. 2.25(b) on page 40 and they have been successfully used in the tilt reduction [77,80]. Originally, the concept was presented with asymmetrically mounted clamps [62, 82], which, however, require individual adjustment for each structure. Similar effects can be obtained also using monolithic flexure elements, which have reinforced, or thickened, sections. These are usually manufactured using electric discharge machining. In this work, the clamps are used because they clearly decreased the tilting, as will be demonstrated in the becoming Chapter 4.3.3, and electric discharge machining was not readily available.

3.3 Manufacturing tolerances

The lowest acceptable modulation depth sets the limits for the tilt angle. This limits the maximum errors in the manufacturing and the assembly. In Chapter 2.5.1, it was defined that one single error is allowed to decrease the modulation depth not more than 0.05 units at 3000 cm^{-1} with the

stroke length $z_0 = 3$ mm and with the beam diameter of $D = 25$ mm. The corresponding tilt has to be less than 14 μrad. The different manufacturing errors were estimated by using the example cases defined in Table 3.A on page 46. In all cases, the width of the porch swing was assumed to be $w = 50$ mm.

At first, the tolerances were estimated using the tilt angle 14 μrad. The general model for pitch rotation, or Eq. (3.3) and Eq. (3.4) (p. 45) was used to approximate the limits for the length differences of the arms and the flexures, or Δl and Δh. Secondly, the tolerances, which are practically achievable by the modern machining tools and the careful assembly, were estimated. The tilt angle and the modulation depth were calculated using these practical tolerances. The estimated tolerances are summarized in Table 3.B on page 54.

The porch swing structure is the most sensitive to the difference in the arm lengths Δl and the angle ϕ between the ends of the arms. The greatest allowed arm length differences varied from 0.02 mm to 0.06 mm between the cases. However, the maximum error $\Delta l \leq 0.01$ mm is achievable by careful machining. We used the error value 0.02 mm in the calculations not to underestimate the error. Additionally, the tolerance can be further relaxed by extending the arms. So, these tolerances do not seem to limit the usefulness of the bearing.

The second major source of tilting is the non-parallelism of the arm ends, which causes angle ϕ between the principal axes of inertia of the flexures. The maximum allowed angle was from 230 μrad to 680 μrad according to Eq. (3.9). This corresponds 0.01 mm . . . 0.03 mm difference in the lengths of the opposite sides of the arm ends. Therefore, the usual machining tolerance of 0.02 mm should be sufficient.

The smallest allowed length difference of the flexures Δh was 0.6 mm in the worst case, where the arm length was $l = 50$ mm. In other cases, the difference was over that. With careful assembly, one can quite easily attain a tolerance of about $\Delta h \leq 0.1$ mm, which decreases the modulation depth to about 0.999. The measurement of so small decrease is challenging. It is interesting to observe that the tilting caused by Δh is clearly nonlinear and asymmetric as illustrated in Fig. 3.9 on page 55. For example, if the porch swing has dimensions $l/h = 50/100$ and the flexure lengths differ from each other by $\Delta h = 1.5$ mm, the resulting modulation, as a function of the mirror position z_0, seems to be about to the polynomial of the fourth order shifted to the left from the zero mirror position. These nonlinearities and asymmetries were considered in the estimations of the tolerances.

The neutral axes of the flexures become non-parallel if, for example, the other flexure end is mounted away from its correct position in the x direction. A positioning accuracy of 0.2 mm should be possible by at least some care in the assembly. The angles between the neutral axes are then $\theta \leq 4$ mrad. According to Eq. (3.8), the most rigid required tolerance is

Table 3.B Minimum and reasonable practical tolerances estimated using four example cases at the mirror position $z_0 = 3$ mm. The tilt angle α and the corresponding modulation depth m at 3000 cm^{-1} and diameter $D = 25$ mm are also estimated. The length differences of the arms and the flexures are Δl and Δh, respectively. The angle between the neutral axes of the flexures is θ and the angle between the principal inertia axes is ϕ. The driving force is at height $a = h + a_{\text{extra}}$.

	l	[mm]	50	100	150	50
	h	[mm]	50	50	50	100
	w	[mm]	50	50	50	50
Min	Δl	[mm]	0.02	0.04	0.06	0.04
Practical	Δl	[mm]	0.02	0.02	0.02	0.02
	α	[μrad]	24	12	8	12
	m		0.96	0.99	1.00	0.99
Min	Δh	[mm]	0.6	1.2	1.9	1.5
Practical	Δh	[mm]	0.1	0.1	0.1	0.1
	α	[μrad]	-4	-2	-1	-1
	m		1.00	1.00	1.00	1.00
Min	θ	[mrad]	8	15	23	15
Practical	θ	[mrad]	4	4	4	2
	α	[μrad]	7	4	2	2
	m		0.99	1.00	1.00	1.00
Min	ϕ	[μrad]	230	450	680	230
Practical	ϕ	[μrad]	400	400	400	400
	α	[μrad]	24	12	8	24
	m		0.85	0.96	0.98	0.85
Min	a_{extra}	[mm]	4	90	235	65
Practical	a_{extra}	[mm]	6.0	6.0	6.0	6.0
	α	[μrad]	-15	-4	-2	-7
	m		0.94	1.00	1.00	0.99

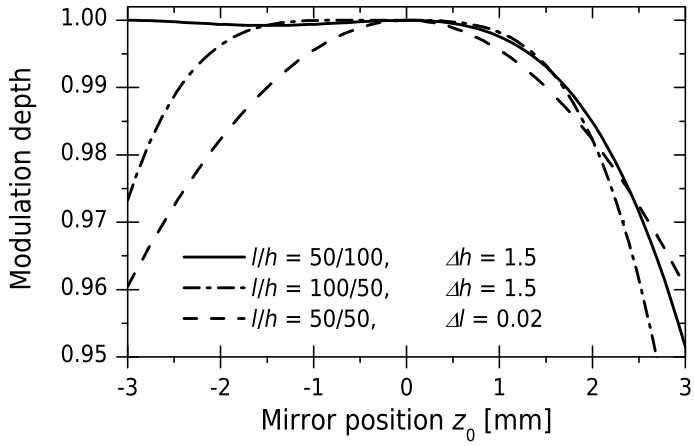

Figure 3.9 Examples of the modulation depth curves with some dimension errors. The length difference Δh of the flexure elements typically produces asymmetric modulation decrease while the arm length difference causes symmetric error. The graph is reproduced from [68].

about 8 mrad with the smallest porch swing or $l = h = 50$ mm, so even the worst example satisfies this. The greatest decline, in the modulation depth, was about 0.015 with the smallest porch swing. However, a more common arm length in FTIR is about 150 mm, which leads to a decline of about 0.002 in the modulation depth.

Exerting the driving force to the movable arm is sometimes more practical than to design an extra overhang or additional mechanisms for pushing the arm at the ideal position. Thus, we used the force position, $a = h + a_{\text{extra}}$, and Eq. (3.10) to estimate the tolerances. We selected, as a practical limit, $a_{\text{extra}} = 6.0$ mm, which decreased the modulation depth to 0.94 in the worst case, which was the smallest porch swing with $l = h = 50$ mm. In the other cases, the modulation was over 0.98. With a typical arm length of $l = 150$ mm, the drop in the modulation depth was about 0.001.

Hatheway [84] estimates that his example porch swing would produce the tilt angles over 300 μrad in the worst case. This is much greater tilting than our estimations indicate. The difference results mainly from significantly larger values for tolerances and a longer 5 mm stroke used in Hatheway's example. Incidentally, over 80 % of these angle values came from the arm length error and the non-parallelism of the arm ends.

In the REFIR project, the balloon borne spectrometer had the interferometer with a double pivot bearing [85]. This suspension corresponds to Fig. 2.25(c) on page 40. The designers estimated that a manufacturing tolerance of 0.1 mm is sufficient. The tilting values were ± 400 μrad in the yaw and ± 200 μrad in the pitch rotations during the travel of ± 6 mm. However, the device was designed to the far infrared region where a greater tilt is acceptable because of longer wavelengths.

Clearly, the most essential properties of the porch swing are the length difference of the arms and the non-parallelism of the arm ends. These have already been noted by many authors, for example by Walker and Rex [18] and Strait [75] who both have designed an adjustment mechanism to minimize these errors. However, the previous calculations about tolerances show that any adjustment mechanisms are not necessarily required at all. This simplifies the construction and may reduce the manufacturing costs.

3.4 Bending of the spring elements

3.4.1 Force constant

The driving force **F** produces the displacement z_0 of the porch swing structure. Because the porch swing movement is based on springs, it is reasonable to assume that the driving force is nearly proportional to the displacement, or $F = \kappa z_0$, when the displacement is small. Thus the constant κ can be regarded as the force constant (or the spring rate or the spring constant) of the porch swing mechanism. To be exact, the force-deflection relationship is slightly non-linear mainly because of anticlastic curving of the flexures. However, with displacements used in this work, the effect of non-linearity is less than one percent of the force constant [86].

The force constant can be used to estimate the natural frequencies of the structure. Natural frequencies are required when designing the vibration isolation for the device. The vibration damping system must have sufficient attenuation at lowest natural frequency. Additionally, the force constant is needed when designing the driving motor capable of producing the sufficient force to deflect the movable arm to desired maximum displacement. The force constant could be quite easily estimated numerically. However, the analytical model would be more convenient in early design stage when the structure is sketched and major dimensions are optimised.

When flexure elements are flat springs, their bending can be modeled using the simple beam bending theory, which results in the polynomial spring shape [87–91]. The total deflection of the spring end is equal to z_0. It can be expressed as function of the driving force, which gives the force constant. In the following, the expressions for the force constant of the flat spring without and with stiffener clamps are presented. The force constant was also studied experimentally. The results differed from the simple bending theory when the stiffener clamps length was nearly the spring length or the bending springs were short.

3.4.2 Flat springs

One flat spring, which length is h, width is b and thickness is t, is drawn to Fig. 3.10(a). Both ends of the spring are mounted on the arms of the porch swing. The spring has uniform rectangular cross section and

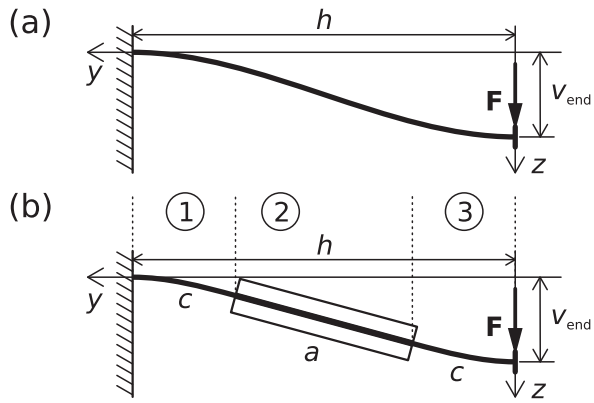

Figure 3.10 Bending of the flat spring with (a) and without (b) stiffener clamps.

it is initially straight. Tension and compression forces are assumed to be negligible. The only loading force is the driving force **F**. The spring material is assumed to be homogenous and isotropic, or its elastic modulus E is equal in tension and compression. Deflections are so small that the limits of elasticity or proportionality are not exceeded, so the spring follows Hooke's law. Additionally, Bernoulli's assumption is assumed to be valid or each cross sectional plane is assumed to remain planar. The spring is long and slim, or $h >> b$ and $h >> t$.

Simple beam bending model of the flat spring without stiffening clamps is presented in Fig. 3.10(a). The total deflection of the beam end is [89]

$$z_0 = v_{\text{end}} = \frac{Fh^3}{12EI}, \tag{3.12}$$

where I is the second moment of area of the spring in reference to x. According to Eq. (C.3), it is

$$I = \frac{bt^3}{12}. \tag{3.13}$$

The product EI is called the flexural rigidity of the spring. Above equations are derived in Appendix C.1. The force constant of one flexure element is

$$\kappa = \frac{F}{v_{\text{end}}} = \frac{Ebt^3}{h^3}. \tag{3.14}$$

Therefore, the force constant is proportional to the cube of the ratio t/h. In other words, the force constant increases very rapidly if the spring thickness t is increased or the spring length h is decreased, which is reasonable.

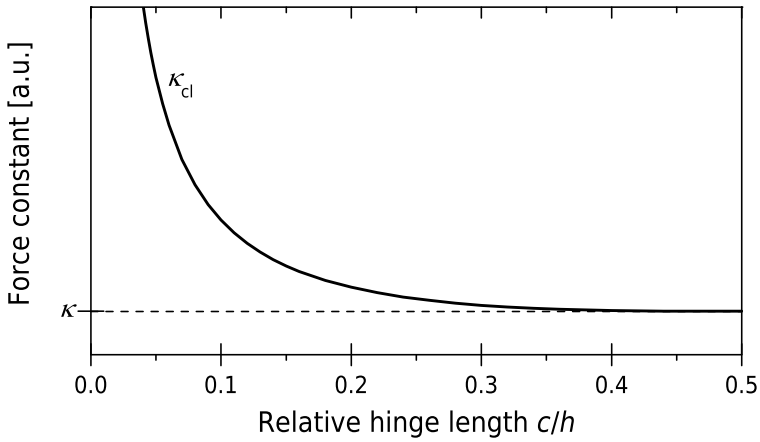

Figure 3.11 The force constant κ_{cl} of the flexure element with the stiffener clamps according to Eq. (3.16). When the hinge length is $c = \frac{1}{2}h$, the flexure element corresponds the flat spring without the stiffening clamps and the force constant is equal to κ from Eq. (3.14).

3.4.3 Springs with stiffeners

When the stiffening clamps are mounted in the middle of the spring, the situation is as in Fig. 3.10(b). The flexural rigidity EI of the stiffener part is very much larger than flexural rigidity of the spring parts. Thus, the flexure element, or the spring with stiffeners, is now bent only in its ends, or in the parts 1 and 3. The total deflection of the flexure element end is

$$v_{\mathrm{end}} = \frac{Fc}{6EI}\left(4c^2 - 6ch + 3h^2\right), \tag{3.15}$$

where c is the length of one bending part, either the part 1 or 3 [80]. The force constant of the flexure element is then

$$\kappa_{\mathrm{cl}} = \frac{6EI}{c\,(4c^2 - 6ch + 3h^2)}. \tag{3.16}$$

If the clamp width a is zero, then $c = h/2$ and the above equation reduces to Eq. (3.14) or the force constant of the flat spring without the clamps. If the length of the hinge c is decreasing the spring rate increases very rapidly, which is illustrated in Fig. 3.11.

3.4.4 Experiments on force constant

The force constant of the porch swing structure was measured without and with the stiffener clamps mounted on the flat springs. The force constant was determined from the total deflection of the porch swing resulted by the known force. The experiments were repeated with various combinations of the hinge lengths c and the spring lengths h to study the dependencies of the force constant to these parameters.

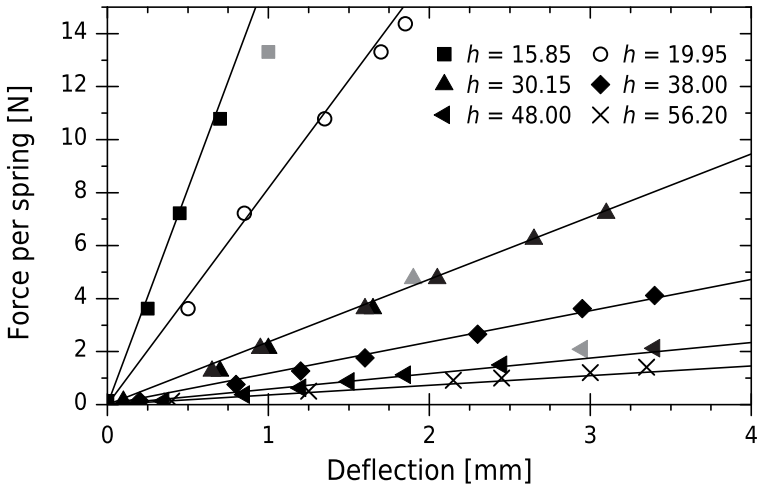

Figure 3.12 The force–deflection curve of the spring without stiffening clamps. Six different spring lengths h in millimeters were used. Lines were calculated using Eq. (3.14), $EI = (5300 \pm 400)$ Nmm^2 and $a = 0$. Grayed points were excluded from analysis.

The porch swing was assembled with two similar flat steel springs with the cross section of (12.7×0.31) mm^2. The porch swing was orientated so that the gravity was in the x direction according to Fig. 3.2 or in parallel to the springs. The movable arm was displaced by different weights coupled to the arm by a thin wire that ran over a pulley. The friction in the pulley and the strain of the wire were estimated negligibly small. Thus the mass of weights produced the driving force. The displacement of the arm was measured with a slide caliper.

At first, the force–deflection curves without the stiffening clamps were measured to verify and to calibrate the value for the flexural rigidity EI. Data is plotted in Fig. 3.12. The force seems to be linearly proportional to the deflection as assumed earlier. Thus, straight lines were fitted to data using the least squares method with interception fixed to zero. The values of the flexural rigidity EI were then calculated using Eq. (3.14) with $a = 0$ and are plotted in Fig. 3.13. The flexural rigidity should be independent of the spring length but there seems to be some trend. However, we calculated the average of the flexural rigidity as $EI = (5300 \pm 400)$ Nmm^2, where the error corresponds to 95 % confidence limit if the error is assumed normally distributed. Therefore, the modulus of elasticity is about $E = (170 \pm 20)$ GPa, which is acceptably close to the value of 200 GPa in literature [28] because it is reasonable to assume that the flexural rigidity value has some error too. Thus, we will use it later as the calibrated value. The lines in Fig. 3.12 are not the fitted lines but calculated from Eq. (3.14) using the calibrated EI.

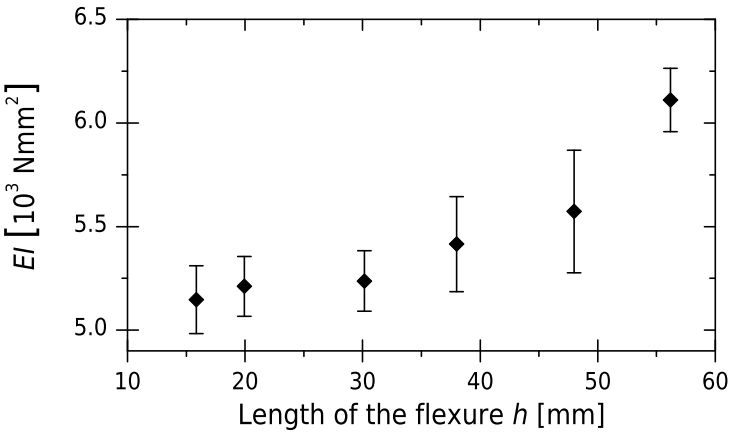

Figure 3.13 The flexural rigidity EI of the flat spring with thickness of 0.31 mm and without stiffening clamps ($a = 0$).

After that, force–deflection curves of the springs with 30 mm and 44 mm long stiffener clamps were determined. Again, the force was clearly proportional to the deflection, so lines were fitted to these curves as earlier. Slopes of these lines represent force constants of flexure elements. Constant values were also calculated using Eq. (3.16). Measured and calculated values were plotted to Fig. 3.14.

When the hinge length c is longer than about 6 mm, measurement results agree with Eq. (3.16) very well. With shorter hinges, the model seems to overestimate the force constant. Experiments were repeated using also springs of thicknesses 0.20 mm and 0.50 mm but results were similar. The short hinge is very wide compared to its length although the long and slim spring was supposed in the beginning. Wide beams are usually more rigid than formulas presented in the previous section indicate. In the first approximation, this can considered by replacing the elastic modulus E with $E(1 - p^2)$, which lowers the elastic modulus value about ten percent because Poisson's ratio of the steel is about $p = 0.28$ [88, p. 76–78]. Even then, results of the hinges shorter than 3 mm do not still agree. This might be because of the force constant depends also on the spring length and width [86].

Problems of the theory with short hinges resulted probably from that the initial assumptions of the simple beam bending theory are no longer valid [87, 91]. For example, shear strains were neglected. However, these can be added to the model [87, p. 170–175] but the shearing increases the deflection only about 0.1 percents with 1 mm long spring, so it does not explain the difference.The theory fits best on the middle of the beam because strains near beam fixing points may be very complicated. The very short beam is probably missing the middle region where strains are simple. Ad-

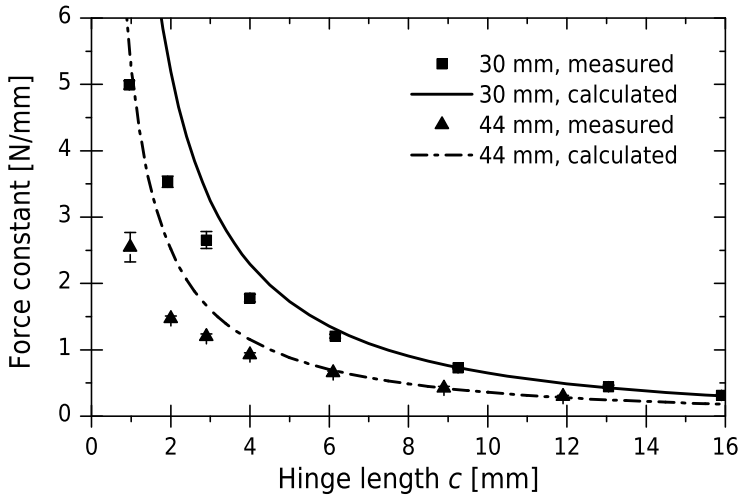

Figure 3.14 Measured and calculated force constants of the spring of thickness 0.31 mm and stiffening clamps mounted as in Fig. 3.10(b). Clamp lengths were 30 mm and 44 mm.

ditionally, the small imperfections of fixing points may substantially affect the strains.

The bending may also be nonlinear so the linear theory fails although, according to the experiments, the total deflections were proportional to the force. The first nonlinear approach might be the large deflection model, where the differential equation Eq. (C.1) for the bending is not linearised. This model can be solved for example by using elliptic integrals or numerically [92–94]. Other models for wide beams can be found, for example, in Roark's Formulas [91, Ch. 8.11]. Some theory of the bending of plates or the numerical modeling might also be used. However, these are out of the scope of this work.

Furthermore, the possibility of systematic measurement error can not be excluded. Several measurements were shortly repeated to uncover possible errors in experiments but results seemed very repeatable. However, the measurement system might still produce errors. For example, the gravity orientated parallel to springs might had affect to the force constant. Additionally, the pulley friction or the wire strain may have had some effect although they were estimated to negligibly small. Determining the force constant should be possible by using also the natural frequency of the bearing suspension. That could also be measured directly rather than the force constant. However, the force constant is required when modeling vibration modes of the structure thus knowing it is very useful. As a whole, the modeling of the force constant leaves, unfortunately, not fully complete.

Chapter 4

Experiments on Michelson interferometers with porch swing

4.1 Introduction

The main part of this work was designing, building and studying experimentally low resolution FTIR interferometers based on the porch swing bearing. Firstly, the porch swing concept was tested to find if it will work at all. Quite a simple interferometer, called Swing 0, was built on the optical bench and tested using Helium-Neon laser. The tilting during the driving was sufficiently low and the device was remarkably stable during 20 °C temperature change. Because of the promising results, the next version, Swing I, was designed. It was suitable for the infrared beam although experiments were made with a laser. Swing I was very stable in heating cycles but was quite complicated to assemble and also too big. The following version, Swing II, was not stable in temperature changes but it could be used to study the tilting and parasitic motions. The bearing of Swing II was adjusted to nearly perfect and thus removed the mirror tilting during the driving almost completely. Finally, Swing III was assembled also with infrared optics. It had acceptable driving stability without any adjustments but the temperature stability was not as good as desired. However, it was able to measure infrared spectra with success.

We measured the modulation depth of the interferometers regularly during the development work because it is the essential property of the FTIR interferometer. The modulation depth of the Michelson interferometer built using plane mirrors depends mainly on the mirror tilting. Hence, the modulation depth is a measure of the alignment stability of the interferometer. A few methods were used to measure the tilt angle. The simplest methods were based on the analysis of the fringe pattern created using the collimated Helium-Neon laser beam. A more sophisticated method was measuring the modulation depth of the laser beam coming out from the interferometer and then estimate the tilt angle that could produce the observed modulation depth. With Swing III, the modulation depth was also determined from spectra using 100 percent transmittance lines.

In this chapter, the design process of the interferometers is discussed mainly in the chronological order because the next version of the interferometer always depended on observations from previous versions. These

observations and other designing details are discussed in detail. However, experimental methods for the determining the mirror tilting are firstly discussed.

4.2 Measuring the mirror tilting

4.2.1 Fringe pattern methods

The modulation depth of the interferometer can be estimated using the angle between output beams. This angle is twice the tilt angle of the mirror and it can be determined by using a monochromatic light beam, which is directed through the interferometer as illustrated in Fig. 4.1. The output beam is projected to the screen. If the wave front of the beam has phase errors, or the optical path difference varies over the beam cross section, fringes are appearing on the screen. The fringe pattern methods are based on the fact that the optical path difference of one wavelength on the wave front produces one complete fringe to the screen. By analysing the fringe pattern, the tilt angle can be estimated. To be exact, the angle between the output beams 2α is determined rather than the tilt angle of any single optical component. The fringe patterns can be recorded periodically by using for example a web cam [50], which was often used also in this work.

According to Eq. (2.10) on page 9, the mirror tilt angle is

$$\alpha = \frac{k\lambda}{2D}, \tag{4.1}$$

where k is number of fringes across the beam diameter D and λ is the wavelength. Thus, the tilt angle can be determined by simply counting the fringes on the fringe pattern as illustrated in Fig. 4.2. The maximum

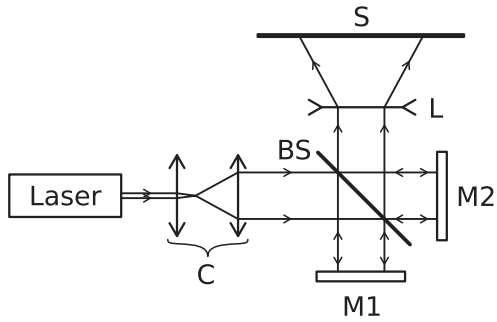

Figure 4.1 Measurement setup for determining the number of fringes k across the beam or the distance between the adjacent fringes d. The laser beam goes through the collimator C to the interferometer input as a plane wave. The diverging lens L can be used before the screen S to improve accuracy of the fringe distance d. Figure is reproduced from [68].

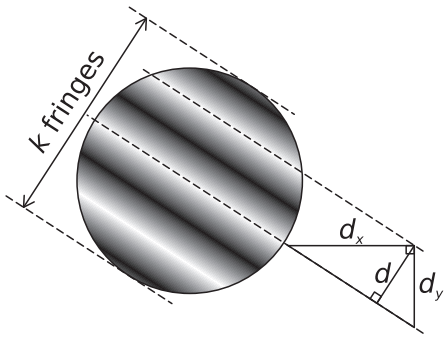

Figure 4.2 Determining the tilt angle by measuring the distance d between adjacent fringes or counting the number of fringes k across the beam. Figure is reproduced from [68].

relative measurement error based on the total differential of Eq. (4.1) is

$$\left|\frac{\Delta\alpha}{\alpha}\right| \leq \left|\frac{\Delta k}{k}\right| + \left|\frac{\Delta D}{D}\right| + \left|\frac{\Delta\lambda}{\lambda}\right|. \tag{4.2}$$

Hence, the wavelength error can be usually neglected and the beam diameter is typically fixed, the only practical way to reduce measurement error is to increase the fringe number k as much as possible. The tilt angle could also be determined using the distance between the adjacent fringes d. Because the beam diameter is $D = kd$, the tilt angle is

$$\alpha = \frac{\lambda}{2d}. \tag{4.3}$$

The fringe distance d is also fairly simple to measure using a ruler or a millimeter scale attached to the screen as presented in Fig. 4.2. The one strength of this method is that it is possible to obtain direction of fringes and thus to deduce the direction of tilting. This may be a great help when trying to find the origin of the tilting. Hence, it is practical to measure the distance between adjacent fringes in orthogonal directions, or d_x and d_y, as in Fig. 4.2. The distance d is then

$$d = \frac{d_x d_y}{\sqrt{d_x^2 + d_y^2}}. \tag{4.4}$$

Using the total differential, the relative error of the fringe distance d is

$$\left|\frac{\Delta d}{d}\right| \leq \left|\frac{\Delta d_x}{d_x} - \frac{(\Delta d_x)\, d_x}{d_x^2 + d_y^2}\right| + \left|\frac{\Delta d_y}{d_y} - \frac{(\Delta d_y)\, d_y}{d_x^2 + d_y^2}\right|, \tag{4.5}$$

where Δd_x and Δd_y are measurement errors of orthogonal fringe distances. The obvious way to decline the measurement error is to measure distances d_x and d_y over several fringes. Furthermore, the measurement error can be reduced by enlarging the fringe pattern with a diverging lens L.

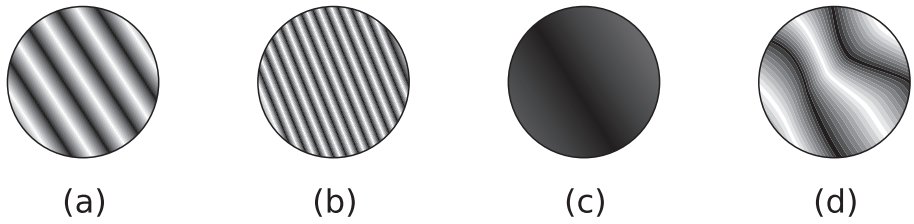

Figure 4.3 Schematic examples of different fringe patterns. The optimal fringe count is near the pattern (a). Difficulties are typically encountered if fringes are very dense as in (b), very sparse as in (c) or uneven as in (d).

Although, it is quite simple and straightforward to analyse the fringe pattern, this method has some uncertainties. Firstly, if fringes are too dense or sparse, their adjacent distances become harder to determine, as illustrated in Fig. 4.3(b) and (c). Usually, the best results are obtained if the number of fringes is about four to five, as in Fig. 4.3(a). Curved fringes, usually caused by the unflatnesses of optical surfaces, make impossible to determine the adjacent fringe distance. The fringe pattern should also remain sufficiently stable, thus the external vibrations or the air convection in the interferometer can cause problems.

Fringe pattern methods are generally simple and easy to use. Additionally, the experiment can be set up quickly. Results are obtained soon and straightforwardly. Furthermore, it is possible to distinct the vertical and horizontal tilting of pitch and yaw rotations, which is very helpful when eliminating effects that produced the tilting. The method is also independent of intensity variations of the laser beam, which is usually non-uniform. However, small changes in the fringe pattern are very hard to observe. Fringe pattern methods require often also manual work, which is laborious. Methods based on the modulation depth provide better accuracy and automated experiments.

4.2.2 Modulation depth methods

Visible laser beam as a light source

When changes of the tilt angle are very small, the resolution of the fringe pattern methods is not sufficient. Then it is more useful to do the opposite and measure the modulation depth first and then estimate the tilt angle from it using

$$m = \frac{2J_1\left(2\pi D\alpha\nu\right)}{2\pi D\alpha\nu}. \tag{2.8}$$

The measurement of the modulation depth can be done with the very similar setup as earlier but the output beam from the interferometer is focused to a photodiode instead of projecting it to the screen as depicted in Fig. 4.4. The modulation depth of the monochromatic light is equal to its visibility

$$m = \frac{V_{\max} - V_{\min}}{V_{\max} + V_{\min}}, \tag{2.12}$$

where $V_{\max}$ and $V_{\min}$ are maximum and minimum values of the sinusoid signal, as in Fig. 2.4 on page 10 resulted when the optical path difference is varied by moving the other interferometer mirror. The modulation reaches its maximum value $m = 1$, when the wave front is perfectly planar and there is no tilting, because then the light is completely faded, when the destructive interference happens, and $V_{\min} = 0$.

To obtain a sinusoidal signal from a photodiode, the optical path difference must be varied. The simplest method used in this thesis, was to let the movable arm of the porch swing to vibrate freely. Then the arm was continuously in motion exited by some external vibrations always present. The drawback of this method was that the arm movement was pretty much uncontrolled and the unflat frequency response of the photodiode circuit may have affected the results. In later experiments, these errors were reduced

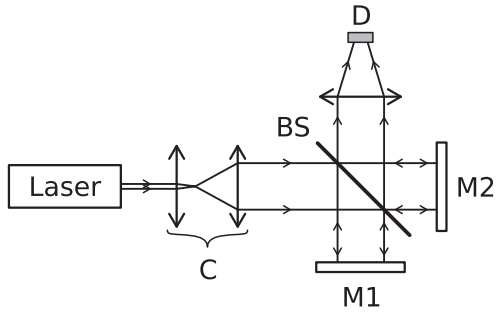

Figure 4.4 Measurement setup for determining the tilt angle of mirrors using the modulation depth of the laser beam. The setup is similar to Fig. 4.1 but the output beam from interferometer is focused to the detector D. Figure is reproduced from [68].

Table 4.A Summary of statistics of the modulation depth data series calculated using four methods for estimating maximum and minimum values of data block of the signal proportional to the intensity of the interferometer output beam.

Method description	MinMax-method number	Modulation depth m	
		Goog alignment	Bad alignment
The minimum and the maximum of the short data block	1	0.929 ± 0.005	0.30 ± 0.19
The mean of local minima and the mean of local maxima of the data block	2	0.91 ± 0.01	0.26 ± 0.19
The lowest maximum and its nearest minimum; Determined by polynomial fit	3	0.913 ± 0.009	0.25 ± 0.19
The lowest maximum and its nearest minimum; Determined by actual data points	4	0.921 ± 0.009	0.27 ± 0.19

by using a voice-coil to produce the driving force. However, the voice-coil system did not produce very stable motion either. The best method was to stop the arm by a rigid rod and then alter the arm position by pushing the rod mount carefully by hand or heating it by a resistor. The thermal expansion drove the mirror over few wavelengths. This generated few sinusoid cycles with very low frequency.

Four methods were used to determine maximum and minimum values of the voltage signal. Methods are described in Table 4.A. Methods were compared to each other by applying them to the same measurement data. Thus, four different series of modulation depth values were obtained. Data were collected using Swing I (see Chapter 4.4 from page 83) with the freely vibrating arm. One measurement was done with a good alignment, or $m > 0.9$, and the another with a poor alignment, or $m < 0.4$. Table 4.A summarises the statistics of these modulation series having 4500 points each. The 100 seconds long sample of the series are plotted to Fig. 4.5.

The first observation is that differences between the methods are fairly small and systematic. Minmax-method 1 results the greatest values, which is reasonable because the noise increases the maximum value and decreases the minimum value, so the modulation is slightly overestimated. Results using methods from 2 to 4 are quite near each other. Modulation depth values of Minmax-method 4 are a bit larger because of the same reason with Minmax-method 1. The variation of modulation depth values in the poor alignment case was probably produced by the vibration of the porch swing structure, which tilted the mirror. However, all the methods are following each other very well. As a summary, any Minmax-method may be

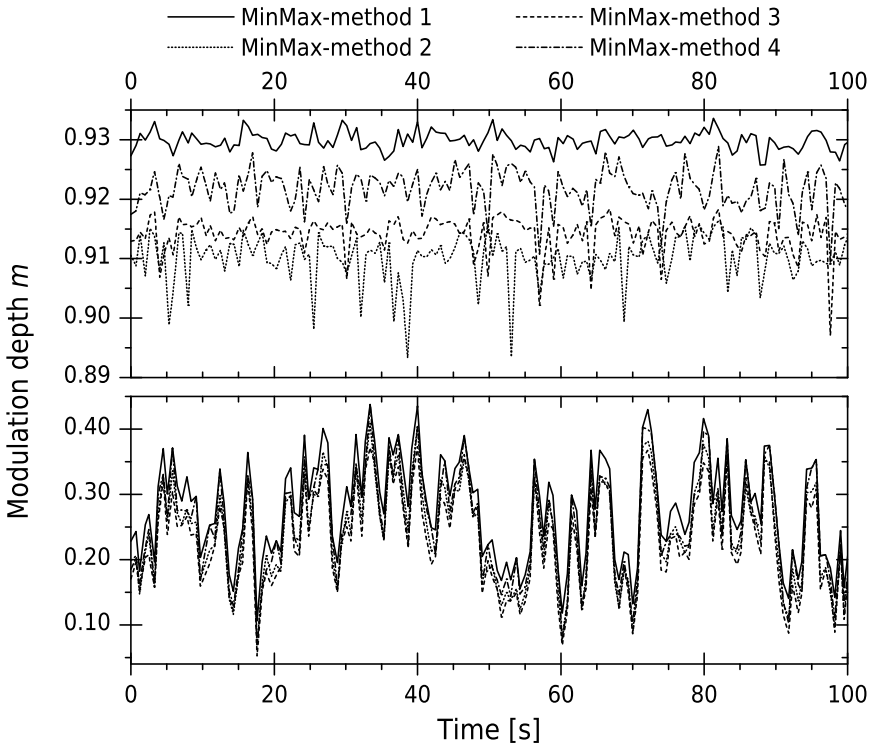

Figure 4.5 Comparison of four methods used for determining minimum and maximum values of the photodiode signal. Methods are summarised in Table 4.A. The upper graph shows data with a good interferometer alignment and the lower with a poor alignment.

used to estimate the modulation depth, because modulation depth changes are more interesting than the exact value of it. Every method is suitable for that.

According to Eq. (2.12), the absolute error of the modulation depth, caused by noise in the voltage signal, is

$$|\Delta m| \leq \frac{2\,|\Delta V|}{V_{\max} + V_{\min}}, \tag{4.6}$$

where it has been assumed that $V_{\max} > V_{\min} \geq 0$ and $\Delta V \equiv |\Delta V_{\max}| \approx |\Delta V_{\min}|$. That is, the voltage error is assumed to be additional. Other noise sources additional to noise and Minmax-method, are the diffused light from the surroundings, which prevents the minimum voltage to reach zero, and the unflatnesses of the optics and other phenomena that cause phase errors to the wavefront. Furthermore, the frequency of the sinusoid voltage signal may change in the relatively broad band, thus the frequency response of the electronics may affect the results.

The main advantage of estimating the tilt angle by using the modulation depth method is sensitivity to very small variations in the modulation

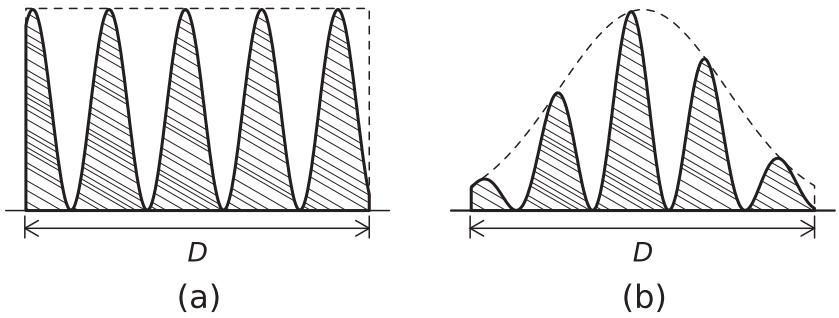

Figure 4.6 Intensity across the fringe pattern with the uniformly distributed monochromatic light beam (a) and Gaussian distributed beam (b), which decreases the weight of the fringes in edges.

depth. For example, if the modulation depth of Helium-Neon laser beam with diameter 2 cm decreases from 0.96 to 0.95, the tilt angle changes about 1 μrad according to Eq. (2.8), which is hard to determine by using the fringe pattern. Moreover, a voltage signal from a photodiode can be easily acquired by a computer and then data analysis and storage can be automated with only little effort. However, the modulation depth method loses the information of the fringe orientation, so nothing can be deducted about the direction of the tilting. Additionally, it is not possible to distinct if the modulation was decreased by the tilting or the unflatness of the optics. Lastly, the modulation depth depends on the intensity distribution of the collimated and monochromatic light beam, which should be usually considered, as shown in the following.

Effect of the non-uniform intensity of the laser

The non-uniform intensity distribution of the laser beam may affect substantially the relation between the tilt angle and the modulation depth, which has to be considered when estimating the tilt from measured modulation values. The intensity distribution of the expanded laser beam from a gas laser is usually Gaussian [95]. The fringes on the edges of the Gaussian distributed beam have much less energy than the corresponding fringes of the uniform beam profile as illustrated in Fig. 4.6. The fringes on the edges of Gaussian beam have less contribution to the modulation depth, which makes the modulation depth less sensitive to the tilt angle compared to the uniform beam. The effect of the Gaussian beam to the modulation depth is studied in detail and modeled by Välikylä and Kauppinen [96] (see also Chapter 5). In the following, we summarise the results and the experimental verification of this model. The derivation of the model is summarised in Appendix A.2.

If the light beam entering to the interferometer has the radius R and Gaussian intensity distribution with the standard deviation σ, the modulation depth of the interferometer output beam, with the tilt angle α, is

$$m_G = G_0 \int_{-2\alpha R}^{2\alpha R} \exp\left[-\frac{y^2}{8(\alpha\sigma)^2}\right] \left[\int_{-q(y)}^{q(y)} \exp\left(-\frac{u^2}{2\sigma^2}\right) \mathrm{d}u\right] \exp\left(\mathrm{i}2\pi\nu y\right) \mathrm{d}y, \tag{4.7}$$

where $q(y) = \sqrt{R^2 - [y/(2\alpha)]^2}$. The position u, the extra optical path difference y and the coefficient G_0 are defined in Eq. (A.6) and Fig. A.2. This equation can approximated with very good accuracy using the convolution of the aperture weighting function $B(y)$ and Gaussian function as

$$m_{G*} = M_0 \left(\mathcal{F}\left\{B(y)\right\} * \mathcal{F}\left\{\exp\left[-\frac{y^2}{8(\alpha\sigma)^2}\right]\right\}\right), \tag{4.8}$$

where the constant M_0 is the reciprocal of the convolution at zero and $B(y)$ is defined in Eq. (A.2). According to Eq. (A.11), the convolution m_{G*} can be proved to be the function of the number of the fringes k across the beam and the standard deviation of the distribution σ, or $m_{G*} = m_{G*}(k, \sigma)$. The accuracy of the model $m_{G*}(k, \sigma)$ can be increased by scaling the deviation σ by the factor

$$\sigma_c = \sigma \left[1.23 - \frac{0.23}{1 + \left(\frac{4.3\sigma}{2R}\right)^{2.8}}\right]$$

and defining the convolution model as

$$m_{Gc}(k, \sigma) = m_{G*}(k, \sigma_c). \tag{4.9}$$

The convolution model m_{Gc} was verified experimentally [96] by using two cases. In the first case, Gaussian distribution of the beam was clearly affected the modulation depth as seen in Fig. 4.7(a) on page 71. The ratio of the beam standard deviation and the beam diameter was 0.19, which is clearly below 1. The beam distribution has clearly affected the results, as illustrated in the graph. In the second case, the width of Gaussian distribution was wide related to the beam size and the corresponding ratio was 0.99, so the beam could be approximated as uniform as presented in Fig. 4.7(b).

The convolution model Eq. (4.9) can be used to estimate the tilt angle from the measured modulation depth value. Firstly, the distribution of the laser beam should be measured and its standard deviation determined. The deviation of the laser beam used in this work was about 4.1 mm. Then the tilt angle can be estimated, for example, by calculating the values of the function $m_{Gc}(k, \sigma)$ and interpolating the tilt angles. Finally, the modulation depth in the infrared region can be estimated by the tilt angle values using Eq. (2.8). Actually, it is then assumed that the infrared beam is uniform but its distribution could also considered if required. This conversion is possible to present graphically as in Fig. 4.8.

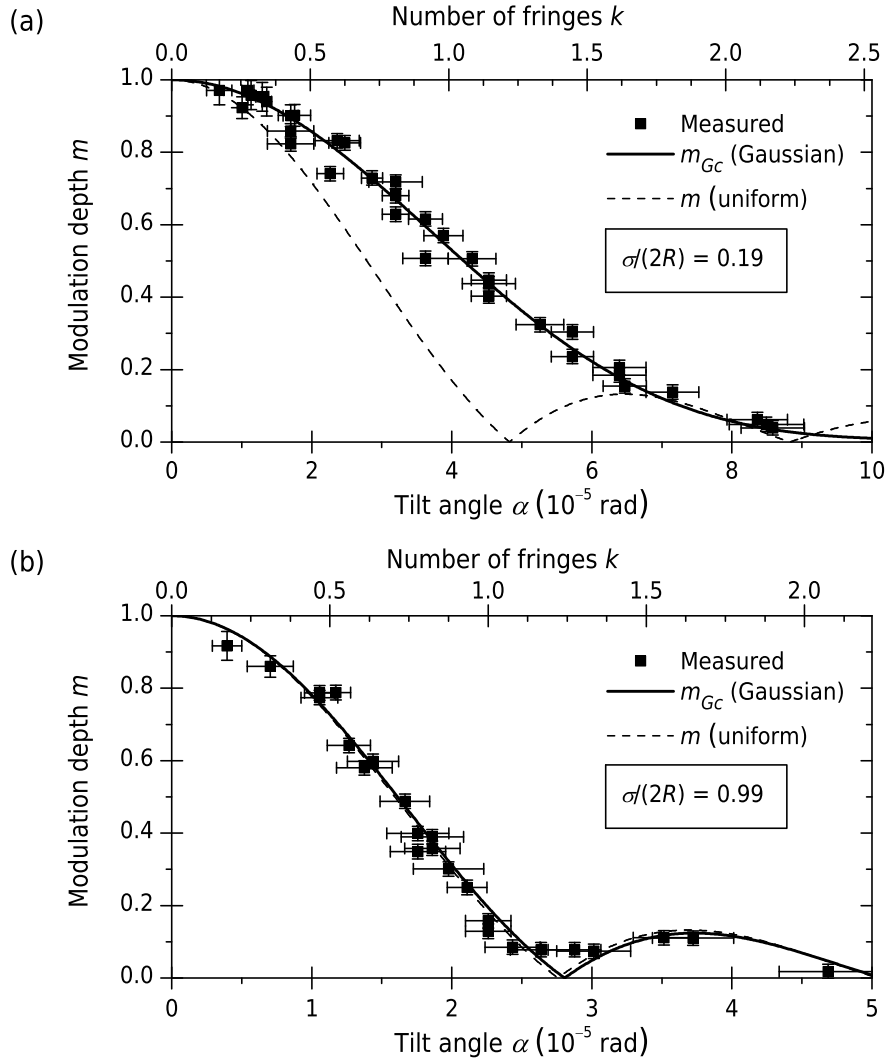

Figure 4.7 Comparison of the modulation depth from experiments and the convolution model m_{Gc} Eq. (4.9) for a Gaussian beam and Eq. (2.8) for a uniform beam. In the graph (a), the standard deviation of the beam intensity was 1.48 mm and the beam diameter was 8.0 mm (ratio $1.48/8 = 0.19$). In the graph (b), the beam deviation was 13.8 mm and the diameter was 14.0 mm (ratio $13.8/14 = 0.99$). Figure is reproduced from [96].

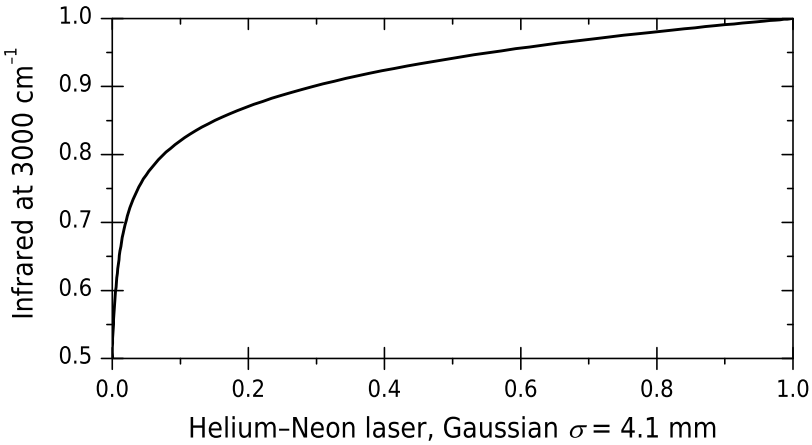

Figure 4.8 Conversion of the modulation depth measured using Gaussian distributed Helium-Neon laser beam with $\sigma = 4.1$ mm to the modulation depth at 3000 cm^{-1}. The beam diameter is 25 mm.

Infrared beam as a light source

The modulation depth can be measured also using infrared radiation. This is done by recording two successive background spectra. The ratio of backgrounds, or the background transmittance, is related to the modulation depth although it is not the absolute value of it, but rather the modulation depth related to the first background. This transmittance is often given in percent and called a 100 percent line hence its baseline is a horizontal line at height 1 (or 100 %) if the spectrometer was stable during the data recording. In practice, the alignment and the source emission will not keep exactly constant and the 100 percent line depends on their changes.

The misalignment typically causes parabolic 100 percent line because the modulation depth is roughly proportional to the squared wavenumber, as in Eq. (2.8) on page 9. This is illustrated in Fig. 4.9, where two 100 percent lines are recorded during warm up of the interferometer Swing III when the interferometer temperature changed and caused alignment alterations. Parabolae were fitted to the data in the least squares sense excluding the data in the strongest water and carbon dioxide bands and in the noisy part below 700 cm^{-1}. The measured transmittance seems to have parabolic shape, which is typically a sign of the tilting.

Another typical origin of modulation changes are temperature variations of the infrared source. Small temperature changes produce almost linear baseline to the modulation curve, as illustrated in Fig. 4.10 on page 74, where it is assumed that the measured spectrum is proportional to the energy density of the ideal black body radiation $u(\nu, T)$ of Eq. (2.15) on page 24. Thus, the ratio of energy densities, or $u_2(\nu, T_2)/u_1(\nu, T_1)$, corresponds the 100 percent line. Temperature values were $T_2 = T_1 \pm 20$ K and

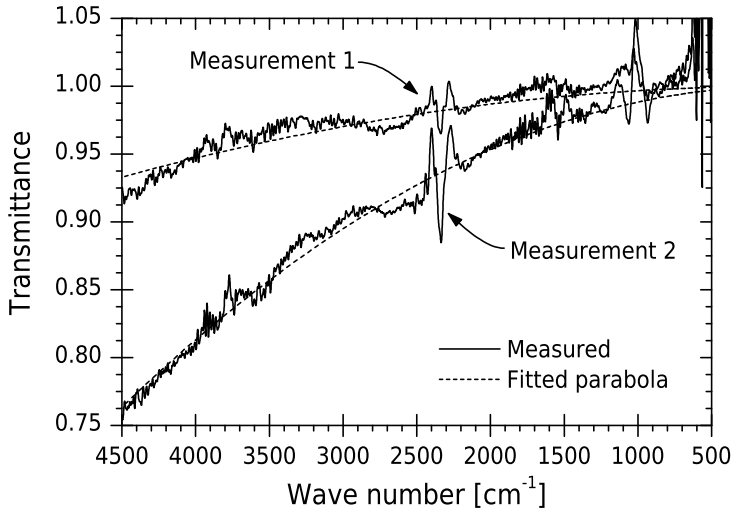

Figure 4.9 Examples of 100 percent transmittance used to study the modulation depth of the interferometer. Fitted parabolae illustrate the shape of the baseline. Data was recorded during the warm up of Swing III (see Chapter 4.6).

$T_1 = 1173$ K (900 °C). The modulation depth with tilt angle $\alpha = 10$ μrad is also plotted to the same figure for comparison. The figure demonstrates that the tilting results quite parabolic modulation curve but small variations in the source temperature produce nearly linear curves. This can be used to deduct if the origin of the modulation depth decrease is the tilting or the source.

This method is useful only when the whole spectrometer is built. The method measures effectively the stability of the whole instrument because the 100 percent line depends not only on the tilt angle but also on the source emission, transmittance changes of the beam splitter, the detector response variations and changes of the absorption in the sample. Therefore, it is sometimes difficult to use it to study the interferometer alignment, which can be measured better using laser beam techniques because they are much more sensitive to the misalignment.

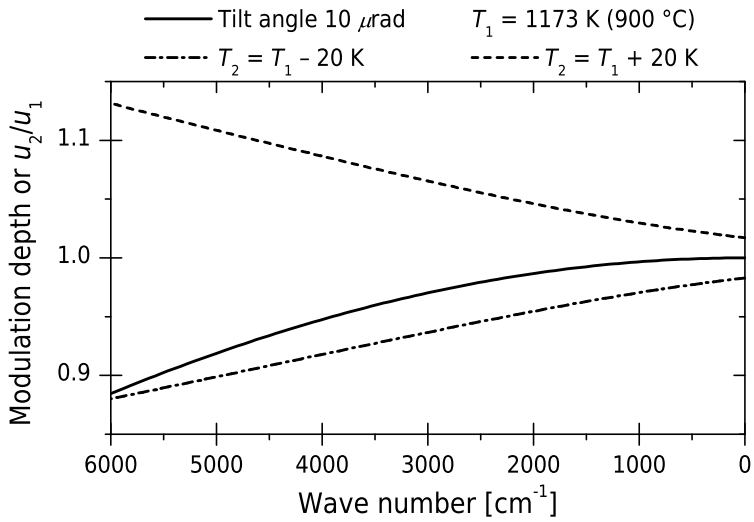

Figure 4.10 Effect of the source temperature change on the modulation depth calculated using the ratio of energy densities of two ideal black body radiators, or $u_2(\nu, T_2)/u_1(\nu, T_1)$, according to Eq. (2.15). Diameter of the infrared beam was $D = 26$ mm. The modulation depth with tilt angle $\alpha = 10$ μrad is plotted for comparison.

4.3 Swing 0

4.3.1 Monolithic porch swing

At first, it was tested if it is possible to achieve the required motion linearity and the temperature stability using the porch swing type bearing. These requirements are main targets and usually most limiting properties of the bearing, so it is natural to begin with them. Two different porch swing structures were tested. The first was a monolithic porch swing and the second was assembled from two rigid aluminum arms and four flat steel springs.

Two monolithic bearings were cnc machined from one aluminum piece. The side profiles of the pieces are depicted in Fig. 4.11. The obvious advantage is that the monolithic bearing component can be mounted much more accurately and cost effectively than the bearing, which is assembled using several separate pieces. The machining with cnc milling turned out to be very challenging, since the milling cutter broke the narrow part of the hinges very easily. Perhaps, the more suitable machining method might be the wire electrical discharge machining (wire EDM).

The larger version of two monolithic bearings or the one in Fig. 4.11(a) was first tested by mounting the bearing to the interferometer and monitoring the fringe pattern formed by expanded Helium-Neon laser beam. The porch swing was moved stepwise by the pushing the upper arm at its centre by a rod. The total fringe number over the beam was observed. The tilt angle values estimated using Eq. (4.1) are plotted to Fig. 4.12. The tilting was clearly much over the acceptable limit of ± 14 μrad set in Chapter 2.5.1. Because of the very poor alignment stability during the mirror travel, the monolithic bearings were rejected and the work was continued with the structure assembled from separate components.

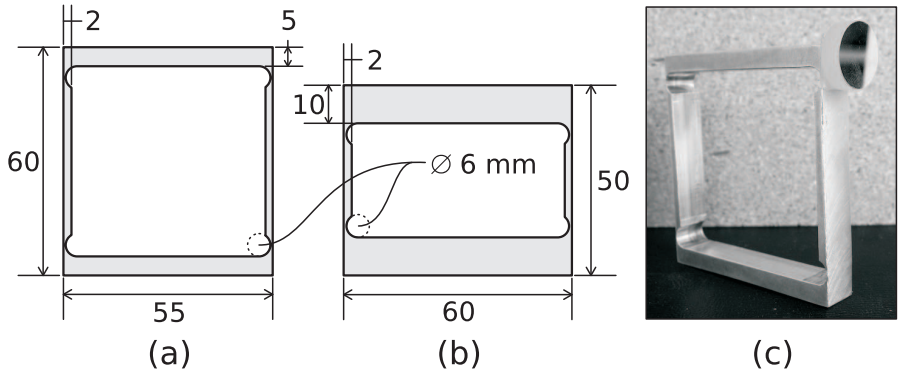

Figure 4.11 Monolithic porch swings cnc machined from aluminum. Thicknesses of pieces were 10 mm. Results presented in Fig. 4.12 were measured with the left one.

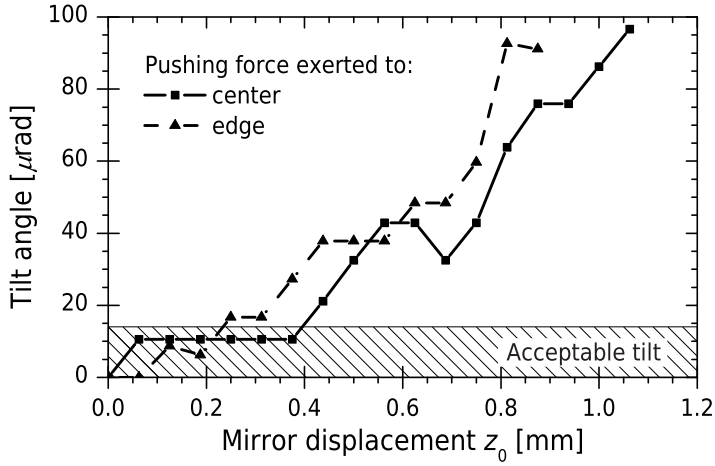

Figure 4.12 Tilting of the monolithic porch swing against the mirror displacement. The bearing is drawn in Fig. 4.11(a). The maximum acceptable tilt, ± 14 μrad, is marked with skewed lines.

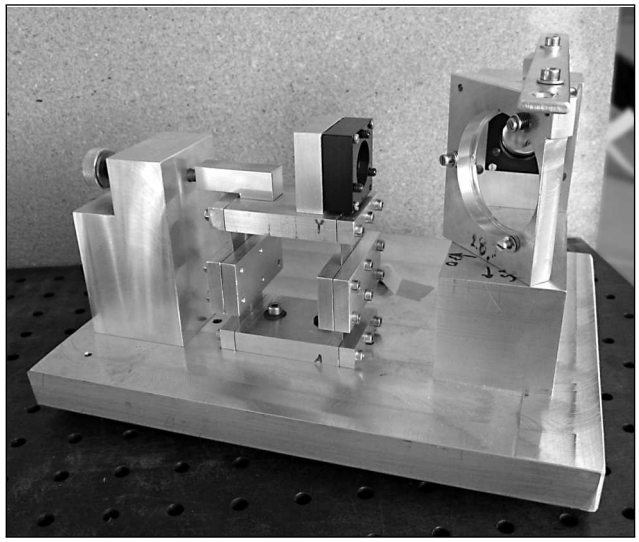

Figure 4.13 The first stable version of the porch swing bearing, Swing 0, mounted on the optical bench. The plate beam splitter for visible light was unmounted when the photo was taken.

4.3.2 Porch swing assembled using flat springs

After difficulties with the monolithic bearing, the porch swing was assembled using two rigid aluminum bars and four flat steel springs as illustrated in Fig. 4.13. The most significant dimensions of the bearing are listed in Table 4.B. The stiffener clamps were mounted in the middle of the springs after their effect to the driving stability was successfully demonstrated. Swing 0 was the first version, which filled the requirements for motion linearity and temperature stability. Because it was still a preliminary version, it is numbered with zero.

Michelson interferometer using the Swing 0 as the bearing for the movable mirror was mounted on the optical bench. The material of the components was aluminum always when possible. This should minimize the differences between the thermal expansion of the separate parts. The interferometer consisted of few separate components, which is not the optimal structure as discussed later. The optical bench had three legs to separate it from the laboratory table and minimizing their different thermal expansion. The displacement of the arm was produced by a pushing rod with blunt head and moved by the fine threads. The rod and its mount were made of aluminum. The small piece of glass was between the rod and the arm as a slide bearing. The glass plate reduced the friction forces at the contact point and reduced the tilting to smaller than the other origins of the tilting.

All the optics of the interferometer were mounted using the same principle. The mirrors were pressed against three supports by the spring force as in Fig. 4.14. The supports were studs machined directly on the mount and the mirror reflective side was against them. The spring force eliminated the effect of the extra forces produced by the thermal expansion. The optimal mounting plane for the beam splitter is the surface with beam splitting coating, which, however, can not be used if the compensating plate is mounted

Table 4.B Dimensions of the Swing 0.

	Symbol	Value	Unit
Arm length	l	50.0	mm
Flexure length	h	50.0	mm
Swing width	w	28.0	mm
Number of springs		4	
Spring thickness	t	0.31	mm
Spring width		12.7	mm
Space between springs		2.6	mm
Stiffening clamp length		25.0	mm
Beam diameter		20	mm

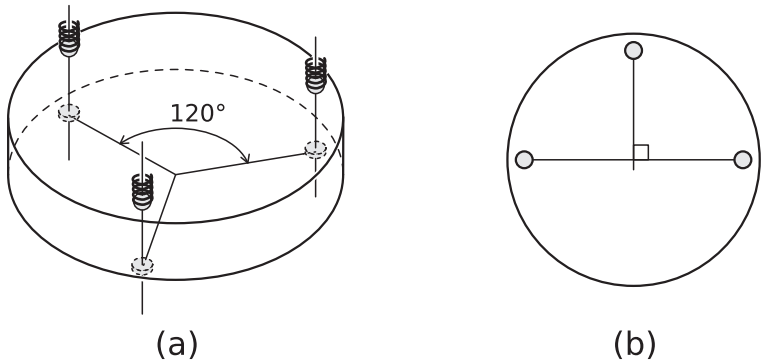

Figure 4.14 Principle of three point mirror mount pressed with the spring force. The left drawing shows the usual symmetric stud distribution. The right one illustrates orthogonal stud location for easy alignment.

against the beam splitter. Because the both surfaces of the beam splitter must be interferometrically flat, the either surface may be used. One mirror had mechanism to adjust the alignment. The mirror was pressed against three fine threaded screws with blunt heads. The screws were tightened by the stack of disc springs.

4.3.3 Motion linearity and the effect of the stiffener clamps

The very first requirement for the interferometer is sufficient motion linearity of the movable mirror, so it wast studied first. The motion linearity was determined over the mirror travel by analysing the fringe pattern formed by the Helium-Neon laser beam, whose diameter was 20 mm. The fringe pattern method was similar than described in Chapter 4.2.1 but the fringe pattern was magnified about 9.2 times using a double concave lens with effective focal length $f = -25.0$ mm. Purpose of the magnifying was to reduce the measurement error of the fringe distance d. The distances between adjacent fringes were measured vertically and horizontally from the fringe pattern projected over a millimeter scale. The total distance between fringes d can finally be calculated using Eq. (4.4) and the tilt angle by Eq. (4.3). The tilt angles were compared to the initial tilt angle α_0. The resulting tilt $\Delta\alpha = \alpha - \alpha_0$ over the mirror travel is plotted to Fig. 4.15.

Errors in the tilt angle values were about $(10 \ldots 20)$ μrad or relatively $(7 \ldots 17)$ %. If the tilt angle would have been measured by counting the fringes across the non-magnified beam, the measurement error would have been determined by the resolution of the method that is about half fringes. Thus, the error value would have been approximately $|\Delta\alpha| \leq 4$ μrad or about 3 %, according to Eq. (4.2). It is substantially less than the method with the magnified fringe pattern. Therefore, the magnification method did not reduce the error although the magnification was measured and the lens aberration corrected. The major error source was the reading error 1.5 mm

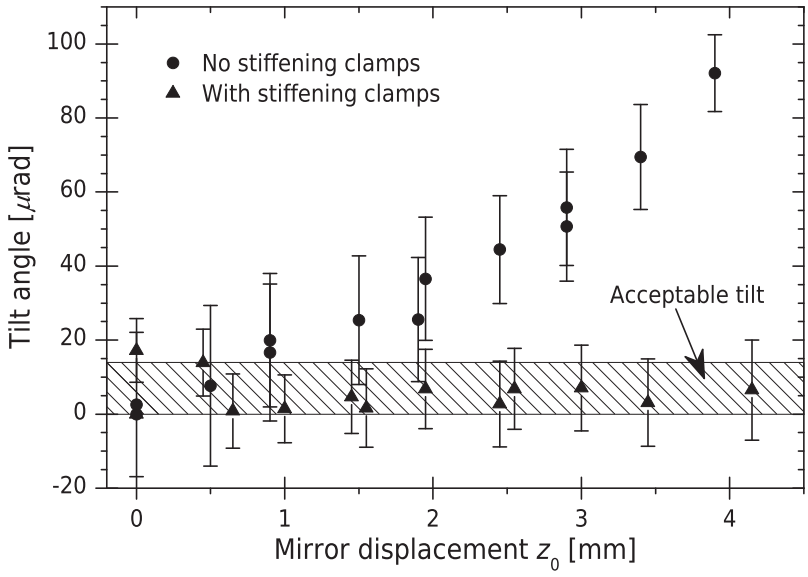

Figure 4.15 Tilting of Swing 0 as a function of the mirror displacement z_0 with and without the stiffener clamps. The clamps reduced the tilting to the allowed range. Figure is reproduced from [68].

of distances between magnified fringes. This error should have been a few times smaller to obtain more accurate results but improving the measurement setup was regarded worthless.

The most important result is that without stiffener clamps, the tilt angle was about 90 μrad after 4 mm translation but with clamps the tilt kept well below 14 μrad over the whole travel. Therefore, two major conclusions can be made. Firstly, the alignment stability over the mirror travel of Swing 0 with stiffener clamps was acceptable. Secondly, stiffener clamps really seem to improve the stability of the moving arm as proposed in Chapter 3.2.6.

4.3.4 Swing 0 in the weather chamber

The temperature stability of Swing 0 was studied in the weather chamber, which was a large thermally insulated box with a door in one side. Swing 0 and the laser were inside the chamber. The fringe pattern was projected to the chamber wall and recorded by a webcam. The interferometer temperature was measured from the unused screw hole and the inside air temperature at height of the interferometer.

The chamber could be heated by an electric heater with adjustable power. Because the heater had no thermostat, each heating was done with a constant and continuous power. The chamber was cooled by waiting that the heat was leaking out or more quickly by slightly opening the chamber door. The heating and the cooling by opening the door produced convection of the air in the interferometer arms, which resulted in irregular and

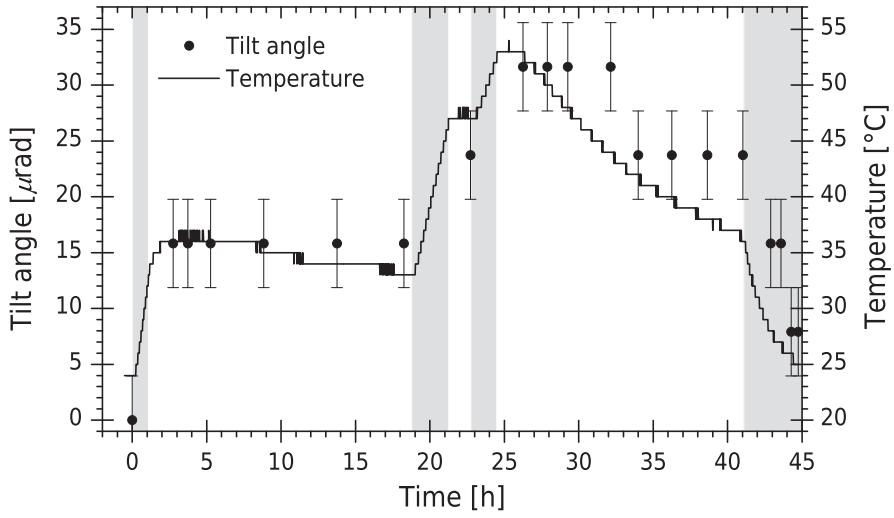

Figure 4.16 The tilt angle and the temperature of the Swing 0 during the first measurement. Heating and cooling periods are marked with light grey.

fluctuating fringes in the pattern. All the analyses were done using stable fringe patterns.

The tilt angle was estimated from the number of fringes k across the beam using fringe pattern method and Eq. (4.1). The results of the two heating experiments are plotted in Fig. 4.16 and Fig. 4.17. Heating and cooling periods are marked to the figures. The measurement error of the tilt angle corresponds to the resolution of the fringe pattern method, which is about half fringes corresponding to about 4 μrad tilt angle.

In the first measurement, the tilt angle followed the temperature quite clearly. It was about 32 μrad when the temperature was between 44 °C and 53 °C. The tilt angle returned to about half a fringe away from the initial value so some permanent misalignment had happened. The maximum tilt angle corresponds to the modulation $m = 0.74$ at 3000 cm^{-1} with 25 mm beam, according to Eq. (2.8). The average change of the modulation was then about 0.026 per Celsius. The interferometer was much more stable in the second measurement. The only observed instability was happened during the first heating period when the temperature was raised from 23 °C to 39 °C in 2.5 hours. After that, the tilt angle was kept constant between the equilibrium states of the temperature.

The mounts and the optical bench of Swing 0 were quite massive. It took over two hours to stabilize the temperature of the aluminum blocks. Before that, the temperature gradients of the structure often produced the tilting. Therefore, the future versions of the interferometer should be made lighter to reduce the settling time.

Although some permanent misalignment occurred during rapid changes of the temperature, results were, as a whole, so promising that designing of

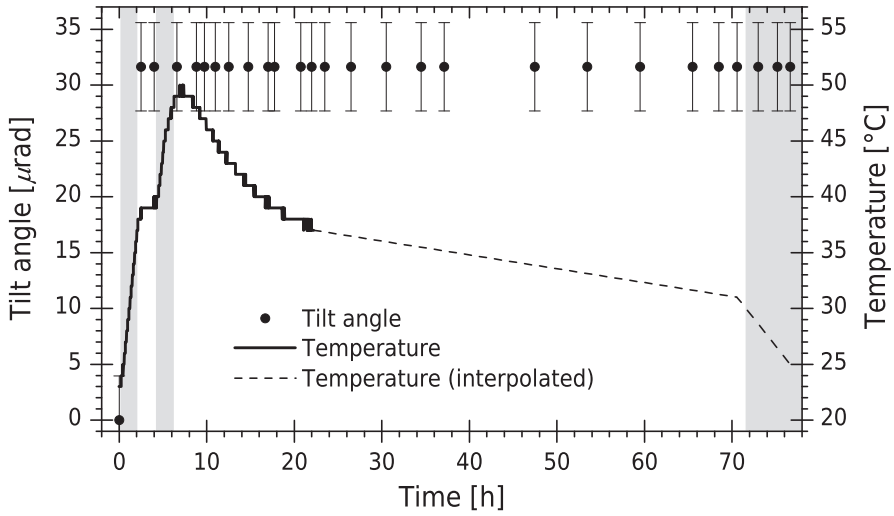

Figure 4.17 The tilt angle and the temperature of the Swing 0 during the second measurement. The temperature logging was stopped at 22 h because of the battery run down. The last two temperature values are actually the chamber air temperature but they are almost equal to the Swing 0 temperature hence the system was in equilibrium. Heating and cooling periods are greyed.

more sophisticated interferometer was started. It would have more solid and compact structure rather than a punch of separate components mounted on the optical bench.

4.3.5 Notes about thermal stability

In this section, the properties and technical solutions, which were observed to affect the thermal stability of the interferometer, are summarised. The first principle is that the coefficient of thermal expansion of the different parts must be as near as possible with each other. Often this means that all the parts should be same material. Additionally, the number of the separate parts should be minimized. Ideally, the interferometer is machined from two solid blocks by milling the openings for light beams, optics, mounting screws and other required components. In Swing 0 the beam splitter mount was an overhang fixed just from its bottom. This mount was not stable, so the extra aluminum bar had to be added between the top of the beam splitter mount and the stationary mirror mount as in Fig. 4.13.

Screws are usually different material than the other parts. This is not necessarily a problem although the screws are effectively tightened or loosened when the temperature is varied. But, for example, if a component is mounted using the screws from different directions, the thermal expansion can cause extra loads to the component and it may bend and produce misalignment as happened with Swing 0. This can be avoided by designing the fixing properly or using screws made from body material. Furthermore, the

tightening torque of screws should not be too much because it may cause bending of mounts and thus the misalignment of the optics.

One of the most thermally stable mounting for the optics is to press them against three flat and smooth studs using spring force as mentioned in Chapter 4.3.2 and illustrated in Fig. 4.14. The spring force stays practically constant although the other parts have been thermally expanded. However, the pressing force should not be too strong because it may cause the bending of the optics. The studs should be on the reflective side of the optics. The coating of mirror is best to remove under the studs because the thermal expansion moves the studs slightly over the mirror surface and may scrape the coating off, which may cause tilting. The mirror used for the alignment of the interferometer, can be supported by three screws with blunt and smooth tip. These screws must have equal coefficient of thermal expansion than the body material. Orthogonally distributed studs as in Fig. 4.14(b) make the interferometer alignment more straightforward.

The cube beam splitter was observed to be unsuitable because it caused tilting in temperature changes. We tried many different mountings but none of them was stable enough. The cube beam splitters are assembled from two prisms glued together. The layer of glue is probably the reason for the tilting hence it may expand unevenly in the temperature change. Instead, the plate beam splitter and a compensation plate are a better choice for temperature stability. All the results of temperature stability in this work are measured using the plate beam splitters.

4.4 Swing I

4.4.1 Interferometer and porch swing as a single block

The next interferometer, Swing I, was the first properly designed version. It was made using the solid block principle and, actually, the whole spectrometer based on it was designed. Swing I had the best thermal stability of the all four version built in this work. Firstly, the structure and the optics are described following by the reports about alignment and thermal stability. Along with heating experiments, errors and noise in modulation depth time series recorded with laser beam are discussed.

The best thermal stability is achieved when the interferometer is made from the single block of homogenous material where holes and other openings are made for the optics and light beams. After the temperature change, the whole structure had expanded equally and the tilting is minimal. Even the hinges of the porch swing could be machined to the solid block. However, separate springs as the flexure elements were used to make Swing I so at least two separate pieces were required for the interferometer. These were machined from aluminum because its easy machinability, low density and good thermal properties, as large thermal conductivity.

The optical layout of Swing I is drawn to Fig. 4.18. The radiation from the infrared source was collimated by the off-axis parabolic reflector OAP1 and then guided to the interferometer by the mirror M3. The interferometer consisted the beam splitter BS, the compensating plate CP and the mirrors M1 and M2. The interferometer was aligned by tilting M2. The mirror M1 was driven. The output beam from the interferometer was focused to the detector by OAP2 that was the similar reflector than OAP1. The reference laser beam was designed to run beside the infrared beam. When the Helium-Neon laser was used as the light source, the laser beam was collimated and focused using lenses and reflectors OAP1 and OAP2 were unmounted.

Much of the optics was placed inside the bearing to save space as illustrated in Fig. 4.19. This made the bearing larger than Swing 0 but also more insensitive to the tilting. The dimensions of the whole bearing assembly were about $(138 \times 63 \times 105)$ mm^3 as listed in Table 4.C. The drawing from 3D model of the interferometer and the spectrometer are in Fig. 4.20. The photo of the Swing I with the Helium-Neon laser is in Fig. 4.21.

—Text continues on page 86.—

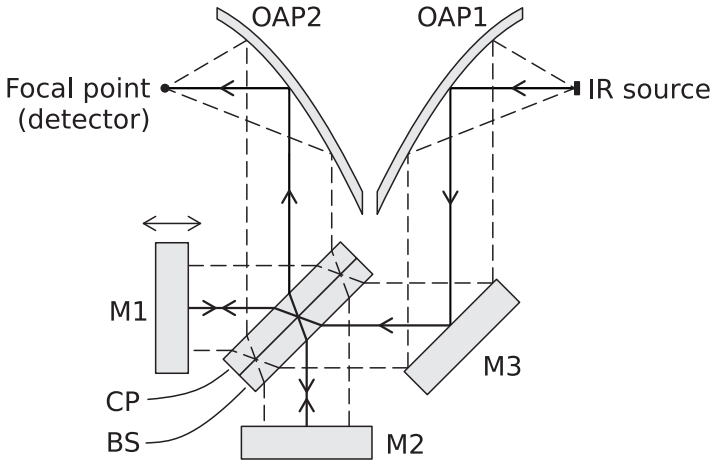

Figure 4.18 Layout of infrared optics of Swing I. The solid thick line represents the beam center and the dashed one the beam edges. OAP1 and OAP2 are similar off-axis parabolic mirrors. The alignment is adjusted using mirror M2. The optical path difference is varied by moving the mirror M1. BS and CP are the beam splitter and the compensating plate. When Helium-Neon laser was used, the collimated beam was pointed directly to the flat mirror M3 and focused using a lens.

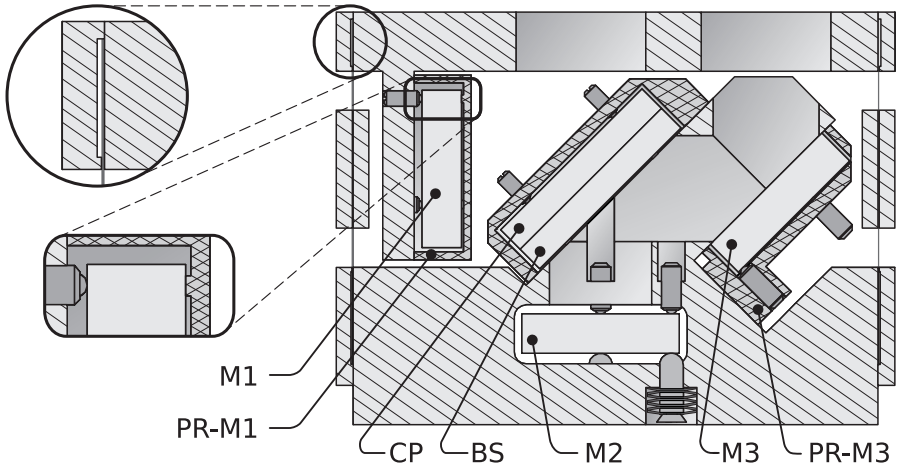

Figure 4.19 Section of Swing I illustrating the layout and the optics mounting. Some details are not drawn for clarity. The active coating of the beam splitter BS was on the side against the compensating plate. The small air gap between BS and the compensating plate CP is not distinctive. The mirror M2 could be aligned with three fine threaded screws positioned as in Fig. 4.14(b). The mounting screws of the holder PR-M1 (not shown) were aluminum. The holder PR-M3 was tightened with parallel screws.

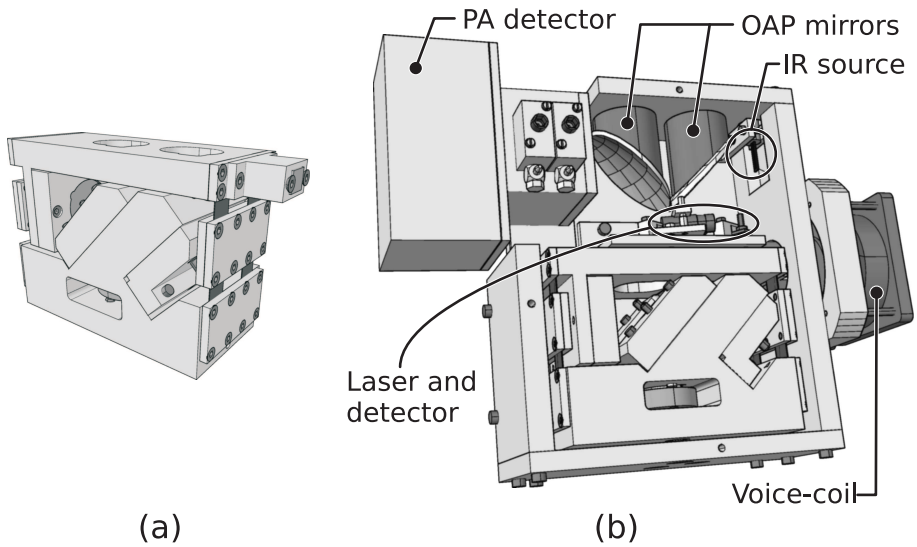

Figure 4.20 Schematic drawings of the 3D model of Swing I. The left drawing illustrates the interferometer and the right one the spectrometer with photoacoustic (PA) detector. OAP mirrors are similar off-axis parabolic mirrors.

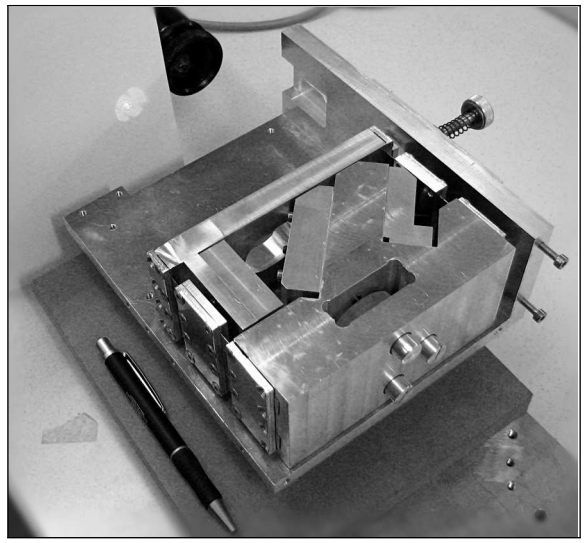

Figure 4.21 Photo of Swing I without the cover. Expanded Helium-Neon laser beam illustrates the interference. The swing motion was prevented by the pushing rod.

Table 4.C Dimensions of the Swing I.

	Symbol	Value	Unit
Arm length	l	133.5	mm
Flexure length	h	50.0	mm
Swing width	w	46.1	mm
Number of springs		4	
Spring thickness	t	0.31	mm
Spring width		12.7	mm
Space between springs		20.9	mm
Stiffening clamp length		30.0	mm
Beam diameter, IR		25.0	mm
Beam diameter, laser		≤ 6.0	mm

—Continued from page 83.—

The lower arm was the body of the interferometer. It was mounted to the back plate of the casing by three points, which had spacers to separate those parts from each other. The beam splitter, compensating plate and mirror M2 were mounted to the body. The alignment and the position on the optical axis of M2 could be adjusted by three aluminum screws with fine threads. These alignment screws were spring loaded using a stack of disc springs to remove effects from the thread clearance. The body had also an extra mirror M3, whose purpose was to turn the incoming beam to the beam splitter. Because it was not part of the interferometer, it was not mounted by the three point principle hence small tilting of it would have only negligible effect. However, its holder PR-M3 was fixed by two parallel screws to avoid bending of the body by thermal expansion.

The upper arm of the movable arm was mounted to the body using four flat steel springs of thickness 0.31 mm. The springs had 30.0 mm aluminum stiffening clamps in the middle. The presses fixing the flat springs had grooves as depicted in the enlarged circle in Fig. 4.19 to make the fixing regions more accurate. The similar mounting has been used at least by Villar et al [97]. The arm had openings for the infrared and the reference laser beams. Three studs determining the mirror M1 alignment were not optimally on its holder PR-M1 rather than in the arm to make machining easier. Thus, the fixing screws of PR-M1 had to aluminum to avoid bending by thermal expansion.

The interferometer optics were mounted using the three point principle depicted in Fig. 4.14. The optics were pressed against studs using the set screws with a rolling-ball tip. Wave spring washer, presented in Fig. 4.22, was tested for replacement of the set screws because it would save space. However, it was not stable enough in the temperature changes. Although

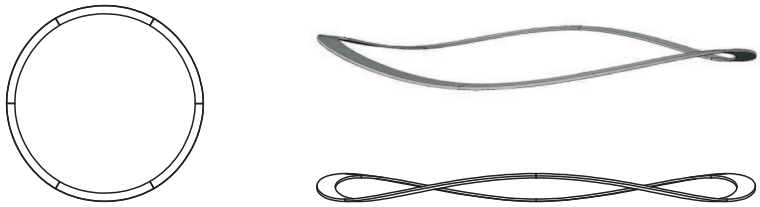

Figure 4.22 The schematic drawing of the wave spring washer tried in clamping the beam splitter.

the best is to place the studs on the reflective side, the mirror M2 studs, which were actually the alignment screws, were on the back side to minimise the space. Flatness of the optics was $\lambda/10$. The plane mirrors were aluminum coated round mirrors with dimensions 40×10 mm^2. When the laser beam was used, the beam splitter with broad band visible coating and with dimensions 50.8×7 mm^2 was mounted. The mounting fitted also to the beam splitter and compensating plate pair made of KBr and coated for infrared region.

The mirror M2 could be positioned along the optical axis. The other extreme position corresponded the equilibrium of the flexure elements, which would allow even about ± 3 mm mirror travel or unapodised spectral resolution of 1 cm^{-1}, according to Eq. (2.20). However, this would have required driving the arm over the equilibrium position of the flexure elements. This would require the change of the driving force direction in the middle of the scan, which was expected to produce wobbling of the arm. Therefore, the zero optical path difference position could be adjusted to 1.5 mm off from the equilibrium by adjusting the mirror M2 position on its optical axis. Then, the driving force direction would keep unchanged during the scan. However, the maximum mirror travel was shortened to ± 1 mm, which could provide only 6 cm^{-1} resolution.

The spectrometer sketched in Fig. 4.20(b) and utilizing Swing I was also designed but it was never built or tested because it would not be meaningful after the experimental results made with the laser were obtained. The spectrometer would have been the casing containing the mountings for infrared source, the collimating optics, the photoacoustic infrared detector, the voice coil motor, the solid state laser for the reference and the laser detector.

4.4.2 Driving stability

Tilting over mirror travel

The tilting was studied over the mirror travel by displacing the arm stepwise using the pushing rod with fine threads. Between the rod and the arm, there was a glass plate as a slide bearing to reduce the misalignments caused by the friction on the contact point. The arm lengths of Swing I were slightly tuned by adding thin spacers between the flat springs and the arm. This effectively lengthened the arm by small amount. After tuning, the tilting over the mirror travel was so small that changes in the fringe pattern were not distinctive by human eye. Therefore, the tilting was estimated using the expanded laser beam with diameter 25 mm. The beam exiting from the interferometer was focused to photo diode detector and the signal was studied with the digital oscilloscope. The modulation depth was determined using Minmax-method 1 described in Table 4.A on page 67. The tilt angle was estimated from the laser modulation depth using Eq. (4.7), which takes account the Gaussian distribution of the beam. The modulation depth of uniform infrared beam at 3000 cm^{-1} was approximated by Eq. (2.8). The results of the modulation depth and the estimated tilt angle values are presented in Fig. 4.23.

The modulation depth as a function of mirror displacement z_0 had a parabolic shape, which was illustrated by fitting a parabola to it by the least squares method. According to Eq. (2.8), the modulation depth decreases on the square of the tilt angle, which is probably proportional to

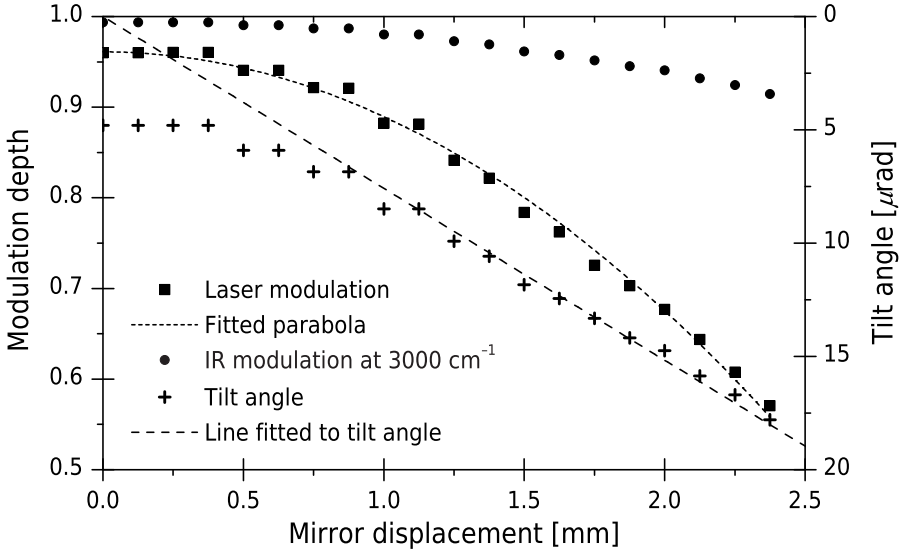

Figure 4.23 Modulation depth and the estimated tilt angle of Swing I during the mirror travel. The estimation of the tilt angle and the modulation at 3000 cm^{-1} are described in the text.

the mirror displacement when the displacements are small. Therefore, the line was fitted to the tilt angle data excluding the first seven points, whose modulation values were probably dominated by the unflatnesses of the optics. Indeed, the tilt angle seems to follow the line very well as expected.

Over the designed maximum travel length 1 mm, the modulation was decreased approximately 0.07 units. It corresponds about 8 μrad tilt or about 0.98 modulation at 3000 cm^{-1}. If Swing I would have been optimally aligned at mirror displacement 1.5 mm and driven around this position by ± 1 mm as designed, the tilting would be acceptable. However, the substantially better alignment results were obtained when the arms were tuned more rigorously, as with Swing II, or machined more accurately, as with Swing III, which are both discussed later.

Mirror velocity

The velocity of the mirror was quickly measured for demonstration. The interferometer was driven with the voice-coil. The triangle voltage pulse from an analog signal generator was fed to an audio amplifier, whose output was connected to the voice-coil. The light source was a collimated Helium-Neon laser beam focused to the photodiode. The laser signal from the photodiode was then recorded during driving of the interferometer. The baseline was removed from the laser signal by the high-pass filter with 200 Hz cut-off frequency. The mirror velocity v_{mirror} and the laser frequency f_{L} were determined by the interpolating the zero-crossings of the laser signal as described in Chapter 2.3.5 and Eq. (2.22) and Eq. (2.23). The laser frequency and the mirror velocity of one typical driving cycle is plotted to Fig. 4.24. The mirror velocity in the graph is actually the absolute value, which does not take account that the direction of the movement was reversed in each driving cycle.

The mirror velocity was continuously changing over the scan and there was no constant region, which is mandatory for the acceptable driving. Additionally, the back and forth velocities were not similar. Reasons for the unsatisfactory driving were many. Firstly, the mirror travel was approximately 0.23 mm in one direction, which is a very short travel. Possibly, the driving had not enough time to achieve the stable velocity before it had to decelerate again. Secondly, the amplifier was an audio model, optimized for listening music and not driving the interferometer. For instance, the driving ramp frequency was about 7 Hz but the amplifier response is probably optimized for the audible region or from 20 Hz to 20 kHz. Much more better and usable driving system was developed later for Swing III and is discussed in Chapter 4.6.

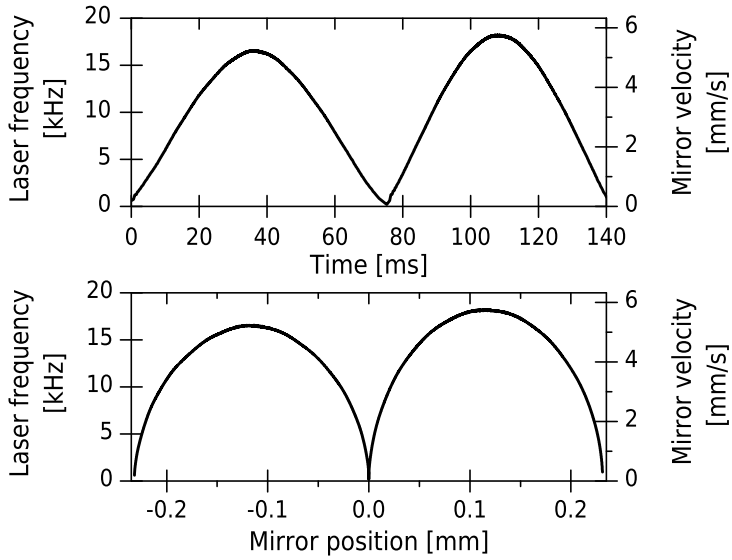

Figure 4.24 Typical laser frequency and the absolute value of the mirror velocity of Swing I during one complete driving cycle, or one back and forth movement.

4.4.3 Experiments on temperature stability and modifications of Swing I

Measurement setup

The thermal stability of Swing I was extensively studied using the same weather chamber as with Swing 0. In total, 37 single experiments, where the external temperature was varied, were made. The total measurement time was about 97 days. Most of the experiments lasted about a day but six of them continued over five days. Experiments include also studies on the stability of the measurement system and the components of it. Eventually, the measurement setup was achieved to become reliable and Swing I was modified so that very good stability was obtained.

The weather chamber setup is presented in Fig. 4.25. The laser was stabilized single mode Helium-Neon laser. It was placed outside the chamber, because its feedback control became mad when the temperature was too high. The expanded and collimated laser beam was pointed through the small plastic window in the chamber wall and then to the interferometer via two flat mirrors. After the interferometer, it was focused to the photodiode so the setup was principally similar to Fig. 4.4, on page 66, and the mirror tilting was analysed by the modulation depth of the laser. In few experiments, the output beam was divided by an extra beam splitter and both the fringe pattern and the photodiode signal were able to record. The temperature of the interferometer was measured from the screw hole near the holder PR-M3, thus it represents the temperature of the Swing I. The air temperature inside the chamber was measured at the same height

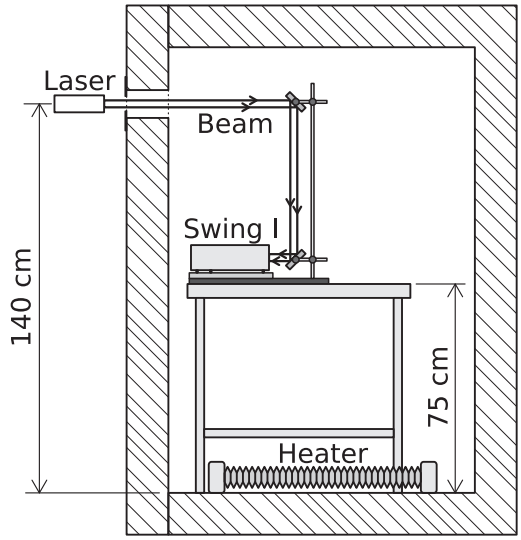

Figure 4.25 Measurement setup schematically for thermal stability experiments of Swing I. The optical setup on the table was as in Fig. 4.4, but the laser beam ran through the chamber window and by two flat mirrors to the interferometer.

as the interferometer. Usually, the casing was on the interferometer during the experiment to reduce temperature gradients inside the interferometer. When the equilibrium had been reached, the interferometer and the air temperatures differed from each about 1 °C at maximum. The power of the electric heater was adjustable and it was equipped with thermostat so very slow and quite smooth heating was possible. Temperature gradients inside the chamber were reduced by the small axial fan which produced a weak convection inside the chamber.

Laser detector response and measurement setup stability

The stability of the measurement setup was studied during the experiments when searching the sources of the instabilities. The linearity of the output voltage of the laser detector and its amplifier circuit was compared to the intensity probe from Thorlabs Inc. The intensity of the laser beam was varied by two polarisers and neutral density filters. The intensity was measured with both detectors. The photodiode detector voltage against total incident power on the Thorlabs probe are plotted in Fig. 4.26. The dependence is highly linear, which was quantified by fitting a line to the data by the least squares. The relative error of the slope was below 0.2 percent.

The frequency response of the photodiode detector and its circuit was estimated by several laser signals, whose amplitude was clearly decreasing by the increasing frequency. Very short travel length of 50 μm, was used to minimize the signal decrease by the misalignments. The heights of the peaks and valleys were plotted against the frequencies estimated from the adjacent

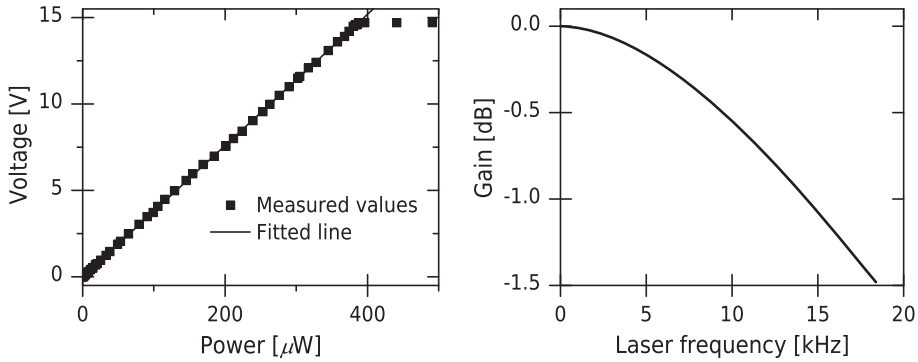

Figure 4.26 Linearity and frequency response of the photodiode detector used to determine the modulation depth. The detector amplifier circuit saturated at about 390 μW.

peak and valley locations. The frequency response is approximately as in Fig. 4.26. The response decreases smoothly about 1.5 dB from zero to 18.5 kHz. Therefore, the modulation depth is best determined using the adjacent peaks in the laser signal and at about the equal frequency in each signal, so the Minmax-method 3 or 4 (see Table 4.A on page 67) are the best choices for laser signal analysis.

The temperature response of the photodiode detector was studied using the setup in Fig. 4.25 without the interferometer. The beam was focused directly to the detector. The mean values of the short signal block were recorded among with the air temperature near the detector. The weather chamber was heated to 60 °C and cooled with the cooling compressor even to 0 °C. The results of this experiment are presented in Fig. 4.27. Mean values varied quite little over the experiment. Short term drops in the signal were caused by condensed moisture on the chamber window. Later, Chapter from page 99, it was expected that even small variations of the mean values of the signal might produce errors to the modulation depth because it is determined in ratio to the mean value (see a chapter on page 99).

Furthermore, the scattered light from the environment affected the results of the modulation depth. This was minimized by making the chamber openings as small as possible and by casing of the detector. Additionally, the chamber window was occasionally cleaned between the experiments. The condensed moisture on the window was tried to avoid by cooling the chamber to only a little down the room temperature.

The above results showed that the photodiode detector is very linear, its frequency response is unflat and it is slightly dependent on the temperature. By taking account these properties, the measurement setup was regarded as sufficiently stable for studying the thermal stability of the interferometer Swing I.

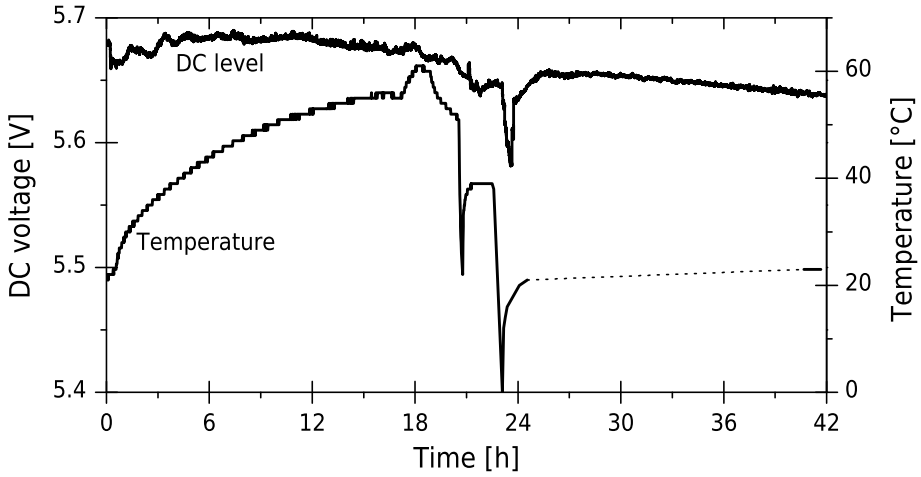

Figure 4.27 Temperature stability of the laser detector. The mean value of the signal from the detector represents the stability. Temperature resolution was 1 °C and its recording was off from 25 h to 41 h.

Modifications of Swing I to improve stability

The interferometer structure was modified to improve the thermal stability according to results from weather chamber experiments. Most significant improvements are summarised here. Maybe the most important modification was replacing steel screws fixing the holder PR-M1 by aluminum screws. Steel screws were effectively tightening during the temperature rise and thus bending the holder PR-M1, which determined the mirror M1 alignment. Additionally, thin aluminum spacers were added between the holder and the arm to set fixing points more accurately and reduce bending of the holder. After these changes, the fringe count changed only half fringes during about 30 °C rise. Adjustment screws were originally brass to avoid thread stuck. These screws had also to replace by aluminum screws hence the different thermal expansion of those materials could cause too much tilting. Seizing was prevented by a thin lubricant in threads. The third significant improvement was to use grooved presses fixing the flexure element to arms as presented in the zoomed circle in Fig. 4.19. The fixing region of flexures became more accurately determined by the grooving.

Several minor things were also considered. The holder PR-M3 was slightly separated from the overhang for the beam splitter and fixed with parallel screws. This reduced the bending of the body. Alternatively, aluminum fixing screws could have used. Arm and body lengths differed about 0.05 mm, which was estimated to produce about 5 nrad tilt angle in 30 °C temperature rise so it was negligible. Thin aluminum spacers were added under the beam splitter holder to reduce bending of the holder. The optimal material for stiffener clamps were thought to be steel, which was the spring material.

Results of heating experiments

Firstly, it was tested if Swing I is stable enough by two heating experiments. In the first test, the chamber was heated to 58 °C and the modulation depth of the laser beam decreased from 0.95 to about 0.5 but not returned to its initial value in cooling back to the room temperature, thus some irreversible and typically instantaneous misalignment, called "a snap", had been occurred. The Swing I was realigned and the heating was repeated. Then the interferometer kept stable at this time so the next stability experiments, where the temperature was risen stepwise, were started.

During the temperature change, the modulation depth fluctuates because the interferometer has temperature gradients causing misalignment. The modulation values between the equilibrium states are not very valuable, because it is very difficult to compare them to anything without information of the temperature distribution in the interferometer. Thus the modulation depth was determined when the interferometer and the chamber were in thermal equilibrium, which was typically reached one or two hours after the chamber air temperature had stabilised. The thermal stability was therefore studied by changing the temperature in steps.

Two experiments, where the temperature was raised by about 5 °C and lowered by 10 °C steps, were made. The low heater power and thermostat were used to obtain slow heatings. The interferometer and chamber air temperatures were recorded along with the modulation depth of Swing I. In the end of each heating and cooling step, the thermal equilibrium condition was ensured by waiting that the interferometer and its surrounding air had nearly equal temperatures. Data of these experiments is plotted to Fig. 4.28. In the first experiment, there is a gap in the modulation data because of the recording software was crashed. The temperature points have connected with dotted lines to help in the following the temperature change, so the lines does not represent the actual temperature values. In end of the second experiment, the chamber was cooled quite rapidly with the cooling compressor at about 264 h. Then the modulation depth was dropped to zero and some snap has been happened because the modulation was left below 0.65.

The modulation depth was calculated as a mean of about 100 points in the stabilized part of the time series. The measurement error, or the fluctuation of the modulation values, was estimated by the standard deviation of the data samples. The tilt angles were estimated from the modulation values by using Eq. (4.7) which is the model for the Gaussian distributed beam intensity. In principle, this method is actually valid only, if the modulation depth depends exclusively on the tilting, which is not exactly true because, for example, the optics were not perfectly flat. However, in practice the method works well especially with the modulation depth values less than about 0.9. The modulation depth in infrared region at 3000 cm^{-1} was es-

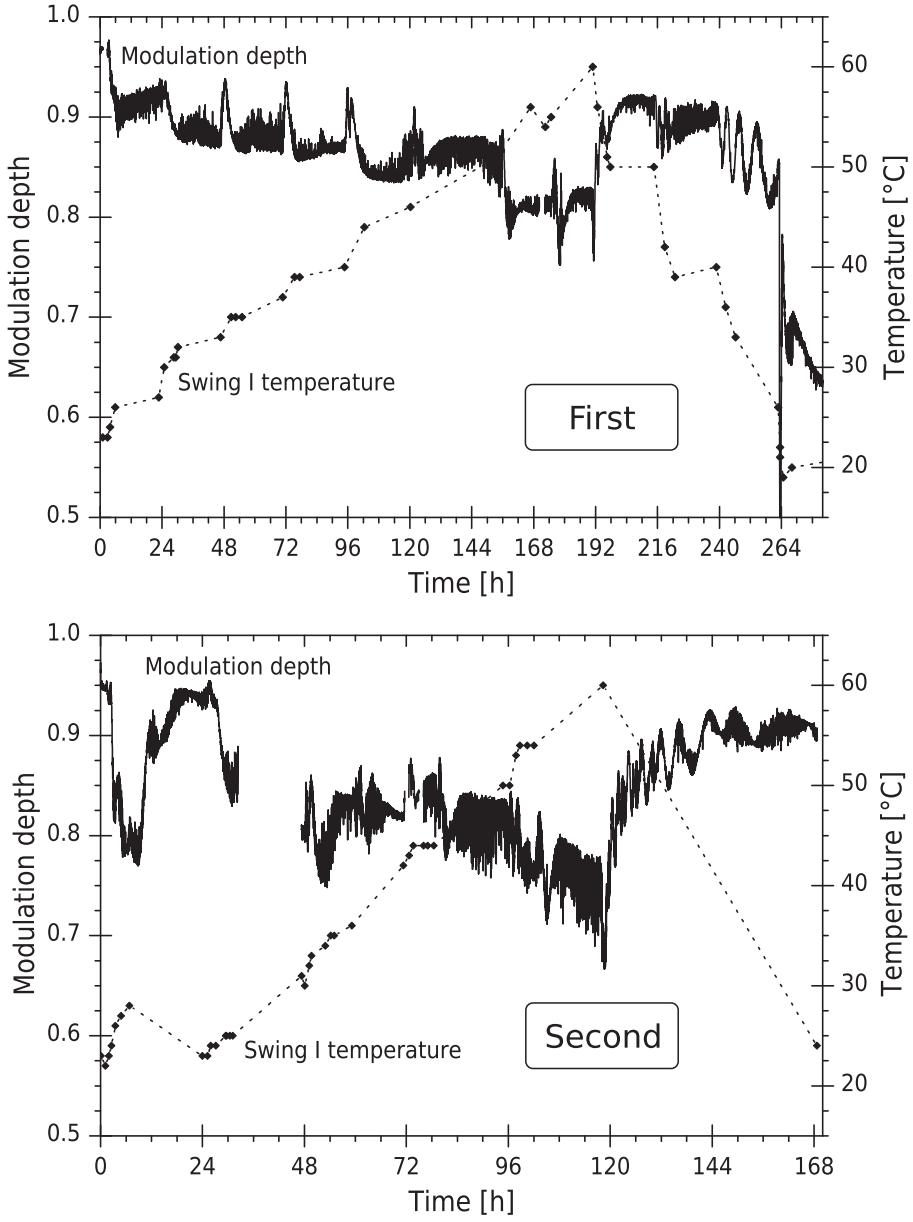

Figure 4.28 The modulation depth of the laser beam and the temperature in the stepwise heatings. The temperature was raised by about 5 °C steps. The cooling was done continuously and slowly in the first experiment and by about 10 °C steps in the second. The dotted lines just make the following of the temperature change easier and does not represent actual data.

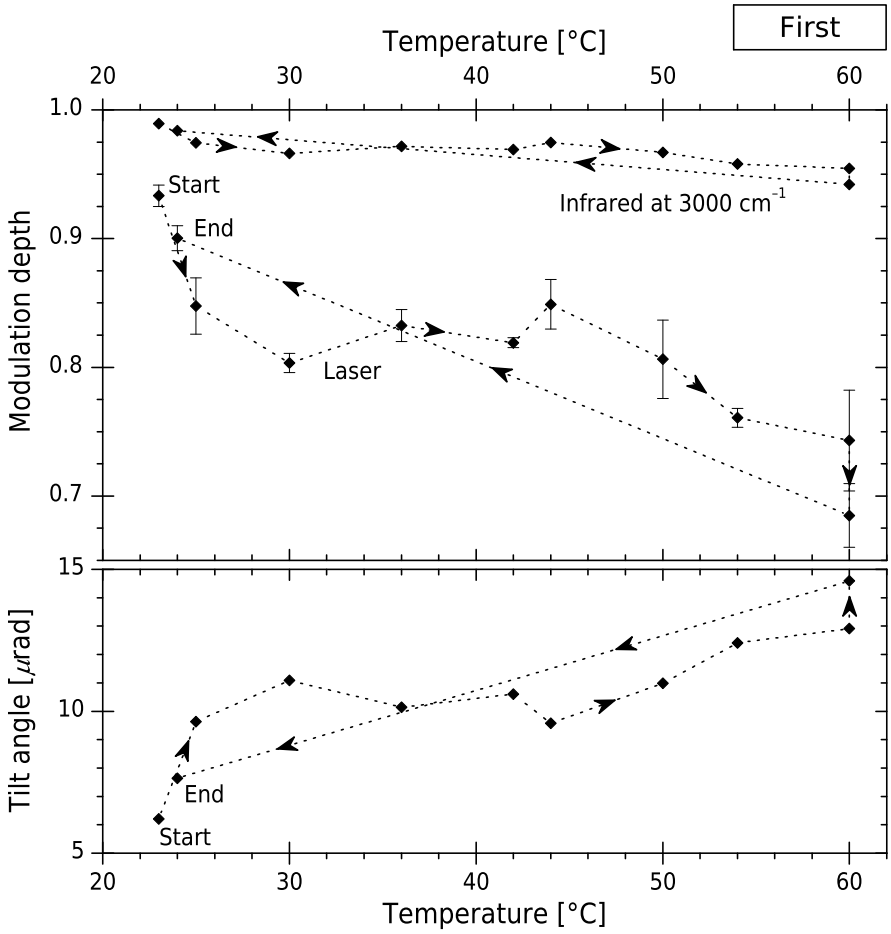

Figure 4.29 The measured modulation depth and estimated modulation values at 3000 cm^{-1} are plotted to the upper panel as a function of Swing I temperature in the *first* stepwise heating. In the lower panel are the estimated tilt angle values. Dotted lines with arrows indicate the chronological order of points. Measurement data is in the upper panel of Fig. 4.28.

timated using the tilt angles using Eq. (2.8), which assumes uniform beam intensity. The modulation and tilt angle values are plotted as a function of the interferometer temperature to Fig. 4.29 and Fig. 4.30.

In the first stepwise experiment, the modulation returned to its initial state and no permanent misalignment occurred. In the second, the cooling of the interferometer was probably too rapid hence the interferometer was not reversible. Thus, some snap had been happened in the mirror alignment. The results of the modulation and the tilt angle are collected to Table 4.D. The fast cooling is not included to the results of the second experiment because of the snap. During the temperature raise, the modulation depth at 3000 cm^{-1} changed averagely about 0.0009 units per Celsius. However, the decrease rate was not smooth and there was also higher rates than the

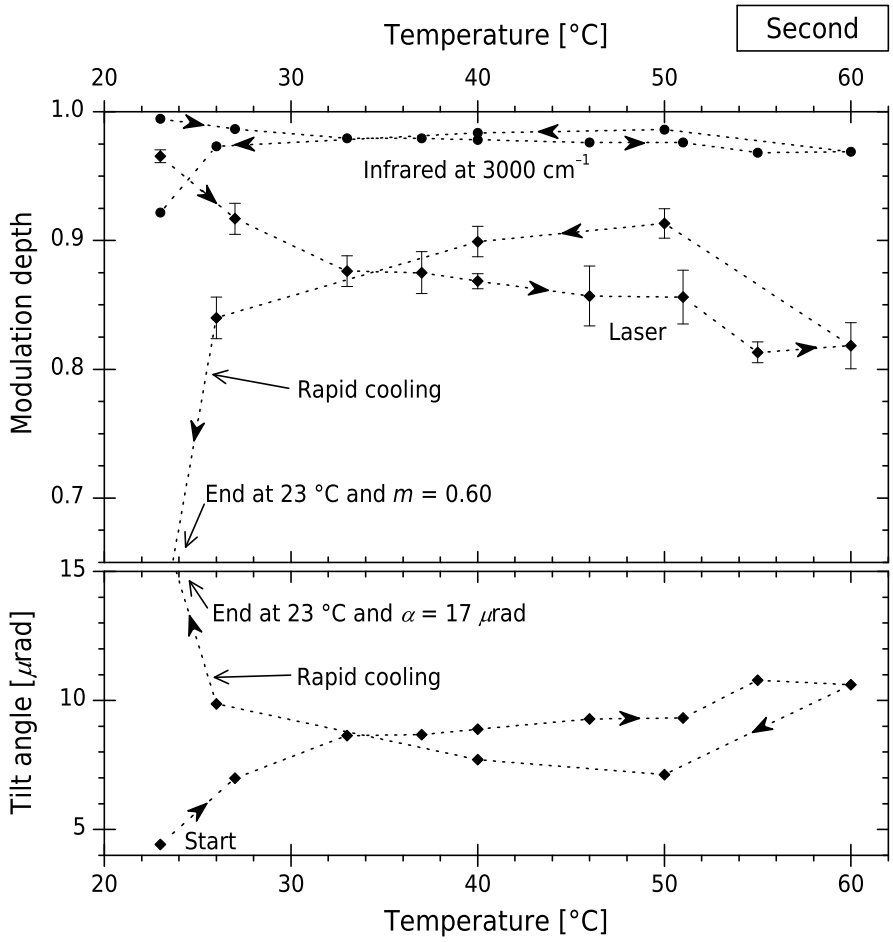

Figure 4.30 The measured modulation depth and estimated modulation values at 3000 cm^{-1} are plotted to the upper panel as a function of Swing I temperature in the *second* stepwise heating. In the lower panel are the estimated tilt angle values. Dotted lines with arrows indicate the chronological order of points. Measurement data is in the lower panel of Fig. 4.28.

average. The maximum rate between the equilibrium states was −0.007 per Celsius per 1 °C at 3000 cm^{-1}. In total, the estimated tilt angles kept below 15 μrad and 12 μrad, respectively. The total tilting was then acceptable hence the limit was 14 μrad. As a whole, the results are acceptable.

Between the stepwise heating experiments, two other tests were made. The first was similar continuous heating as described earlier. In this experiment, the modulation of laser beam was decreased to the same level as in the stepwise heatings in Fig. 4.28. Additionally, the modulation was fully reversible. The second experiment tested the stability of the Swing I in a constant temperature over 90 hours. The modulation depth kept very stable during the whole experiment as presented in Fig. 4.31. The slight variations of the modulation were probably caused by the measurement setup rather

Table 4.D Changes of the modulation depth and the tilt angle per 1 °C of Swing I. The modulation depth was measured with 25 mm Helium-Neon laser beam, whose intensity was Gaussian distributed with standard deviation σ = 4.1 mm. Tilt angle and modulation depth values at 3000 cm^{-1} are estimations. Maxima are the greatest changes between two successive equilibrium states. The fast cooling was not considered in results of the second experiment.

	Temperature change [°C]	Laser modulation [per 1 °C]	Tilt angle [μrad/°C]	Infrared modulation [per 1 °C]
Stepwise heating 1				
(Fig. 4.29)				
Total; heating	37	−0.0051	0.18	−0.00094
Total; cooling	−36	−0.0060	0.19	0.0012
Maximum		−0.043	−1.7	−0.0074
Stepwise heating 2				
(Fig. 4.30)				
Total; heating	37	−0.0040	0.17	−0.00069
Total; cooling	−34	−0.00067	0.022	0.00012
Maximum		−0.012	−0.64	−0.0020

than the interferometer itself. For example, the environment light, room temperature or the laser intensity might have been altered during the measurement. The noise and other fluctuations in the modulation depth time series are discussed in the following section.

As a whole, temperature stability of Swing I was very good. The best commercial spectrometers have stability of about (0.2 . . . 0.6) per centage units per Celsius as summarised in Table 2.C on page 37. The average rates of the modulation change with Swing I were smaller. However, the maximum short-term rates per Celsius were about 1 percentage units. Furthermore, the Carousel interferometer still has the record with its figure of 0.03 percentage units.

The comparison has some problems, because it is somewhat unambiguous to determine, how the rate of change of the modulation should be reported because it has non-linear nature. Additionally, the rate of temperature change affects the results very much. If the device temperature has gradients, the tilting may be very much larger than in equilibrium conditions. However, the biggest issue of Swing I were snaps, or the permanent misalignment due to release of some tension between components of different materials. After a snap, the interferometer should be realigned. Furthermore, after many heating cycles, the modulation depth may gradually drift far away from the optimal alignment and the signal may weaken very significantly. Thus it is essential to find the origin of snaps.

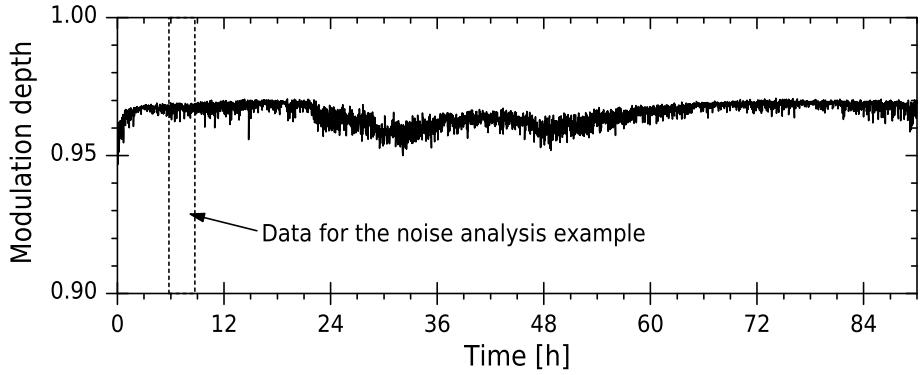

Figure 4.31 The modulation depth of the laser beam with Swing I in a constant temperature. The marked data was used in the example of the noise analysis in Chapter 4.4.3 and in Fig. 4.32.

Noise and errors in modulation depth time series

Modulation data is very noisy as shown in Fig. 4.28. Firstly, there is high frequency noise all over the data. Secondly, the modulation depth is swaying with lengthening period. The swaying begins usually after a rapid temperature change and continues for some time until it fades away. In this section, the noise and other errors in the modulation depth time series are discussed in detail.

The noise was analysed using several stable sections of modulation time series. Some statistics of the section marked to Fig. 4.31 are presented in Fig. 4.32. Clearly, the noise is not normally distributed. Additionally, the autocovariance shows practically no correlation between successive data points and the frequency distribution has no structure. Therefore, the noise seems to be random white noise, which is not normally distributed.

The modulation depth was calculated from adjacent peaks in the laser signal using Minmax method 3 described in Table 4.A on page 67, so the noise in the laser signal affect the modulation values. However, the laser signal noise was low, as illustrated in Fig. 4.33. Adjacent peaks were selected so that their frequency would not vary very much. The bottom right graph in Fig. 4.32 shows that the modulation depth values had merely a weak dependence of the corresponding frequency of the laser signal, thus unflat frequency response of the detector has only minor effect to the noise. Furthermore, the sampling rate was 100 kHz and laser signal frequencies were below 1 kHz. Therefore, the origin of this noise is elsewhere than in the detecting of the laser signal.

The modulation depth noise is most probably caused by the envelope in the laser signal as presented in the middle graph of Fig. 4.33. This envelope was probably caused by interferometer itself rather than the laser detector. Thus, the origin is tilting, and most probably tilting of movable mirror M1.

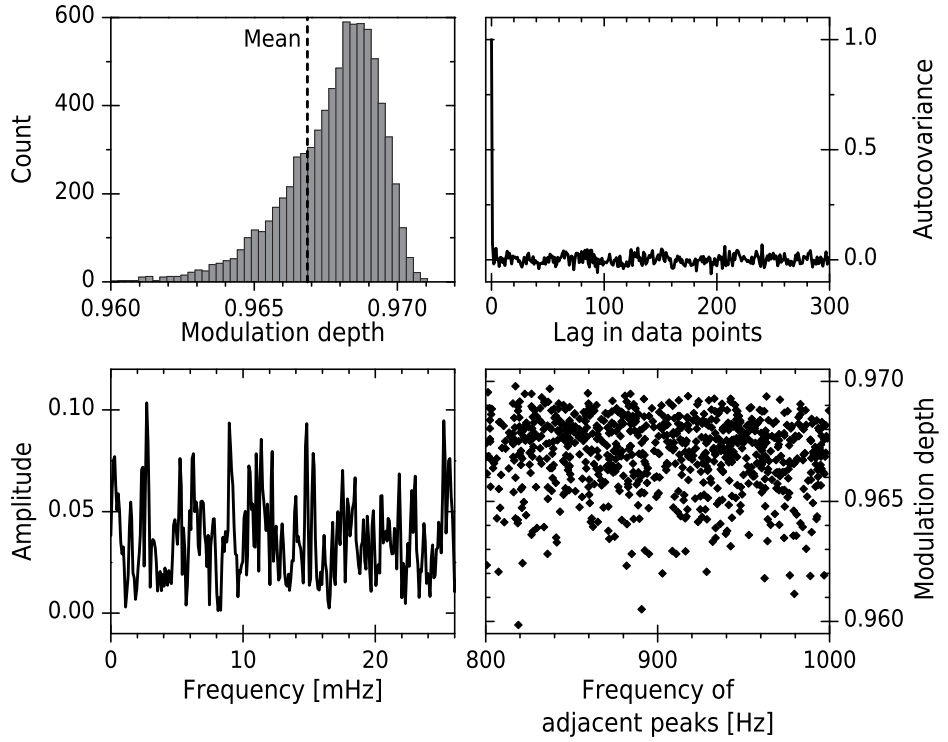

Figure 4.32 Noise analysis of data in Fig. 4.31 from 5.82 h to 8.73 h. The top left graph is the histogram of the modulation values. The top right one shows values of the autocovariance function. The bottom left figure is the amplitude spectrum. The bottom right graph is the modulation depth as a function of the frequency of those adjacent peaks, which were used to calculate the modulation depth.

Some higher vibration mode might have been excited. However, it could most likely produce periodical error and not random as observed. Instead, the friction in the mechanical contact of the driving force could result small and random tilting of M1. This was shortly tested by driving the mirror at some position with a constant voltage applied to the voice-coil. When the arm was slightly detached from the voice-coil tip and then carefully put back, the modulation depth had slightly changed. Therefore, the friction in the contact point was most probably affected to the tilting and thus to the modulation depth. Another random variation could be the fluctuations of the air in the interferometer, which produces phase errors to the wave fronts and thus affects the modulation depth.

The another major error type in the modulation time series was the slow swaying after the temperature changes. The DC level of the laser signal sways in phase with the modulation depth as demonstrated in Fig. 4.34, on page 102, where the modulation depth during the first stepwise heating (Fig. 4.28) and the corresponding DC value are plotted. Because the modu-

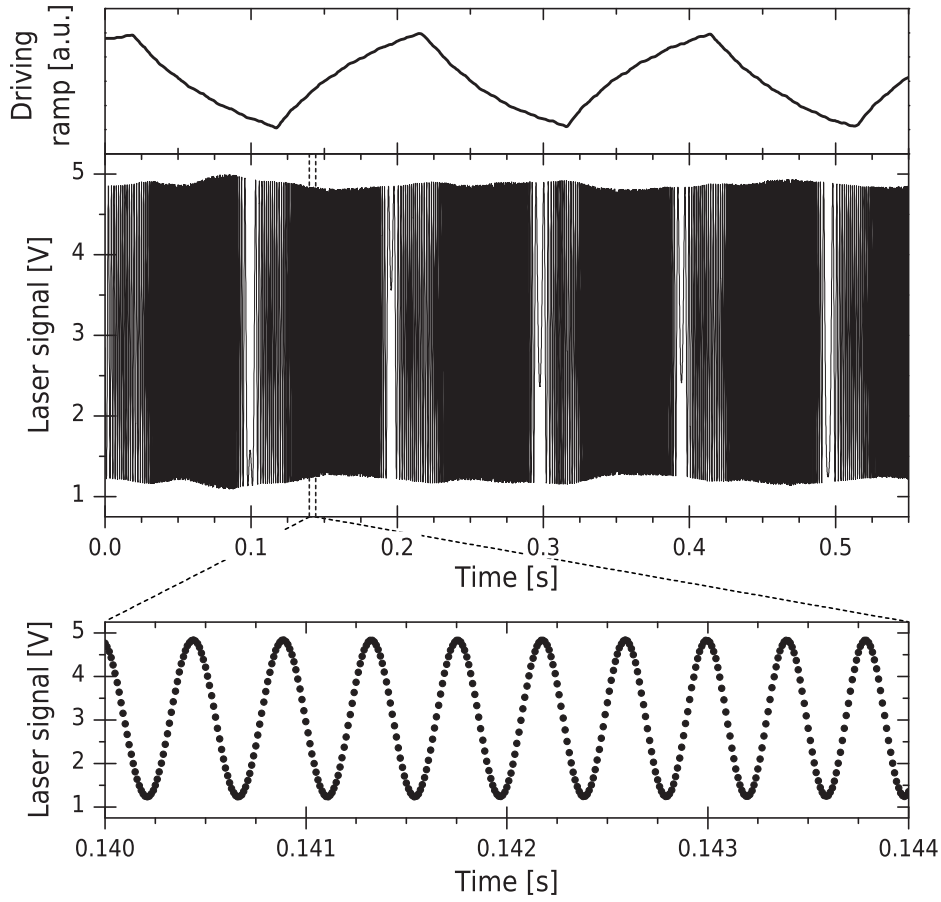

Figure 4.33 Example of the driving ramp and the laser signal with Swing I. The sampling rate of 100 kHz was clearly sufficient. The laser signal amplitude is constantly fluctuating.

lation is the ratio of the amplitude to the DC level, this explains the swaying. The DC response of the detector might have depended on the temperature. Furthermore, the scattered radiation, visible or infrared, could also produce fluctuation of the DC level. In one experiment, the heater switching frequency was observed. The thermostat controlled the heating by switching the heater, which produced small periodical temperature variations, as illustrated in Fig. 4.35. It is also possible that temperature gradients in the interferometer fluctuated and thus caused tilting but they were probably weak. One source may be two flat mirrors guiding the beam from the laser to the interferometer. They were mounted on relatively long vertical bar, which may have bent during the measurements and shift the beam slightly off from the detector.

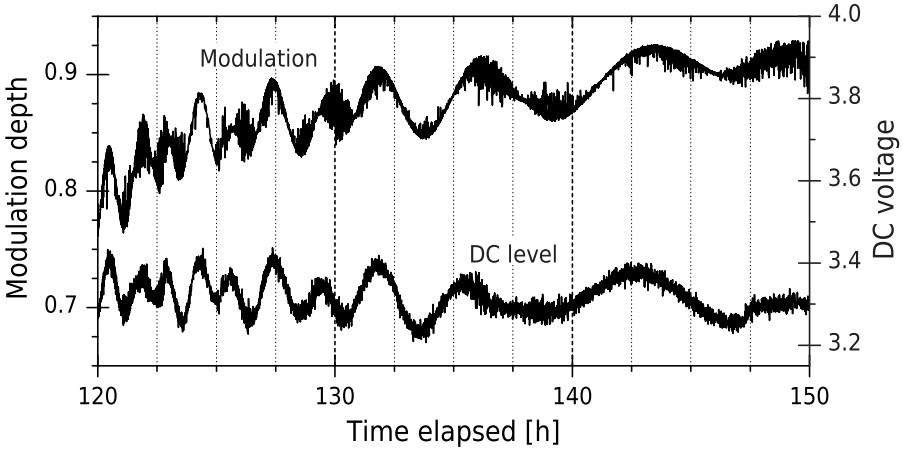

Figure 4.34 The modulation depth and the DC level of corresponding laser signal. The DC level of the laser signal affects to the modulation depth because it is defined as a ratio of the amplitude to the DC level.

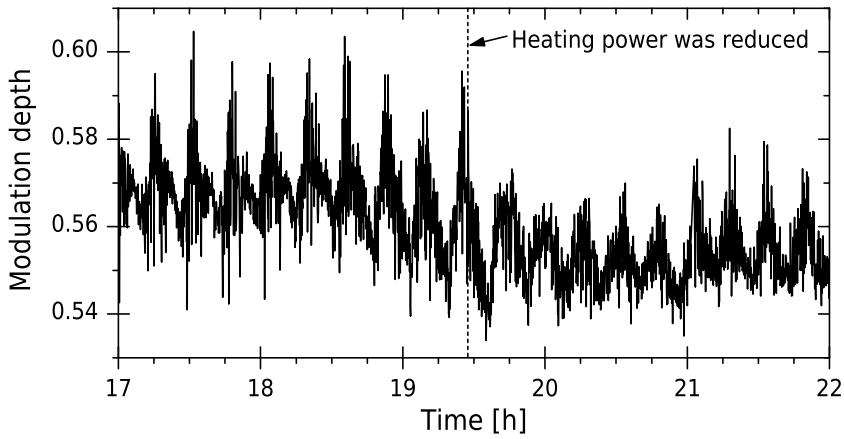

Figure 4.35 The periodical component of the modulation depth time series caused by the weather chamber thermostat. The heating power was lowered from 410 W to 180 W, which changed the amplitude. The period was about 15 min.

4.4.4 Summary of the results with Swing I

The movable arm and the body of Swing I were machined from a single aluminum block to reduce the thermal expansion between separate components. The aluminum was selected because it is easily machined, has good thermal conductivity and rather low density. The size was reduced by placing much of the optics inside the porch swing structure. Swing I provided sufficiently linear mirror travel length up to ±3 mm, thus enabling even about 1 cm^{-1} resolution, although the sufficient resolution could be achieved with 2 mm travel. The mirror tilted about 8 μrad over 1 mm mirror travel. If the uniform infrared beam is used, the modulation decrease is approximately 0.02 units at 3000 cm^{-1}.

The main result was the very good temperature stability of Swing I, which was achieved after extensive testing of different properties of the interferometer. As a summary, the most important observation was that mounting studs aligning the mirror M1 should be directly on the arm rather than on the holder. Then, the mounting would be much more stable because the mirror alignment becomes immune to small holder deformations. The mounting was corrected by using aluminum screws but, in future, the studs should placed to the arm. Another improvement was the grooves on presses fixing flexure elements. Grooves made the fixing region more accurate and thus improved the thermal stability. There were also many small details affecting the thermal stability. These details were already listed in Chapter 4.4.1 and thus not repeated here.

The best stability figures were obtained when the surrounding temperature of the Swing I was changed by steps of about 5 °C or 10 °C. The maximum modulation depth decrease was approximately 0.7 percentage units per Celsius at 3000 cm^{-1}. The average change over 30 °C was about 0.07 percentage units per Celsius. These are very good results and also better than commercially available spectrometers. These experiments proved that the mounting principles of the structure and the optics are working properly. The next step was to fix issues of the first version and to reduce the size of it.

4.5 Swing II

4.5.1 The improved version of Swing I

The next interferometer version, named Swing II, was actually an improved version of Swing II and its purpose was to test, how improvements and corrections of the design influence on thermal stability. However, the most important result obtained with Swing II was extremely low misalignment over the mirror travel. Thermal stability objectives were, unfortunately, not reached.

Mechanics design was done in intensive collaboration with Gasera, Ltd. The optical design and related details were made using instructions mainly from the author. Optical layout was similar as earlier and it is illustrated in Fig. 4.18 on page 84. The interferometer was designed for the same beam splitter and compensation plate as Swing I. Major improvements from Swing I were the removal of its faults. Metal parts of the device were aluminum. Swing II is illustrated in Fig. 4.36(a) and its basic dimensions are given in Table 4.E. The interferometer unit of Swing II was slightly smaller than the first model. The whole spectrometer, sketched in Fig. 4.36(b), was also designed, but, as with the first version, it was not built.

Firstly, the mounting of the movable mirror M1 in the upper arm was reversed so that fixed mounting studs were machined on the arm and not the holder as depicted in Fig. 4.37 on page 106. Additionally, the overhang for the mirror was designed to more robust by adding some material for support. The mirror M1, and other interferometer optics, were mounted using the same three point mount principle as earlier. Alignment screws of the mirror M2 were on the mirror back side and made from aluminum. Their threads were lubricated with thin heat-resistant oil to avoid stuck. The holder for the beam splitter and compensation plate was lightened but the mounting principle was kept similar. The holder PR-M3 of the mirror M3 was redesigned to be slightly off the slanted overhang for the beam splitter, so the bending of the beam splitter mount by thermal expansion was avoided.

Flat springs of the bearing were slightly smaller than in the first version. They had holes for alignment pins, which remarkably helped the assembly because stiffener clamps and the whole flexure elements were able to easily position accurately. Holders of springs had grooves to fix the springs precisely on the small region. The spring material was spring steel. Stiffener clamps were aluminum.

The arm and the body were lightened from the first version. Additionally, they masses were made almost equal to reduce the settling time after the temperature change. The interferometer was mounted on the bottom plate of the casing at three points with raising bushes. The sealing of the system casing was improved because the beam splitter for infrared was to be KBr, which has tendency to fog by air moisture.

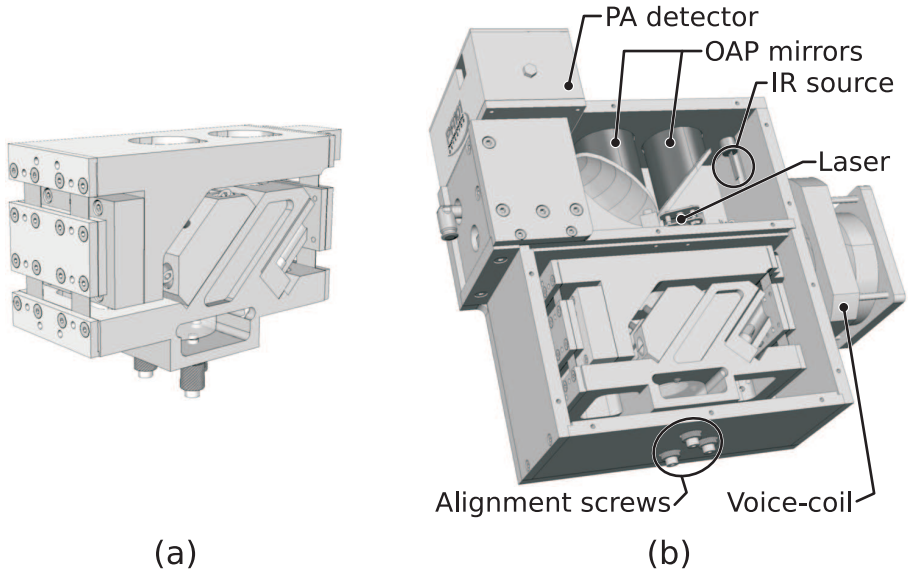

Figure 4.36 Schematic drawings of the 3D model of Swing II. The left one illustrates the interferometer inside to the porch swing bearing. The interferometer was designed as a part of the photoacoustic infrared spectrometer, as in the right figure, but it was not tested in this configuration. Openings of the body part were for lightening the mass.

Table 4.E Dimensions of the Swing II.

	Symbol	Value	Unit
Arm length	l	133.5	mm
Flexure length	h	50.0	mm
Swing width	w	46.5	mm
Number of springs		4	
Spring thickness	t	0.20	mm
Spring width		12.5	mm
Space between springs		21.5	mm
Stiffening clamp length 1		30.0	mm
Stiffening clamp length 2		44.0	mm
Beam diameter, IR		25.0	mm
Beam diameter, laser		≤ 6	mm

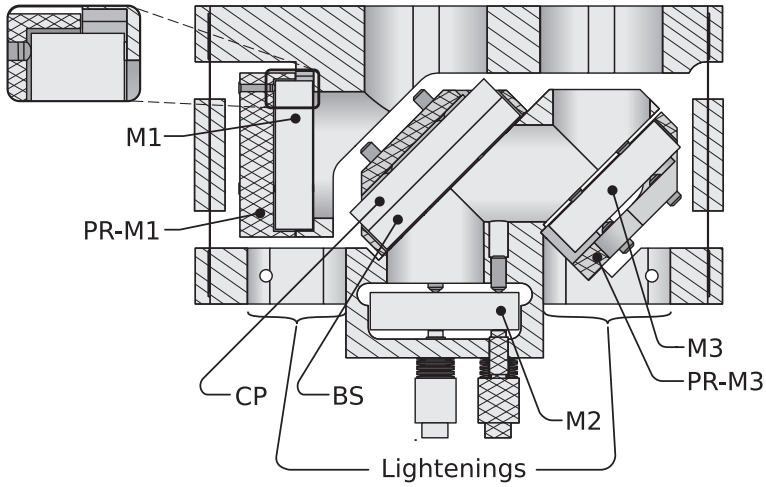

Figure 4.37 Section of Swing II. Some minor details are not drawn for clarity. The optical layout is similar to Swing I presented in Fig. 4.18 (p. 84). The mounting of the mirror M1 was reversed in comparison with Swing I. The mirror M2 could be aligned with three fine threaded screws positioned as in Fig. 4.14(b) (p. 78). The small air gap between BS and CP is not distinctive here. The body part was lightened using extra openings.

4.5.2 No tilting over mirror travel

Tilting of unmodified Swing II

After the machining of parts for Swing II, the interferometer was assembled with visible band beam splitter. The alignment stability over mirror travel was studied using the fringe pattern of the collimated Helium-Neon laser beam. After 2 mm mirror travel, the fringe pattern had about extra two or three fringes, which corresponds the tilt angle between about 20 μrad and 30 μrad. Because fringes were increased in both horizontal and vertical direction, so there was both yaw and pitch rotation of the mirror. Using a slide caliber, the length difference between the movable arm and the body was measured to about $(0.05 \ldots 0.10)$ mm. Additionally, the the arm ends were not parallel because the sides A and B of the movable arm, as in Fig. 4.38, were about 0.05 mm different in length. According to Eq. (3.5) and Eq. (3.6) on page 47, the observed pitch could result from 0.13 mm arm length difference, which is consistent with the measurements. Therefore, the interferometer driving stability was poor.

Tuning the arm length

Errors in arm lengths were corrected by fine tuning arm lengths by adding thin spacers between the flat spring and the arm. This effectively lengthens the arm under the flat spring. Spacers were pieces of flat springs or aluminum foil, whose thicknesses were from 0.01 mm to 0.20 mm. The tuning

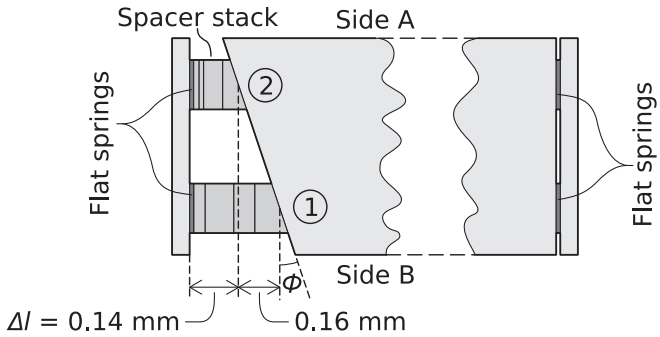

Figure 4.38 Schematic drawing about tuning the movable arm length of Swing II with stacks of thin spacers. Dimensional errors and spacer thicknesses are exaggerated. Mounting screws of spring holders are not drawn for clarity.

is described also in the article by Välikylä and Kauppinen, see Chapter 5 or [68].

At first, the yaw rotation of arm was removed by adding spacers under the flexure end ① in Fig. 4.38. This effectively lengthened the side B of the arm and thus changed the angle ϕ between the non-parallel arm ends. Spacer thickness of about 0.16 mm eliminated the yaw over 2 mm travel measured using the fringe pattern of the 20 mm laser beam. Flexures were then probably very close to parallel so the angle $\phi \approx 0$. Measured pitch and yaw tilt angles among the calculated yaw angles from Eq. (3.9), both at the mirror travel 2 mm, are presented in Fig. 4.39, where the angle $\phi = 0$ corresponds to equal lengths of sides A and B. The pitch did not seem to fully independent of the angle ϕ, although the opposite could be expected. It is probably due to some uncertainty in the measurement. For example, only the upper arm end ① were adjusted, so some errors might have remained in the lower arm dimensions.

The pitch tilt was removed by adding more spacers under both springs ① and ②, while keeping the difference of thickness between two spacer stacks at about 0.16 mm to keep the yaw nearly zero. Pitch and the yaw rotations were almost completely eliminated, when thicknesses of spacer stacks were about 0.14 mm and 0.30 mm as presented in Fig. 4.38. This corresponds to the arm length difference $\Delta l = 0.14$ mm. The pitch rotation was also calculated using Eq. (3.6), on page 47. Measured and calculated values at the mirror travel 2 mm are plotted to Fig. 4.40. Measured length differences, or stack thicknesses, are related to the zero pitch.

In addition to the tilt elimination, we can compare the pitch tilt values to the estimated pitch values from Eq. (3.5) and Eq. (3.6). According to Fig. 4.40, the measured and calculated pitch rotation follows each other quite closely. The slight difference is probably a result from measurement errors, such as some yaw tilt presented almost every measurement point. As a whole, the results of the tuning experiment are in agreement with approximations of the pitch tilting.

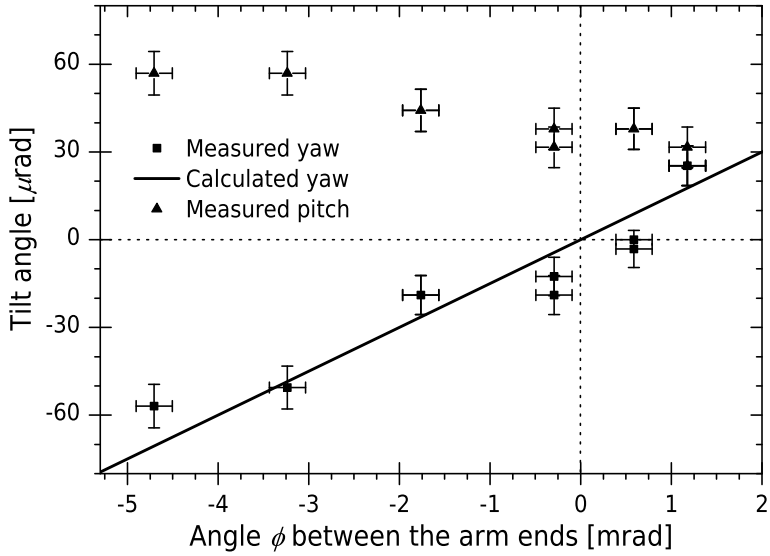

Figure 4.39 Measured pitch and yaw tilt angle and the calculated yaw angle using Eq. (3.9) as a function of the angle ϕ between arm ends or the angle of non-parallelism of inertia axes of flexures. The tilting is determined at mirror travel 2 mm. Error bars represent the maximum measurement errors. Figure is reproduced from [68].

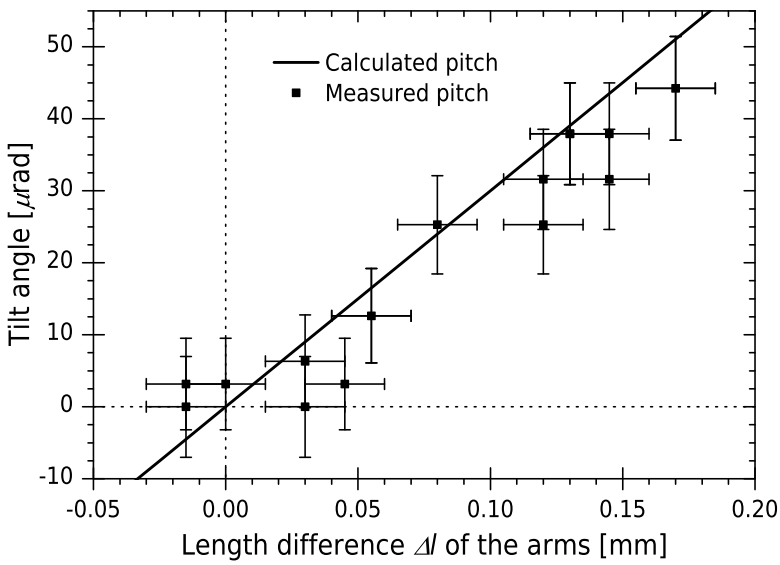

Figure 4.40 Measured and calculated values of the pitch tilt as a function of the length difference Δl between the arms. The pitch was caused by the length difference of arms. The tilting is determined at mirror travel 2 mm. Error bars represent the maximum measurement errors. Figure is reproduced from [68].

Results of tilting over mirror travel

Despite the above tuning, there was still some tilting left. After 2 mm mirror travel, the tilt angle was about 13 μrad, which causes the modulation depth 0.989 at 3000 cm^{-1} using 25 mm uniform beam. So, this is a quite good result. Anyway, there was some possibilities to decrease the tilting even more. Firstly, the 30 mm stiffening clamps were replaced by the 44 mm clamps. Thus, the flexible parts of the springs shortened from 10 mm to 3 mm, which should improve stability. Then, spacers stacks were tuned again. Final thicknesses of stacks were 0.20 mm at the end ① and 0.06 mm at ②. Thus, the difference between sides A and B was 0.14 mm. Additionally, the holder of the flexure element at the end ① was positioned more accurately. After these modifications, the misalignment during over the mirror travel was extremely low.

Hence, the tilting was very low, it was estimated from the modulation depth of the collimated Helium-Neon laser beam using Min-max method 1 described in Table 4.A and Eq. (2.12). The zero position of the mirror displacement z_0 was the equilibrium position of the flat springs. The movable arm was displaced by a pushing rod with fine threads. In each mirror position, the rod mount was pushed carefully by hand to get a movement of a few fringes to find values for the minimum and maximum voltages. Although this is not the most accurate way to determine the modulation depth hence the noise is on these voltage values, our experience has shown that it gives a very good approximation especially when the signal has low noise as in this case.

The measurement results are presented in Fig. 4.41. In the first two experiments, the initial modulation depth was aligned to about 0.92, which was as close to 1 as possible with optical components already mounted. Over 3.0 mm travel, the modulation depth was decreased not more than about 0.04 units. The result corresponds to about 4 μrad tilt angle when the Gaussian distribution of laser intensity is considered. This tilt is below the 14 μrad limit set in Chapter 2.5.1. It would cause about 0.005 decrease in the modulation at 3000 cm^{-1} with a uniformly distributed beam with diameter 25 mm.

According to Eq. (2.8) the modulation depth is approximately $m \approx 1 - \text{constant} \cdot \alpha^2$, so the modulation depth decreases roughly in the squared tilt angle. Thus, the greater initial tilt should cause more rapid modulation decrease than the zero tilt at the beginning. The modulation was measured also with two initial tilt values and those results are presented in Fig. 4.41. The modulation depth seems to be still nearly constant over 3 mm mirror travel indicating very low tilting because the initial tilt should remarkably increase the sensitivity of the modulation depth to the tilt angle.

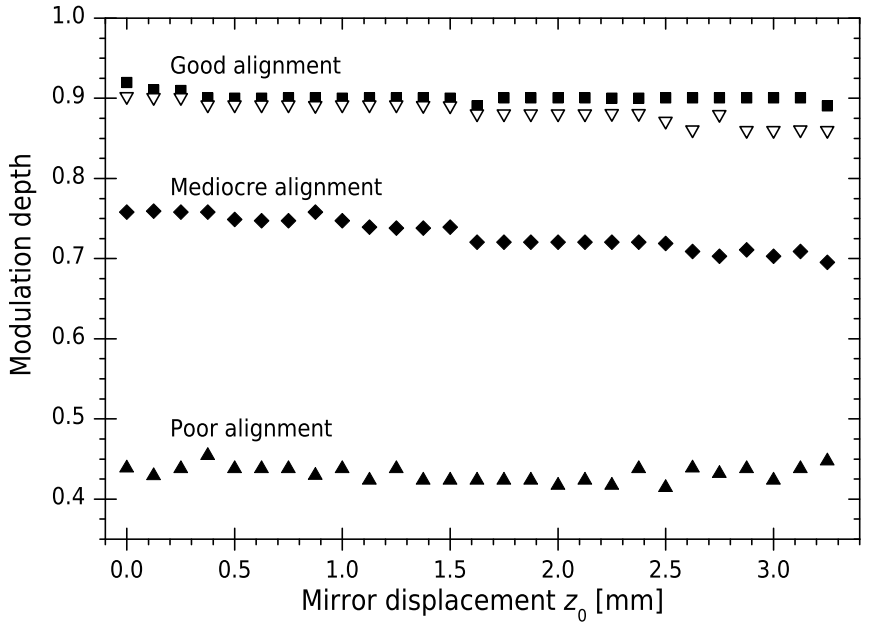

Figure 4.41 The modulation depth of Swing II after fine tuning the arm lengths and using 44 mm stiffening clamps, which resulted about 3 mm long hinges as flexible parts of the springs. Four different initial tilt angles were used. The zero of the displacement was the equilibrium position of the spring elements. The maximum measurement error in the modulation was about 0.01 and in the position about 0.03 mm. Figure is reproduced from [68].

Measurement error in tilt angles

The maximum errors of the measured pitch and yaw tilt angles were estimated using Eq. (4.2) on page 64. The reading error of the number of fringes was about $\Delta k = 0.5$ and the error in the beam diameter $\Delta D \approx 0.5$ mm. The wavelength error was assumed to be negligible. Therefore, the absolute errors of the tilt angle values were typically from 6 μrad to 8 μrad.

The non-ideal position and alignment of the driving force, including the friction in the contact point, produced error less than about 0.5 μrad. The error caused by the length difference of the flexures was estimated to keep below 3 μrad. Other possible error sources were the dirt between the spacers in stacks of them, the small alignment uncertainty of the stiffener clamps and the error when setting the mirror travel to 2 mm.

Literature comparison

Walker and Rex [18] used an interferometer, which had the flexure pivot bearing as in Fig. 2.25(c) on page 40. They reported that the tilting was about 150 μrad right after the assembly. The biggest assembly issue is that the rotating axis of flexure pivots differ quite much from one piece to an-

other. Hence, they designed an adjustment mechanism to one pivot. After careful adjusting, they achieved to decrease the tilt to 5 μrad. Kemp and Huppi [71] used the similar interferometer and reported 5 μrad maximum tilt over 5 mm travel. They did not mention if any adjustments were required but it is very likely that they had adjusted the bearing after manufacturing the components.

The interferometer of Onillon et al [73] used a porch swing, which maintained the tilt below 5 μrad over $\pm$2 mm motion range and apparently had no arm length adjustment system, but it was not designed for FTIR spectrometer but rather for surface scanning. Auguson and Young [98] have reported the tilting of five fringes after 1 cm travel with interferometer based on ball bearing and for far infrared band. With 3.75 inches beam they apparently used, the tilt was about 17 μrad, which would have been too much for mid infrared. The interferometer of the spectrometer in REFIR project had a double pivot bearing [85] based on the similar flexure pivot as the type in Fig. 2.25(c) on page 40. The tilting values were $\pm$400 μrad in the yaw and $\pm$200 μrad in the pitch rotations during the travel of $\pm$6 mm. The spectrometer was intended to far infrared, so these quite high tilt values were accepted.

Several authors have demonstrated the tilting of the porch swing bearing itself. Jones [62] has reported the tilt of 34 μrad with a porch swing made with spring strips and asymmetrically mounted stiffening clamps. He used the clamps to reduce the tilting. The position of the clamps had to be determined by trial and error method, which is not possible in production environment. Hatheway [84] used monolithic flexures, where the flexure element and the clamps pressing it to the arm were machined in one piece. These elements provide much easier and accurate assembly than the flexure elements made of a punch of small pieces. The lowest mentioned tilt values were pitch of 5 μrad and yaw of 39 μrad. However, he has noted that these values may not always be repeatable because reassembling the bearing increased the tilt significantly. It seems that, both, Jones and Hatheway, did not use the arm length adjustments. Muranaka et al [82] have built a porch swing with adjustable arm lengths and have achieved the tilt angle less than about 0.5 μrad with the maximum stroke of $\pm$3 mm. However, their device is more suitable for studying the parasitic motions than a bearing in an interferometer.

Sizes of all interferometers and demonstration bearings discussed in this section were comparable to the porch swings used in Swing I to III. Thus, tilting values can be compared to each other. Swing II tilted finally about 4 μrad. As the author knows, the minimum reported tilt is about 5 μrad, thus Swing II seems to be in the same level as the earlier porch swing models.

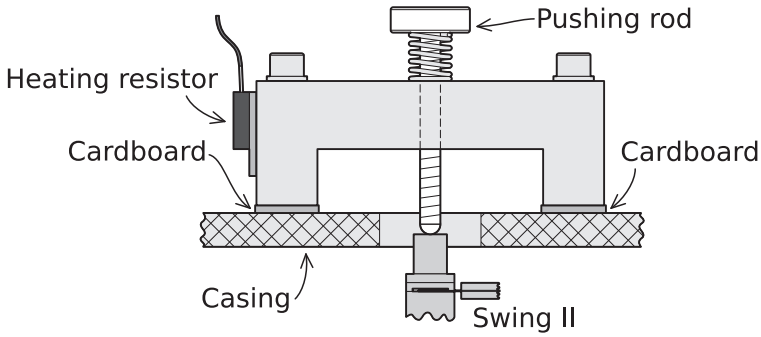

Figure 4.42 Heated rod driving used in Swing II to measure the modulation depth. When the pushing rod mount was heated, the expansion of the rod pushed the arm by a small amount. The modulation depth was easy to determine because the laser signal varied slowly.

4.5.3 Temperature stability was not acceptable

Mirror driving with heated rod

Modulation depth time series have usually had quite a strong noise and fluctuations as discussed in Chapter starting from page 99 and illustrated for example in Fig. 4.28. Many of these errors are related to the driving, especially the varying mirror velocity and the friction in the contact point of the driving force. These could be avoided by driving the mirror slowly and keeping the travel length short. This can be done by using the thermal expansion.

The pushing rod was mounted to the interferometer casing with cardboard plates between them as thermal insulation, as presented in Fig. 4.42. The rod mount was heated by the heating resistor. Thermal expansion of the mount and the rod moved the arm slowly about few micrometers travel corresponding several complete wavelengths of Helium-Neon laser. Because the driving was slow, the short period of the laser signal was nearly constant. Therefore, a laser signal block, with duration of 0.66 s, was sampled and the mean of it was calculated to reduce the noise. The time series of these blocks formed a sinusoid, whose single complete cycle corresponds the optical path difference of one wavelength. The modulation depth could be determined using two successive maximum and minimum and Eq. (2.12), as illustrated in Fig. 4.43. The heated rod method provided less noisy modulation depth values than obtained using other driving methods using a laser beam. However, the measurement could not be continuous because the rod had to cool between single recordings. The cooling was quite slow, so the measuring would be tedious during the cooling.

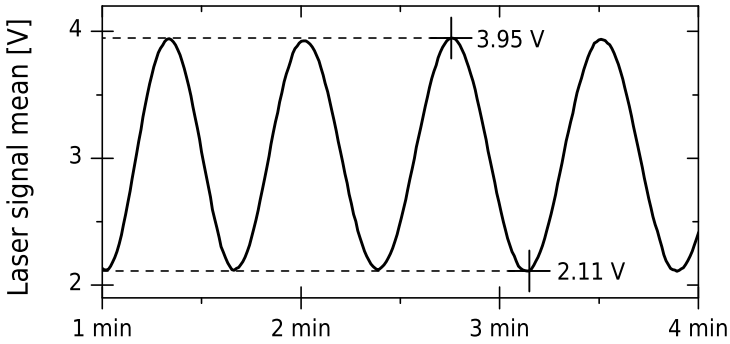

Figure 4.43 The data for determining the modulation depth when the heatable rod driving was used with Swing II. The modulation depth was 0.30 according to the marked values.

Heating experiments

Swing II was also tested on the weather chamber presented in Fig. 4.25 as the previous models. Temperature in the chamber was controlled by a electric heater and thermostat. In the most of the heatings the temperature was risen slowly to avoid the snaps caused by the release of the tensions produced by thermal expansion. In the first measurements, the voice coil driving was used but later the heated rod was preferred. The modulation depth was determined using Helium-Neon laser beam at equilibrium conditions when the interferometer had nearly uniform temperature. Table 4.F summarizes the results from the most substantial experiments. The tilt angles values were estimated from the measured modulation values by taking account the Gaussian intensity distribution of the laser beam by using Eq. (4.7). The beam diameter was 25 mm and the standard deviation of the distribution was 3.0 mm. The modulation depth values in infrared at 3000 cm^{-1} were approximated from the tilt angles.

Results from the experiments 1 and 2 were promising as Fig. 4.44, on page 115, presents. The modulation depth at 3000 cm^{-1} was dropped to 0.98 after 32 °C raise. The average modulation decrease in infrared was about 0.23 percentage units per Celsius, which was more than with Swing I but these were yet the first experiments. The modulation was almost reversible in the measurement 1 and fully reversible in the measurement 2. Unfortunately, the later heatings produced more discouraging results.

Because the modulation depth was irreversible in the next few experiments, the interferometer was tested on the constant temperature. The modulation drifted clearly even in the constant temperature in the experiments 5 and 9 so it was not very stable. The origin of misalignment was expected to be the disc spring stacks under the adjustment screws of the mirror M2. Therefore, the bottom and the top surfaces of the disc springs were smoothed to flat and the cylindrical bushings were mounted around

Table 4.F Summary of results from selected heating experiments of Swing II. Temperature values represent the equilibrium conditions. Modulation HeNe values are measured values. Tilt angles and modulation in infrared at 3000 cm^{-1} were estimated numerically.

#	Temperature [°C]	Modulation HeNe	Tilt angle [μrad]	Modulation infrared	Test description and result
1	22	0.94	6	0.99	1st heating: Irreversible
	54	0.59	17	0.92	
	23	0.77	12	0.96	
2	23	0.92	7	0.99	2nd heating: Reversible
	53	0.58	18	0.92	
	23	0.92	7	0.99	
5	23	0.61	17	0.92	2 days at 33 °C: Drifted
	33	0.61	17	0.92	
	33	0.50	20	0.90	
9	23	0.93	6	0.99	3 days at 23 °C: Drifted
	23	0.87	9	0.98	
10	23	0.95	5	0.99	5.5 h: Stable
11	23	0.94	6	0.99	Slow heating and rapid cooling: Irreversible
	58	0.05	41	0.60	
	22	0.71	14	0.95	
12	23	0.94	6	0.99	Slow heating and cooling, repeated twice: Irreversible in both
	58	0.10	36	0.68	
	23	0.42	22	0.87	
	58	0.21	30	0.77	
	24	0.30	26	0.82	

them to keep the stack still. After that, the modulation stayed very stable for about 5.5 hours in the measurement 10 and so, despite this quite a short time, the heating tests were started again. In the experiment 11, the heated rod driving was used for the first time. The heating was slow and cooling fast. The permanent misalignment has been occurred because the modulation was not restored. The interferometer was realigned and then heated and cooled slowly but the interferometer was again irreversible. Because the snaps are occurred often in the first heating after some modification, the heating was repeated directly after the last cooling without touching the interferometer. However, the initial state was not reached after the heating cycle. Because the designing and manufacturing of the next interferometer version was ongoing, the heating experiments were discontinued.

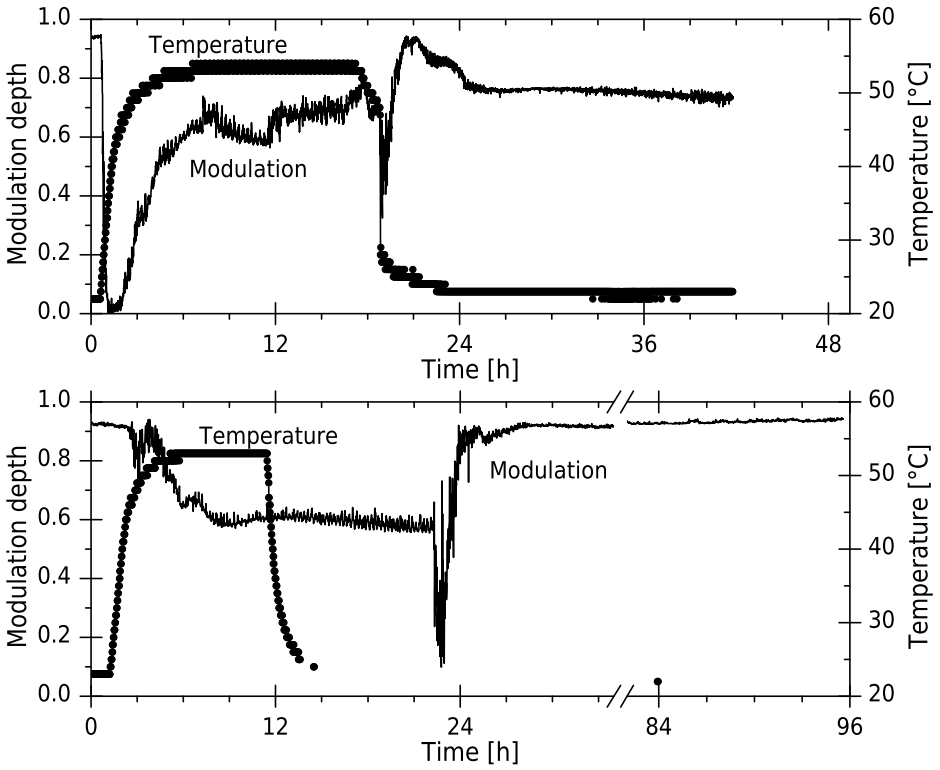

Figure 4.44 The first two heating experiments using Swing II. After the first test (the upper graph), Swing II was not returned to initial modulation, so a snap has happened. The bottom graph is from the second, and only heating, where the modulation was restored.

4.5.4 Major results of Swing II

As a summary, the thermal stability of Swing II was not acceptable. Its alignment restored to the initial state only in one heating experiment, where the modulation decrease was, however, about 0.23 percentage units per Celsius, which was quite near the best results with Swing I. Unfortunately, the alignment was irreversible in the all following experiments. Nevertheless, the alignment stability during the driving over the maximum mirror travel length was very good: the tilting kept below 4 μrad, which is very low value. Furthermore, the studies of the alignment stability during the driving, supported the models of the parasitic motions presented in Chapter 3.

4.6 Swing III

4.6.1 Redesigned interferometer using infrared optics

The major aim of the third version of the interferometer, or Swing III, was to finally design it for FTIR spectrometer. This included infrared optics, a source for infrared radiation, a reference laser, a compact driving motor, supporting electronics and a casing. Mechanics and electronics were designed in Gasera, Ltd. in collaboration with the author. Despite of the punch of new components, the size of the device was achieved to kept moderate. The interferometer itself was even smaller than previous models, as can be seen from Table 4.G. The outer dimension of the whole interferometer were $(197 \times 95 \times 79)$ mm^3 without the infrared detector.

Biggest changes in optics were the new placement of the infrared source and the new beam splitter. The source and the off-axis parabolic mirror were placed inside the porch swing bearing as presented in the optical layout in Fig. 4.45. This saves space but the disadvantage is the excess heat, which is warming the interferometer. The off-axis parabolic mirror was OAP10 from Optiforms, Inc and had gold coating. The round beam splitter was replaced by the rectangular one, which made possible to narrow the interferometer body. The material of the beam splitter and compensating plates were ZnSe because it provides sufficient transmission range, does not fog and is mechanically easier than often used KBr. To reduce costs, the surface flatness was only $\lambda/4$ hence it is barely acceptable in middle infrared. Beam splitter and compensating plates were manufactured by Tydex J.S.Co. The transmittance $T = 1 - R$ calculated from the measured reflectance R provided by Tydex is plotted in Fig. 4.46. The beam splitter had also coating for visible region on one side.

Plane mirrors M1 and M2 were made from BK7 substrate and coated with aluminum. The mirror flatness was $\lambda/10$ grade. The mirror M2 background had also $\lambda/10$ flatness because its alignment was determined by the back surface. Around plane mirrors, there was supports with elastic presses

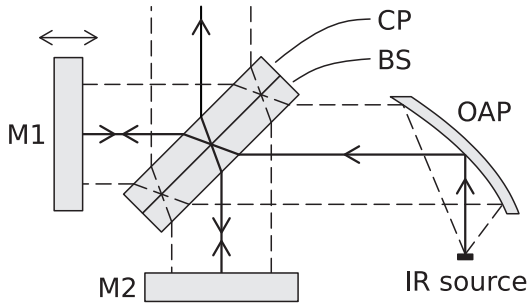

Figure 4.45 Optical layout of infrared beam in Swing III. Off-axis parabolic mirror OAP collimates the infrared radiation to the interferometer assembled from two plane mirrors M1 and M2 and the beam splitter BS and the compensator CP.

Table 4.G Dimensions of the Swing III.

	Symbol	Value	Unit
Arm length	l	110.10	mm
Flexure length	h	53.0	mm
Swing width	w	65.0	mm
Number of springs		4	
Spring thickness	t	0.20	mm
Spring width		10.0	mm
Space between springs		45.0	mm
Stiffening clamp length		51.0	mm
Beam diameter, IR		25	mm
Beam diameter, laser		3	mm

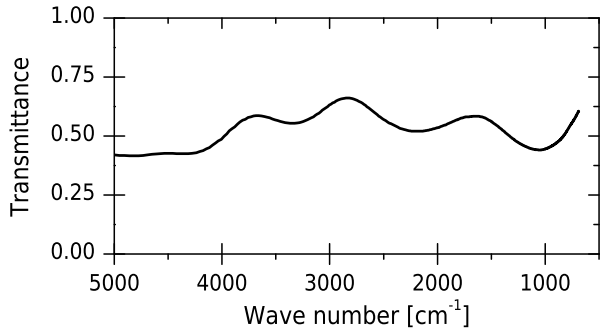

Figure 4.46 Beam splitter transmittance at 45° angle of the light incidence.

to prevent sideward movements of the mirrors. However, they were not used in most of the measurements because they were suspected to cause misalignments.

The mechanical structure and bearing were very similar to Swing II as Fig. 4.47 and Fig. 4.48 illustrate. However, arms were about 15 mm shorter. Flat springs were more apart from each other but the interferometer was totally narrower than earlier models because of the rectangular beam splitter. Pivots were 1 mm long or half of the pivot length in Swing II. The optics was mounted using the same three point principle used in all earlier versions and described in Fig. 4.14(b) on page 78). The mirror M2 could be aligned using three orthogonally placed fine threaded aluminum screws, which were anodized to avoid thread stuck and to eliminate the need for any lubricants. Flexure elements of the porch swing bearing were locked in their positions by leaving locating pins on their holes. This prevented the misalignment produced by the arm creeping over time.

The driving motor was Actuator 2. It was the linear voice-coil actuator LA12-17-000A from Bei Kimco Magnetics. It was driven with electronics de-

signed by Gasera, Ltd. Actuator 2 was mounted outside the interferometer because the smaller actuator was originally designed but later observed to be insufficient when damping the external vibrations. The smaller voice-coil LA-10-08-000A, or Actuator 1, was instead used as a damper. Its damping performance was improved by replacing the coil part by solid copper cylinder to maximize the eddy currents and thus the damping force.

The infrared source was Norton Igniter Model 301 (at present manufactured by Coorstek Inc.) illustrated in Fig. 4.49. The component is actually made for igniting flammable gases but it is suitable for infrared source also. The emitting area of the source is rectangular with dimensions about 4 mm $\times$ 2 mm. The source was not sealed so it was in contact with air. Additionally, no reflector was placed around the source so its efficiency was not very good and the excess heating was quite strong. The low efficiency also raised the power consumption of the source.

The solid-state laser was selected as the reference because traditional gas lasers were too bulky. The reference laser was a single-mode vertical-cavity surface-emitting laser (VCSEL) manufactured by Interspectrum OÜ. The wavelength was specified as 655 nm and the output power 0.8 mW. The laser component had its own stabilisation electronics to enable single-mode operation and built-in collimating optics. Its coherence length was sufficient because significant modulation decrease was not observed over 3 mm optical path difference. The laser beam ran besides the infrared beam, which was thus not cut by the laser beam. However, the laser detector board cut the infrared beam slightly on one edge. The detector was sealed to reduce the signal from the scattered light from the surroundings. The laser signal was over-sampled as illustrated in Fig. 4.33 on page 101. Zero-crossings of the signal were interpolated and then the interferogram was interpolated using those zero-crossing values as described in Chapter 2.3.5.

Supporting electronics consisted not only the already mentioned laser detector board and the amplifier for the actuator but also the main control board. It powered all the other electronics, created the output voltage ramp for Actuator 2 and processed the laser signal. The algorithms for processing the infrared detector signals were not completely ready when the measurements and tests were made for this work, so the interferometer was computer controlled with Labview software.

Voltage signals from the laser and infrared detectors were over-sampled. The optical path difference values were determined by the interpolating the zero-crossings of the sinusoidal laser signal as described in Chapter 2.3.5. The actual interferogram points were linearly interpolated from the over-sampled interferogram according to the optical path difference values. The interferogram could be apodised and zero-padded if desired. The spectra were power spectra calculated as in Eq. (2.24) using FFT. The number of spectra could be averaged to enhance the signal to noise ratio.

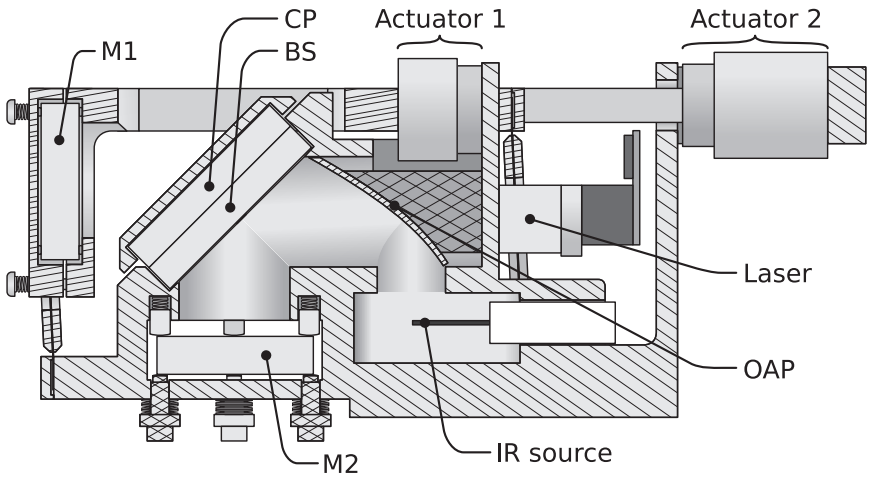

Figure 4.47 Schematic section of Swing III. Some minor details and screws are not shown for clarity. The movable arm is moved to near its maximum displacement. Actuator 1 acted as a damper and Actuator 2 as the driving motor. Each mirror holder was pressed against three studs using three screws. Mirror M2 could be aligned with three fine threaded screws positioned as in Fig. 4.14(b) (p. 78).

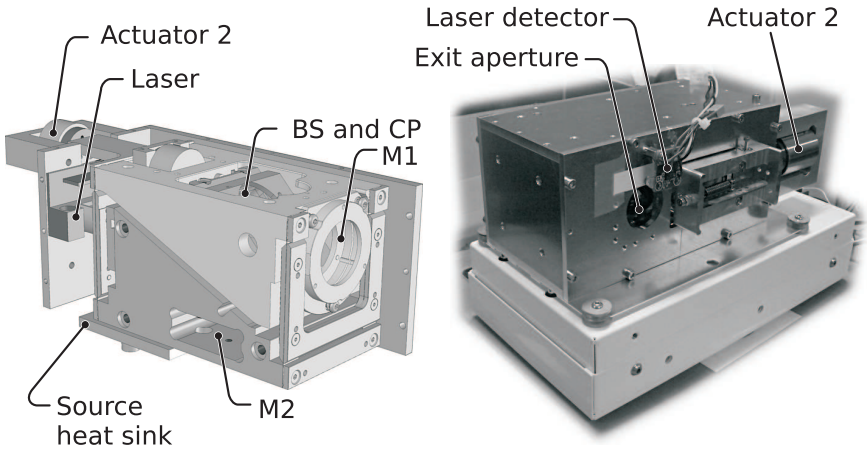

Figure 4.48 Swing III interferometer with main components marked. The left one is from the computer model. The right one is the photograph of the assembled interferometer with the casing.

Figure 4.49 Infrared source Model 301 Ceramic Igniter for Swing III manufactured by Coorstek, Inc. The size of the emitting area is about 4 mm × 2 mm.

4.6.2 Tilting over mirror travel

Again, the experiments were begun by studying the misalignment during the mirror travel. The interferometer was assembled directly from machined components and no modifications were done to them. The tilt angle was estimated using the modulation depth of the collimated 20 mm Helium-Neon laser beam. The mirror was displaced by pushing the arm in steps by the pushing rod with fine threads. At each mirror position, the pushing rod was pushed carefully by hand to get a small change in the optical path difference. The modulation depth was then determined by Minmax-method 1 described in Table 4.A on page 67, or the global minimum and maximum of the short block of the signal from photodiode. The modulation depth results from seven measurements are presented in Fig. 4.50. The small variations between these measurements were caused by slight alignment changes of the pushing rod and the friction in its contact point on the arm end. These altered the alignment of the driving force. However, the results are consistent with each other.

The modulation depth decreased about 0.05 units after the travel from zero to about 3 mm [68]. The laser beam was Gaussian distributed, so this corresponds about 5 μrad tilt angle. It causes approximately 0.007 unit decrease in the modulation depth in infrared at 3000 cm^{-1}. After the travel of 3 mm the modulation depth started to decrease more rapidly. Still, at

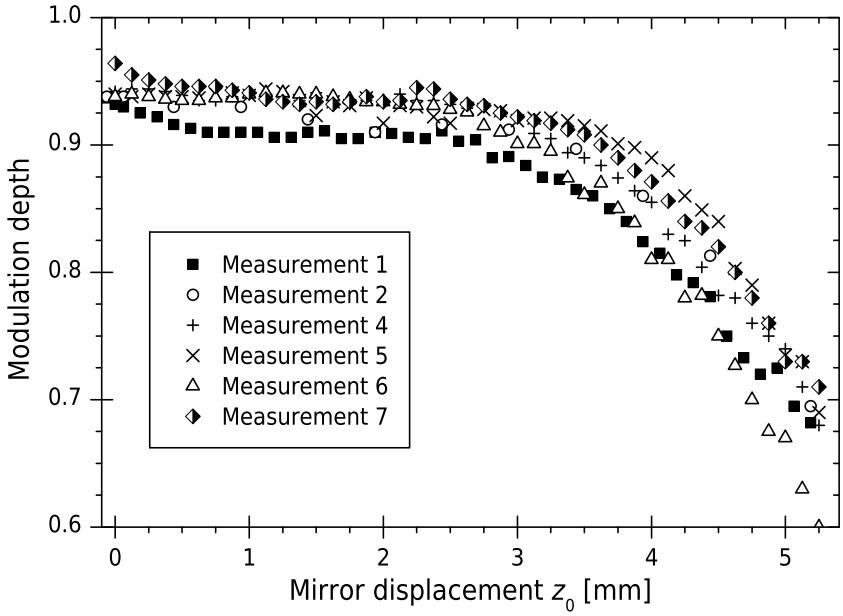

Figure 4.50 Modulation depth of Swing III during the mirror travel. The zero of the displacement z_0 was the equilibrium position of the spring elements. The maximum measurement error in the modulation depth was about 0.01 and in the position about 0.03 mm. Figure is reproduced from [68].

about 5 mm the modulation depth was at least 0.65, so the mirrors were tilted only about 16 μrad. The modulation depth at 3000 cm^{-1} would have been approximately 0.93, which is barely acceptable.

The tilting of Swing III was greater than with Swing II, which achieved tilt of 4 μrad after 3 mm travel (see Chapter 4.5.2 and Fig. 4.41 on page 110). However, Swing II, and actually also Swing I, had to be fine tuned to achieve tilting, which is sufficiently low. The Swing III was clearly machined better because the tilting was readily acceptable without any modifications of tuning of the parts. This shows that by the proper cnc machining and careful assembly, it is possible to manufacture a porch swing bearing, which does not require any adjustment mechanism for length errors.

4.6.3 Thermal stability measured with laser

Removing the permanent misalignments

Temperature stability was studied using the similar weather chamber setup as described earlier in Chapter 4.4.3 on page 90 and Fig. 4.25. The heatings were usually quite slow and the temperature was risen 30 °C during several hours. In the first heating experiments, the modulation depth of Swing III dropped drastically and was not reversible, or some permanent tilt has been remained after a heating and cooling cycle. Actually, the modulation depth was instable even in a constant temperature. The instability was found to result from two major thing, which are described in this chapter. The following two chapters list the properties that were studied but had only minor or negligible effect to the thermal stability.

The biggest problem were the permanent misalignments occurring occasionally after the heating and cooling cycle. Because of the apparent randomness of the misalignments it took some time to find their origin. Eventually, it was realized that the modulation depth decreased continuously even in the constant temperature as presented in Fig. 4.51. In the worst case, the modulation of Helium-Neon laser beam was decreased to 0.84. This corresponds about 10 μrad tilt angle or approximately 0.02 decrease of the modulation at 3000 cm^{-1}. The major source of the misalignment was the creeping of the arm by the gravity. The interferometer was orientated so that the gravity pulled down the arm, or more exactly, the gravity was in the x direction in coordinates defined in Fig. 3.2 on page 43. If the arm was supported against the bottom plate, the modulation stabilised so the creeping had been stopped. The arm alignment was fixed by putting the locating pins on their holes. The pins were originally designed for helping the assembly but they could also be used to keep the pivot structure stable. Is is likely that the instability of Swing II was caused by the corresponding creeping but it was not found until with Swing III. Another major issue causing permanent misalignment were probably the alignment screws of the mirror M2. Furthermore, the interferometer requires aging

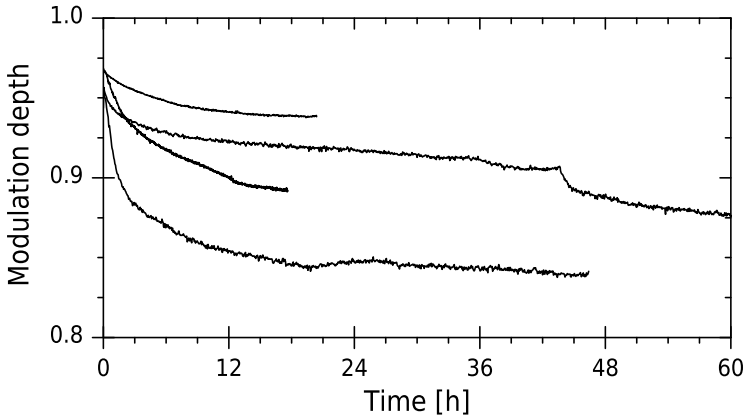

Figure 4.51 Decreasing modulation depth of Swing III at constant temperature before supporting the movable arm. Data is from four separate experiments. The creeping is a result from the slow rotation of the movable arm caused by the sliding of spring element mountings.

after the assembly because the misalignments were usually occurred in the first heating and cooling cycle after the assembly but not anymore in the following cycles. Thus, some stresses had most probably remained in the structure and they were relaxed after the first heating.

Minor stability improvements

In addition to the above, the thermal stability of Swing III was improved by numerous things. Firstly, the mounting of the optics was checked carefully. The smoothness of the mounting studs and correct tightness of the fixing screws of the mirrors were assured. It was checked that the optics was in contact only by the studs and set screws. Additionally, the mirror coatings were removed under the studs. The alignment screws of the mirror M2 were retightened sufficiently because too loose screws tend to move by the thermal expansion. The screws had an anodized aluminum oxide layer on them. The thermal expansion of this layer was estimated to be so small that it hardly causes problems. Furthermore, the body component was fixed to the bottom casing by suitably tightened screws to avoid the bending of the body, which could cause misalignments.

The beam splitter and the compensating plates were separated by three small and thin metal plates. These plates rotated these two components slightly with each other to reduce the interference from their surfaces. The correct assembly of these plates was assured to avoid bending of the beam splitter by the force pressing them against the studs on the interferometer body. The bended beam splitter causes wave front errors and thus reduce the modulation depth.

Other tested things

All above mentioned things improved the thermal stability of Swing III but also many other properties affected only little or negligibly to the stability were tested. Those properties were either in order from the beginning and had nothing to fix or they had only minor effect on stability. These are listed in the following.

The most important "negative" result was that the reassembling the interferometer was not decreasing its stability. Swing III was completely dismantled, carefully cleaned and then reassembled at least once. Partly dismantlings and reassemblies were done numerous times. As a whole, the assembly seemed to be repeatable, which is a very important in industrial production, which is one big aspect in this work.

Flexure elements were H-shaped as illustrated in Fig. 4.48 on page 119. Hence stiffener clamps were steel, they were expected to produce extra tensions and possibly misalignments in thermal expansion but the expectation was not true observed by cutting the middle bar of H. If fixing screws in mirror mounts had correct tightness, poking the mirror holders or the screws with wooden stick or hand caused no misalignments. Additionally, screws aligning the mirror M2 were quite robust so their design seemed to be stable enough. The thermal expansion of the steel screws in the mirror mounts was estimated to have negligible effect on the tilting. Surfaces of the mirror M2 were non-parallel, which was thought to produce tilting. This was tested by reversing the mirror so that it was aligned by the reflective surface, thus the beam had to transmit the mirror substrate before and after the reflection. The reversing had no effect on the thermal stability so aligning M2 on its back surface seemed to sufficiently stable, at least if the background surface has a good flatness. Flexible rubber supports around the mirrors were designed to prevent sideways movements. No effect on thermal stability was observed by the supports although the opposite was expected. Swing III was once heated to about 125 °C because the thermostat of the heater was accidentally disconnected. Although some measurement equipment was damaged, the only harm to Swing III was a moderate misalignment.

Results of temperature experiments

The modulation depth of 25 mm Helium-Neon laser beam in three successive heating and cooling cycles of Swing III is presented in Fig. 4.52. This is one of the best thermal stability results obtained using Swing III. Firstly, the modulation depth, and so the alignment, was reversible in all three cycles. Because the heatings were continuous, comparable modulation depth values are obtained only before and after the heating when the interferometer was in thermal equilibrium. Tilt angle values were estimated from these modulation values by accounting the beam distribution. Modulation values

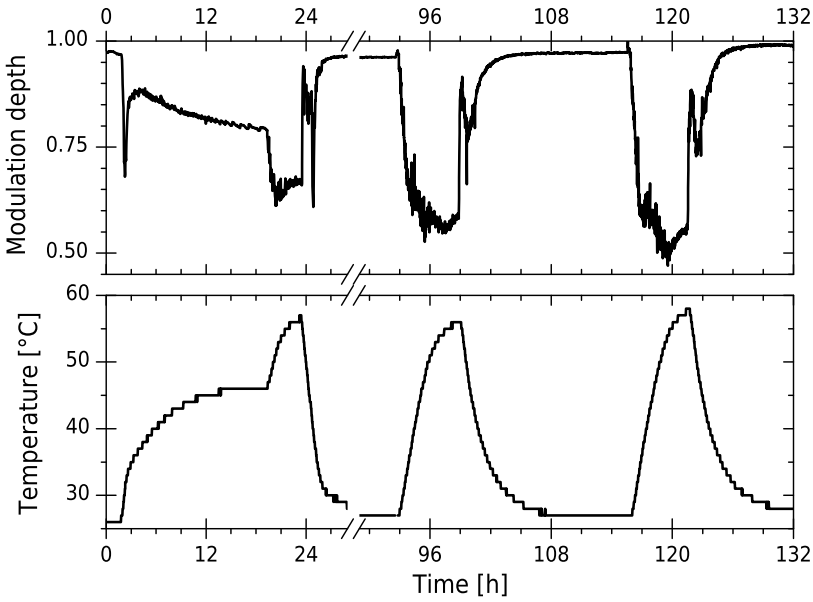

Figure 4.52 Modulation depth of Helium-Neon laser beam at the exit of Swing III in the weather chamber experiment containing three successive heating cycles. Note the axis break from about 30 h to 90 h.

Table 4.H Results of the Helium-Neon laser modulation depth of three successive heating and cooling cycles presented in Fig. 4.52. Tilt angle values are approximated using the model for Gaussian distributed laser beam, whose width was 25 mm. Modulation changing rates are at 3000 cm^{-1} with an uniform beam.

Cycle	Temperature change [°C]	Laser modulation	Total change of tilt angle [μrad]	Infrared modulation per 1 °C
1	30	$0.98 \rightarrow 0.67$	12	0.0020
2	29	$0.96 \rightarrow 0.58$	13	0.0027
3	29	$0.97 \rightarrow 0.55$	14	0.0030

in infrared were estimated from tilt angle values. Results are collected to Table 4.H. The tilt angle was increased in total about 14 μrad during each heating, which is acceptable. Therefore, the average rate of change of the modulation depth at 3000 cm^{-1} was at most 0.003 per Celsius. This is about the same order of magnitude than the maximum decrease rate of Swing I, which was 0.007 per 1 °C (see Chapter 4.4.3 on page 94). However, the mean rate with Swing I during 30 °C temperature rise was below 0.0009 per 1 °C or over three times less. Thus, the thermal stability of Swing III was clearly lower than with Swing I. More thermal stability results with Swing III obtained using the excess heat from the infrared source are presented in Chapter 4.6.5 from page 143.

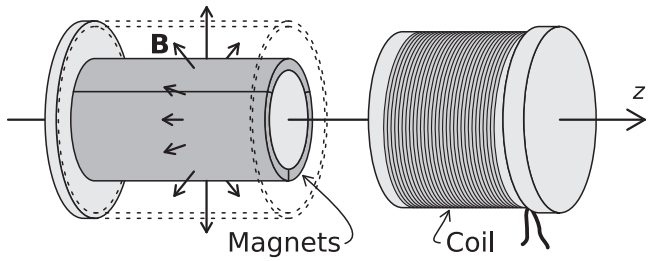

Figure 4.53 Schematic drawing of the voice-coil actuators used for driving Swing III interferometer. The left component had strong permanent magnets producing nearly uniform magnetic field in to the gap under the casing drawn using dashed line. The wired component moves in this field when a current is flowing in the wire.

4.6.4 The mirror driving

Driving with the voice-coil linear actuator

The voice-coil type linear actuators were used to the drive Swing III. The most important advantage of the voice-coils is that the driving force has no mechanical contact but instead is coupled by a magnetic field. This removes problems caused by the friction. The quality actuators can produce very linear motion and have good position accuracy. The actuators manufactured by BEI Kimco Magnetics were used. These actuators consisted of two cylindrical components: the one with the permanent magnet and the one with the coil as depicted in Fig. 4.53. The motion produced by actuators can be quite easily controlled, because the coil position is practically proportional to the coil voltage, which is justified by the simple model of the driving system at first in this chapter. Furthermore, the driving voltage ramps and the linearity of the driving motor are discussed.

The movable arm can be modeled as a simple spring-mass system with damping. Its equation of motion in one dimension is

$$m\frac{\mathrm{d}^2 z}{\mathrm{d}t^2} = -kz - b\frac{\mathrm{d}z}{\mathrm{d}t} + mg\cos\theta + F(t), \tag{4.10}$$

which is a linear non-homogeneous second order differential equation so the system acts such as a harmonic oscillator. In this equation m is the mass of the arm, k is the total force constant of the springs and b is the damping factor, g is the gravity acceleration, θ is the angle between the z axis and the gravity direction. The force $F(t)$ is the driving force produced by the voice-coil. The expression for the driving force is derived in Appendix D and it is

$$F(t) = \frac{k_f}{R}\Big[V(t) - k_b v(t)\Big], \tag{4.11}$$

where k_f is the force-current ratio, $V(t)$ is the voltage across the voice-coil and k_b is the back emf constant. During the mirror travel, its velocity is

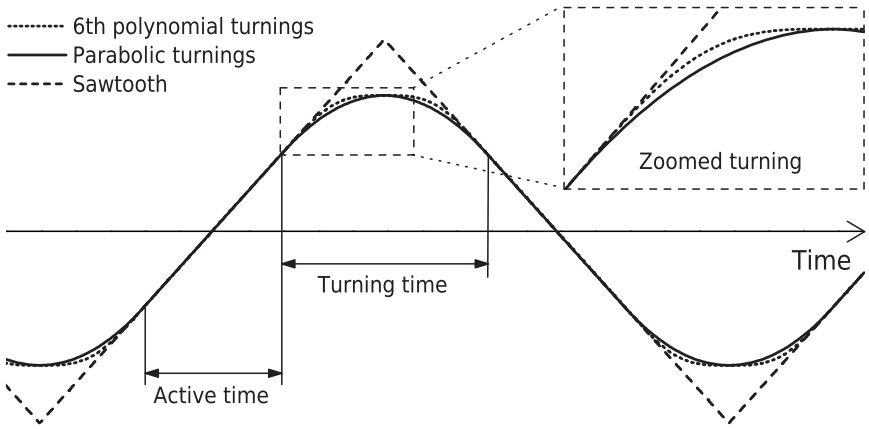

Figure 4.54 Driving voltage ramps tested with Swing III. These ramps have very long turning times to emphasize their differences.

kept constant, or $\mathrm{d}z/\,\mathrm{d}t = v_{\mathrm{mirror}}$. Then the acceleration is $\mathrm{d}^2z/\,\mathrm{d}t^2 = 0$. If Eq. (4.11) if substituted to the equation of motion and the velocity is assumed constant, we obtain after rearranging

$$z(t) = \frac{1}{k}\left[\frac{R}{k_f}V(t) - (b + k_f k_b)\, v_{\mathrm{mirror}} + mg\cos\theta\right]. \tag{4.12}$$

This shows that the arm, or the mirror, position is proportional to the driving voltage when the mirror is moving at constant speed. Therefore, to maintain the constant mirror velocity, the driving voltage should change linearly.

Hence the system is a harmonic oscillator, its step response is a damped sinusoidal oscillation at the natural frequency of the system when the system is in the under-damped condition as Swing III was. These oscillations are typically excited by the external vibration, which are discussed later, or the sudden changes in the arm motion. In other words, the arm tends to vibrate when the direction of its motion is reversed at the end of the every scan. The interferogram data is not valid until these vibrations are died so they should be minimised to not waste the valuable mirror travel length. One way to reduce the oscillations, when the mirror motion is reversed, is tuning the driving voltage. The simplest driving voltage is just a sawtooth pulse as depicted in Fig. 4.54 but its sharp corners excite oscillations. If the corners are replaced by the parabolically changing voltage, the acceleration during the turning is approximately constant and the velocity changes linearly. The voltage derivative was demanded to stay continuous over the ramp and be zero at the rest positions. The accelerating and decelerating parts should be equal. The example of the voltage ramp with parabolic turnings is illustrated in Fig. 4.54. The parabolic smoothing reduced the vibrations after the reversing of the mirror motion. The sixth degree of polynomial was

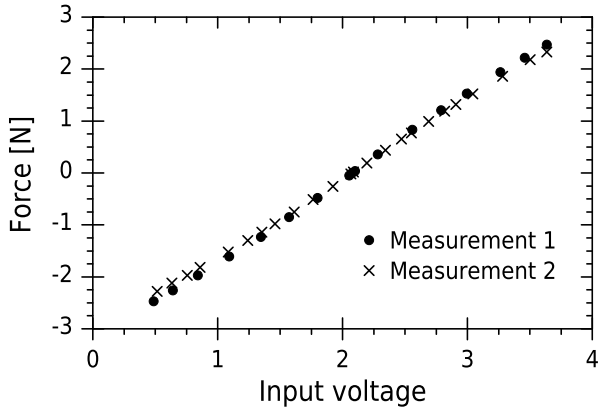

Figure 4.55 The force produced by the small actuator as a function of the input voltage of the amplifier designed to drive the actuator.

also tested in the turning points. Although it should provide the smoothly changing acceleration, it was not substantially better than the parabolic one, so the parabolic turning was used because of it is more simple. Another way, to reduce vibrations and further stabilise the mirror velocity, would have been the feedback system because the mirror position is measured anyway to get the wavenumber reference for the interferogram. The feedback for the driving velocity was thought to be done by the main board but its computation capacity was insufficient.

Driving ramps were created digitally and then converted to the analog voltage fed to the analog amplifier designed and manufactured by Gasera Ltd. The linearity of the amplifier and Actuator 1 was measured. Actuator 1 was the model LA10-08-000A from BEI Kimco Magnets. The force produced by the actuator driven with DC voltage was measured using a precision balance with a small bias weigh. The voltage values and the balance readings scaled to units of the force are presented in Fig. 4.55. The force is clearly very linear to the input DC voltage of the amplifier as it should be. The force-current ratio of the actuator was determined as $k_f = 3.8$ N/A, which was near the value 3.61 N/A given by the manufacturer. However, the amplifier had separate halves for the negative and positive output voltages. These halves had slightly different gains, which changed of the driving velocity slope at halfway of the mirror travel as illustrated in Fig. 4.56 on the following page. This was solved by adding 10 Ω resistor in series with the voice coil actuator. The driving velocity with 20 Ω extra resistor is presented in Fig. 4.55 although 10 Ω was sufficient.

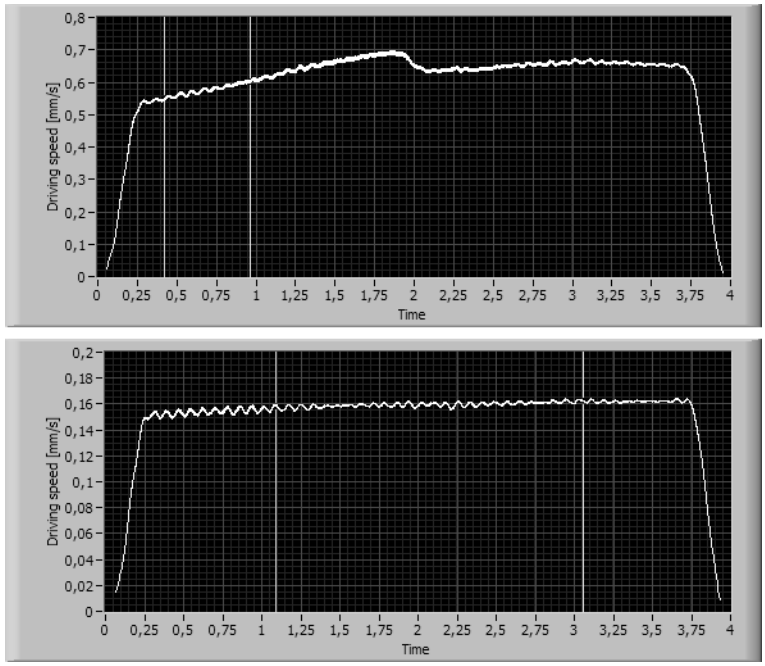

Figure 4.56 The amplifier halves had slightly different gains, which caused a change on the slope of the mirror velocity as in the upper graph. The resistor in series with the actuator neglected the gain difference as in the bottom graph.

Mirror velocity range

The range of the laser frequency was estimated by varying the mirror velocity and analysing velocity errors. The lowest useful frequency was about from 0.5 kHz. Then the peak-to-peak velocity fluctuations were from 15 to 30 percents, which is quite much. The optimal frequency was about 6.2 kHz, when the peak-to-peak errors were below 7 percents of the driving velocity. When the frequency was raised above 10 kHz, the sinusoidal shape of the laser signal was beginning to distort. At 15 kHz distortion was clear and the frequencies above that were unusable. The corresponding mirror velocity range was approximately from 3 mm/s to 30 mm/s and the best performance was achieved with about 20 mm/s velocity.

Vibration isolation

The response of the infrared detectors depends typically very strongly on the frequency. The noise in the mirror velocity adds noise to the interferogram and thus also to spectrum. Therefore, keeping the mirror velocity as constant as possible is important. However, the optical path difference can be still measured with sufficient accuracy because either the sampling of the interferogram is triggered from the laser signal or the both signals are over-sampled and then interpolated. When the driving system itself

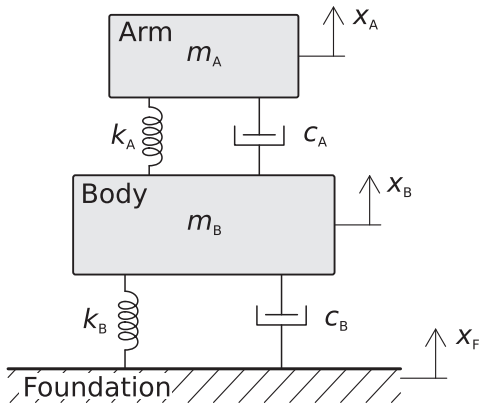

Figure 4.57 Two mass model of the vibration isolation system for Swing III. The interferometer body is coupled to the floor (or ground, laboratory table, etc.) by the spring and damper. The interferometer arm is coupled to the body with the spring elements having some damping also. The aim is to minimize the relative motion between the arm and the body or $|x_\mathrm{B} - x_\mathrm{A}|$ caused by the motion of the foundation x_F.

is optimised as previously on page 125, the main source of velocity errors is the external vibrations. Thus, the interferometer might need the extra vibration isolation to reduce the undesired vibratory motions between the arm and the body. Another vibration issue are the shock vibrations. Hence, they are hard to isolate, the spectrometers usually reject the data distorted by shock vibrations.

Swing III mounted on the vibration isolation system, which is placed on the laboratory table or a corresponding place, can be modeled as a two mass system as in Fig. 4.57. This is as a rather simplified model but it can be used to explain the principle of the isolation. The table is called the foundation. The arm and the body are coupled by the flexure elements modeled as spring A having the force constant k_A and possibly by the voice-coil as a damper. The body is coupled to the foundation by the vibration isolator, which is be modeled as a linear spring B and a linear damper. The damping force of the both dampers is linear so they are viscous dampers and the damping force proportional to the velocity of the moving object [99].

The system can be separated in two parts. The first subsystem FB consists the foundation and the interferometer body. The second is the body and the arm, or AB. These two subsystems are coupled by forces exerted to the body. The foundation is moving sinusoidally according to

$$x_\mathrm{F} = x_0 \sin(\omega t),$$

where x_0 is the amplitude, ω is the angular frequency and t is time. In practice, the vibration is usually broadband but it can be always treated as the sum of sinusoidal components so it is sufficient to study one component. The motion of the foundation is transmitted to the interferometer body by

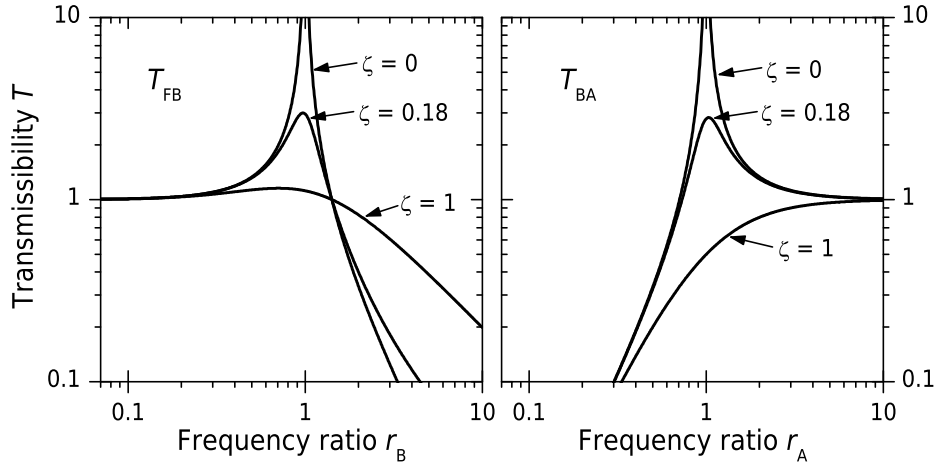

Figure 4.58 Absolute and relative displacement transmissibilities, or T_{FB} and T_{BA} respectively, with few different relative damping ζ values. The frequency ratio is $r = \omega/\omega_{\mathrm{n}}$, where ω_{n} is the natural frequency of the isolation system (according to Eq. (4.14)).

forces exerted by the spring k_{B} and damper c_{B}. The transmission efficiency is measured with transmissibilities, which tell how much of the motion or force or acceleration is transmitted from the source to the object [99]. The absolute motion transmissibility, or the kinematic excitation, is the ratio of vibration amplitudes of the object to the source. In the case of the foundation and the body, the absolute motion transmissibility is

$$T_{\mathrm{FB}} = \frac{|x_{\mathrm{B}}|}{|x_{\mathrm{F}}|} = \frac{\sqrt{1 + (2\zeta_{\mathrm{B}} r_{\mathrm{B}})^2}}{\sqrt{\left(1 - r_{\mathrm{B}}^2\right)^2 + (2\zeta_{\mathrm{B}} r_{\mathrm{B}})^2}} \tag{4.13}$$

where $r_{\mathrm{B}} = \omega/\omega_{\mathrm{B}}$ and the natural frequency of the isolation system B is

$$\omega_{\mathrm{B}} = \sqrt{k_{\mathrm{B}} \frac{m_{\mathrm{B}} + m_{\mathrm{F}}}{m_{\mathrm{B}} m_{\mathrm{F}}}} \tag{4.14}$$

and the relative damping coefficient is

$$\zeta_{\mathrm{B}} = \frac{c_{\mathrm{B}}}{c_{\mathrm{cr,B}}}, \qquad \text{where} \quad c_{\mathrm{cr,B}} = 2\omega_{\mathrm{B}} \frac{m_{\mathrm{B}} m_{\mathrm{F}}}{m_{\mathrm{B}} + m_{\mathrm{F}}}, \tag{4.15}$$

where c_{cr} is called the critical damping coefficient [99–101]. The T_{FB} is plotted with several damping coefficient values in Fig. 4.58. The transmissibility is below the unity when the frequency ratio is $r_{\mathrm{B}} > \sqrt{2}$. At lower frequencies, no damping exists. Actually, with sufficiently small damping coefficient, there is a resonance peak where the vibration is amplified.

In the subsystem BA, the motion of the body is transmitted to the arm. The target is to reduce the relative motion between the arm and the

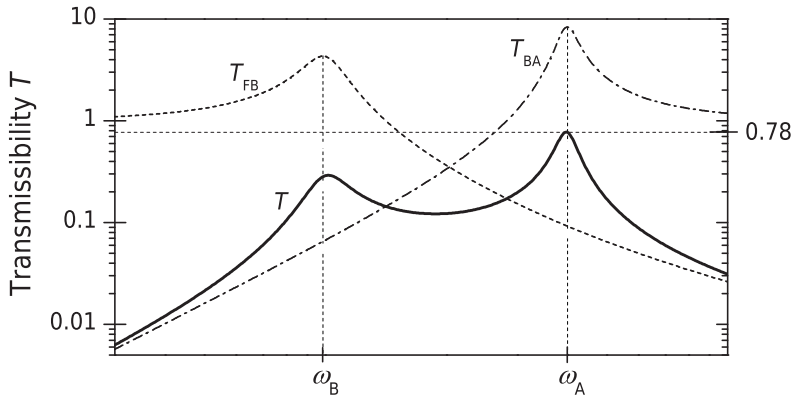

Figure 4.59 Total displacement transmissibility T of the complete isolation system in Fig. 4.57 as a function of the angular frequency ω. The total transmissibility is the product of the transmissibilities of the subsystems FB and AB. The relative damping coefficients were $\zeta_A = 0.06$ and $\zeta_B = 0.12$.

body, which efficiency is described by the relative displacement transmissibility [99]

$$T_{BA} = \frac{|x_B - x_A|}{|x_B|} = \frac{r_A^2}{\sqrt{\left(1 - r_A^2\right)^2 + \left(2\zeta_A r_A\right)^2}} \tag{4.16}$$

where r_A and ζ_A are defined correspondingly as Eq. (4.14) and Eq. (4.15). Few relative transmissibilities with different damping coefficients are plotted in Fig. 4.58. The relative motion is damped below the resonance peak in contrary to the subsystem FB where the vibration is isolated above the resonance.

The total motion transmissibility of the system is the product $T = T_{FB}T_{BA}$ [99]. One example about the total transmissibility and its components is depicted on Fig. 4.59. The natural frequency of the subsystem FB should be low and clearly distinct from the resonance of AB to avoid overlapping. Then the subsystem FB firstly damps the frequencies $\omega > \sqrt{2}\omega_B$ and passes or amplifies the lower ones. So, the subsystem AB is mainly exited by the low frequency vibration which produces the relative motion between the arm and the body with very low efficiency. Furthermore, if the damping is strong enough, as in Fig. 4.59, the vibration is isolated even at the natural frequencies. However, in this example the maximum transmissibility is still about 0.78, which corresponds to about 22 % decrease of the amplitude, so it is not very good isolation. The isolation efficiency could be improved from this by adding the damping or separating the natural frequencies further.

The above system is an idealization. The metallic springs are usually very near to the idealized model, but the dampers are not. The dampers have typically non-linearities, especially the ones made from elastomer, such

as rubber, and damping depends on other than just speed. The whole system usually has also more than two natural frequencies. Nevertheless, the above ideal system described the main characteristics of the vibration isolation system quite well. [99]

In Swing III, the Actuator 1 was used a damper. The wired component of the actuator was replaced by the solid copper cylinder to maximise the eddy currents and so the damping coefficient. The voice-coil is an example of very linear damper [99] indicated also by Eq. (D.1). The friction dampers and gas shock absorber were also tested, but they had problems with static friction. The voice-coil damper has not friction problems so it enables smooth motion required in the interferometer. Furthermore, the damping was increased by the back electromotive force (see Appendix D) of Actuator 2, which actually had almost equal damping coefficient than Actuator 1 with the copper cylinder.

As the vibration isolator, the springs were tested with and without elastic dampers. The damper material was manufactured of the soft silicone gel by Advanced Antivibration Components. The very good isolation results were obtained also without the dampers, or using only four springs. Comparison of the driving velocity with and without the isolation is in Fig. 4.60. The natural frequency of the spring support was about 4 . . . 5 Hz. The variation of the velocity extremes was over 50 % without the isolation and about 9 % with the isolation. Finally, the mirror velocity had noise less than 5 % in low vibration conditions. The major disadvantage of the isolation system is the lack of the support in the horizontal direction, which have to be solved in future designs.

Comparison to Carousel interferometer

The driving of Carousel interferometer [7] was studied for comparison. The laser signal and the driving ramp were recorded from the diagnostics connectors on the main board of Gasmet spectrometer containing Carousel interferometer. During the recording, the spectrometer was firstly kept on the laboratory table and then some shock vibrations were produced by hand. The mirror velocity was calculated using the zero crossings of the laser signal and assuming the wavelength of Helium-Neon laser (632.8 nm).

Carousel interferometer is based on the rotational motion of the block of four plane mirrors as sketched in Fig. 2.11(c) on page 18. The block mass was quite high and it has spring with a rather small force constant, or the spring is “soft”, so the natural frequency is low. The driving motor is a voice-coil coupled to the block by the porch swing linkage with high natural frequency and the patented mechanical sliding surface, which acts as a reduction gear with the reduction ratio about 1/10. Because of the very distinct natural frequencies, the reduction gear and supporting the block from its centre of gravity, external vibrations are transmitted very

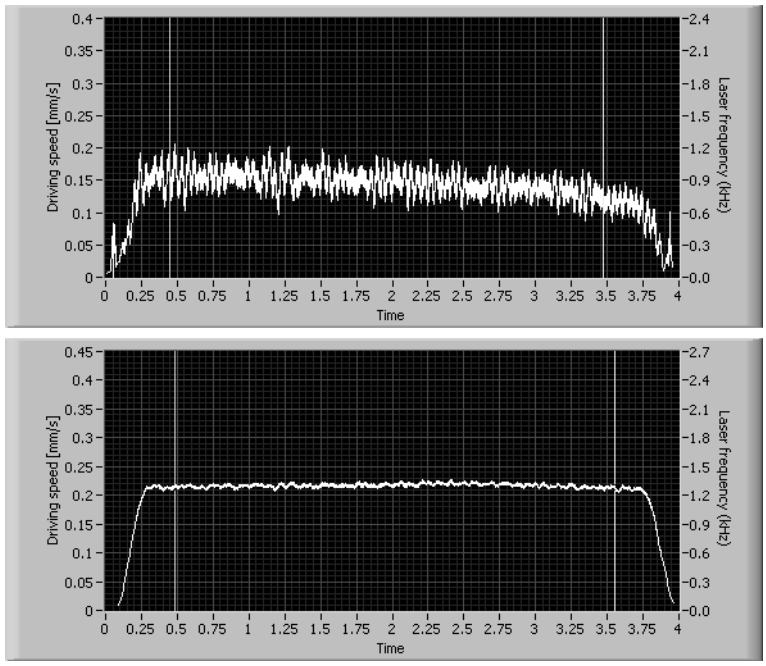

Figure 4.60 Comparison of the mirror velocity of Swing III with and without the vibration isolation. The upper figure shows the velocity without isolation and the lower one the velocity with the isolation formed from four springs.

inefficiently to rotations of the mirror block. Therefore, the mirror velocity should become very stable.

The driving ramp and the mirror velocity during low vibrations are plotted in Fig. 4.61 on the next page. The laser frequency is about 60 kHz. In the other direction, the mirror velocity is very constant but, in the other direction, it has a quite a linear slope. The peak to peak variation of the constant part was about 8 % and the slope part about 17 %. In the middle of the velocity signal, there is ripple probably caused by the corresponding ripple in the driving ramp. The turning part of the driving ramp seems to have some deceleration jump just before the direction change. The driving was very repeatable. If the spectrometer experienced moderate shock vibrations, the mirror velocity variations were increased to 17 %. As a whole, the mirror velocity of Carousel interferometer was as good as of Swing III but Carousel tolerated the vibrations better, especially the shock vibrations. Swing III requires very probably the extra vibration isolation.

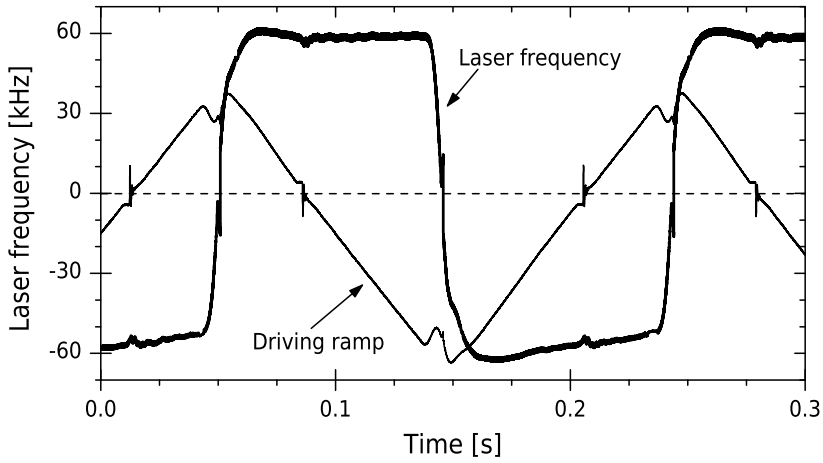

Figure 4.61 The laser frequency f_L and the corresponding driving ramp signal of Gasmet spectrometer with Carousel interferometer. The sign of the frequency indicates the different driving directions.

4.6.5 Experiments with FTIR setup

Spectrometer setup

A complete FTIR spectrometer using Swing III interferometer was assembled and then studied experimentally. The infrared source was Norton Igniter Model 301. The infrared detector was DLaTGS detector from Bruker, Inc. The detector was sealed by KBr window and its active area diameter was about 2 mm. The infrared beam from the interferometer was focused to the detector by using similar OAP10 off-axis parabolic mirror as in collimating.

Sample spectra were measured using the gas cell Storm™ 10 distributed by Specac, Ltd. It was made from stainless steel and had BaF_2 windows. The cell is single pass design with absorption length 10 cm and the clear aperture 39 mm. The sample gas could be changed using two valves. The measured transmission of the cell is represented in Fig. 4.62. The transmission drops quickly from 1500 cm^{-1} to 1000 cm^{-1} due to cell windows. So it, unfortunately, limits the spectral range because the beam splitter range reaches to approximately 750 cm^{-1}. The spectrum in this figure is very noisy. Later, the noise was vastly reduced by improving the signal wiring.

The Figure 4.63 shows a background spectrum or the room air measured with Swing III spectrometer without the sample cell. The measurement time was about a minute, Hanning apodisation was used and the resolution was about 6 cm^{-1}. The laser frequency was about 6.3 kHz. The shape of the black body emission curve is also plotted to illustrate the spectrum of the emitted radiation. Two observations can be readily made. Firstly, the spectral range is approximately from 700 cm^{-1} to 4500 cm^{-1}. The range is probably limited by the beam splitter although it should have

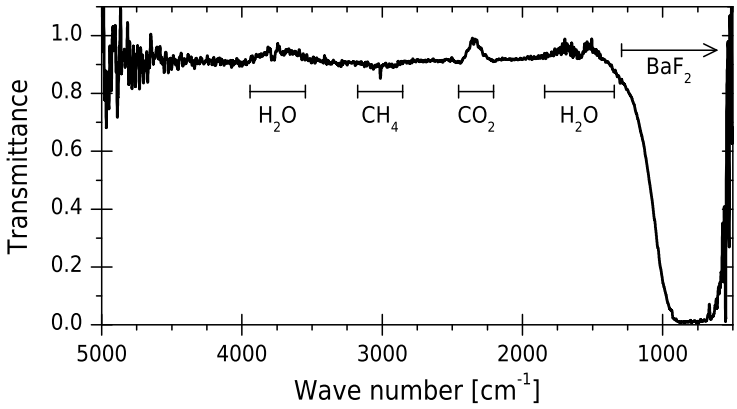

Figure 4.62 Transmittance of the stainless steel gas cell with BaF_2 windows. Sample was room air, containing water, carbon dioxide and some methane left to the cell.

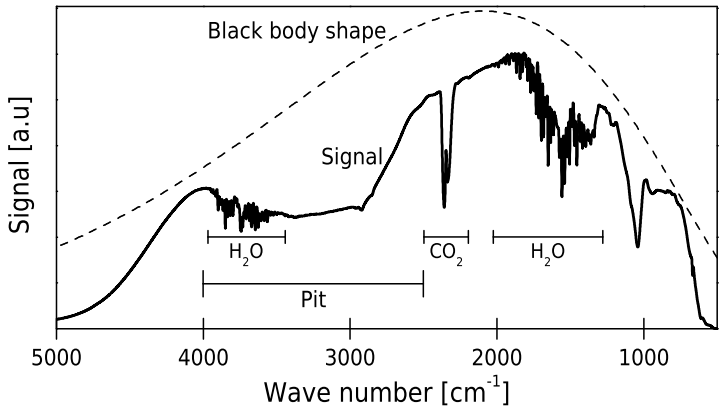

Figure 4.63 Background of the room air measured with Swing III without sample cell. The black body emission curve is for illustration of its shape only.

somewhat broader transmission range. Secondly, the signal drops quickly from 2500 cm^{-1} and thus have a pit in between 4000 cm^{-1} and 2500 cm^{-1} which is also probable because of the coatings of the beam splitter or the compensating plate. Often, the anti-reflection coatings have regions of the poor transmission as illustrated in Fig. 2.15 on page 22. It is likely that other components have not a pit such as this because the emission is near to the black body, mirror reflectance curves are very flat and detector response also flat despite of the fogged sealing window. The transmittance of the beam splitter was measured but the data has, unfortunately, been lost so the complete confidence can not be obtained. Additionally, the transmittance of the beam splitter may be sensitive to the temperature, which may cause problems because the interferometer operating temperature is quite high because of the excess heat from the source. During recording the data for Fig. 4.63 the interferometer at 62 °C.

Wavenumber accuracy

One of the first tasks was to calibrate the wavenumber axis. It is often done by using the water line at 1918 cm^{-1}. Because the water lines are mainly too dense for low resolution of Swing III, the methane lines were also used. Thus, the calibration covers wider spectral band although the one point calibration should be sufficient because of the highly linear measurement method. The methane and water spectra were recorded with Swing III and compared to the library spectra from Northwest-Infrared Vapor phase infrared spectral library [102] provided by Pacific North-West National Laboratory (PNNL). Additionally, the methane spectrum was measured with laboratory spectrometer Tensor 37 manufactured by Bruker, Inc. Methane samples were from the same gas supply with methane concentration 1000 ppm.

The peaks of Swing III were clearly off from the correct positions. At first, the laser wavelength was estimated to be about 670 nm instead of 665 nm specified by the manufacturer. After that, the small shift caused by the imperfect collimating of the infrared beam was approximated. The limiting collimator was the detector part, because the collimating mirrors are similar and the detector is smaller than the source. The detector active area had radius of about $r = 1$ mm and the effective focal length of the collimating mirror was $f_{\mathrm{EFF}} = 18.8$ mm. According to Eq. (2.16) and Eq. (2.17), the wavenumber axis correction is $\nu_{\mathrm{actual}} \approx 1.0007078 \cdot \nu_{\mathrm{measured}}$. After these two corrections, the wavenumber values were very near to correct line positions, as presented in Fig. 4.64. However, the total correction does not necessarily consist of particularly these two components.

The wavenumber accuracy was affected by the interferometer temperature probably because of instability of the laser. The zoomed portion of 1000 ppm methane spectra recorded in three different interferometer temperatures are presented in Fig. 4.65. The line, that was at 3075.3 cm^{-1} with 60 °C is shifted by +1.4 cm^{-1} at 64 °C and by +2.6 cm^{-1} at 74 °C. This indicates, that the laser wavelength has been slightly shortened. The temperature effect could be corrected by calibrating the spectrometer in different temperatures. Another solution is to improve the stability of the laser or even replace the whole component. Furthermore, the interferometer temperature may be stabilised but it is not the objective of this work.

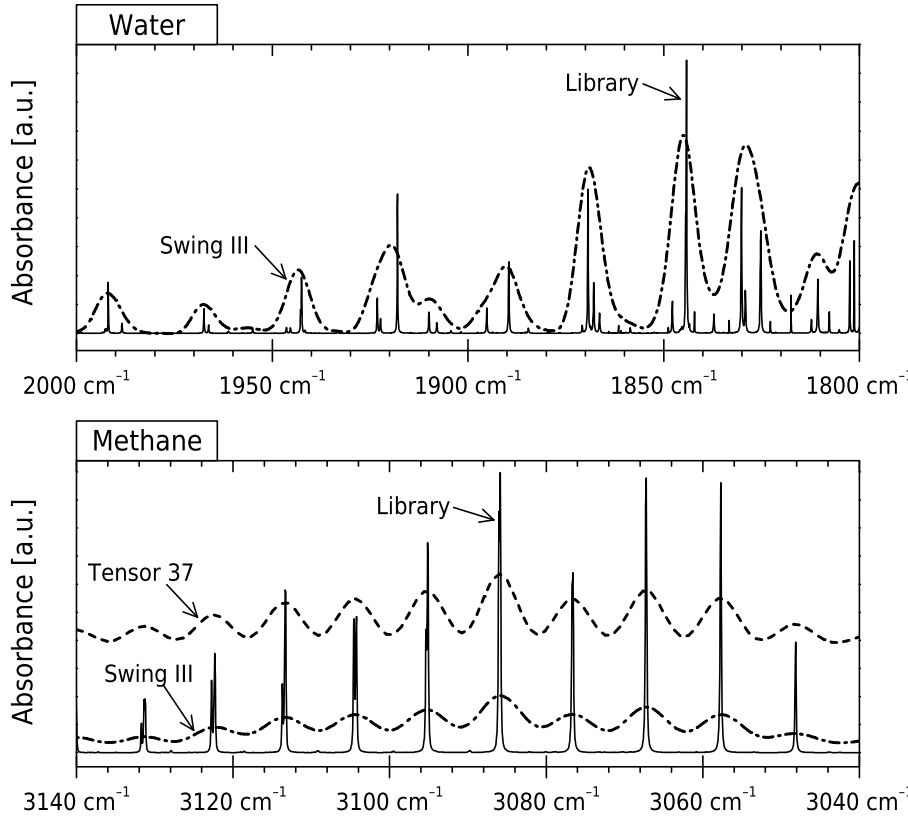

Figure 4.64 Portions of the water and the methane spectra measured with Swing III representing the wavenumber accuracy after the wavenumber axis calibration. The library spectra are from PNNL [102]. The methane spectrum was also measured with Tensor 37 (Bruker Inc.) for reference. Constant baselines are added for clarity.

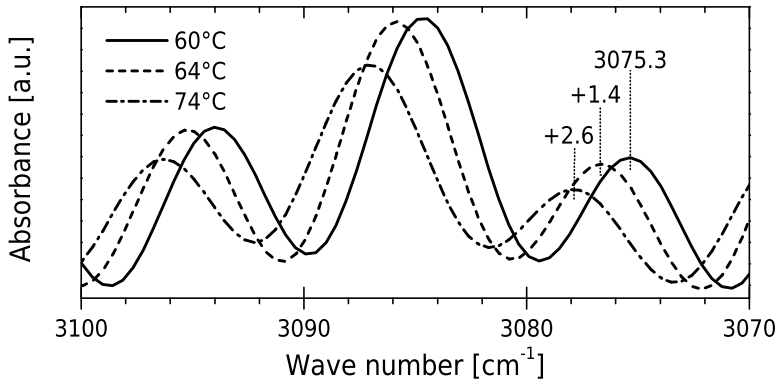

Figure 4.65 Portion of the methane spectrum recorded at three interferometer temperatures. Changes of one peak position in relation to the position at 60 °C are marked.

Noise in spectrum

The noise in the spectrum was analysed in the band from 2200 cm^{-1} to 2000 cm^{-1} because the strong absorbers of the air, the water and carbon dioxide, are practically always present in the spectra but they have no lines in this region [2,43]. Additionally, the the source emission had its maximum near this region. The noise was measured using 100 % lines. Two successive background spectra were divided by each other. Spectra were recorded with about 1 min measurement time, or 64 scans, with the best possible resolution and the laser frequency $f_L = 6.3$ kHz.

Four noise samples were chosen to represent the noise and the effects of the few noise reduction methods used. The first sample was without apodisation, the second with Hanning apodisation and the third with Blackmann-Harris 3-Term apodisation. The last one was computed from interferograms filtered digitally with the second order Butterworth low-pass filter with cut-off frequency 10 kHz. Each sample had 440 data points with interval 0.46 cm^{-1}. The noise samples are plotted in Fig. 4.66.

The both, apodisation and the filtering, reduce the noise. The effect of the apodisation functions is based on the fact they lower the resolution, which lowers the noise. The digital filter decreased the high frequency noise, which was present in the interferogram although the interferograms were analogically filtered to avoid aliasing. Finally, the quantization noise was distinctive as shown in the scaled portion of 100 % line with the lowest noise level in Fig. 4.66.

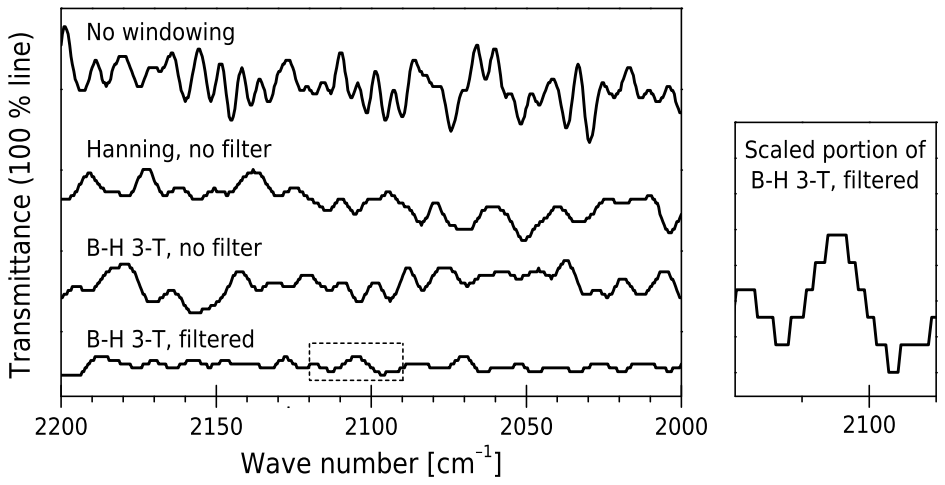

Figure 4.66 Some noise samples represented as 100 % lines and measured with Swing III and DLaTGS detector. The interferograms were processed with different combinations of two apodisation functions and the digital low pass filter with cut-off frequency 10 kHz. The abbreviation B-H 3-T refers to Blackmann-Harris 3-Term apodisation function. The right plot represents a scaled portion of data with the lowest noise level.

Table 4.I Summary of noise and SNR values of the sample spectra between 2200 cm^{-1} and 2000 cm^{-1} recorded using Swing III.

Apodisation	Low pass filter	Rms noise $[\cdot 10^{-5}]$	SNR
Hanning	Off	6.9	15000
Blackmann-Harris 3-Term	Off	6.8	15000
Blackmann-Harris 3-Term	On	3.0	34000

The noise had probably standard distribution, according to the shape of its histogram and Kolmogorov-Smirnov test with the risk factor 0.05. The standard deviation of 100 % noise is equal to the root-mean-square (rms) of the noise [2]. The signal to noise ratio (SNR) is reciprocal of rms noise. The rms noise and the corresponding SNR values of three noise samples are summarised in Table 4.I. The best SNR was about 34 000:1, which required the use of the digital filter. If the 100 % line has an slowly changing component, for instance due to the modulation depth change, the rms noise value is naturally increased.

Comparing the SNR values of the spectrometers is not straightforward because SNR depends strongly on the measurement time, resolution, spectral band and calculation method [43]. For example, increasing the measurement time t decreases the rms noise by factor $\sqrt{t}$. Additionally, the peak-to-peak noise is generally few times bigger than the rms noise so it is essential to report the calculation method. According to manufacturer (ABB, Inc.), MB3000 spectrometer has SNR 50 000:1 determined by rms noise with one minute measurement time, 4 cm^{-1} resolution and "at response peak" [39]. Another comparable specification is SNR of Monolithic 20™ (FTRX llc) spectrometer is better than 45 000:1 in the same band as here but the resolution is not given [54]. Thus, Swing III with current spectrometer setup is near the commercially available devices although the SNR is not even very well optimised.

Properties of methane, water and carbon dioxide spectra

The spectra on three gas samples were recorded to study and to demonstrate the properties of the spectra produced by Swing III with the 10 cm sample cell. Methane and water are often used samples because they are easily and commonly available. Additionally, the methane strongest band is at about 3000 cm^{-1} and the water at 1600 cm^{-1}, so they cover the most interesting range in the middle infrared. The methane lines are also nicely distinctive even with low resolution. We also measured the carbon dioxide spectrum for demonstration of the spectrum of the dense lines.

The methane and carbon dioxide samples were mixtures of the nitrogen N_2 and the sample gas with concentration 1000 ppm, so quite high signals were obtained. The water sample concentration was unknown hence it was made by flowing a scientific grade nitrogen N_2 through Nafion pipe lying inside moisturized towels. Nafion is a polymer highly permeable with water and with very good selectivity.

The driving frequency was $f_\mathrm{L} = 6.3$ kHz and the resolution enabled by the maximum optical path difference was about 3.2 cm^{-1}. The apodisation function was not properly documented but probably Hanning apodisation was used. The methane and carbon dioxide were recorded with 64 scans of both the signal and the background and without the digital low-pass filter on interferogram. The water had 32 scans and the low pass filter. Wavenumber values were corrected, as described earlier on page 136.

Recorded spectra are presented in Fig. 4.67. PNNL library spectra [102] are plotted for wavenumber reference. Firstly, measured spectra look very nice. Peaks of the methane stronger band around 3000 cm^{-1} are clearly distinctive and in correct positions. Line shapes are quite symmetric. The weaker band near 1300 cm^{-1} had dense and low peaks, so they were observed as three wide peaks. Because water peaks are irregular and dense, single peaks are seldom distinctive but peak clusters are quite clear. For example, the peak at 1918 cm^{-1}, commonly used as a wavenumber reference, has other peaks so close that they are summed to one peak by the instrument function of the spectrometer. The carbon dioxide has clean regular peaks in a narrow band near 2350 cm^{-1}. These were observed as two wide banks. Although, single peaks can not be separated because of the low resolution, the spectrometer could be well used in gas analysis.

The resolution was estimated using full widths at half height, or FWHH, of several lines. The resolution at about 3080 cm^{-1} was approximately 4.8 cm^{-1} determined from the methane spectrum. At 1800 cm^{-1}, the resolution was about 6.8 cm^{-1} estimated from the water spectrum. Figures are not equal because of errors in determining the peak baselines, dense water lines and the fact that resolution usually changes somewhat along the spectrum. The optical path difference should have enabled 3.2 cm^{-1} resolution. However, Hanning apodisation would have broadened these lines

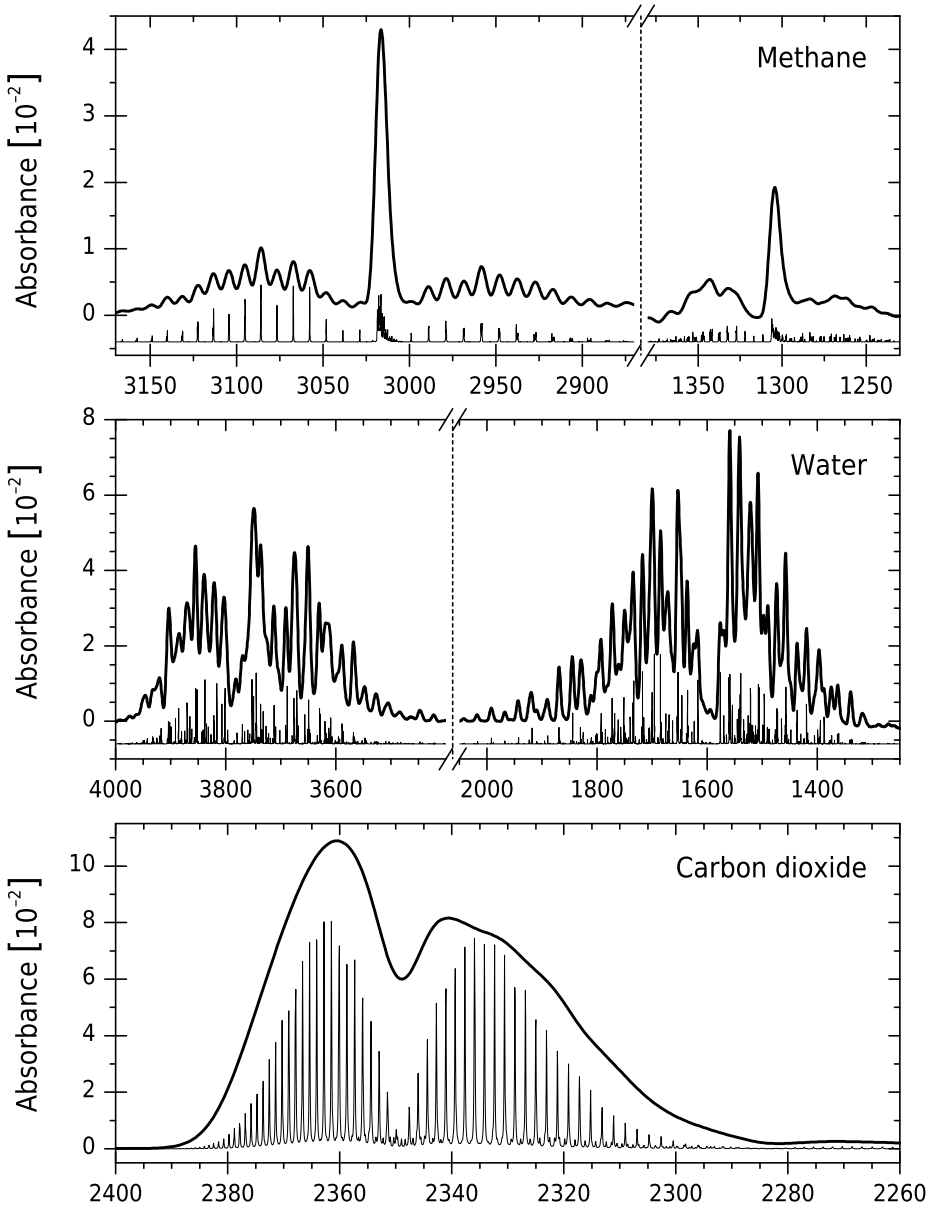

Figure 4.67 Spectra of 1000 ppm methane, water and 1000 ppm carbon dioxide recorded using Swing III. The water concentration was unknown. PNNL library spectra [102] are plotted with thin lines for wavenumber reference. Values of horizontal axes are wavenumbers in cm^{-1}.

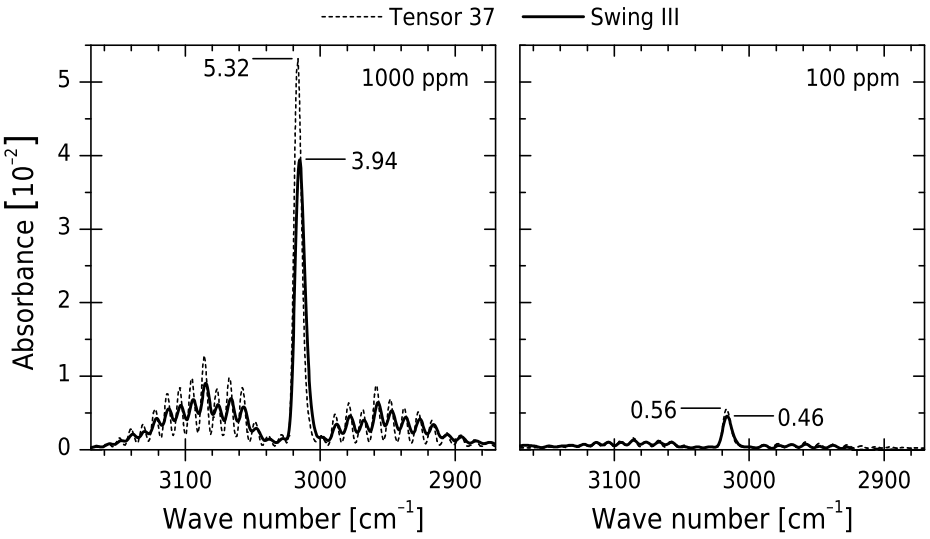

Figure 4.68 Comparison of spectra of two methane concentrations: 100 ppm and 1000 ppm. Ratios of center peak heights are about 9.6 with Tensor 37 and 8.6 with Swing III.

to about 5.3 cm^{-1} and Blackmann-Harris 3-Term to 6.1 cm^{-1}, which are both quite near to estimated resolution values from the measured data. Apodisation functions are defined in Table 2.B on page 30.

The best possible resolution of Swing III near 3000 cm^{-1} without apodisation was determined by increasing the mirror travel length until the resolution was not improving anymore. The resulted resolution was about $3\ \mathrm{cm}^{-1} \ldots 4\ \mathrm{cm}^{-1}$. Then the aperture broadening was dominating and limiting the best possible resolution. According to Eq. (2.18) and with the detector radius of $r = 1$ mm and the effective focal length of $f_{\mathrm{EFF}} = 18.8$ mm, the resolution limited by the aperture at 3000 cm^{-1} would be about 4.2 cm^{-1}. However, the mirror travel could have been further increased to provide the maximum optical path difference of 4.01 mm, which would have enabled 3.0 cm^{-1} resolution in itself. In the spectra in Fig. 4.67, the two major origins of the broadening were firstly the aperture effect and then the widening by the apodisation function.

The detector linearity was shortly tested by recording the spectra of the methane at concentrations 100 ppm and 1000 ppm. The same samples were measured successively with Swing III and Tensor 37 with as similar measurement parameters as possible so the spectra should very well comparable. The spectra are plotted in Fig. 4.68. The ratio of the centre burst heights measured with Tensor 37 are about 9.6 and with Swing III 8.6. These ratios are quite near each other especially when the possible errors in estimating the baselines of the spectra are taken account. Thus the detectors of the these devices seemed to approximately equally linear.

Temperature stability

Temperature stability was studied using 100 percent transmittance lines recorded during the warm up of Swing III. The interferometer was initially at the room temperature and heated by the excess heat from the infrared source. The initial background was measured immediately after the device was turned on. This background was used as a reference to the following signals. The interferometer initial temperature was actually about 30 °C, so it was somewhat warmed up because the room temperature was about 26 °C. During the warm up, taking about 2 hours, 100 percent lines were recorded with corresponding interferometer temperature measured from a screw hole in the interferometer body.

The modulation depth was estimated at wavenumbers 2000, 2800 and 4300, each in cm^{-1}. The most traditional values, 3000 cm^{-1} and 4000 cm^{-1}, were not used, because the spectra had water and methane residues at these wave numbers. The selected figures, however, represent the modulation depth values sufficiently well. Three series of modulation values as a function of the temperature were recorded and plotted to Fig. 4.69. Maximum and average changing rates of the modulation depth at 2800 cm^{-1} are summarised in Table 4.J. The spectral resolution was about 4 cm^{-1}. In the first measurement, the initial background had 128 scans corresponding about 2.2 min measurement time and next ones had 32 scans, or 0.5 min. The second and the third series had 60 scans, or 1.1 min, in the initial background and respectively 32 or 16 scans in later ones. Laser frequencies were from 6.3 kHz to 7.8 kHz.

The greatest change in the modulation depth at 2800 cm^{-1} was 2.5 percentage units per Celsius and occurred in the first series between 56 °C and 59 °C. This indicates snapping or the permanent misalignment. Elsewhere, the modulation at 2800 cm^{-1} was very stable. The second series was much more stable. There was no sign of snapping and the average change was even 0.04 percentage units/°C, which is at the same level as the results of Swing I, see Table 4.D on page 98. Furthermore, the second series decreased quadratic and this dependency became stronger with increasing wavenumber. Thus, it followed nicely Eq. (2.8) if the tilting is assumed to

Table 4.J Summary of the modulation depth at 2800 cm^{-1} as a function of the Swing III temperature. The values are calculated from data in Fig. 4.69.

Series	Rate of change of modulation depth [percentage units per 1 °C]		Average rate of change is calculated using points in Fig. 4.69
	At maximum	In average	
1	2.5	0.2	first and last
2	0.6	0.04	first and last
3	0.9	< 0.1	lowest and highest values

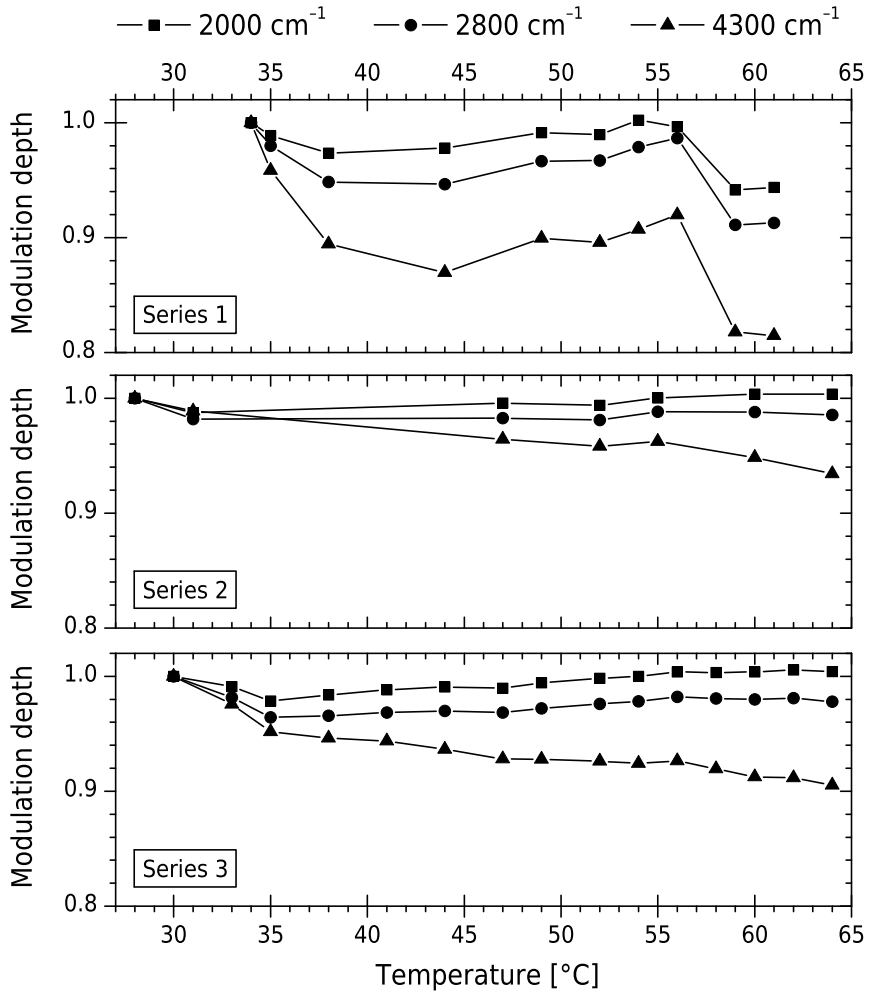

Figure 4.69 Three series of modulation depth values estimated from 100 % lines. Spectra were measured during the interferometer warm up period, which took about two hours.

be proportional to the temperature change. Figures of the third series were near to the first two.

However, the third modulation series differed from the two. In the first and second series, the modulation depth series acted similarly at all three wavenumbers. In the third one, the modulation at 4300 cm^{-1} decreased but increased at the lower wavenumbers. More detailed analysis of spectra showed that the successive 100 percent lines crosses each other near 3000 cm^{-1}, which explains the resulted rates of modulation curves. In principle, the modulation should act similarly, either to increase or decrease, in all wavenumbers but in this case it is clearly not true. The most possible reason is the beam splitting coating of the beam splitter. It is probably based on the interference on the stack of thin layers. The thermal expansion may

change the layer thicknesses, which might affect differently to the transmission at different wavenumbers. Another observation is that the modulation is increasing with the temperature. The interferometer was aligned at the final temperature, which was its operating temperature. Because the reference background was at low modulation, the modulation gets values slightly over 1. The better reference background would have been some record at over 60 °C.

Similar results were observed, in other experiments during the temperature change. Additionally, the alignment was kept after many successive heatings, which resulted from shutting down the spectrometer for nights and weekends. As a whole, the interferometer itself seemed to very temperature stable and the permanent misalignment rarely occurred.

The excess heating of the source was used to warm up the interferometer. Actually, the heating of the interferometer 40 °C over the surrounding temperature is really undesired. If the external temperature would be 50 °C the instrument could be overheated. The high temperature caused already instability of the reference laser and possibly problems with the beam splitter transmission. One immediate improvement of the design is adding a spherical reflector to the back of the infrared source. It would reflect most of the radiation energy, which is emitting to the wrong direction, back to the source. Then the source power could be lowered and the excess heat would decrease without weakening the signal. Additionally, the source mount could be designed to better conduct the heat out from the interferometer. Further, anodizing the aluminum body and the casing as black might improve the heat emission of the interferometer parts. The warm up time could be shortened by lightening the structure and optimizing the heat paths. For applications, where the power consumption is not critical, the interferometer may be equipped with active heat control to speed up the warm up and to prevent the overheating.

Comparison with commercial laboratory spectrometer

The performance of Swing III was compared to the high quality laboratory FTIR spectrometer, Tensor 37, manufactured by Bruker, Inc. Tensor has Bruker's RockSolid™ interferometer, which is based on two corner cube mirrors moved by a patented inverted double pendulum mechanism [15,103]. Pivots of the mechanism are compliance elements so they are almost wear-free. According to manufacturer, SNR is 45 000:1, which is determined by peak-to-peak noise in 2200 cm^{-1} ... 2100 cm^{-1} with about four minutes background and one minute sample measurement times, 4 cm^{-1} resolution and Blackmann-Harris 3-Term apodisation [103]. Because the peak-to-peak noise is typically few times more than the rms noise, the SNR calculated from rms noise could be few times higher than this.

At first, noise levels were compared by using 100 percent transmittance lines between 2200 cm^{-1} and 2000 cm^{-1} recorded in one minute and with comparable resolutions. Tensor 37 used Blackman-Harris 3-Term apodisation. Swing III interferograms were digitally low pass filtered using cut off frequency 10 kHz and then Hanning apodised. Both had room air in the absorption path. The 100 percent lines are plotted to Fig. 4.70. Table 4.K summarises the resulted rms noise and SNR values. The rms value is the standard deviation of the noise sample from where a linear line was firstly subtracted to reduce baseline effect. The SNR is reciprocal of the rms value. The noise level and SNR of Swing III using digital filter and Tensor 37 are quite close each other. Additionally, Tensor value corresponds the value in its commercial brochure [103]. As a whole, the noise of Swing III is well comparable to the existing commercial device.

The second comparison was made with mixture of 1000 ppm methane

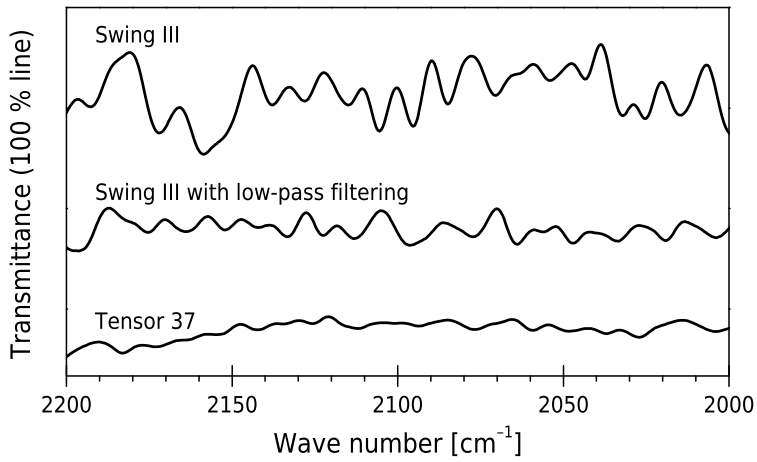

Figure 4.70 Comparison of noise between Swing III and Tensor 37 spectrometer from Bruker Inc. The resolution and the measurement time were adjusted to almost equal. The both used Blackmann-Harris 3-Term apodisation.

Table 4.K Summary of noise and SNR values from the comparison between Swing III and Tensor 37.

Device	Rms noise $[\cdot 10^{-5}]$	SNR
Tensor 37	2.2	45 000
Swing III, with low-pass filter	2.6	38 000
Swing III, without llow-pass filter	7.4	14 000

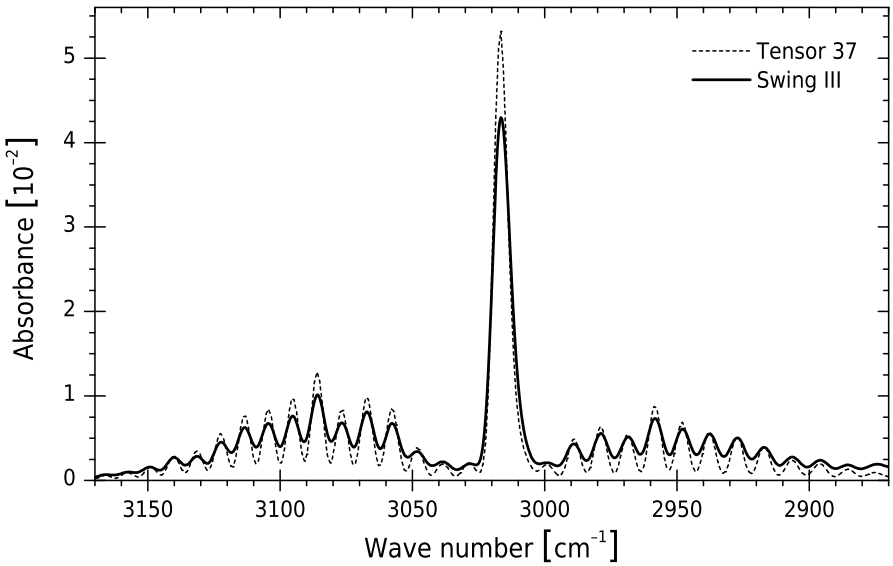

Figure 4.71 Comparison of methane spectra recorded with Swing III and Tensor 37 (Bruker Inc.). The interferogram of Swing III was low pass filtered and Hanning apodised. Tensor 37 used Blackmann-Harris 3-Term apodisation.

and nitrogen N_2 put inside the 10 cm sample cell at the air pressure. The two samples were not exactly the same but they were taken from the same gas bottle, so the concentration should be very nearly equal. Tensor 37 used Blackmann-Harris 3-Term apodisation and 4 cm^{-1} resolution. Swing III had Hanning apodisation and the digital low pass filter as above. The resolution of Swing III was better than 6 cm^{-1}. Both devices used 32 scans in the background and the sample but the measurement times were not equal. Swing III measurement time was about one minute. The spectra are very similar as shown in Fig. 4.71. The peak positions are very near each other. However, the peaks in Swing III spectrum are clearly lower than in Tensor 37 results. This is probably because of the different apodisation functions and thus lower resolution of Swing III. Additionally, the sample pressures were not exactly equal so the pressure broadening might have been slightly different. Swing III spectrum had also more noise than Tensor 37 data as could be expected.

4.6.6 Discussion about Swing III

The third interferometer, Swing III, was designed more further than the previous models. The infrared source, the reference laser, a proper driving system and the supporting electronics were designed. Therefore, the full spectra were finally able to record using the interferometer. The spectrometer and the interferometer itself were further smaller than the former ones.

The mirror tilting over 3 mm travel was about 5 μrad, which corresponds approximately 0.007 unit decrease of the modulation at 3000 cm^{-1}. It is remarkable that this alignment stability was achieved using directly machined components, which was not possible with earlier versions. Furthermore, the travel length could be readily increased to even 5 mm without severe modulation decrease although it is not required in this work. The mirror velocity errors of Swing III on the vibration isolation mount were almost at the same level as in Gasmet$^{\mathrm{TM}}$ spectrometer based on Carousel interferometer.

The external temperature rise of 30 °C resulted about 13 μrad tilting measured with the expanded laser beam technique. This corresponds approximately 0.3 percentage units per Celsius decrease of the modulation depth in infrared at 3000 cm^{-1}. It was accepted although over three times better stability was obtained with Swing I. When used as spectrometer, the excess heat from the infrared source heated the interferometer. According to 100 percent lines, its thermal stability was at most about 0.2 percentage unit per Celsius in average over 30 °C temperature change. This figure contains also the changes in the source emission. The spectrometer was in the room temperature hence it would have over-heated if put in the heated environment. Therefore, the controlling the excess heat of the interferometer source should be better controlled in the future.

The wavenumber values were calibrated to very close to the PNNL library spectra and the reference spectra recorded with Tensor 37 spectrometer from Bruker, Inc. The best signal to noise ratio determined from 100 percent line recorded using Swing III was 38 000:1, which was quite close to Tensor. The best possible unapodised resolution of Swing III was about 4 cm^{-1} and about 6 cm^{-1} when Hanning or Blackmann-Harris 3-Term apodisation was applied. The methane and water spectra were quite good in comparison with the library spectra and the spectra recorded with Tensor 37. The lines were at their correct positions and the peak heights were reasonable.

As a whole, the interferometer was very good. The alignment kept stable over the mirror travel. Its thermal stability was acceptable and it fared well in comparison with the spectrometers available in the market. The spectra could be recorded with sufficient quality at least for the gas analysis.

The main issues, which could be improved in the possible future ver-

sions, are to better control of the external vibration and the excess heat from the infrared source. The lowest natural frequency of the porch swing bearing should be make higher, for instance by reducing the moving mass and increasing the force constant of flexure elements. Possibly, some numerical analysis of the structure might be useful. Furthermore, the need of vibration isolation should also be studied. The excess heat from the infrared source should be better controlled. Firstly, the efficiency of the source should be increased for example by adding a spherical reflector behind it. Additionally, the excess heat should be better transferred away from the interferometer.

Furthermore, few other things should be solved. The transmittance of the beam splitter was suspected to have some sensitivity to temperature, thus it should be studied. The mounting of flexure elements should made immune to creeping because it caused much misalignment. The optics was inadequately supported sideways, which may cause permanent misalignment thus mirror mounting should be further enhanced and probably adapting the techniques presented in the literature, for example in [51].

4.7 Summary of experiments

Studying the porch swing bearing for FTIR interferometer was started by testing how the bearing type works. This was done by using Michelson interferometer named Swing 0, which was assembled on the optical bench. The alignment was acceptably stable, or the tilting sufficiently low, over the desired mirror travel. Additionally, the tilting was very low during about 30 °C temperature rise. Because of these results, the porch swing bearing seemed very promising and the development of the next version was started.

The following version, Swing I, was designed for as a spectrometer although the full spectrometer was never built. The interferometer body was machined from two main components to minimize the number of separate parts. The mirrors were mounted by the principle of three rigid studs. The size was reduced by placing some of the optics inside the porch swing bearing. The modulation depth decrease along the mirror travel was adequate. The temperature stability was studied by measuring the modulation depth of the laser beam. The thermal stability of Swing I was the best achieved in this work. The average change in the modulation depth was less than 0.09 percentage units per Celsius at 3000 cm^{-1}, which corresponds to about 0.2 μrad change in the tilt angle. The short term maximum changing rates were at most 0.7 percentage units per Celsius or below 2 $\mu\mathrm{rad}/^{\circ}\mathrm{C}$. These figures are very good in comparison with those found in the literature and summarised in Table 2.C on page 37. However, some permanent misalignment was sometimes occurred. Studies with Swing I revealed many details contributing the stability as, for instance, the driving force must be coupled without mechanical contact and the mirror mounting studs should be on the reflective side rather than the background of the mirrors. Swing I showed that high stability can be achieved with Michelson interferometer using the porch swing bearing and so a very good FTIR interferometer can be developed using them.

Studies and the results on the motion linearity of Swing II provided the most valuable information obtained with it. The porch swing components were fine tuned to achieve nearly constant alignment, or extremely low tilting, along the mirror travel. The models for the parasitic motions presented in Chapter 3.2.2 substantially helped the tuning process, because the experimental results were well inconsistent with the model. The temperature stability aim was not reached because the efforts had already been assigned to the next version.

Swing III was the first version really designed as a full spectrometer although the two earlier versions had had the schematics of the spectrometer. The infrared source, the reference laser, the driving motors, the supporting electronics and other things were properly designed from the beginning. The design was made with intensive collaboration with Gasera Ltd. by detailed instructions from the author. The interferometer was smaller than

the earlier models, because, for example, the infrared source was placed inside the bearing. The alignment was sufficiently stable during the mirror driving without any modifications after the machining. The thermal stability was not as good as with Swing I but it was still acceptable. Additionally, because the permanent misalignment due to thermal expansion occurred rarely and the interferometer was aligned at the operating temperature, the alignment was mostly repeatable. The sample spectra recorded using Swing III were good in comparison with the commercial laboratory spectrometer, Tensor 37, and with PNNL library spectra. The signal to noise ratio was approximately 38 000:1, which is almost as good as with Tensor 37. The resolution was limited by the detector size and was below 4 cm^{-1} without apodisation and about 6 cm^{-1} with Hanning apodisation. The major issues were the vibration sensitivity and, additionally, the low signal from 4000 cm^{-1} to 2500 cm^{-1}, which was probably caused by the beam splitter imperfections. The detector in the spectrometer setup was DLaTGS type. Unfortunately, building the setup for the photoacoustic detector was not possible at this time although it would have been very interesting. Altogether, Swing III performed very well in the spectrometer and its stability was near the target, thus it has much potential for the low resolution FTIR interferometer.

Because of the sensitivity of the interferometer to even the smallest changes in its structure, its stability is determined by numerous tiny things, which must be taken account is the design. The ideal Michelson interferometer is manufactured from a solid block so its material is homogenous and thus the thermal expansion is uniform. Because this is not practically possible, the number of the separate components should be minimised to maintain the material homogeneity. The optics mounting is critical hence the optical materials have very different thermal and mechanical properties than the other components usually made of aluminum alloy. A very stable mounting principle based on three fixed studs machined directly on the interferometer body was used thorough this work. The optics was pressed against the studs with a spring force, which substantially reduces extra forces exerted to the mirror by the thermal expansion. Furthermore, if the flexure elements of the porch swing bearing are assembled from the separate components, they should be rigidly fixed to avoid the creeping of the movable arm, hence the creeping will produce misalignments.

The porch swing bearings are often sensitive to the external vibrations because the moving mass is not supported on its centre of gravity. This is the biggest disadvantage of the bearing in comparison with the suspensions based on the rotational motion. The lowest natural frequency of the bearing should be designed as high as possible, which requires minimising the moving mass and increasing the force constant of the flexure elements. However, one may still need an extra vibration isolation, whose natural frequency mode is well below the lowest mode of the bearing structure.

The tolerance to the shock vibrations requires to design the rigid optical mounting and a method for the rejection of the distorted data.

The method for estimating the mirror tilting from the measured modulation depth was improved by taking account the intensity distribution of the laser beam. The tilting is very straightforward to estimate from the changes in the fringe pattern but small tilting is very hard to observe. Additionally, the modulation depth estimated using the 100 percent transmission lines are affected also by the changes in the source emission and detector sensitivity. For these reasons, the tilting is best to estimate using the modulation depth of the collimated laser beam because it measures the properties of the interferometer itself and is more accurate especially when the tilting is very low. This method requires to take account that the intensity of the collimated laser beam decreases from the beam centre to the beam edges. Thus, the fringes on the beam centre are weighted over the fringes on the edges, which reduces the sensitivity of the modulation depth to the tilt angle. The method for estimating the correct tilt angle from the modulation depth of Gaussian distributed laser beam was developed and experimentally verified. Furthermore, the noise and the error sources in the laser modulation depth time series were analysed.

In the possible future versions, the thermal stability could be still increased. Especially, the permanent misalignment sometimes occurring during the heating and cooling cycles and the effects from the temperature gradients inside the interferometer could be further reduced. Additionally, the better control of the excess heat from the infrared source is required to increase the efficiency of the source component and decrease the heating of the interferometer. The tolerance to the external vibrations should be improved.

Chapter 5

Summary of papers published

Paper I: Modulation depth of Michelson interferometer with Gaussian beam

In this thesis, a lots of experiments, where the modulation depth of the expanded laser beam was measured, were made. It was observed that the beam intensity distribution has substantial effect on relation between the angle between beams and the modulation depth. This was thoroughly studied using Gaussian distributed beam, which is a common distribution of laser beams. The Gaussian distributed beam has more intensity on the beam centre than in the beam edges, so the beam centre has greater weight when the modulation depth is determined. In the paper, the calculation model for the modulation depth and its experimental verification were presented. Results are used in Chapter 2.2.3 and summarised in Appendix A.

The paper is originally published in *Applied Optics* in 2011 [96] and it is published in this thesis under OSA (Optical Society of America) Copyright Transfer Agreement.

Paper II: Experiments on the Porch Swing Bearing of Michelson Interferometer for Low Resolution FTIR

Linear motion of the porch swing bearing for FTIR interferometer was studied and demonstrated. Simplified models for parasitic motions were presented and verified experimentally. Almost ideal porch swing, which produced practically no tilting, was demonstrated. Additionally, results obtained with porch swing assembled from carefully machined components were presented to show that the bearing is sufficiently stable using normal machining tolerances and without any special tuning, which makes it suitable for mass production. Linear motion models and manufacturing tolerances are discussed based on this article in Chapter 3 and Appendix B. Experimental results of the article are used in this thesis when discussing the alignment stability of Swing II in Chapter 4.5.2 and Swing III in Chapter 4.6.2.

The paper is originally published in *Advances in Optical Technologies* in 2013 [68] and is published in this thesis under Creative Commons Attribution License.

Chapter 6

Conclusion

FTIR spectroscopy is a general tool for studying the material, which interacts with infrared radiation. Therefore, this technique is well suitable for the gas analysers, which can recognise even a few tens of the components and their concentrations of the unknown sample. In industry and especially in the security business, there is a constant requirement for new portable gas analysers, which can be carried by the worker. The portability sets special requirements because it experiences the temperature variations, vibrations and other changes in its external conditions during its operation. FTIR spectrometers are based on the interferometer, which provides extreme sensitivity in the measurements but, in the other hand, it easily observes even the smallest changes in its structure caused by the external conditions. As the author knows, the available or otherwise reported interferometers, which are sufficiently stable for portable use, are bulky and expensive. Additionally, the small or low cost interferometers have stability issues. The objective of this work was to design FTIR interferometer suitable for portable, or even hand-held, use. Because of the commercial potential, it was also aimed as early prototype of a possible commercial product.

Michelson interferometer was selected as the interferometer type, because it is the simplest possible FTIR interferometer and thus enables the smallest possible size when the beam diameter is fixed to ensure the high signal to noise ratio. For the same reasons and to save expenses, the plane mirrors were decided to use instead of more usual cube corner mirrors. Thus, the motion linearity of the movable mirror became critical. The porch swing bearing was used, hence it provides sufficiently linear mirror motion. Additionally, the bearing is simple, robust and very durable. Furthermore, the interferometers built in this work were especially designed to have very high thermal stability.

The best thermal stability was obtained with the first interferometer version Swing I. The misalignment during 30 °C temperature rise was about ten times less than reported with the commercially available models. As the author knows, only Carousel interferometer has better thermal stability but it is more complicated and thus bigger. Furthermore, it is not currently commercially available. The highest alignment stability over the mirror travel was recorded using the second version Swing II. The alignment changes were

hard to distinct even if the error effects were substantially magnified.

The small misalignments were estimated using the modulation depth of the expanded laser beam run through the interferometer. However, the laser intensity has typically non-uniform distribution, which effects substantially to the relation between the mirror tilt angle and the corresponding modulation depth. These effects were modeled. The model was experimentally verified and then used always when appropriate through this work.

The final version, Swing III, was built as a full spectrometer. The alignment stability over the mirror travel was sufficient and the thermal stability was acceptable. The mirror velocity errors were at about the same level as the interferometer in Gasmet™ spectrometer. However, Gasmet™ tolerated the external vibrations better. The best resolution of Swing III was below 4 cm^{-1} without apodisation and about 6 cm^{-1} with typical apodisation functions. Thus, the resolution is sufficient for the low resolution. The highest signal to noise ratio was 38 000:1, which is almost as good as with the laboratory spectrometer used as reference. The methane, water and carbon dioxide spectra were recorded. They were clean looking, had symmetric line shapes and had the correct line positions. The interferometer size was very close to the minimum possible size, which is ultimately limited by the beam diameter fixed to 25 mm. Therefore, the most of the major requirements for the portability were satisfied and thus the presented design is the well suitable interferometer for the low resolution portable FTIR spectrometer. Additionally, the presented design has much potential for a commercial product.

A few properties of the interferometer might be enhanced in the possible future version. The structure is still quite sensitive to the external vibrations so it had to be solved. Additionally, the excess heat from the infrared source should better conducted to outside the device and the response time to the temperature changes could be shortened. Possible solutions for these issues were presented but studying their effects leaves to the future work.

The current interferometer is suitable for FTIR spectrometer and it is in the phase where the academic research is changing to the product development. In fact, the next version might already be an early prototype of the commercial product. However, in addition to the improvements mentioned, the productisation still requires development in the supporting electronics and software and also in mechanics. This work shows that the current design has much potential for a commercial product. Furthermore, the interferometer might be optimised for the photoacoustic detecting by tuning it for the low mirror velocities. Additionally, the photoacoustic detector could be optimised for the interferometer to obtain hand-held spectrometer capable of recording FTIR spectra of small volume gas samples with very low concentrations. This could be further developed into the gas analyser having very broad applications for example in customs, rescue or other security businesses, or in industry.

Bibliography

[1] J. K. Kauppinen and J. O. Partanen, "High resolution IR spectroscopy (gas phase) instrumentation," in *Encyclopedia of Spectroscopy and Spectrometry*, J. C. Lindon, Ed. Elsevier, 2000, ch. Fundamentals of Spectroscopy: Methods and Instrumentation, pp. 784–794.

[2] P. R. Griffiths and J. A. de Haseth, *Fourier Transform Infrared Spectrometry*, 2nd ed. John Wiley & Sons, Inc, 2007.

[3] C. S. Williams, "Mirror misalignment in Fourier spectroscopy using Michelson interferometer with circular aperture," *Applied Optics*, vol. 5, no. 6, pp. 1084–1085, 1966.

[4] J. E. Chamberlain, *The Principles of interferometric spectroscopy.* John Wiley & Sons, 1979.

[5] J. Kauppinen, J. Heinonen, and I. Kauppinen, "Interferometers based on the rotational motion," *Applied Spectroscopy Reviews*, vol. 39, no. 1, pp. 99–130, 2004.

[6] M. V. R. K. Murty, "Some more aspects of the Michelson interferometer with cube corners," *Journal Of The Optical Society Of America*, vol. 50, no. 1, pp. 7–10, 1960.

[7] J. K. Kauppinen, I. K. Salomaa, and J. O. Partanen, "Carousel interferometer," *Applied Optics*, vol. 34, no. 27, pp. 6081–6085, 1995.

[8] J. Kauppinen and V.-M. Horneman, "Large aperture cube corner interferometer with a resolution of 0.001 cm^{-1}," *Applied Optics*, vol. 30, no. 18, pp. 2575–2578, 1991.

[9] R. S. Jackson, "Continuous scanning interferometers for mid-infrared spectrometry," in *Handbook of Vibrational Spectroscopy*, J. M. Chalmers and P. R. Griffiths, Eds. John Wiley & Sons, Ltd, 2002, vol. 1, ch. Instrumentation for Mid- and Far-infrared Spectroscopy, pp. 264–282.

[10] G. A. Vanasse and H. Sakai, *Fourier Spectroscopy*, ser. Progress in Optics, E. Wolf, Ed. Elsevier B.V., 1967, vol. 6.

[11] E. R. Peck, "A new principle in interferometer design," *Journal of the Optical Society of America*, vol. 38, no. 1, pp. 66–66, 1948.

[12] ——, "Theory of the corner-cube interferometer," *Journal of the Optical Society of America*, vol. 38, no. 12, pp. 1015–1015, 1948.

[13] S. Yazdi and B. Rashidian, "Two new swinging interferometers," *Journal of Optics A: Pure and Applied Optics*, vol. 9, no. 7, pp. 560–564, 2007.

[14] H. Rippel and R. Jaacks, "Performance data of the double pendulum interferometer," *Microchimica Acta*, vol. 95, no. 1-6, pp. 303–306, 1988.

[15] A. Simon, J. Gast, and A. Keens, "Fourier spectrometer," U.S. Patent 5 309 217, 1994.

[16] G. F. Hohnstreiter, T. P. Sheahen, and W. Howell, "Michelson interferometer-spectrometer for on-board space vehicle measurements," in *Aspen International Conference on Fourier Spectroscopy 1970*, G. A. Vanasse, A. Stair Jr., and D. J. Baker, Eds., Air Force Cambridge Research Laboratories. United States Air Force, 1971, pp. 243–254.

[17] R. A. Hanel, B. Schlachman, F. D. Clark, C. H. Prokesh, J. B. Taylor, W. M. Wilson, and L. Chaney, "The Nimbus III Michelson interferometer," in *Aspen International Conference on Fourier Spectroscopy 1970*, G. A. Vanasse, A. Stair Jr., and D. J. Baker, Eds., Air Force Cambridge Research Laboratories. United States Air Force, 1971, pp. 231–241.

[18] R. P. Walker and J. D. Rex, "Interferometer design and data handling in a high vibration environment – Part I: Interferometer design," in *Multiplex and/or High-Throughput Spectroscopy*, ser. Proceedings of the Society of Photo-optical Instrumentation Engineers, G. A. Vanasse, Ed., vol. 191, August 1979, pp. 88–91.

[19] C. J. Manning, "Tilt-compensated interferometers," U.S. Patent 6 469 790 B1, 2002.

[20] D&P Instruments Ltd., "TurboFT^{TM} portable FT-IR spectrometer," Instruction Manual, 2006. Available online: www.dpinstruments.com

[21] ——, "Model 102 portable FTIR," Instruction Manual, 2006. Available online: www.dpinstruments.com

[22] W. Wadsworth and J.-P. Dybwad, "Rugged high-speed rotary imaging Fourier transform spectrometer for industrial use," in *Vibrational Spectroscopy-based Sensor Systems*, ser. Proceedings of The International Society for Optical Engineering, S. D. Christesen and A. J. Sedlacek III, Eds., vol. 4577, 2002, p. 83.

[23] J. Kauppinen and J. Partanen, *Fourier Transforms in Spectroscopy*, 1st ed. Wiley-Vch Verlag Berling GmbH, 2001.

[24] C. Manning, M. Gross, J. Jennings, J. Wuthrich, and A. Samuels, "Miniature FT-IR spectrometer for passive and active sensing," in *Chemical and Biological Sensors for Industrial and Environmental Monitoring II*, ser. Proceedings of The International Society for Optical Engineering, S. D. Christesen, A. J. Sedlacek III, J. B. Gillespie, and K. J. Ewing, Eds., vol. 6378, 2006, p. 63780T.

[25] R. A. Spragg, "IR spectrometers," in *Encyclopedia of Spectroscopy and Spectrometry*, J. C. Lindon, Ed. Elsevier, 2000, ch. Fundamentals of Spectroscopy: Methods and Instrumentation, pp. 1048–1057.

[26] Tydex J.S.Co., "Brochures CVD-ZnSe, Germanium and Coating," Commercial brochures, 2010. Available online: www.tydexoptics.com

[27] Synchrotron Infrared Beamlines at The Advanced Light Source (ALS) at Berkeley Lab, "IR window materials," last accessed: Dec 7th 2013. Available online: http://infrared.als.lbl.gov/content/web-links/90-window-materials

[28] W. M. Haynes, Ed., *CRC Handbook of Chemistry and Physics*, 93rd ed. CRC Press/Taylor and Francis, internet version 2013.

[29] Thorlabs, "Zinc selenide (ZnSe) windows and plane mirror coatings," last accessed: Dec 7th 2013. Available online: www.thorlabs.de

[30] H. Bujis, "Incandescent sources for mid- and far-infrared spectrometry," in *Handbook of Vibrational Spectroscopy*, J. M. Chalmers and P. R. Griffiths, Eds. John Wiley & Sons, Ltd, 2002, vol. 1, ch. Instrumentation for Mid- and Far-infrared Spectroscopy, pp. 337–338.

[31] E. P. Goodwin and J. C. Wyant, *Field Guide to Interferometric Optical Testing*. Society of Photo-Optical Instrumentation Engineers (SPIE Press), 2006.

[32] A. H. Pfund, "An infrared spectrometer of large aperture," *Journal of the Optical Society of America*, vol. 14, no. 4, pp. 337–338, 1927.

[33] E. Theocharous and J. R. Birch, "Detectors for mid- and far-infrared spectrometry: Selection and use," in *Handbook of Vibrational Spectroscopy*, J. M. Chalmers and P. R. Griffiths, Eds. John Wiley & Sons, Ltd, 2002, vol. 1, ch. Instrumentation for Mid- and Far-infrared Spectroscopy, pp. 349–367.

[34] T. Kuusela and J. Kauppinen, "Photoacoustic gas analysis using interferometric cantilever microphone," *Applied Spectroscopy Reviews*, vol. 42, no. 5, pp. 443–474, 2007.

[35] V. Koskinen, J. Fonsen, K. Roth, and J. Kauppinen, "Progress in cantilever enhanced photoacoustic spectroscopy," *Vibrational Spectroscopy*, vol. 48, no. 1, pp. 16–21, 2008.

[36] J. Uotila, "Use of the optical cantilever microphone in photoacoustic spectroscopy," PhD Thesis, University of Turku, 2009.

[37] F. J. Harris, "On the use of windows for harmonic analysis with the discrete Fourier transform," *Proceedings of the IEEE*, vol. 66, no. 1, pp. 51–83, 1978.

[38] J. W. Brault, "New approach to high-precision Fourier transform spectrometer design," *Applied Optics*, vol. 35, no. 16, pp. 2891–2896, 1996.

[39] ABB Inc. Analytical Measurements, "MB3000 FT-IR laboratory analyzer brochure," Commercial brochure, 2012. Available online: www.abb.com/analytical

[40] Agilent Technologies Inc., "Agilent 4100 Exoscan FTIR: Operation manual," Commercial brochure, 2011. Available online: www.chem.agilent.com

[41] D. M. Macbride, C. G. Malone, J. P. Hebb, and E. G. Cravalho, "Effect of temperature variation on FT-IR spectrometer stability," *Applied Spectroscopy*, vol. 51, no. 1, pp. 43–50, 1997.

[42] C. A. Young, K. Knutson, and J. D. Miller, "Significance of temperature control in FT-NIR spectrometers," *Applied Spectroscopy*, vol. 47, no. 1, pp. 7–11, 1993.

[43] B. T. Bowie and P. R. Griffiths, "Measurement of the sensitivity and photometric accuracy of FT-IR spectrometers," *Applied Spectroscopy*, vol. 54, no. 8, pp. 1192–1202, 2000.

[44] M. Flik and Z. Zhang, "Influence of nonequivalent detector responsivity on FT-IR photometric accuracy," *Journal of Quantitative Spectroscopy and Radiative Transfer*, vol. 47, no. 4, pp. 293–303, 1992.

[45] P. Giesen and E. Folgering, "Design guidelines for thermal stability in optomechanical instruments," in *Optomechanics 2003*, ser. Proceedings of The International Society for Optical Engineering, A. E. Hatheway, Ed., vol. 5176, 2003, pp. 126–134.

[46] R. Hanel, D. Crosby, L. Herath, D. Vanous, D. Collins, H. Creswick, C. Harris, and M. Rhodes, "Infrared spectrometer for Voyager," *Applied Optics*, vol. 19, no. 9, pp. 1391–1400, 1980.

[47] A. Jacobson and Z. Bleier, "Monolithic interferometer with optics of different material," U.S. Patent 7 995 208 B2, 2011.

[48] Z. Bleier and I. Vishnia, "Monolithic optical assembly," U.S. Patent 6 141 101, 2000.

[49] P. R. Yoder Jr., *Opto-Mechanical systems design*, 1st ed., ser. Optical Engineering. Marcel Dekker, Inc., 1986.

[50] B. Saggin, E. Alberti, L. Comolli, M. Tarabini, G. Bellucci, and S. Fonti, "MIMA, a miniaturized infrared spectrometer for Mars ground exploration: Part III. Thermomechanical design," in *Sensors, Systems, and Next-Generation Satellites XI*, ser. Proceedings of The International Society for Optical Engineering, vol. 6744, 2007.

[51] B. Saggin, M. Tarabini, and D. Scaccabarozzi, "Infrared optical element mounting techniques for wide temperature ranges," *Applied Optics*, vol. 49, no. 3, pp. 542–548, 2010.

[52] Gasmet Technologies Ltd, "Gasmet^{TM} DX-4000 multicomponent FTIR gas analyzer," Commercial brochure, 2009. Available online: www.gasmet.com

[53] H. L. Buijs and J. McKinnon, "Two-beam interferometer for Fourier transform spectroscopy with double pivot scanning mechanism," U.S. Patent 7 480 055 B2, 2009.

[54] FTRX llc, "INT10-M ⌀1.00" mid-IR monolithic Michelson interferometer," Commercial online brochure, last accessed: Dec 7th 2013. Available online: www.ftrx-llc.com

[55] E. Herrala, P. Niemelä, and T. Hannula, "Miniaturized FT-IR spectrometer for industrial process measurements," in *In-Process Optical Measurements and Industrial Methods*, ser. Proceedings of The International Society for Optical Engineering, H. A. Macleod and P. Langenbeck, Eds., vol. 1266, 1990, pp. 86–90.

[56] A. A. van Veggel and H. Nijmeijer, "Stable mounting of beamsplitters for an interferometer," *Precision Engineering*, vol. 33, no. 1, pp. 7–17, 2009.

[57] J. A. Simonds, W. E. Costello, R. J. Combs, and R. T. Kroutil, "Internal diagnostics for FT-IR spectrometry," in *Electro-Optical Technology for Remote Chemical Detection and Identification II*, ser. Proceedings of The International Society for Optical Engineering, M. Fallahi and E. A. Howden, Eds., vol. 3082, 1997, pp. 106–120.

[58] L. Comolli and B. Saggin, "Evaluation of the sensitivity to mechanical vibrations of an IR Fourier spectrometer," *Review of Scientific Instruments*, vol. 76, no. 123112, 2005.

[59] N. J. Burton and T. J. Parker, "A high precision hydraulic moving mirror drive for use in Fourier transform spectroscopy," *International Journal of Infrared and Millimeter Waves*, vol. 5, no. 6, pp. 803–814, 1984.

[60] D. R. Nohavec, L. S. Schwartz, and D. L. Trumper, "Super-hybrid magnetic suspensions for interferometric scanners," *JSME International Journal Series C*, vol. 40, no. 4, pp. 570–582, 1997.

[61] H. Kobayashi, Ed., "Interferometric monitor for greenhouse gases (IMG) – project technical report," IMG Mission Operation & Verification Committee CRIEPI, Tech. Rep., 1999.

[62] R. V. Jones, "Parallel and rectilinear spring movements," *Journal of Scientific Instruments*, vol. 28, no. 2, pp. 38–41, 1951.

[63] S. T. Smith, *Flexures – elements of elastic mechanisms*, 1st ed. Gordon and Breach Science Publishers, 2000.

[64] R. V. Jones and I. R. Young, "Some parasitic deflexions in parallel spring movements," *Journal of Scientific Instruments*, vol. 33, no. 1, pp. 11–15, 1956.

[65] Z. Bleier and A. Jacobson, "Flexure mount for an optical assembly," U.S. Patent 8 205 853 B2, 2012.

[66] R. V. Jones, "Some uses of elasticity in instrument design," *Journal of Scientific Instruments*, vol. 39, no. 5, pp. 193–203, 1962.

[67] S. Awtar, "Synthesis and analysis of parallel kinematic XY flexure mechanisms," PhD Thesis, Massachusetts Institute of Technology, 2004.

[68] T. Välikylä and J. Kauppinen, "Experiments on the porch swing bearing of Michelson interferometer for low resolution FTIR," *Advances in Optical Technologies*, vol. 2013, 2013, article ID 948638.

[69] G. W. Small, R. T. Kroutil, J. T. Ditillo, and W. R. Loerop, "Detection of atmospheric pollutants by direct analysis of passive Fourier transform infrared interferograms," *Analytical Chemistry*, vol. 60, no. 3, pp. 264–269, 1988, pMID: 3354837.

[70] R. J. Huppi, R. B. Shipley, and E. R. Huppi, "Balloon-borne Fourier spectrometer using a focal plane detector array," in *Multiplex and/or High-Throughput Spectroscopy*, ser. Proceedings of The Society of Photo-optical Instrumentation Engineers, G. A. Vanasse, Ed., vol. 191, 1979, pp. 26–32.

[71] J. C. Kemp and R. J. Huppi, "Rocket-borne cryogenic Michelson interferometer," in *Multiplex and/or High-Throughput Spectroscopy*, ser. Proceedings of The Society of Photo-optical Instrumentation Engineers, G. A. Vanasse, Ed., vol. 191, 1979, pp. 135–142.

[72] E. H. Wishnow, R. E. Wurtz, S. Blais-Ouellette, K. H. Cook, D. J. Carr, I. T. Lewis, F. Grandmont, and C. W. Stubbs, "Visible imaging Fourier transform spectrometer: Design and calibration," in *Instrument Design and Performance for Optical/Infrared Ground-based Telescopes*, ser. Proceeding of The International Society for Optical Engineering, M. Iye and A. F. M. Moorwood, Eds., vol. 4841, 2002, p. 1067.

[73] E. Onillon, S. Henein, P. Theurillat, J. Krauss, and I. Kjelberg, "Interferometer scanning mirror mechanism," in *Mechatronic Systems 2002: A Proceedings Volume from the 2nd IFAC Conference*, ser. IFAC Proceedings Series, M. Tomizuka, Ed. Elsevier Ltd, 2003.

[74] G. L. Auth, "Ruggedized compact interferometer requiring minimum isolation from mechanical vibrations," U.S. Patent 4 693 603, 1987.

[75] D. R. Strait, "Moving mirror tilt adjust mechanism in an interferometer," U.S. Patent 4 991 961, 1991.

[76] R. F. Lacey, "Support for a moving mirror in an interferometer," U.S. Patent 4 710 001, 1987.

[77] G. R. Walker and R. A. Hookman, "Precision frictionless flexure based linear translation mechanism insensitive to thermal and vibrational environments," U.S. Patent 6 836 968 B1, 2005.

[78] K. C. Schreiber, "Support for a movable mirror in an interferometer," United States Patent Application Publication 2002/0149777, 2002.

[79] S. Sen, "Beam constraint model: Generalized nonlinear closed-form modeling of beam flexures for flexure mechanism design," PhD Thesis, University of Michigan, 2013.

[80] S. Awtar, E. Sevincer, and A. H. Slocum, "Charasteristics of beam-based flexure modules," *Journal of Mechanical Design*, vol. 129, no. 6, pp. 625–639, 2006.

[81] L. L. Howell, *Compliant mechanisms*. John Wiley & Sons, Inc., 2001.

[82] Y. Muranaka, M. Inaba, T. Asano, and E. Furukawa, "Parasitic rotations in parallel spring movements," *International Journal of Japan Society of Precision Engineering*, vol. 25, no. 3, pp. 208–213, 1991.

[83] A. E. Hatheway, "The kinetic center of the cantilever beam," in *Optomechanical Design and Precision Instruments*, ser. Proceedings of The Society of Photo-Optical Instrumentation Engineers, A. E. Hatheway, Ed., vol. 3132, 1997, pp. 218–222.

[84] ——, "Alignment of flexure stages for best rectilinear performance," in *Optomechanical and Precision Instrument Design*, ser. Proceedings of The Society of Photo-Optical Instrumentation Engineers, A. E. Hatheway, Ed., vol. 2542, 1995, pp. 70–80.

[85] G. Bianchini, F. Castagnoli, M. Pellegrini, and L. Palchetti, "Frictionless mirror drive for intermediate resolution infrared Fourier transform spectroscopy," *Infrared Physics & Technology*, vol. 48, no. 3, pp. 217–222, 2006.

[86] D. M. Brouwer, J. P. Meijaarda, and J. B. Jonker, "Large deflection stiffness analysis of parallel prismatic leaf-spring flexures," *Precision Engineering*, vol. 37, no. 3, pp. 505–521, 2013.

[87] S. Timoshenko, *Strength of materials – Part I Elementary Theory and Problems*, 3rd ed. Robert E. Krieger Publishing Company, 1984.

[88] ——, *Strength of materials – Part II Advanced Theory and Problems*, 3rd ed. Robert E. Krieger Publishing Company, 1983.

[89] E. Pennala, *Lujuusopin perusteet*, 2nd ed. Otakustantamo, 1982.

[90] R. J. Stephenson, *Mechanics and properties of matter*. John Wiley & Sons Inc., 1952.

[91] W. C. Young and R. G. Budynas, *Roark's Formulas for Stress and Strain*, 7th ed. McGraw Hill Companies, Inc., 2002.

[92] K. E. Bisshopp and D. C. Drucker, "Large deflection of cantilever beams," *Quarterly of Applied Mathematics*, vol. 3, no. 3, pp. 272–275, 1945.

[93] M. H. Ang Jr., W. Wei, and L. Teck-Seng, "On the estimation of the large deflection of a cantilever beam," in *Proceedings of the IECON '93 – 19th Annual Conference of IEEE Industrial Electronics*. IEEE, 1993, pp. 1604–1609.

[94] T. Beléndez, C. Neipp, and A. Beléndez, "Large and small deflections of a cantilever beam," *European Journal of Physics*, vol. 23, no. 3, pp. 371–379, 2002.

[95] R. Magnusson, "Light sources and optics," in *Encyclopedia of Spectroscopy and Spectrometry*, J. C. Lindon, Ed. Elsevier, 2000, ch. Fundamentals of Spectroscopy: Methods and Instrumentation, pp. 1158–1168.

[96] T. Välikylä and J. Kauppinen, "Modulation depth of Michelson interferometer with Gaussian beam," *Applied Optics*, vol. 50, no. 36, pp. 6671–6677, 2011.

[97] F. Villar, J. David, and G. Genevès, "75 mm stroke flexure stage for the LNE watt balance experiment," *Precision Engineering*, vol. 35, no. 4, pp. 693–703, 2011.

[98] G. C. Auguson and N. O. Young, "A liquid-helium-cooled Michelson interferometer," in *Aspen International Conference on Fourier Spectroscopy 1970*, G. A. Vanasse, A. Stair Jr., and D. J. Baker, Eds., Air Force Cambridge Research Laboratories. United States Air Force, 1971, pp. 281–288.

[99] E. I. Rivin, *Passive Vibration Isolation*, 1st ed. ASME Press (American Society of Mechanical Engineering), 2003.

[100] D. J. Inman, *Engineering vibration*, 2nd ed. Prentice-Hall Inc., 2001.

[101] J. P. den Hartog, *Mechanical Vibrations*, 4th ed. Dover Publications, Inc., 1985.

[102] Pacific Northwest National Laboratory, "Northwest-infrared vapor phase infrared spectral library," last accessed: Dec 7th 2013. Available online: http://nwir.pnl.gov/

[103] Bruker Inc., "TENSOR series brochure," Commercial brochure, last accessed: Dec 7th, 2013, 2012. Available online: www.bruker.com/products/infrared-and-raman-spectroscopy/ft-ir-routine-spectrometers/tensor

[104] M. Abramowitz and I. A. Stegun, Eds., *Handbook of Mathematical Functions with formulas, graphs, and mathematical tables*, 9th ed. Dover Publications, Inc., 1972.

[105] M. R. Spiegel and J. Liu, *Mathematical Handbook of Formulas and Tables*, ser. Schaum's outline series. McGraw Hill Companies, Inc., 1999.

Appendix A

Modulation depth of circular beam

A.1 Circular uniform beam

Interferogram without a constant component at Michelson interferometer output is $I(x)$, where x is the optical path difference. The beam cross section is circular with radius R. If the mirror misalignment angle or tilt angle α is non-zero, extra optical path difference y is added to x as represented in Fig. A.1(a). Intensity at the exit aperture is then $I(x+y)$. According to Fig. A.1(b), the mean of the intensity on the aperture is

$$\begin{aligned} I_B(x) &= \frac{\text{Mean power on aperture}}{\text{Aperture area}} \\ &= \frac{1}{\pi(2\alpha R)^2}\int_{-2\alpha R}^{2\alpha R} I(x+y)\cdot 2\sqrt{(2\alpha R)^2-y^2}\cdot\,\mathrm{d}y \\ &= \int_{-\infty}^{\infty} I(x+y)B(y)\,\mathrm{d}y, \end{aligned} \tag{A.1}$$

where

$$B(y)=\begin{cases} \dfrac{2\sqrt{(2\alpha R)^2-y^2}}{\pi(2\alpha R)^2} & |y|\le 2\alpha R \\ 0 & \text{elsewhere.} \end{cases} \tag{A.2}$$

Function $B(y)$ can be regarded as the aperture weighting function of the intensity. If interferogram $I(x)$ in Eq. (2.6) is substituted to Eq. (A.1) as $I(x+y)$ the mean of the intensity will be

$$I_B(x)=\int_{-\infty}^{\infty} E(\nu)\exp\left(\mathrm{i}2\pi\nu x\right)\underbrace{\left[\int_{-\infty}^{\infty} B(y)\exp\left(\mathrm{i}2\pi\nu y\right)\,\mathrm{d}y\right]}_{\equiv\, m}\mathrm{d}\nu. \tag{A.3}$$

The integral inside square brackets is the modulation depth of the interferometer m. It is actually the Fourier transform of the function $B(y)$ or

$$m=\frac{1}{\pi(2\alpha R)^2}\int_{-2\alpha R}^{2\alpha R} 2\sqrt{(2\alpha R)^2-y^2}\exp\left(\mathrm{i}2\pi\nu y\right)\,\mathrm{d}y.$$

By changing variables $u=y/(2\alpha R)$, we obtain

$$m=\frac{2}{\pi}\int_{-1}^{1} e^{\mathrm{i}\pi k u}\sqrt{1-u^2}\,\mathrm{d}u,$$

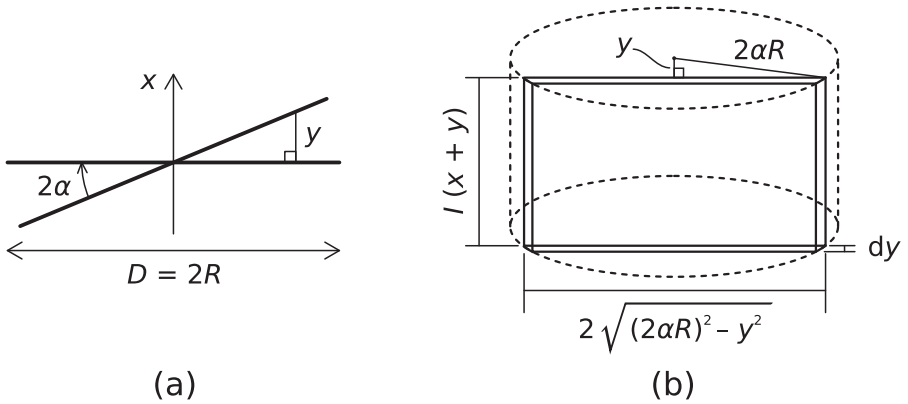

Figure A.1 The tilt angle α produces the angle 2α between the output beams as is drawing (a), which causes extra optical path difference y in addition to x. The drawing (b) illustrates the calculating of the mean intensity on the circular exit aperture.

where $k = 4R\alpha\nu$. After applying Euler's formula, this equation becomes

$$m = \frac{4}{\pi}\int_0^1 \cos(\pi k u)\sqrt{1-u^2}\,\mathrm{d}u. \tag{A.4}$$

From integral tables [104, Eq. (9.1.20) p. 360], one can find that

$$J_n(x) = \frac{2\left(\frac{1}{2}x\right)^n}{\sqrt{\pi}\,\Gamma\left(n+\frac{1}{2}\right)}\int_0^1 \cos(xt)\left(1-t^2\right)^{n-\frac{1}{2}}\,\mathrm{d}t,$$

where $J_n(x)$ is Bessel function of the nth kind. By substituting $n = 1$ and $\Gamma(3/2) = \sqrt{\pi}/2$ [105], we obtain the relation

$$\frac{\pi}{2}\frac{J_1(x)}{x} = \int_0^1 \cos(xt)\sqrt{1-t^2}\,\mathrm{d}t \tag{A.5}$$

Using Eq. (A.5), we can express Eq. (A.4) using Bessel function and obtain Eq. (2.9) on page 9, or

$$m = \frac{2J_1(\pi k)}{\pi k}. \tag{2.9}$$

A.2 Circular Gaussian beam

If the intensity of the beam has Gaussian distribution, which is symmetrical and centred at origin, then intensity has a form

$$g(t,u) = g_0 \exp\left(-\frac{t^2+u^2}{2\sigma^2}\right), \tag{A.6}$$

where g_0 is a constant, t and u are coordinates of cross section of the beam as illustrated in Fig. A.2(a) and σ is the standard deviation of the distribution. Since the tilt angle α is very small, the relation between the optical path difference y and the aperture coordinate t is $y = t\tan 2\alpha \approx 2\alpha t$ according to Fig. A.2(b). Using this relation, the weighting function $G(y)$ for a small extra optical path difference $\mathrm{d}y$ is defined (or the intensity of one beam on a small $\mathrm{d}t$ wide area on aperture is calculated) as

$$G(y)\frac{\mathrm{d}y}{2\alpha} = \exp\left[-\frac{y^2}{8(\alpha\sigma)^2}\right]\left[\int_{-q(y)}^{q(y)} \exp\left(-\frac{u^2}{2\sigma^2}\right)\mathrm{d}u\right]\frac{\mathrm{d}y}{2\alpha}, \tag{A.7}$$

where

$$q(y) = \sqrt{R^2 - \left(\frac{y}{2\alpha}\right)^2}.$$

This corresponds the weighting function $B(y)$ in Eq. (A.2). Similarly as with Eq. (A.3), the mean of the intensity at the exit aperture is

$$I_G(x) = \int_{-\infty}^{\infty} E(\nu)\exp(\mathrm{i}2\pi\nu x)\underbrace{\left[G_0\int_{-\infty}^{\infty} G(y)\exp(\mathrm{i}2\pi\nu y)\ \mathrm{d}y\right]}_{\equiv m_G}\mathrm{d}\nu, \tag{A.8}$$

where the integral in square brackets is the modulation depth m_G. The coefficient G_0 sets the value of the modulation depth to the interval $0 \leq m_G \leq 1$. The coefficient G_0 includes also the coefficient 2α from exchange of variables in Eq. (A.7). Eventually, the modulation depth at the circular exit aperture with Gaussian distributed beam is Eq. (4.7) or

$$m_G = G_0\int_{-2\alpha R}^{2\alpha R}\exp\left[-\frac{y^2}{8(\alpha\sigma)^2}\right]\left[\int_{-q(y)}^{q(y)}\exp\left(-\frac{u^2}{2\sigma^2}\right)\mathrm{d}u\right]\exp(\mathrm{i}2\pi\nu y)\,\mathrm{d}y.$$

Equation (4.7) can be simplified by approximating the Gaussian intensity distribution as a constant along the u-axis. Then, the integral over u will be

$$\int_{-q(y)}^{q(y)}\exp\left(-\frac{u^2}{2\sigma^2}\right)\mathrm{d}u \approx \int_{-q(y)}^{q(y)}\mathrm{d}u = 2q(y) = 2\pi\alpha R^2 B(y), \tag{A.9}$$

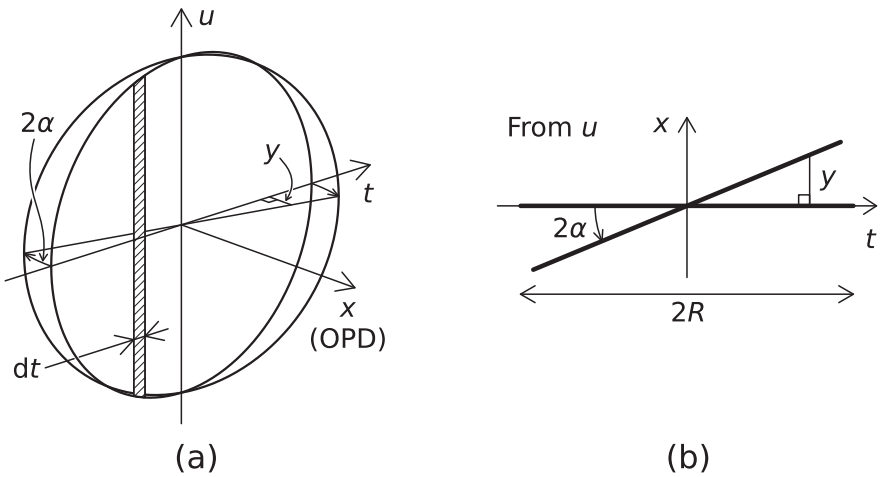

Figure A.2 Drawing (a) is the cross section of two interfering beams having Gaussian intensity distribution. The angle 2α between the beams produces extra optical path difference y in addition to x, as illustrated in (b). Figure is reproduced from [96].

which is the function $B(y)$ scaled with a constant. Thus, Equation (4.7) is approximately

$$m_G \approx M_0 \int_{-\infty}^{\infty} B(y) \exp\left[-\frac{y^2}{8(\alpha\sigma)^2}\right] \exp\left(\mathrm{i}2\pi\nu y\right)\, \mathrm{d}y \equiv m_{G*},$$

where M_0 is normalizing constant, which includes coefficients from Eq. (4.7) and Eq. (A.9). The above equation represents actually the Fourier transform of the product of $B(y)$ and Gaussian function, which can be expressed in the convolution form

$$m_{G*} = M_0 \left(\mathcal{F}\left\{B(y)\right\} * \mathcal{F}\left\{\exp\left[-\frac{y^2}{8(\alpha\sigma)^2}\right]\right\}\right), \tag{A.10}$$

Constant M_0 is the reciprocal of the value of the convolution at zero. The Fourier transform of $B(y)$ is given in Eq. (2.8) on page 9. The Fourier transform of Gaussian function is

$$\mathcal{F}\left\{\exp\left[-\frac{y^2}{2(2\alpha\sigma)^2}\right]\right\} = 2\sqrt{\frac{2}{\pi}}\,\sigma\alpha\, \exp\left[-2\left(2\pi\sigma\alpha\nu\right)^2\right]. \tag{A.11}$$

Thus, the modulation depth can be expressed as a convolution of Bessel and Gaussian functions, which is much more easier to conceive than the original double integral form.

By using $k = 4R\alpha\nu$ from Eq. (2.10) on page 9, we can express the right side of Eq. (A.11) as

$$\sqrt{\frac{2}{\pi}}\,\frac{\sigma k}{2R\nu}\, \exp\left[-2\left(\frac{\pi\sigma k}{2R}\right)^2\right].$$

When using the monochromatic light beam and a fixed beam diameter, the transform Eq. (A.11) is actually a function of the number of the fringes in across the beam k and the standard deviation of the beam σ. Because the Fourier transform of the $B(y)$ is a function of k according to Eq. (2.9), the convolution approximation m_{G*} is a function of k and σ or $m_{G*} = m_{G*}(k, \sigma)$.

The approximation of Gaussian distributed intensity as a constant along the u-axis in Eq. (A.9) decreases the accuracy of the convolution approximation m_{G*} in some extent when the ratio of the beam standard deviation and the beam diameter is $\sigma/(2R) < 1$. The accuracy of the convolution model can be further improved by replacing the actual standard deviation with the effective standard deviation σ_c, which was determined by numerical calculations described in detail in [96]. Hence, the convolution model m_{Gc} is finally defined as

$$m_{Gc}(k, \sigma) = m_{G*}(k, \sigma_c), \tag{A.12}$$

where

$$\sigma_c = \sigma \left[1.23 - \frac{0.23}{1 + \left(\frac{4.3\sigma}{2R} \right)^{2.8}} \right].$$

Appendix B

Models for parasitic motions

B.1 Intersection of two circles

The intersection of two circles can be calculated if centres and radii of the circles are known. Let the first circle be centred at P_0 and have the radius of r_0 and the second at P_1 with the radius of r_1, as illustrated in Fig. B.1(a). The distance between the centers of the circles or the points P_0 and P_1 is

$$d = \sqrt{(z_1 - z_0)^2 + (y_1 - y_0)^2}, \tag{B.1}$$

By applying Pythagorean theorem to triangles $\triangle P_0AP_2$ and $\triangle AP_1P_2$, one obtains equations

$$a^2 + p^2 = r_0^2 \tag{B.2a}$$
$$b^2 + p^2 = r_1^2, \tag{B.2b}$$

where a is the length of the line $\overline{P_0A}$, b is the length of $\overline{AP_1}$ and p is the length of $\overline{AP_2}$. By subtracting these equations from each other and substituting $b = d - a$, the distance from P_0 to A is obtained as

$$a = \frac{r_0^2 - r_1^2 + d^2}{2d}. \tag{B.3}$$

When this is substituted to Eq. (B.2a), one obtains the length of the line $\overline{A\ P_2}$, which is

$$p = \sqrt{r_0^2 - a^2}. \tag{B.4}$$

Using the ratios of the similar triangles as in Fig. B.1(b), one can apply relations

$$\frac{z_1 - z_0}{z_A - z_0} = \frac{d}{a} \qquad \text{and} \qquad \frac{y_1 - y_0}{y_A - y_0} = \frac{d}{a},$$

where z_A and y_A are coordinates of the point A. Coordinates of the point A are then

$$z_A = z_0 + \frac{a}{d}(z_1 - z_0) \tag{B.5a}$$
$$y_A = y_0 + \frac{a}{d}(y_1 - y_0). \tag{B.5b}$$

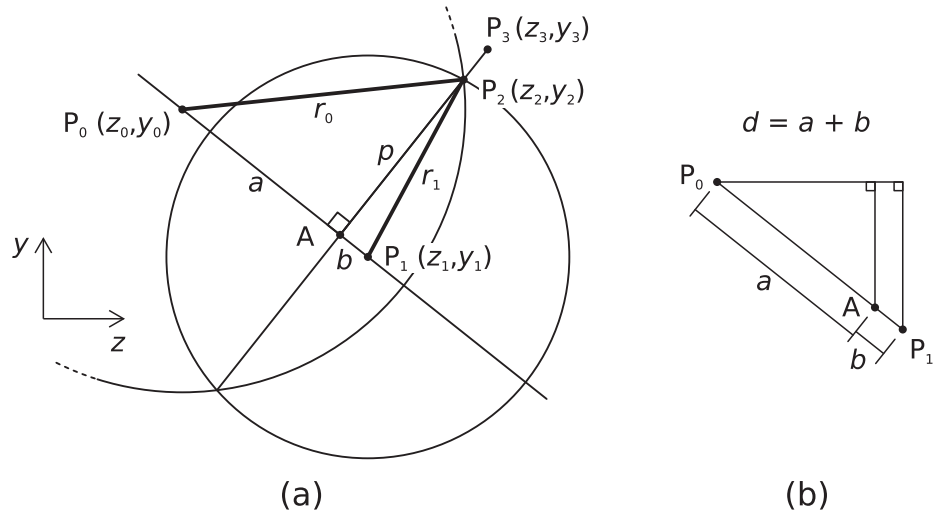

Figure B.1 Determining coordinates of the intersection P_2 of two circles.

If we put a vector of length d to start from P_0 and pointing to P_1, coordinates of its end point (at P_1) are

$$z_1 = z_0 + (z_1 - z_0)$$
$$y_1 = y_0 + (y_1 - y_0)\,.$$

If we move this vector to the point A and rotate it 90° so that it is pointing to P_2, coordinates of its end will be

$$z_3 = z_A - (y_1 - y_0)$$
$$y_3 = y_A + (z_1 - z_0)\,.$$

When the length of this vector is scaled from d to κ and coordinates of the point A are substituted from Eq. (B.5a) and Eq. (B.5b), we obtain coordinates of the point P_2 as

$$z_2 = z_0 + \frac{a}{d}(z_1 - z_0) - \frac{p}{d}(y_1 - y_0) \tag{B.6}$$
$$y_2 = y_0 + \frac{a}{d}(y_1 - y_0) + \frac{p}{d}(z_1 - z_0)\,. \tag{B.7}$$

B.2 Approximation with small deflection angles

Equations of the pitch rotation angles can be approximated using simpler expressions than equations of the intersection of two circles. Flexure elements are again approximated as rigid links. Additionally, the travel length of the arm and deflection angles are supposed to be small. Then the arm

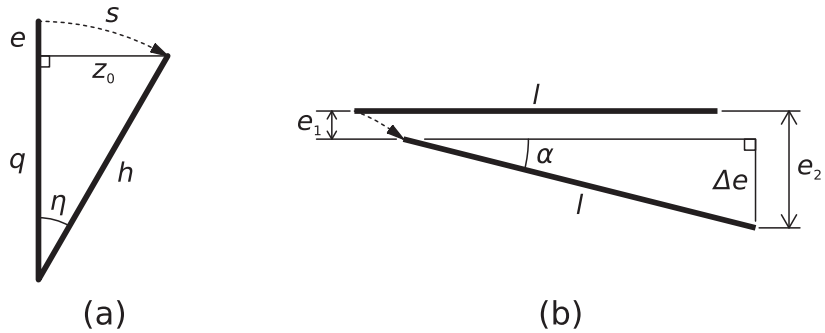

Figure B.2 Estimation of the pitch tilt angle, when only the flexure length h has error. The error is exaggerated.

of length h is pushed to the position z_0, as presented in Fig. B.2(a). Then the rotation angle of the flexure element is $\eta = s/h \approx z_0/h$ and length q is

$$q = h\cos\eta \approx h\left(1 - \frac{\eta^2}{2}\right) \approx h - \frac{z_0^2}{2h}.$$

The vertical shift of the arm is

$$e = h - q = \frac{z_0^2}{2h}.$$

The movable arm will move and rotate as presented in Fig. B.2(b). Vertical shifts of the arm ends e_1 and e_2 correspond flexure lengths h and $h + \Delta h$. The angle of the pitch tilt is approximately the angle α, which can be calculated as

$$\alpha \approx \frac{e_2 - e_1}{l} = \frac{z_0^2}{2l}\left(\frac{1}{\Delta h + h} - \frac{1}{h}\right).$$

Because the error Δh is small compared to the flexure length h, the pitch can be approximated as in Eq. (3.5), or

$$\alpha \approx -\frac{z_0^2 \Delta h}{2h^2 l}. \tag{3.5}$$

If flexures have equal lengths h but arms have the length difference Δl, the arm moves from CF to BE, as illustrated in Fig. B.3. If the error Δl is very small, triangles ABC and DEF are almost congruent. When the triangle DEF is rotated around the point D so that the side DF becomes perpendicular to the side AD, we obtain a new triangle DE'F', which is depicted in Fig. B.3. The angle of this rotation is

$$\varphi = \Delta l/h.$$

Vertical distance e_2 between points E and E' is the product of the angle φ and the length of the line GE. Because the error Δl is small, lengths of the lines GE and HE' are approximately equal to z_0. Then

$$e_2 = \varphi z_0.$$

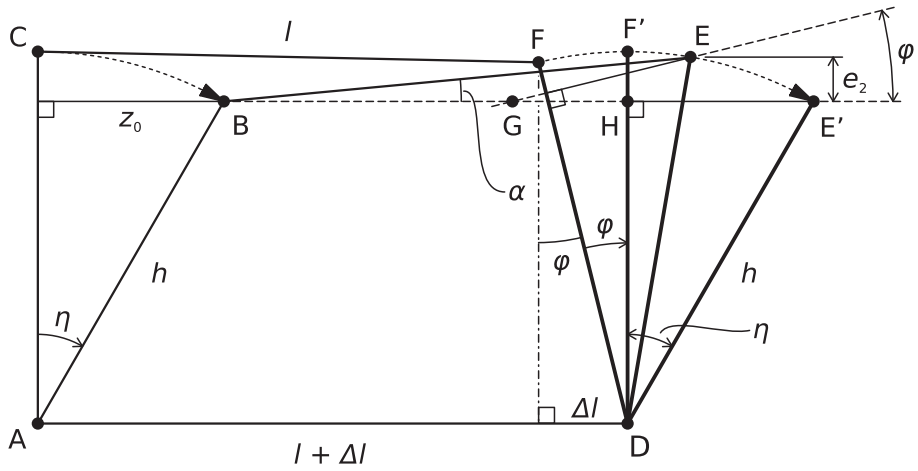

Figure B.3 Approximation of the pitch rotation angle, when only the arm length l has error. The error is exaggerated.

The pitch rotation is approximately equal to the angle ∠EBE', which is e_2 divided by the length l of the line BE', or $\alpha \approx \angle\text{EBE'} \approx e_2/l$. By combining these results, we can estimate the pitch angle as

$$\alpha \approx \frac{z_0 \Delta l}{hl}. \tag{3.6}$$

B.3 Yaw rotations from non-parallel flexures

Let's assume that neutral axes of flexures are rotated to each other by a small angle θ around the z axis as illustrated in Fig. 3.6(a) on page 49 and the angle is symmetrically distributed on the both flexures. The point P is at the other end of the upper arm of the ideal porch swing. Because of the non-parallelism, the point P is rotated around the z axis by the angle $\theta/2$ and ended up to P_1 as depicted in Fig. B.4(a). The distance from the origin remains constant h. Coordinates of the point P_1 are

$$\mathrm{P}_1 : \begin{cases} x_1 = h \sin\left(\frac{1}{2}\theta\right) \\ y_1 = h \cos\left(\frac{1}{2}\theta\right) \\ z_1 = 0. \end{cases} \tag{B.8}$$

Let's define the second frame of reference, which is obtained by rotating the first coordinate system equally as the flexure. This second reference frame is marked with dots in Fig. B.4. In the second frame of reference, the point P_1 is at

$$\mathrm{P}_1 : \begin{cases} x_1' = 0 \\ y_1' = h \\ z_1' = 0. \end{cases}$$

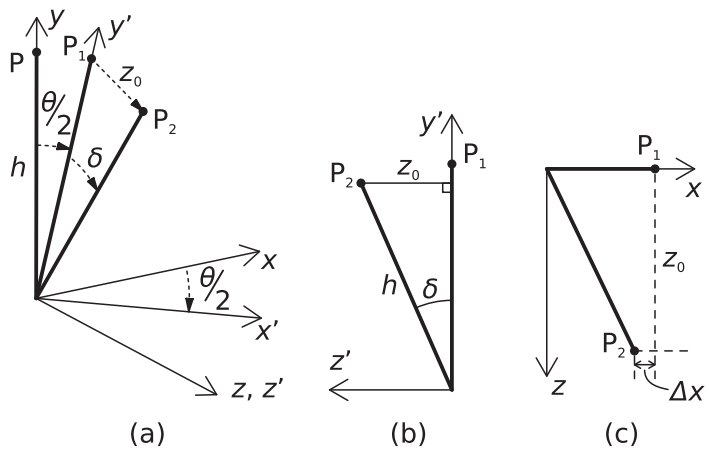

Figure B.4 Non-parallelism of the neutral axes of the flexures. One flexure element is rotated around the z axis by the small angle $\frac{1}{2}\theta$, so the point P at the upper arm end is actually at P_1. When the arm is pushed the travel z_0, the flexure is rotated around the axis x' and P_1 is moved to P_2 as in the drawing (a). The drawing (b) is the $z'y'$ plane viewed from x'. The displacement z_0 causes a slight shift Δx as in the drawing (c). The angle θ is exaggerated.

Now, if the upper arm is pushed by the amount z_0, the flexure tends to rotate around the x' axis instead of the x axis. This causes a slight shift in the x direction. Because corresponding shifts of different flexures are in the opposite directions, the upper arm tends to yaw, or rotate around the y axis. After pushing, the point P_1 is moved to P_2. Using the $z'y'$ plane as in Fig. B.4(b), we can determine coordinates of P_2 and obtain

$$\mathrm{P}_2 : \begin{cases} x_2' &= 0 \\ y_2' &= h\cos\delta \\ z_2' &= z_0. \end{cases}$$

Using direction cosines [105], coordinates of the point P_2 can be expressed in the first frame of reference as

$$\mathrm{P}_2 : \begin{cases} x_2 &= y_2' \sin\left(\frac{1}{2}\theta\right) \\ y_2 &= y_2' \cos\left(\frac{1}{2}\theta\right) \\ z_2 &= z_0. \end{cases} \tag{B.9}$$

During the pushing, the point P_1 at the upper arm is shifted in the x direction by the amount of Δx as depicted in Fig. B.4(c). By using Eq. (B.8) and Eq. (B.9), the shift is

$$\Delta x = x_1 - x_2 \approx \frac{\theta}{2}\left[h - h\left(1 - \frac{z_0^2}{2h^2}\right)\right] = \frac{\theta z_0^2}{4h}.$$

The total yaw rotation angle is then $\beta = 2\Delta x/l$, or

$$\beta = \frac{\theta z_0^2}{2lh}. \tag{3.8}$$

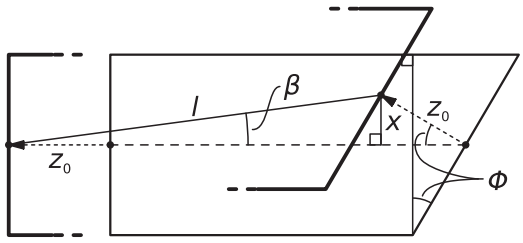

Figure B.5 The yaw tilting produced by the small angle ϕ between the principal axes of inertia of flexures. The ends of the arm tend to move in different direction, which rotates the arm. The angle ϕ is exaggerated.

If ϕ is a small angle between principal axes of inertia of flexures, as in Fig. 3.6(b) on page 49 and in Fig. B.5, the other end of the arm tends to move straight and the other in the angle. This results in the yaw tilting of the arm. The yaw is the angle between the horizontal line, or the initial condition, and the center of the arm displaced at z_0. If angles are small, the vertical shift is $x \approx \phi z_0$ and the tilt angle is $\beta \approx x/l$ according to Fig. B.5. By combining these equations, one obtains the tilt angle as

$$\beta = \frac{\phi z_0}{l}. \tag{3.9}$$

Appendix C

Simple beam bending

C.1 Flat springs

One flat spring, which length is h, width is b and thickness is t, is bent as in Fig. C.1(a). Both ends of the spring are mounted on arms of the porch swing. The spring has uniform rectangular cross section and it is initially straight. Tension and compression forces are assumed to be negligible. The only loading force is the driving force $\mathbf{F}$. The spring material is assumed to be homogenous and isotropic. Deflections are so small that limits of elasticity or proportionality are not exceeded, so the spring follows Hooke's law. Additionally, Bernoulli's assumption is assumed to be valid or each cross sectional plane is assumed to remain planar. The spring is long and slim, or $h >> b$ and $h >> t$.

The deflection curve $v(y)$ is the deflection of the spring in the z direction at y. The deflection is zero at the other end $y = h$, and has its maximum v_{end} at the another end, or $y = 0$. The deflection curve can be calculated using

$$\frac{M(y)}{EI} = -\frac{\mathrm{d}^2 v}{\mathrm{d}y^2}\left[\,1 + \left(\frac{\mathrm{d}v}{\mathrm{d}y}\right)^2\,\right]^{-\frac{3}{2}}, \tag{C.1}$$

where E is the modulus of elasticity of the spring material, I is the second moment of area of the spring and $M(y)$ is the bending moment [87, p. 139]. With small deflections, the term $(\,\mathrm{d}v/\,\mathrm{d}y)^2$ is usually smaller than one and can be neglected, so the equation simplifies to

$$EI\frac{\mathrm{d}^2 v}{\mathrm{d}y^2} = -M(y). \tag{C.2}$$

The second moment of the area I of the spring is calculated in reference to the x axis or $I = I_x$ as depicted in Fig. C.2. It is [89]

$$I \;= \int_A z^2\,\mathrm{d}A = \int_{-t/2}^{t/2} z^2 \cdot b\,\mathrm{d}z \;=\; \frac{bt^3}{12}. \tag{C.3}$$

Because the shear force is constant along the spring, the bending moment is

$$M(y) = M_{\mathrm{A}} - Fy,$$

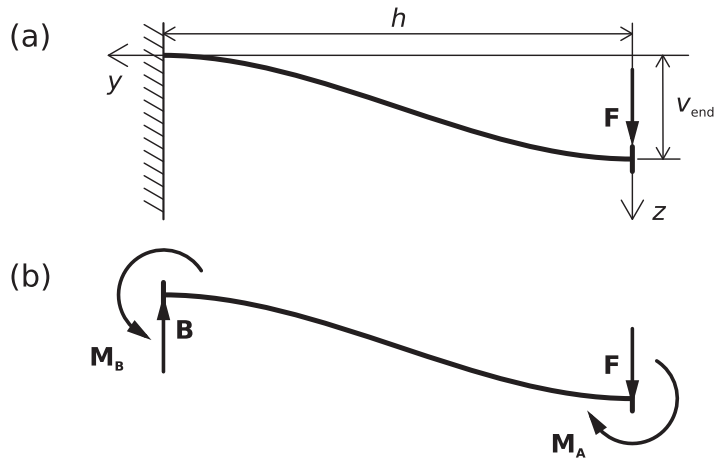

Figure C.1 Deflection of the flat spring (a) and the free body diagram of the spring (b). The left end of the spring is mounted on the lower arm and the right end on the movable arm. The force **F** is the driving force exerted to one spring. The force **B** is the reaction force and moments $\mathbf{M}_\mathrm{A}$ and $\mathbf{M}_\mathrm{B}$ are reaction moments exerted by arms.

where M_A is the reaction moment of the upper arm of the porch swing. The moment M_A cannot be solved from principles of statics, so the situation is statically undetermined. However, it can be solved by substituting the bending moment in Eq. (C.2) and integrating twice. Then one obtains

$$\begin{aligned} EI\frac{\mathrm{d}v}{\mathrm{d}y} &= \frac{1}{2}Fy^2 - M_\mathrm{A}y + C_1 \\ EIv(y) &= \frac{1}{6}Fy^3 - \frac{1}{2}M_\mathrm{A}y^2 + C_1y + C_2, \end{aligned} \tag{C.4}$$

where C_1 and C_2 are integration constants. After applying the boundary conditions

$$\begin{aligned} y = 0 \text{ or } y = h \quad &\Leftrightarrow \quad \frac{\mathrm{d}v}{\mathrm{d}y} = 0 \\ y = h \quad &\Leftrightarrow \quad v = 0 \end{aligned}$$

the constants can be calculated as

$$C_1 = 0 \qquad M_\mathrm{A} = \tfrac{1}{2}Fh \qquad C_2 = \tfrac{1}{12}Fh^3.$$

When these are substituted to Eq. (C.4), one obtains the deflection curve

$$v(z) = \frac{Fh^3}{12EI}\left(1 - 3\frac{z^2}{h^2} + 2\frac{z^3}{h^3}\right). \tag{C.5}$$

Then the deflection of the spring end is [89]

$$v_\mathrm{end} = v(0) = \frac{Fh^3}{12EI}. \tag{C.6}$$

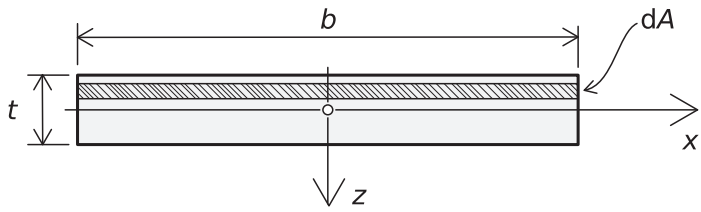

Figure C.2 Calculation of the second moment of area I of the flat spring in reference to the x axis.

C.2 Springs with stiffeners

When the stiffening clamps are mounted in the middle of the spring, the situation is as in Fig. C.3. The flexural rigidity EI of the stiffener part is very much larger than flexural rigidity of the spring parts. Thus, the flexure element is bent only in its ends, or in the parts 1 and 3. The bending moment has the same form as earlier, but the flexure length is now $h = 2c + a$, thus

$$M(y) = \frac{F(2c+a)}{2}\left(1 - \frac{2y}{2c+a}\right). \tag{C.7}$$

The bending curve of each part can be calculated separately because the flexural rigidity is constant in each part. However, actually the deflection of the flexure element end is interested, so solving the deflection curve is not necessary. The parts 1 and 3 are bent symmetrically so their total deflections are equal. The deflection of the part 2 is negligible. Therefore, it is sufficient to calculate the total deflection of one of the parts 1 and 3, and the angle β between the stiffening clamp and the y axis to calculate the deflection of the part 2.

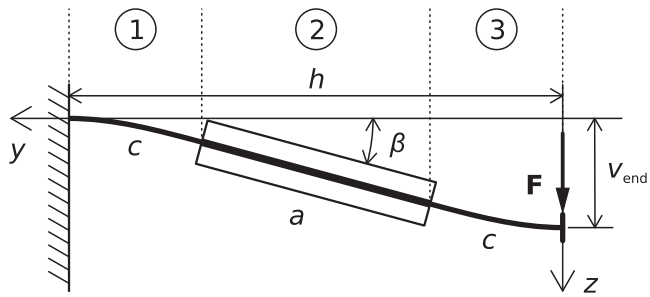

Figure C.3 Deflection of flat spring with the stiffening clamps mounted in the middle of the springs. The left end the spring is mounted on the lower arm and the right end on the movable arm. The force **F** is the driving force exerted to one spring.

The bending curve of the part 1 have to satisfy Eq. (C.2) and Eq. (C.7), which leads to the group of equations

$$EI\frac{\mathrm{d}^2v}{\mathrm{d}y^2} = \frac{F(2c+a)}{2}\left(\frac{2y}{2c+a} - 1\right) \tag{C.8a}$$

$$EI\frac{\mathrm{d}v}{\mathrm{d}y} = \frac{F(2c+a)}{2}\left(\frac{y^2}{2c+a} - y\right) + C_1 \tag{C.8b}$$

$$EIv(y) = \frac{F(2c+a)}{2}\left(\frac{y^3}{3(2c+a)} - \frac{y^2}{2}\right) + C_1 y + C_2. \tag{C.8c}$$

By applying boundary conditions at $y = 2c + a$, where $\frac{\mathrm{d}v}{\mathrm{d}x} = 0$ and $v = 0$, integration constants become

$$C_1 = 0 \qquad C_2 = \tfrac{1}{12}F(2c+a)^3.$$

The deflection at the end of the part 1, or at $y = c + a$, is then

$$\delta_1 = v(c+a) = \frac{F}{12EI}\left(4c^3 + 3c^2a\right).$$

The deflection of the part 2, or the rigid part, can be calculated using the slope D of the bending curve of part 1 at $y = c + a$, which is equal to the slope of the stiffening clamps. With small deflections the slope is approximately equal to the angle β. According to Eq. (C.8b), the slope is

$$D = \left.\frac{\mathrm{d}v}{\mathrm{d}y}\right|_{y=c+a} = -\frac{Fc(c+a)}{2EI}.$$

The deflection of the part 2 in the z direction is then

$$\delta_2 = -aD = \frac{Fca(c+a)}{2EI}.$$

As noted already, the total deflections of the parts 1 and 3 are equal, or $\delta_1 = \delta_3$. Therefore, the total deflection v_{end} of the whole flexure element is

$$\Delta y = 2\delta_1 + \delta_2 = \frac{Fc}{6EI}\left(4c^2 + 6ca + 3a^2\right).$$

Because the length of the stiffening clamps is $a = h - 2c$, this equation can be expressed as

$$v_{\mathrm{end}} = \frac{Fc}{6EI}\left(4c^2 - 6ch + 3h^2\right). \tag{C.9}$$

Awtar et al [80] have been studied the similar flexure element with is also under tension or compression in addition to the driving force **F**. If these

normal forces are zero, the normalised driving force and the normalised reaction moment are, respectively, [80, Eq. (9)]

$$f_{\mathrm{n}} = \frac{6v_{\mathrm{end,n}}}{c_{\mathrm{n}}\left(4c_{\mathrm{n}}^2 - 6c_{\mathrm{n}} + 3\right)} \tag{C.10}$$

$$m_{\mathrm{n}} = \frac{-3v_{\mathrm{end,n}}}{c_{\mathrm{n}}\left(4c_{\mathrm{n}}^2 - 6c_{\mathrm{n}} + 3\right)}. \tag{C.11}$$

where $f_{\mathrm{n}} = Fh^2/(EI)$, $m_{\mathrm{n}} = Mh/(EI)$, M is the bending moment, c_{n} is normalized hinge length or $c_{\mathrm{n}} = c/h$ and $v_{\mathrm{end,n}}$ is the normalised total deflection. The normalized reaction moment in the end of the spring is the moment. By comparing these equations together, one can observe that $m_{\mathrm{n}} = -\frac{1}{2}f_{\mathrm{n}}$. By substituting the normalising factors, one obtains

$$m_{\mathrm{n}} = -\frac{1}{2}f_{\mathrm{n}} \qquad \Leftrightarrow \qquad \frac{Mh}{EI} = -\frac{1}{2}\frac{Fh^2}{EI} \qquad \Leftrightarrow \qquad M = -\frac{Fh}{2},$$

where M is the bending moment at the flexure end. In above, the corresponding moment was $M_{\mathrm{A}} = \frac{1}{2}Fh$ or $M = -M_{\mathrm{A}}$. Therefore, the moments are equal, but the sign convention has been opposite. The total deflection of the flexure element

$$v_{\mathrm{end,n}} = \frac{f_{\mathrm{n}}c_{\mathrm{n}}}{6}\left(4c_{\mathrm{n}}^2 - 6c_{\mathrm{n}} + 3\right), \tag{C.12}$$

is obtained from Eq. (C.10). If Eq. (C.9), is normalised by factors

$$c = c_{\mathrm{n}}h, \qquad v_{\mathrm{end}} = v_{\mathrm{end,n}}h \qquad \text{and} \qquad F = f_{\mathrm{n}}\frac{EI}{h^2}$$

used by Awtar et al, one obtains Eq. (C.12).

Appendix D

Model for voice coil driving

Voice-coil type linear actuators consist of two cylindrical parts: the one with the permanent magnet and the one with the coil, as depicted in Fig. D.1(a). Permanent magnets create nearly uniform magnetic flux density $\mathbf{B}$ in the small cylindrical gap in the magnet component, as in Fig. D.1(b). Thus, the flux density $\mathbf{B}$ can be assumed to be constant in time and in the location around the wire loop. When the coil part is in the field, the current $i(t)$ flows in one loop located in the magnetic field $\mathbf{B}$. The magnetic field exerts to one wire a force

$$\mathrm{d}\mathbf{F} = i(t)\,\mathrm{d}\mathbf{l} \times \mathbf{B},$$

where $\mathrm{d}\mathbf{l}$ is the vector line element of the wire. The direction of the force $\mathbf{F}$ is then upwards in Fig. 4.53(b), or in the z direction in Fig. 4.53(a). Because the magnetic flux density $\mathbf{B}$ is constant, the total force exerted to N wires is

$$F(t) = N \oint_{\text{wire}} \mathrm{d}F = Ni(t)B\ 2\pi r,$$

where r is the radius of the wire loop. If the total resistance of the wire loop is R, the force is

$$F(t) = \frac{2\pi r N B}{R} E(t),$$

where $E(t)$ is the voltage between wire ends.

When the wire is moving in the magnetic field with velocity $v(t)$, the magnetic field induces an electromotive force, the back emf $\mathcal{E}$, to the wire. The back emf lowers the voltage, and thus the current, across the coil. Therefore, it tends to lower the driving force and coil acceleration. According to Faraday's law, the back emf in one wire is

$$\mathcal{E}_1(t) = \oint_{\text{wire}} \big(\mathbf{v}(t) \times \mathbf{B}\big) \cdot\ \mathrm{d}\mathbf{l} = v(t)B2\pi r,$$

If the driving voltage to the voice coil is $V(t)$, the voltage across the coil with N wires is $E(V) = V(t) - N\mathcal{E}_1(t)$ and the driving force, or the force exerted to the moving coil, is

$$F(t) = \frac{2\pi r N B}{R}\Big[V(t) - 2\pi r N B v(t)\Big].$$

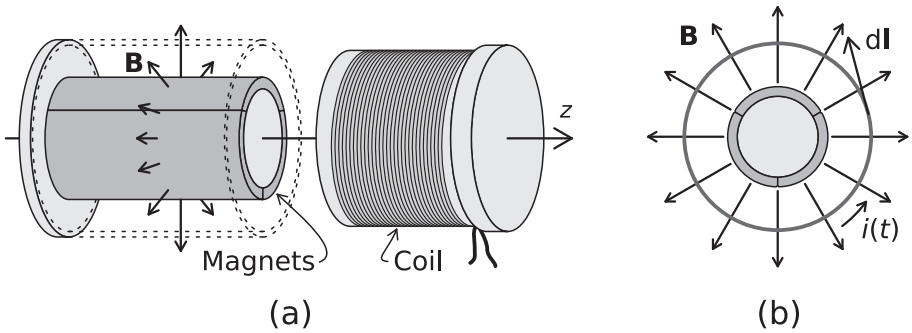

Figure D.1 *Left*: Schematic drawing of voice-coil actuators used for driving Swing III interferometer. The left component had strong permanent magnets producing nearly uniform magnetic field in to the gap under the casing drawn using dashed line. The wired component moves in this field when a current is flowing in the wire. *Right*: The wire loop (b) in the magnetic field with density **B**. The vector line element d**l** is also marked. If the current $i(t)$ flows anti-clockwise, the force **F** exerted to the wire is upwards from the paper plane or in the z direction in (a).

Often this equation is presented as

$$F(t) = \frac{k_f}{R}\Big[V(t) - k_b v(t)\Big], \tag{D.1}$$

where k_f is the force-current ratio and k_b is the back emf constant. The both constants are equal to $2\pi r N B$ in this approximation.